A Multi-Disciplinary Study of the Early Stages of Beta Amyloid Aggregation

Onorio Claudio Mancini

Thesis submitted to the University of Strathclyde for the degree of Doctor of Philosophy

Department of Chemical and Process Engineering
University of Strathclyde
September 2017

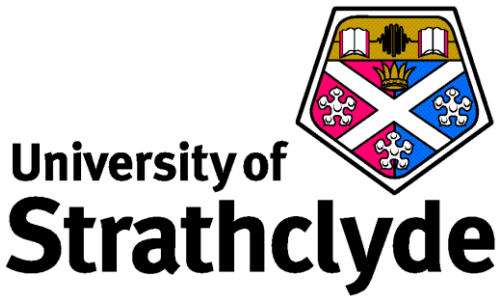

‘This thesis is the result of the author's original research. It has been composed by the author and has not been previously submitted for examination which has led to the award of a degree.’

Signed:

Date:

Acknowledgements

I would like to thank Dr. Paul Mulheran (first supervisor) and Dr. Olaf Rolinski (second supervisor) for the guidance, support and aid given to me throughout the course of my research. I would also like to give thanks to Dr. Karina Kubiak-Ossowska for her assistance with Archie-WeSt and NAMD simulations.

I am also grateful to my colleagues within the “Simulation and Modelling” Group in the Chemical Engineering Department and those within the Photophysics Group, as both were essential to my development towards being a fully-rounded student.

I would also like to thank my close friends and family who supported me throughout the course of my work. Finally, a special thank you to Nicole for her endless love and support.

Abstract

Amyloid fibrils have been linked to many diseases, with different proteins being associated with different health issues. The aggregation of Beta Amyloid (Aβ) peptides can lead to Alzheimer's disease. These peptides are found in the body naturally, although Aβ function is still not clear. The aggregation process is still a matter of research, however it is widely accepted that a lag period is followed by rapid aggregate growth and then a saturation phase where growth halts. Understanding how and why this happens is imperative for disease prevention. It has been found that toxicity occurs during the formation of oligomer.

Collaborative work involving simulation and experimental methods has become commonplace, improving the understanding of this process. Consequently, the work presented here is a multidisciplinary study of the early stages of amyloid aggregation in $A\beta_{1-40}$ and $A\beta_{1-42.}$ These are the two most common species and are 40 and 42 amino acid groups long respectively. They have been studied through the use of Molecular Dynamics (MD) and Monte Carlo (MC) simulations, which have been complemented by probing $A\beta_{1-40}$ with the experimental methods: fluorescence spectroscopy, fluorescence anisotropy and dynamic light scattering.

Experimentation proved challenging, due to the noise encountered in Aβ samples and alternative solvent compositions were studied in an attempt to overcome this. These experiments had limited success but when combined with simulation models, revealed potential insight into the aggregation through the movements of the tyrosine (Tyr) side-chain, an amino acid group found in the Aβ proteins. MD simulations and MC simulations were used in order to probe the underlying mechanisms surrounding Tyr movements and their environments during the aggregation process and how it affects fluorescence anisotropy. The MD simulations also revealed conformational changes in the protein due to the presence of ions and discovered two new Tyr orientations which occur in protofibrils.

Contents

1. Background

1.1. Introduction

The global population that is being affected by amyloid-related diseases (amyloidosis) is growing yearly due to the ever increasing average life expectancy and is expected to affect 65.7 million people by 2030 [1] [2]. There are over 20 diseases that are caused by amyloidosis, including Alzheimer's disease, Type 2 Diabetes (and possibly inclusion body myositis [3]). The aforementioned diseases all share the defining characteristic of amyloid fibrils being deposited in the area of the body related to the specific disease the patient is suffering from, i.e. in the case of Alzheimer's and Dementia the fibrils are localised to the brain formed from Beta Amyloid (Aβ) proteins, and in Type 2 Diabetes the fibril deposits are found in the pancreas, caused by islet amyloid [4]. The fibrils are formed from aggregation of naturally occurring proteins found in the body and they can differ from disease to disease. At some point during the aggregation process it causes extreme cellular degeneration (Figure 1) [5]. In fact, recent studies have pinpointed the toxic nature of the oligomer intermediate (that necessarily forms before large fibrils) as the most probable cause for the cell degeneration [6].

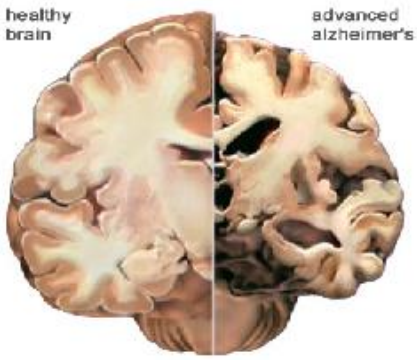

Figure 1 - **Degenerative effects of Aβ** from Jannis Productions [7]

Though these diseases are well documented, there are still significant gaps in the understanding of what causes the aggregation process to occur. This makes prevention of these diseases difficult, as there is no known way to deter, halt or

reverse the process. In a drive to remedy this, researchers all over the world are furthering the work done in the field. However, due to limitations in current experimental methods, it is becoming harder to extract quality information surrounding the fibril aggregation mechanisms as most techniques are open to interpretation, making it very difficult to determine the correct aggregation pathway(s).

In more recent years there has been a lot of collaborative work between experimental and computational work. An example of collaborative work is seen in work by Wagoner et al [8], who have used Molecular Dynamic simulations of various short chain proteins (including Aβ fragments) to see how they aggregated, comparing them to the experimentation. They observed both fibril aggregation and amorphous aggregation caused by various residues contained within the short fragments (which could not be observed experimentally). Another example of collaborative work from Kent Kirshenbaum and Valerie Daggett used molecular dynamics to reproduce results seen experimentally for $A\beta_{1-28}$ at varying pH. This work revealed information about the conformation of the truncated protein chain and also observed the transition from α-helix structure to beta-sheet structure [9]. Zykwinska et al also used atomic force microscopy and Monte Carlo methods to investigate the self-assembly process of small proteins into large beta-sheet rods. They revealed a detailed description of the conformation of the aggregate and used Monte Carlo to reveal that the driving force for the aggregation process was proper alignment of the proteins [10]. It is clear that combining both methods is a powerful tool for discovering more about these amyloid fibrils, for more see literature review below. The work displayed here is used to help bridge the gap between experiment and modelling.

The linking of the two methods in this work has helped create a more cohesive understanding of what the discoveries from the experimental methods are and how they relate to each other, as well as furthering work done previously. The work here helps create a clearer picture of what is potentially happening throughout the aggregation process.

In this thesis a study of Aβ is undertaken; as stated previously Aβ is the protein associated with Alzheimer's disease. Due to the size of Aβ and its aggregate forms, any equipment capable of monitoring and measuring the nanometric and micrometric scales are suitable for extracting information from the protein. The experimental methods produced here are Fluorescence Lifetime Spectroscopy, Fluorescence Anisotropy and Dynamic Light Scattering.

These experimental methods are then complemented using Molecular Dynamics (NAMD) and Monte Carlo computational methods. They have been used to study the aggregation process both on an atomistic level and a larger, coarser level. In doing so, new and old experimental methods may be able to extract more information about what is happening based on these discoveries. While the aforementioned methods are the focus of the research in this project, an overview of other common experimental methods will be given here, which can be read in more depth in the summary of Li et al [11].

1.2. The Aggregation Process

Aβ is formed from the APP precursor which is made of up to 770 amino acids [12]. The APP is cleaved by three enzymes named α, β and γ-secretases (which are different types of proteinase enzymes) [13] [14]. APP is most commonly cleaved at the point between the lysine (K) and leucine (L) residues by the α–secretase shown in Figure 2, creating the sAAPα protein, which contains everything above the lysine residue at the cleaving point shown in Figure 2. The first 16 residues that would make of Aβ proteins are a part of this protein. This is followed by the γ-secretase cleaving the protein, which leaves a small peptide called p3 (made up of the proteins between the two cleave points) to be released into the extracellular space and the rest of the protein to be released to cytoplasm.

However, there is a secondary pathway, which releases sAPPβ due to the β-secretase causing the initial cleave between the methionine (M) and aspartic acid (D) residues. This is then followed by the γ-secretase cleaving the protein, creating an Aβ peptide (length varies depending on the cleavage point) which is released into the extracellular space instead of p3. The remainder is again released into the cytoplasm [12] [15] [16] [17].

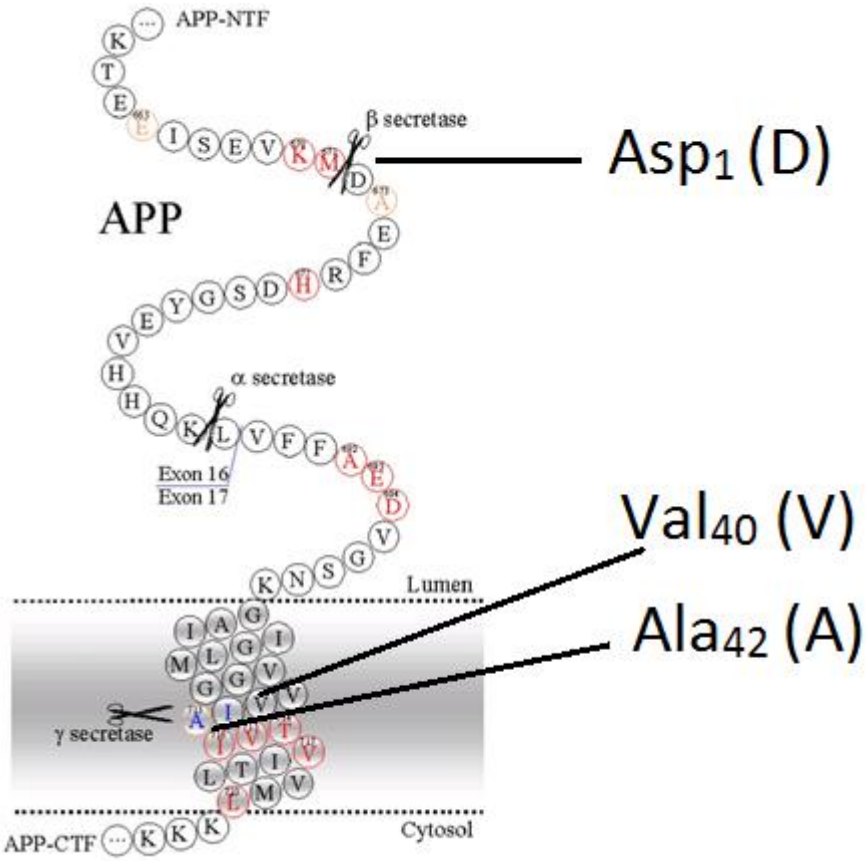

Figure 2 - Amino Acid Sequence of APP edited from "Cellular and animal models for high-throughput screening of therapeutic agents for the treatment of the diseases of the elderly in general and Alzheimer's disease in particular" [13]. Residue labelling here, follows the standard scheme [18]. First and last residues of $A\beta_{1-40}$ and $A\beta_{1-42}$ are highlighted.

Aβ peptides are usually made up of a chain of 36-43 amino acids [19]. This includes the tyrosine (Tyr) residue, shown as "Y" in Figure 2, which is crucial for the fluorescence experiments and is the only fluorescent molecule in Aβ peptides. The most common types of Aβ peptides are $A\beta_{1-40}$, which is made up of 40 amino acids and $A\beta_{1-42}$, which has 42 amino acids. The difference between the two proteins is the addition of two hydrophobic amino acids (isoleucine, I and alanine, A) at the C-terminus (see Figure 3). The hydrophobic sections have been linked to the conformation of the proteins and the aggregation process, giving possible reasons for why $A\beta_{1-42}$ aggregates more readily than its $A\beta_{1-40}$ counterpart. This has been observed through experimentation and simulations [20] [21] [22].

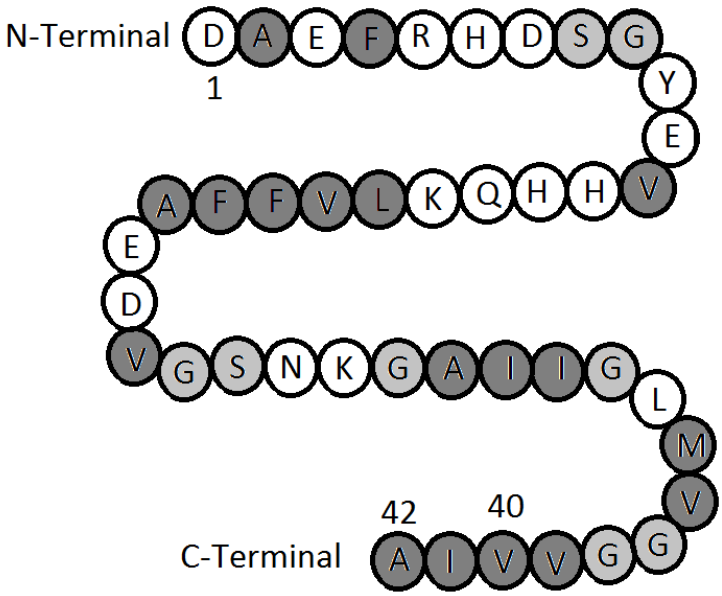

Figure 3 – Representation of $A\beta_{1-40}$ and $A\beta_{1-42}$ amino acid sequence. White circles represent hydrophilic residues. Dark grey represent hydrophobic residues. The light Grey residues are relatively weak and are therefore uncharged. The single letter code is used here for each residue [17].

The normal functionality of Aβ peptides are not fully understood, as animals that lack the presence of this peptide show no notable changes to physiological functions [23] [24] [25]. Despite this there are some potential explanations for the role of Aβ in vivo. Bogoyevitch et al [26], [27] shows that the peptides are a potential requirement for kinase enzyme activation. Other potential uses are oxidative stress protection [28] [29], cholesterol transport regulation [30] [31], as a transcription factor [32] [33] or perhaps Aβ has some role to play in the prevention of microbial activity [34]. Aβ peptides are found in healthy humans and mammals; specifically in the brain and cerebrospinal fluid [35].

Regardless, Aβ peptides must be in one of their native states in order to perform their appropriate functions. As Aβ peptides have various possible conformations, this thesis uses “native” to describe the conformations which do not lead to aggregation (leading to degenerative effects). Those that are theorised to cause aggregation are considered the “non-native” or “misfolded” proteins. It is believed that high concentrations of the protein can lead to it misfolding [36]. If it folds into a non-native conformation, it will not be able to activate on a biological level and this misfolding could lead to the eventual aggregation of the oligomers and then the

rapid growth of fibrils, as shown in Figure 6. The body normally has ways of dealing with misfolded proteins, destroying them instantly [37], but some may still evade the process.

Figure 6 shows an example aggregation pathway that could explain the aggregation of Aβ peptides based on the observation of the lag phase, growth phase and saturation phase seen in experiments. It is widely accepted that the peptides aggregate to form toxic oligomers (dimers, trimers tetramers etc.), which then rapidly grow to form the final fibril structures. The intermediate steps of the aggregation process are short lived, and therefore it is very hard to retrieve any information about these stages. The oligomers start to form beta-sheet structures such as protofibrils (see below in Figure 5 and Figure 6), which can stack to create long protein aggregate strands known as protofilaments. These protofilaments are long single strange fibrils that twist together, forming a “rope-like” structure (see Figure 6) which are the mature fibril structures [38]. The final fibrils tend to be on the micrometric scale and are relatively straight with no branching present with a 6 to 16 nanometer diameter. As detailed above, the aggregation is concentration dependant and if there are not enough proteins in the system the proteins cannot form their aggregates, which suggests there is a critical concentration for aggregation [39].

However, the potential pathways and the mechanisms behind the aggregation process are widely speculated despite the fact that all theories include the lag, growth and saturation phases. A reason for the lag phase can also be explained by proteins initially misfolding slowly and once enough misfolded proteins are present they can aggregate together rapidly [40]. The misfolding could also be responsible for the formation of oligomers (small aggregates such as dimer trimers and tetramers) which then leads to the rapid aggregation. Regardless, at some point during the early stages of aggregation oligomers, protofibrils, protofilaments and fibrils form and a sudden exponential growth phase can be observed. The causes of the potential misfolding and the exponential growth phase are still unclear.

There are many potential models explaining how Aβ misfolds, one example is metal ion binding [41] [42]. The metal oxide bridging point allows the proteins to form dimers, which can then stack to create oligomers. As the oligomer increases in size, the metal oxide breaks away from the aggregate, releasing hydrogen peroxide to the system which would be responsible for the toxic effects. From here, the oligomers

begin rapidly aggregating. However, this is only a hypothesis as aggregation can also occur in systems that do not appear to have metal ions present, as is shown in work at Strathclyde previously [43] [44], as well as the work presented in this thesis.

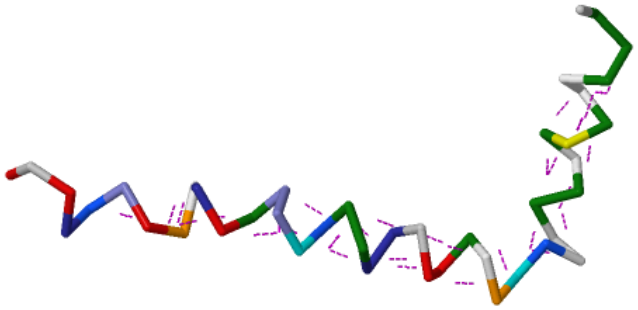

Figure 4 - $A\beta_{1-42}$ backbone with residues highlighted as different colours and hydrogen bonds shown as purple lines. Image from RCSB PDB (www.rcsb.org) ID 1IYT. Visualised using JSmol from RCSB PDB (www.rcsb.org) [45] from work by Crescenzi et al [46]

Another model for what potentially causes the misfolding (if it occurs) involves the formation of β-pleated sheets (beta-sheets). It has been suggested that the protein begins in an α-helical conformation with hydrogen bonds running parallel to the backbone seen above in Figure 4. At some point the protein then misfolds due to perpendicular hydrogen bonding, which creates β-pleated sheets that take on a "hairpin" like shape [47] [48].

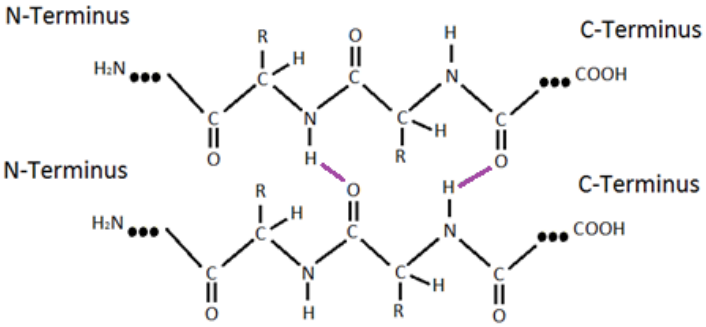

Figure 5 – Example of Parallel β-pleated sheet (beta-sheet) with hydrogen bonds shown in purple. R represents a hydrocarbon chain of any length.

As shown in Figure 5, a beta-sheet forms when two polypeptide chains run adjacent to each other, causing hydrogen bonding between the oxygen and hydrogen atoms from both chains. This leads to an ordered, rigid structure, made up of layers of polypeptides and appear to be a key feature of Aβ fibrils [49]. Beta-sheet structures contain an alternating pattern of the R, carbonyl (C=O) and amine (N-H) groups, which allows for the hydrogen bonding to occur. Beta-sheets are also defined by the

fact that the hydrogen bonds run perpendicular to the backbone, which in Figure 5 shows vertical hydrogen bonding and the backbone running horizontally. When the N and C terminus are mirroring one and other, the beta-sheet is said to be parallel and when they are opposite they are considered to be anti-parallel. The hairpin like structure forms by the protein folding on its backbone, creating a “U” or “J” shape with anti-parallel beta-sheets forming between the two section of the backbone that run adjacent. In the case of $A\beta_{1\text{-}42}$ it appears that there are two folds with three parts of the backbone forming beta-sheets creating a “U”-like shape (or horseshoe) as depicted in Figure 6 for the oligomers and also in Figure 8, shown by the double horseshoe. Regardless of how the misfolding occurs, beta-sheet structures are a key feature of Aβ fibrils, as the hydrogen bonding is the reason for the formation of these long protofibrils (Figure 6).

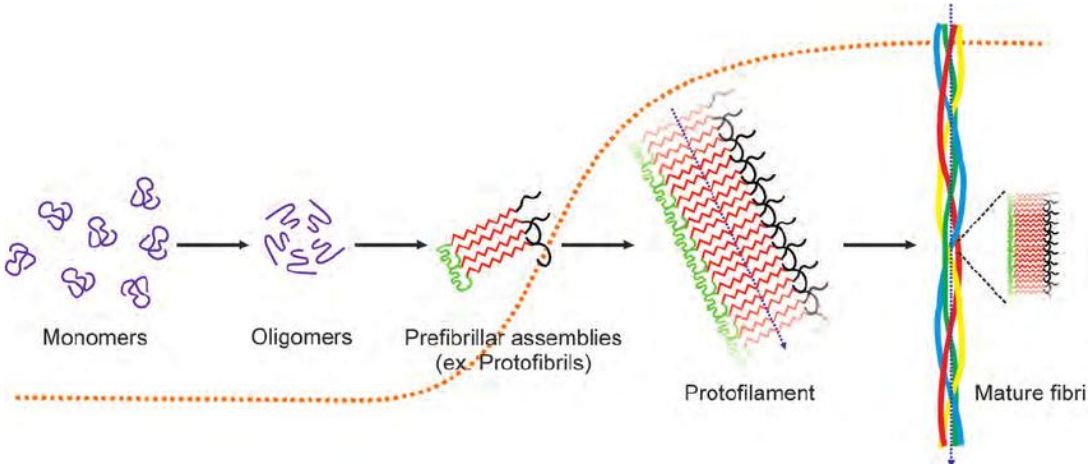

Figure 6 - Depiction of monomers, oligomers and protofibrils and mature fibrils taken from work by H.P. Herzig et al [50]

1.3. Literature Review

There are many experimental methods used to probe Aβ proteins as the monomers are on the scale of nanometers and the aggregates that form are on the micrometre scale and beyond. As there is no single method that encompasses both scales many different techniques are used to create an overall picture of the aggregation process.

1.3.1. NMR Methods and Related Findings

A very common method used to attain information regarding atomic structures of the monomers, oligomers and fibrils is Nuclear Magnetic Resonance (NMR) Spectroscopy. NMR uses the magnetic properties in the atoms ‘nuclei’, the sample

is subjected to radiofrequency irradiation [51] in a strong magnetic field. A 3D model can then be produced through the resonance signals.

Solution-state NMR is used to determine properties of the monomers and oligomers, this is because the initial stages of amyloid aggregation are soluble [52] which is a prerequisite for this method to work, and is the reason it cannot detect the insoluble protofibrils or fibrils. NMR is used to identify residues, but repeating residues which are found in most proteins can cause overlap in the signals. The resulting spectra tend to overlap so much that limited information can be concluded from the method without accompanying information. Oligomers obscure results further as there are multiple peptides with multiple amino acid groups present, increasing the number of repeating units. This makes it very difficult to interpret any of the data, but the changes in the characteristics can be used to monitor the changes in monomer conformation (folding) and can be used to monitor the change from monomers to oligomers [53] [54] [55]. This experimental method was initially used to look at Aβ fragments; there are now methods to do NMR experiments of full chains in aqueous solutions at a neutral pH [56] [57]. The reason for using fragments was originally to increase solubility, prevent the aggregation and dissociate peptide aggregates [58] [59] and the results from this method were also explored using Molecular Dynamics [9]. This method was used in conjunction with circular dichroism (CD) spectroscopy (discussed below) to produce the full chain structure of $A\beta_{1\text{-}42}$ used in the Molecular Dynamics work in this thesis as shown in Figure 7 [46].

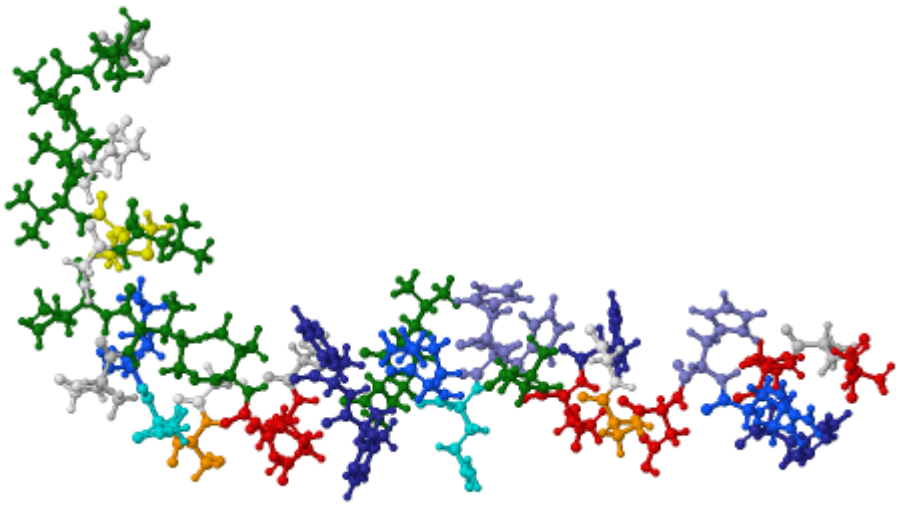

Figure 7 - 1iyt.pdb: Molecular Dynamics $A\beta_{1\text{-}42}$ structure found from NMR and CD experiments from work by Crescenzi et al [46]. Visualised using JSmol from RCSB PDB (www.rcsb.org) ID 1IYT [45]

Another study showed the presence of many different molecular structures of $A\beta_{1\text{-}40}$ and their varying toxicity depending on the environment of the fibril [60]. A full length $A\beta_{1-40}$ fibril structure was found using NMR and the results were different from those shown previously [61]. The researchers deduced that the reason for this is likely the sensitivity of the conditions required for Aβ fibril formation, which were also different in their experiments [47].

Solid State NMR has been used alongside fluorescence methods to show structural differences between the possible nontoxic and toxic forms of Aβ oligomers. It was shown that the residue conformation from 22-29 and 1-9 are different in oligomers than those for fibrils perhaps suggesting these are the cause of the toxicity [62]. NMR and many other methods discussed below have been used more recently to discover the conformation of $A\beta_{1\text{-}42}$ where it bends into a double horseshoe-like shape that potentially leads to the aggregation process that creates these protofibrils shown in Figure 8 [63].

(A)

(B)

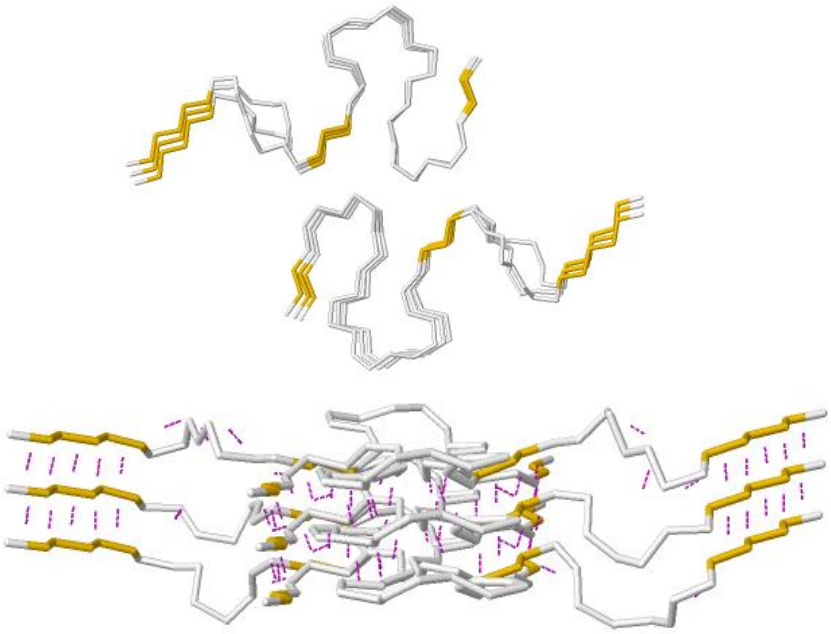

Figure 8 - 2nao.pdb: Molecular Dynamics $A\beta_{1\text{-}42}$ hexamer protofibril structure found from NMR and CD experiments from work by Wälti et al [63]. Visualised using JSmol from RCSB PDB (www.rcsb.org) ID 2NAO [45] (A) is a top down view with the beta-sheets highlighted in orange. (B) is a side view with beta-sheets highlighted in orange and hydrogen bonds highlighted as purple lines running perpendicular to the backbone.

1.3.2. Common Methods for Secondary Structure Detection

Various Methods involving spectroscopy are used to gain valuable information about secondary structures in proteins, primarily in vitro due to its relative simplicity but in some cases can also be used in vivo.

Circular Dichrosim (CD) Spectroscopy is used to measure differential absorption of circularly polarized light, and depending on the wavelength can detect secondary structures in the far ultraviolet region. These secondary structures include α-helixes, which have negative bands at 222nm and 208nm and a positive band at 193nm [64], and beta-sheets, which are detected with a negative band at 218 nm and a positive band at 195 nm [65] [66] (see Figure 9). Therefore, this method has been successfully used to establish that α-helix / random coil secondary structures are unravelled and the formation of beta-sheets begins to occur. It has also been used in studies involving metal-bonded $A\beta_{1\text{-}40}$ and $A\beta_{1\text{-}42}$, which has revealed different initial conformations of the proteins in the presence of different metal ions in conjunction with thioflavin-T fluorescence and scanning force microscopy [67]. It should be noted that this method is limited to in vitro analysis of monomers, oligomers and protofibrils of various proteins [68] [69] [70].

aw

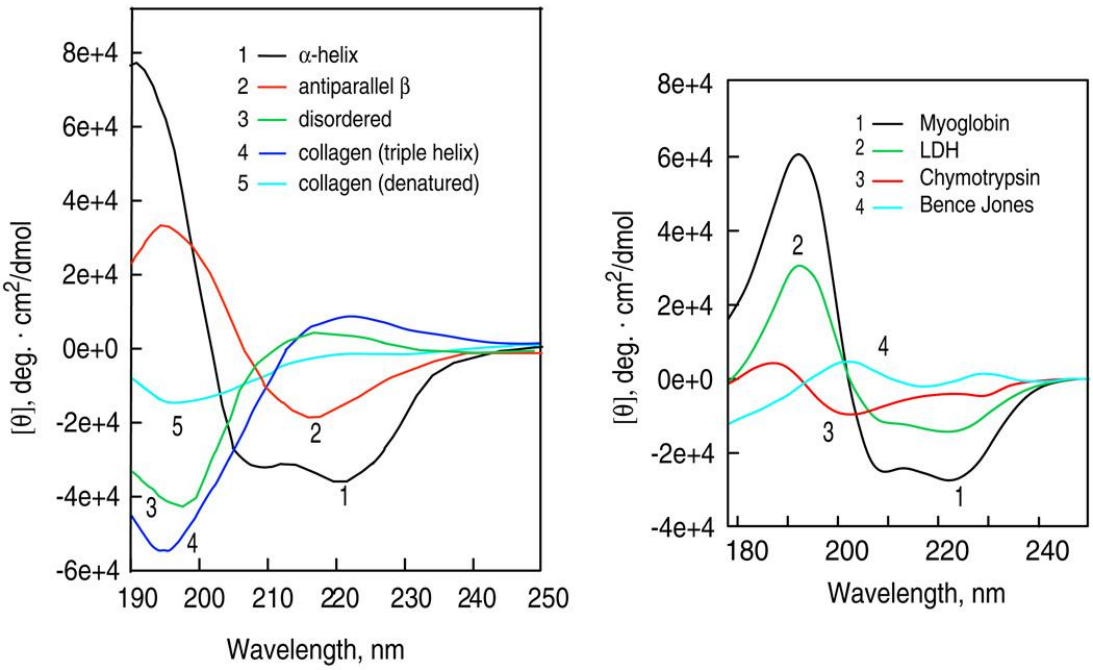

Figure 9 - CD results of secondary structures at pH 5.7. Results by Dr. W.C. Johnson and taken from work by N.J. Greenfeild [66]

X Ray Diffraction can also reveal details about secondary structures and can also determine the preferred orientations of the molecules. This method has successfully shown that almost all amyloid structures have their beta-sheet strands ordered parallel to the fibril axis (as discussed above) [71] and is normally combined with neutron scattering. Small angle neutron scattering method has been used to gain information about the area and length of $A\beta_{1-40}$ amorphous aggregates forming micelles, which was composed of 30-50 monomers and had a 2.4nm radius and a cylindrical length of ~11nm [72]. Although these methods are used to find information regarding the aggregated states, which occur after the damaging oligomer have formed, it is still necessary to study and understand these.

It has also been found that seeding samples with pre-aggregated fibrils greatly affected the amyloid fibril formation of human lysozyme (another fibril forming protein) using a combination of X-ray diffraction, electron microscopy, thioflavin-T binding, and Congo red birefringence [73]. X-ray diffraction has also been used to find that dehydration significantly affects the molecular structure of various beta-sheet forming prions, which is an indicator of water playing a larger role in stabilising amyloid fibril structures [74]. This seems sensible as the previous methods discussed showed the presence of hydrophobic and hydrophilic sections, that we know to be an important part of the process.

The last common method used for in vitro analysis of secondary amyloid structures is by staining the amyloid with a dye, then using spectroscopy to monitor the sample. The most common dyes that are used are Congo Red and Thioflavin T. When Congo Red is bound to a sample, it targets and stains amyloid structures, allowing the formation of fibrils to be monitored [75] [76]. Thioflavin T, on the other hand, has polar and non-polar functional groups which lead to micelles in aqueous solutions that bind to the beta-sheets which greatly enhance fluorescence when compared to unbound Thioflavin T [77].

Fluorescent dyes can affect the aggregation process as shown by Strathclyde researchers, who used the dyes known as 7-diethylaminocoumarin-3-carbonyl and Hilyte Fluor 488 to show how they slowed down the aggregation process and also how it alters the characteristics of oligomerization [43]. They found that samples containing the dyes did not form further beta-sheet structures, maintaining a low-

level response but did note an increase in rotational times implying that oligomers were forming but the dyes prevented the formation of fibrils.

The aggregation profile seen when using Thioflavin T, begins with a lag phase followed by an exponential grow phase and a saturation/maturation phase. This is the important and widely acceptable model for Aβ aggregation. This implies that no beta-sheets (and therefore no fibrils) are present till the later stages of the aggregation, proving the existence of the lag phase. This is a central characteristic as the late presence of beta-sheets allows us to speculate what kind of aggregation mechanisms could cause such a profile and is seen in many proteins including Aβ [78] [79] [80] [81] [82]. As discussed previously, protein misfolding occurring prior to beta sheet formation could be the reason for this lag phase. However it is questionable if the dyes affect the aggregation as results for one experiment revealed changes in the toxicity due to dyes [83].

1.3.3. Microscopy Methods and Structural Findings

Electron microscopy (EM) can be used to attain information regarding the oligomers protofibrils and fibril structures. The first main method used is Transmission EM (TEM), which creates a focused high voltage electron beam, which is then passed over the sample and assuming the sample is thin and electron-transparent then an image can be created by the electrons transmitted. This image can be used to get information regarding the shape, and size of the structure.

TEM can be used to characterise various states regarding Aβ, for example by combining DLS EM and CD spectroscopy the determination of the broad size distribution of the oligomers and fibrils allowed the researchers to create a potential, simplified model seen in Figure 10 [84]. TEM and Atomic Force Microscopy were used to probe $A\beta_{1-40}$ and $A\beta_{1-42}$ monomers and oligomers (dimers and trimers) discovering the toxicity of these species only occurs in the presence of microglia [85]; a non-neural cell found in the brain and spinal cord responsible for functions such as immune defence in the central nervous system and removes infectious agents and unnecessary neurons [86] [87]. This toxicity is responsible for causing nerve cell degeneration [85]. Protofibrils have been found to potentially form from oligomer clustering and then the formation of beta-sheet structures and growth of protofilaments appear to occur almost simultaneous, this appears to be the reason that once beta-sheets form there is rapid growth [88] and fibrils [89]

The TEM method has also been used to observe fibril growth inhibition through the use of small hydrophilic proteins [90]. Inhibiting the growth of the fibrils is important in trying to cure these amyloid related diseases; however inhibiting fibril formation does not prevent oligomers from forming. This work will open up opportunities to study oligomers and their toxicity as well as perhaps eventually find an inhibitor or reversible process.

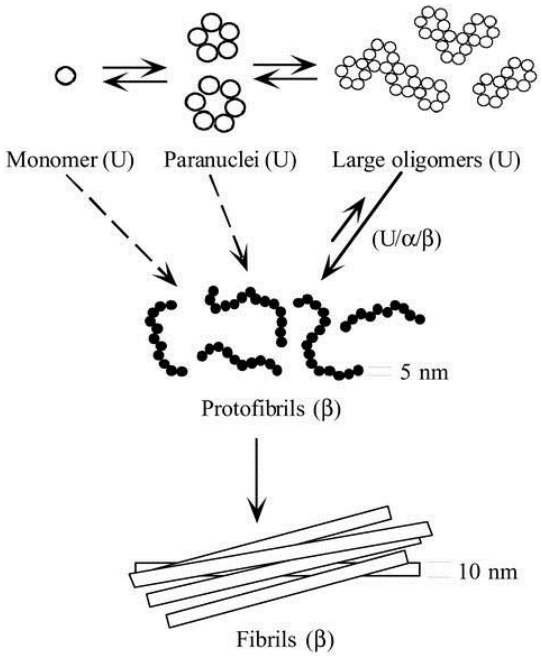

Figure 10 - Simplified Model of Aβ Aggregation Using TEM Method. From work by Bitan et al. [84]

Another method used to gain information about the structure is Scanning Tunnelling Microscopy which uses a sharp conductive tip to scan the sample surface taking note of the surface characteristics, such as the electron density contours of the surface at an atomic resolution. If the tip is close enough to the surface a current is generated and the tip is then scanned over the entire system. The voltage required to maintain the current will increase or decrease as the contours create changing distances between the surface and the conductive tip. This effectively creates an image of the system through scanning due to the sudden changes in the voltage. This only works if the sample is electronically conducting, although it is difficult to determine if proteins are conductive. Some studies do suggest that they are semi-conductors [91]. The ribbon-like (twisting) structure of Aβ filaments was discovered using this method visible in Figure 11 [92] which was then later complemented with the discovery of the right handed twist [93]. Another experiment showed $A\beta_{1-40}$

monomers and oligomers were measured and found to be 3-4nm and 6-7nm [94]. The effect of buffers on aggregation mechanisms is still not fully understood and it is questionable if the buffers affect the aggregation mechanism.

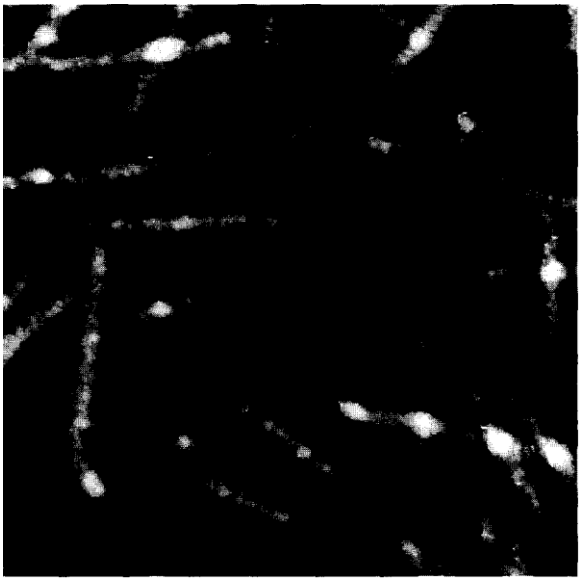

Figure 11 - STM image showing ribbon structure of $A\beta_{1-40}$ filament from work by Shivji et al [92]

More recently NMR and Scanning Tunnelling Microscopy have been used alongside other methods in order to strengthen the findings discussed previously regarding the double horseshoe shape seen for $A\beta_{1-42}$ (Figure 8). They also discovered more features regarding the shape, such as salt bridges and the hydrophobic cores present in dimers [95].

The final method discussed here regarding structure is Atom Force Microscopy (AFM). It is a high resolution topography method. A tip is used to scan the surface of the sample, using repulsion forces to move itself off the surface. This movement can be measured to create the map of the surface structure, assuming the force being applied to the surface remains constant. The use of AMF has discovered the characterization of the assembly process of the oligomers to fibrils. However, as the fibrils must be firmly attached to a support during this method, it will likely cause some variation in the actual process [96].

AFM can monitor oligomer growth all the way through to fibril formation, which makes it advantageous over some of the other methods discussed here. Constant monitoring of $A\beta$ aggregation is extremely important during the first 24 hours or so and thus making this a very valuable technique. Individual $A\beta_{1-42}$ oligomers could be

viewed using this. It was found that the dimensions would vary between 1-3nm in height and 5-10nm for width and length. Protofibrils were found to be 40nm in length with 6nm-8nm. These researchers also diluted the solution to the point that aggregation would not occur past the oligomer stage, to view these oligomers in more detail [97].

1.3.4. Tertiary and Quaternary Structure and More Common Methods

The tertiary structure of a protein is the arrangement of the side-chains and the overall 3D structure and the quaternary structure is the arrangement (and number) of all the proteins within a complex and can even refer to an aggregate as small as a dimer [98] [99]. As structures become larger, some of the techniques used to determine these structural features are required to be low resolution, and so complementary high resolution methods are needed (discussed above).

Quaternary structures can be studied using the Electron Spin Resonance (ESR) spectroscopy, which is similar in principle to NMR but tends to be more accurate. ESR observes the spin of unpaired electrons, whereas NMR studies the spin of nuclei, and due to the fact that proteins do not tend to have unpaired electrons the background noise that would be created in ESR experiments is kept to a minimum. This allows ESR to be commonly used to get information regarding protein structures such as orientation, dynamics and ligand binding. It is also much quicker to run experiments using ESR when compared to NMR due to the sensitivity and lack of noise. One such experiment found that Aβ toxicity could be caused by the production of oxygen radicals during the oligomer stages of the aggregation process [100]. It is proposed that the Met_{35} residue in Aβ proteins causes radicals to form and the cause of fibrillation process of Aβ is toxic.

Further work has shown that these free radical groups could actual form due to metal ions such as Cu(II) and Fe(II). The results suggest that the metal ions binding to Aβ peptides cause the aggregation to occur, although this is widely speculated as aggregation occurs when these ions are not present, as discussed previously. Once the ions are bond it is hypothesised that the dimers are linked by these ions, creating a flat dimer that is the basis of the fibril aggregation process, at some point during the fibrillation the metal oxides get removed and release the free radical Hydrogen peroxide, which could cause the neurodegenerative diseases [41] [42] [101] [102].

X-Ray absorption spectroscopy (XAS) is useful for gaining atomic structural properties of amyloid structures when bonded with metal ions [103]. This method can be used to study the differential copper coordination within Aβ oligomers [104]. As with most methods, only specific information can be gained and so many different methods are required to gain a firm understanding of what happens during the aggregation process. For example, Molecular Dynamics and XAS where combined to determine atypical structural aggregation of Aβ in the presence of Zn ions, which bond near three or four Histidine (His) residues of nearby peptides [105]. The structure was found to only appear in the presence of the superoxide dismutase enzyme, responsible for the catalysing O_2^- radicals into either oxygen (O_2) or hydrogen peroxide (H_2O_2). These findings show the successful collaboration between computational and experimental work. XAS was also used to track the involvement of Iron in the aggregation process in vivo using rats; they were successful in showing the presence of metal oxides indicating that iron could play a role in the early stages of amyloid aggregation, this is only speculation, as discussed above [106].

Hydrogen-Deuterium Exchange is another common method used where hydrogen atoms are replaced by deuterium atoms from the solvent [107]. For Beta amyloid it is typical to use 95% dimethyl sulfoxide and 5% dichloroacetate as a quenching buffer [108]. The system is then diluted with D_2O to prevent the reversible reaction occurring. Information is gained due to the fact that in solution some of the proteins will be more exposed to the buffer than others, creating more exchange to the exposed part than the buried areas. NMR or Mass Spectroscopy is then used to monitor the exchange and thus gives information about the tertiary and quaternary structures. However, it should be noted that replacement of hydrogen atoms could cause structural changes to the protein, which cause them to interact differently and could alter the aggregation process. Regardless, this method has been applied to Aβ fibrils to gained information regarding orientation and structure of Aβ fibrils; the C and N termini were exposed to the solvent and the central section of the protein between Lys_{16}-Val_{36} (except Gly_{25} and Ser_{26}) were buried [109]. This structural analysis was used to propose that the middle section of the monomers must be involved in the formation of beta-sheets. A 3D representation of $A\beta_{1-42}$ was proposed using this technique [110]. Mass Spectroscopy has been used to uncover some

details regarding the difference between the protofibril and fibril states in calmidazolium chloride [111].

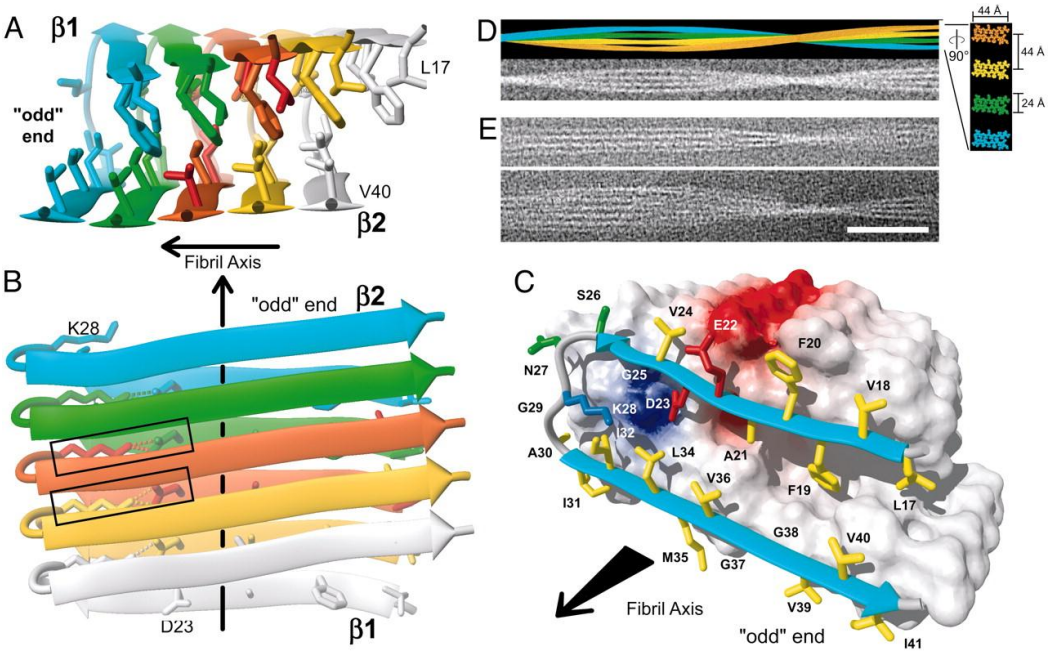

Figure 12 - Proposed Mature Fibril Structure obtained through hydrogen/deuterium exchange measurements from work by Lührs et al [110].

1.3.5. Fluorescence Techniques and Findings

An important method used to observe Aβ aggregates for the work done in this thesis is Intrinsic Fluorescence. Intrinsic Fluorescence (IF) works on the principle of excitation and subsequent emission of the aromatic residue tyrosine (Tyr) in Aβ. This fluorescence is highly sensitive to its local environment, and small changes can greatly affect the emission spectra detected. Environmental changes can cause conformational variations which can lead to the Tyr residue being more or less exposed to the solution. This can change how much the residues are quenched by, which affects the quantum yield. These changes to the local Tyr environment can also be caused by aggregation, due to proximity of other proteins. IF has been used to study the conformational changes of Aβ. The factors that create these changes include; increases in solvent polarity and viscosity results in emissions at lower energies or longer wavelengths, solvent relaxation rate, conformational changes, local environment rigidity, excited state reactions and changes in the radiative and non-radiative decay [112].

In one such experiment Tyr_{10} was substituted for a phenylalanine (Phe) residue and the Try was reintroduced at residue positions 1, 20, 30 or 42. The dynamics of the conformational changes were then monitored by IF, which allowed the researchers to conclude that the C-terminus area of $A\beta_{1-42}$ goes through a great deal of rearrangement during aggregation, whereas the central cluster (17-21) was essential for aggregation to occur and could not be changed [113].

Strathclyde University's Photophysics group have previously studied the IF of Tyr to compare it to Thioflavin T fluorescence. They focused on the section which is commonly known as "lag time" as thioflavin-T fluorescence shows no change in signal at these times. This is because thioflavin-T fluorescence reveals information about the fibril backbone as the dye binds to the beta sheet secondary structure and the early stage interactions from oligomers and monomer-monomer interactions will be completely missed. The Tyr IF experiments show changes in signal through Tyr environmental changes and also demonstrate the effect of concentration on aggregation [114]. An important aspect of subsequent work (that will be discussed in more detail below) is the detection of three lifetimes associated with the Tyr residue (which are linked to the local environment of the Tyr) using IF and the discovery of four rotamer conformations (positions) the Tyr prefers to occupy from collaborative work using MD simulations see Figure 13 [44] .

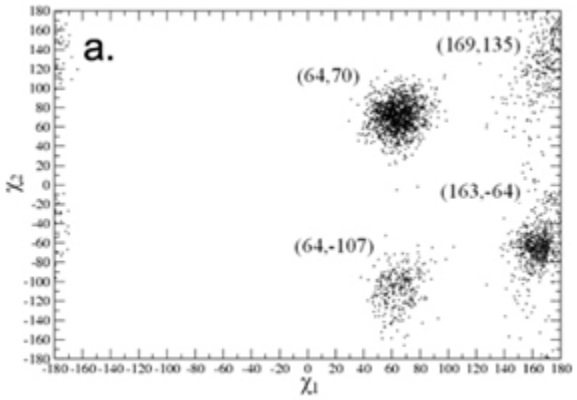

Figure 13- Rotamer states of Tyr observed from previous work at Strathclyde by Amaro et al [44]

Förster Resonance Energy Transfer (FRET) is another fluorescence based technique that works though non-radiative energy transfer from an excited donor fluorophore to an acceptor fluorophore, through long-range dipole-dipole interactions. There must be an overlap in the donor's emission and the acceptor's absorption spectra and adequate alignment of their transition dipole orientations is

required, seen in Figure 14 [115]. The decrease and increase of the donor and acceptor emissions respectively, and the sensitivity to the distance between the fluorophores are the main features of FRET and because of this intra and inter molecular distances can be monitored and measured, as well as protein folding and protein-membrane interactions.

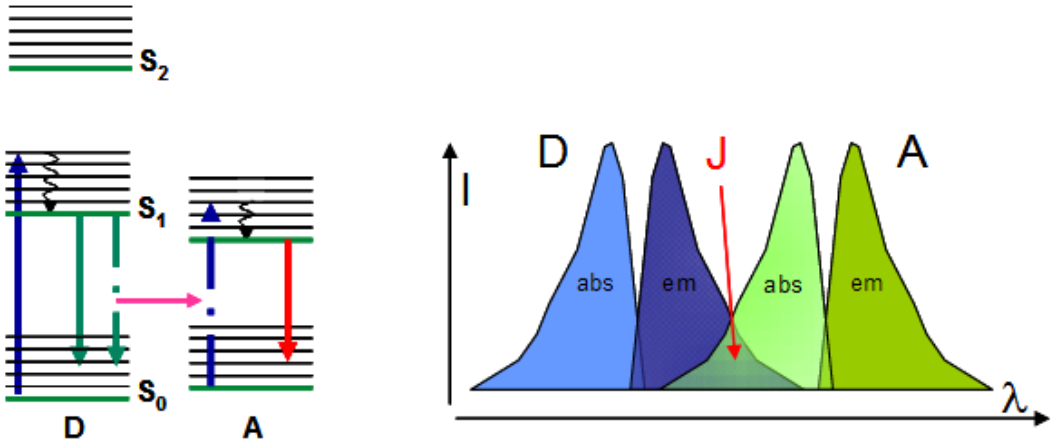

Figure 14 - FRET Mechanics taken from the website of HORIBA Scientific [116]

FRET is usually produced through addition of highly fluorescent fluorophores at points in the protein that will have minimal effect on the aggregation process or mechanisms, whilst allowing FRET to occur. $A\beta_{1-40}$ derivatives containing different fluorophore groups were found to attach to Cys residues in different positions along the sequence. They also found that tryptophan substitution of the Tyr revealed the potential existence of stable $A\beta_{1-40}$ dimers at low concentrations [117]. In another FRET experiment $A\beta_{1-42}$ proteins, which had been altered by replacing 12 hydrophobic residues in the C terminus with other nonpolar residues, were studied using the “green fluorescent protein” (GFP). They studied the aggregation through the fluorescence of the GFP as $A\beta$ aggregation prevents it from folding, which impedes fluorescence from occurring. It was found that these mutant $A\beta$ proteins still aggregated despite the changes to the C terminus, suggesting the mechanisms required for aggregation may not be related the hydrophobicity of this section as other simulations and experiments have suggested [118], further experimentation would be required to verify these findings.

Fluorescence spectroscopy, generally, does not give definitive information regarding the protein and so must be used in conjunction with other techniques, as it is a complimentary technique. Using intrinsic fluorescence of Tyr (or any other

fluorophore) reveals information regarding its local environment. When combined with other techniques that can reveal structural information (beta-sheet formation, conformational information) or information regarding size distributions, it is possible to reveal more information about the sample. It can be used to better probe the sample at a molecular level by revealing changes to the fluorophore environment which is then complimented with the other techniques that can confirm why the changes in the fluorescence lifetimes occur, strengthening the findings and perhaps revealing more information than was possible without the complementary techniques.

1.3.6. Dynamic Light Scattering Techniques and Findings

Size distribution and assembly size measurements are another large topic with regard to fibril formation. Typically used methods include Gel electrophoresis, Photo-Induced Cross-Linking of Unmodified Proteins and Ion-Mobility Spectrometry–Mass Spectrometry which all have good reasons to be used but cannot be used to detect protofibrils or fibrils. That is where size-exclusion chromatography, Analytical ultracentrifugation [11] and Dynamic Light Scattering are superior as they can identify and extract information about fibrils. As Dynamic Light Scattering (DLS) was used in the work presented in this thesis, it will be discussed in further detail.

Light scattering has a variety of different techniques that are used such as Back Scattering, Static Light Scattering, DLS and 3D DLS. DLS measurements are created by firing a laser at a sample and the light that is scattered by the particles in a sample is then detected; it is more suited for large aggregates. This is because larger aggregates will scatter more light because of the proportionality between the square of the particle mass and intensity of the scattered light [119]. DLS may struggle to see the large fibril structures that Aβ eventually become as they are long rod shapes. This is because the equipment gives off inaccurate readings regarding particle size as the fibril becomes longer but the thickness of the fibril strand stays constant, meaning the light that gets scattered (unless it passes through the laser in a specific orientation) will be affected greatly by the change in diffusion speed [120]. This means that the sizes found are not necessarily correct at the later stages, however there is still plenty of information that can be gathered from these experiments and patterns of size increase can be noted, analysed and understood.

DLS is good for resolving the difference between monomer and dimer states if the protein has a known shape, but it cannot in the case of larger oligomers. This is because the hydrodynamic radius is similar to the dimer or monomer state and therefor it cannot be detected, if it differs by less than a factor of 2 [121]. This also means that if the dimer is compact or if there are extended monomers in the system, it will be impossible for DLS to pick up these differences. This is where other methods such as Cross-Linking of Unmodified Proteins, Size-exclusion chromatography and Analytical Ultracentrifugation are more suited to be used in tandem to determine minute size changes more precisely [11].

There has been successful work done in determining the shape and size of the discrete oligomer species which was found in vitro as part of the pathway for oxidative prion aggregation using DLS with complementary methods (EM and CD). The methods were used to study the oligomer pathways taken to create fibrils of $A\beta_{1-40}$ and $A\beta_{1-42.}$ DLS was specifically used to study larger Aβ oligomers which could not be studied with the other methods as shown in Figure 15 [84].

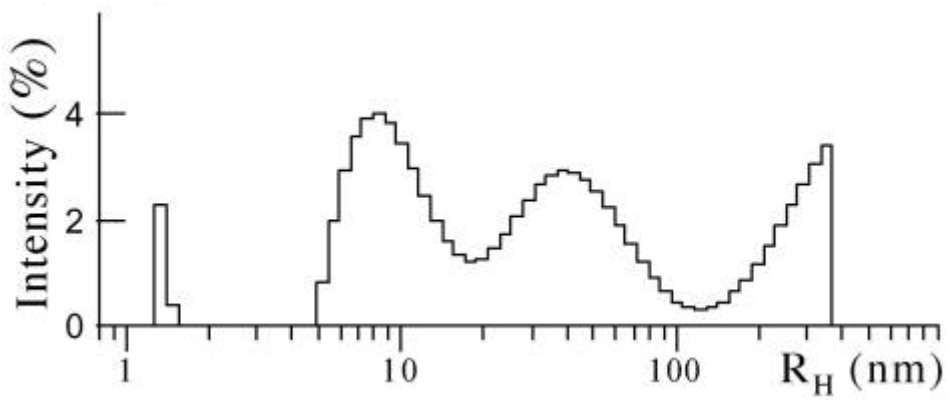

Figure 15 - Size distributions of Aβ oligomers from work by Gal et al [84].

The size distributions found show four distinct populations, which they have attributed to various sizes of oligomers, which is comparable to other experimental methods, further validating the findings.

Using DLS to gain information regarding size distribution at various times throughout an experiment and combining that with other techniques can reveal a much more accurate description of the aggregation pathway. The conformation of the growing size distributions supported by techniques that can reveal, for example, secondary structure information (increase in beta-sheet interactions) or reveal conformational changes reveals at what stage of aggregation that these various features change at.

These distributions can also help with Monte Carlo methods as size distribution over time is important an important factor to consider in these types of simulations.

1.3.7. Molecular Dynamics Techniques and Findings

Molecular Dynamics (MD) is one of the main techniques used currently to get a molecular level insight into many different molecules (See later for more information on how Molecular Dynamics works).

MD simulations with the PRIME20 force field provided further information regarding the reasons for the conformations of the Aβ aggregates, which could be related to the hydrophobic region at the C-terminal, as discussed previously. This was acquired by splitting the monomers into smaller fragments, so that they could see which parts of the protein were involved in the aggregation process. As the proteins were short (5-7 residues long) it allowed for the simulation of many proteins [8]. The hydrophobicity of proteins was studied using MD in order to support potential protein aggregation pathways and which could lead to design of aggregation-resistant proteins [122].

There have been improvements on the AMBER force fields used in MD simulations, such as in 2009 when the corrections of two force fields at 300k were made. The results were compared with NMR experiments and had satisfactory agreement between the two methods. Force fields still have issues such as the over and under estimation of certain variables and improvement through new research avenues is required [123]. However, the current force fields are adequate to give an estimate of many features of proteins.

The CHARMm forcefield, used in the MD work presented in this thesis, have been seen constantly improving and are adequate for studying protein structure as well as other features such as folding and stability. An example of such improvements is seen in 2012 by work by Best et al, where they reported that the model was able to correct the behaviour of the backbone parameters and improved the accuracy of the side chain data for both folded and unfolded proteins. This allows more accurate simulations to be run and the changes did not affect the models ability to simulate the formation of beta-sheet structures in proteins [124]. The work presented here is a combined CHARMm22 and CHARMm27 forcefield model. Recent work comparing older models with the modern CHARMm36 model suggests that there is very little

difference in the conformation and secondary structures but there are differences in the tertiary structures between CHARMm22 and CHARMm36 [125]. Though there are some differences, the use of the force field is still justified as the only notable differences are the tertiary structures which when combined with CHARMm27 give results that are closer to that of CHARMm36.

The potential differences in the secondary structures of $A\beta_{1-40}$ and $A\beta_{1-42}$ were discovered through the use of MD. $A\beta_{1-42}$ has an antiparallel beta-hairpin with involvement from hydrophobic residues 16-21 and 29-36. $A\beta_{1-40}$ also forms an antiparallel beta-hairpin; however the residues involved are 9-13 and 35-37.They also successfully showed that the extra residues attached to the end of $A\beta_{1-42}$ was responsible for the conformational differences between the two [126].

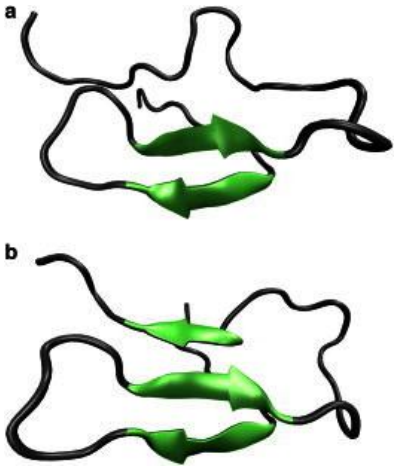

Figure 16 - MD simulation of (a) $A\beta_{1-40}$ and (b) $A\beta_{1-42}$. The anti-parallel beta-sheet structures are highlighted by the green arrows taken from work by Ball et al [126].

The effects of water on Aβ have also been researched using MD simulations, by using fragments of Aβ that form oligomers. Despite the fact that these fragments are not full length Aβ peptides, the results still provide an insight into how the water affects the system. They discovered the presence of different monomer conformations, some of which are prone to aggregation and are positioned similarly within fibrils, which are a possible representation of misfolding. These results showed that the formation of fibrils and oligomers happened in two steps: The first, by expelling water from the hydrophobic sections, which results in disordered oligomers and the second, by aligning to create ordered structures with anti-parallel beta-strand arrangements [127].

The structures and thermodynamics of $A\beta_{16-35}$ monomers (for 5μs) and dimers (for 12μs) were discovered through the use of replica exchange molecular dynamics (REMD). REMD is sampling technique used to take systems that have similar potential energies and sample them at different temperatures, allowing for the discovery of new conformations of proteins. By studying 20 replicas' between 190K and 570K, they could observe the effects of temperature on the structure and also noted the presence of a loop in the backbone chain at residues 22-28 which creates a beta-sheet. It seems this loop acts as an independent unit in both species and is unaffected by local interactions with other side-chains. This loop is also present to some degree in $A\beta_{1-40.}$ These results can be observed in Figure 17. At specific temperatures these results can be compared to NMR results for $A\beta_{21-30}$ [128].

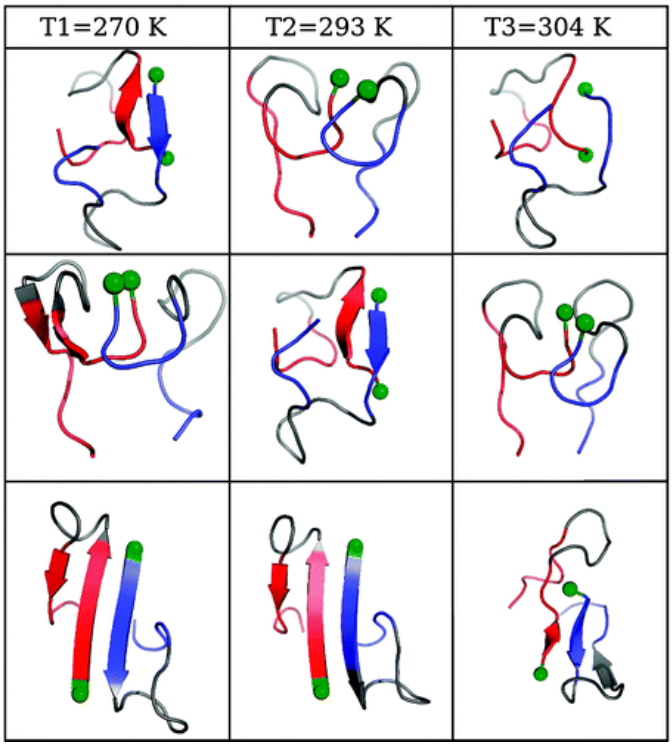

Figure 17 - REMD of Aβ fragments at various temperatures. The two most populated clusters are shown at the top and middle, the bottom is the cluster with the highest beta-sheet content within them. Taken form work by Yassmine et al [128].

Characterisation of $A\beta_{1-42}$ monomers in water was also created using REMD. These simulations were created in order to discover more about the various conformations that $A\beta_{1-42}$ peptides would take in water using an ff99SB force field. In doing so, they replicated results seen in NMR experiments with high accuracy. The results from the MD simulations showed the presence of many different conformations that the

monomers like to undertake. With these structures identified perhaps experimental methods could be created in order to identify the misfolded variants that prefer to aggregate [129].

REMD has also been used to extensively map the Aβ oligomers conformational structures. These aggregates reaching from two to four peptides long, showed different structural shapes from their monomer counter parts and showed the formation of the beta-structure. They also showed that the aggregation interface for these oligomers tend to be within the residue sequence of 10-23. They also compared these results to those seen experimentally with adequate agreement [130].

A simplified version MD, which only solves the equations of motion for particles involved in collisions to save processing time and allow for larger simulations, known as Discrete MD has also been implemented for Aβ aggregation. It was used in order to demonstrate the oligomer forms of $A\beta_{1-40}$ and $A\beta_{1-42}$ and two mutants ($[G_{22}]A\beta_{1-40}$ and $[G_{22}]A\beta_{1-42}$) associated with a similar form of Alzheimer's disease where the 22 residue has been replaced with a glycine. These simulations have led to the ability to predict structural characteristics for in vitro testing. They compared the results here with CD spectroscopy to show that the results were accurate and demonstrated that both forms of the average beta-strand increase in content initially as temperature increases, but above 370K they begin to decrease. They also showed that at physiologic temperatures, both $A\beta_{1-40}$ and $A\beta_{1-42}$ have a collapsed coil conformation with several short beta-stands and a 1% presence of an alpha helical structure [131].

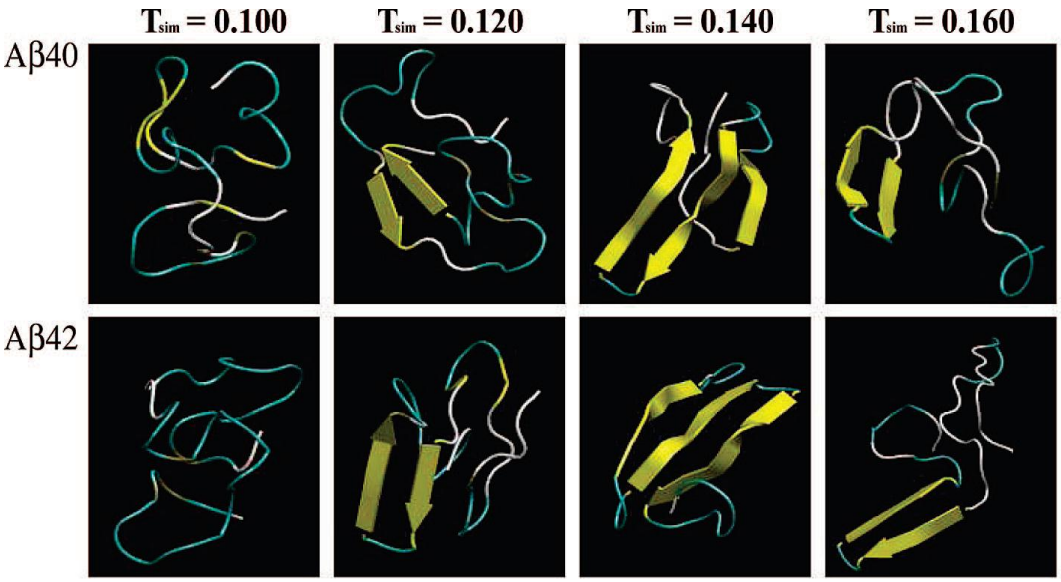

Figure 18 - Conformation found from Discrete MD simulations at different simulation temperatures from work by Lam et al [131].

The oligomer formations of $A\beta_{3\text{-}40}$, $A\beta_{3\text{-}42}$, $A\beta_{11\text{-}40}$, and $A\beta_{11\text{-}42}$ have also been simulated using Discrete MD. $A\beta_{3\text{-}40}$ and $A\beta_{3\text{-}42}$ showed more flexibility, with less beta-sheet structures in them when compared to $A\beta_{1\text{-}40}$. $A\beta_{11\text{-}40}$, and $A\beta_{11\text{-}42}$ showed the N termini formed more contacts, and was therefore much more compact and less exposed to the surrounding water. This means that there were more tertiary and quaternary contacts of the resulting aggregates when compared to the other proteins discussed here [132].

For a more in depth summary of various different simulations associated with MD and MC, please read the Chemical Review published in 2015 from the Journal of American Chemical Society [133].It should be noted that most of these simulations tend to be less than 10 proteins and have limited lengths. This is due to the limitations of current computing power.

1.3.8. Monte Carlo Techniques and Findings

Monte Carlo (MC) simulations can also be used to probe features of various stages of aggregation. MC simulations rely on probabilities and randomness (see chapter 3.3).

MC has been used to study the formation of protein aggregates using various sized systems containing between 20 and 500 proteins that were 6 amino acids long. This was done by assuming that the aggregate kinetics for all aggregation contacts are the same for all species but their rates assumed to be faster the closer they are

together. This meant that the probability of new aggregation contact points forming next to others was higher when they were closer together. The contacts themselves also had a lifetime associated with them (dissociation kinetic), and were longer for those in fibrils. This simulation found the distinct lag phase and exponential growth phase as shown in Figure 19, which only occurs when the dissociation constant associated with the fibrils was 5-20 times higher than that of the monomer contacts. This model suggests that as aggregation proceeds, the probability of new contacts forming to help maintain the aggregate increases, which creates the lag and exponential growth phases. The results relate quite heavily to beta-sheet structures as the interactions within these can work in a similar way [134].

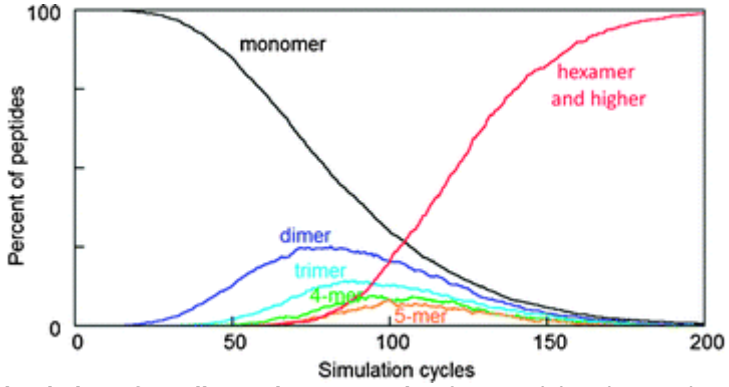

Figure 19 - MC simulation of small protein aggregation from work by Björn and Sara Linse [134].

In an attempt to create an improved energy model that efficiently samples the thermodynamically dominant conformation of proteins, diffusion process-controlled Monte Carlo was used. This was done by generating conformations for both denatured and native proteins using an extremely coarse grain method, where many side-chains had been model as beads. The four proteins used had been shown to adopt α, $\beta\beta$, $\alpha\beta$ $\beta\beta\alpha$ conformations experimentally, which they successfully modelled by running 20 simulations for each protein. This simulation demonstrated the successful use of the energy model and was used to investigate protein folding and how the various secondary structures could cause the tertiary shape of the proteins [135].

All-atom MC simulations of $A\beta_{1\text{-}42}$ and many other mutant forms with implicit solvent were used to investigate how the peptides could spontaneous form a dimer. All the dimers had differing conformational characteristics, with some overall similarities. Intermolecular antiparallel beta-sheet structures were the most common

conformation found for these dimers. It was found here that hydrophobic interactions were always responsible for the aggregation. There was also evidence that the loop in the residues around the 20-30 in these simulations could show significant conformational differences, further suggesting that the loop is independent of the rest of the protein. The probability of the loop being between the 25-30 residue region increases once the dimer has formed. This region is where the loop is found in the aggregated $A\beta_{1-42}$ fibrils. This suggests that the misfolding seen here plays a major part in the aggregation [136].

The kinetics and mechanisms of the formation of amyloid fibrils have also been modelled using the MC method. This was done using coarse grain lattice models that were made up of 8 connected beads in length, known as a chain and each bead was hydrophobic, charged or polar. The models were studied as a function of time and number of chains. During each MC cycle a protein was selected randomly and then the protein could either be moved, rotated 90 degrees or have a conformational change. The movements and rotation were accepted with a 0.1 probability and the conformational changes where accepted at a rate of 0.9. Interacting chains could lead to formation of aggregates. The simulations showed similar characteristics to those seen in the more detailed MC simulations, as partially unfolded monomers whose conformations mirrored that of the final fibril structures were seen to be causing aggregation. They also noticed that during these simulations there were three stages of aggregation; the first was when oligomers form as monomers rapidly come together. These oligomers caused the peptides within them to take on the misfolded conformation and got larger over time. The final stage involves these misfolded aggregates being used as a template for the aggregation for the unfolded monomers or smaller oligomers to dock and convert into the fibril structures [137].

MC simulations and MD simulations (Amber ff99SB force field) involving copper and zinc ions bonded to $A\beta_{1-40}$ and $A\beta_{1-42}$ were undertaken to see how the presence of the ions affect the aggregation process, as some believe that the metal ions cause the aggregation process to begin as discussed above. They compared structure and thermodynamic properties to experimental work and investigated many characteristics such as Gibbs free energy, binding affinity, conformational enthalpy and entropy. They noticed distinct conformational differences in the aggregates containing copper ions (when compared to aggregates involving the more stable

zinc ions), as beta-sheet formation along the N-terminal region (Asp_1, Arg_5 and Tyr_{10}) was shown to be decreased in $A\beta_{1-40}$ and absent in $A\beta_{1-42.}$ They also found some decreased formation of beta-sheets in the C-terminal as well and hypothesis that this could lead to amorphous aggregates rather than fibrils [138].

This review is a general overview of what is seen in the literature but does highlight the importance of combining methods in order to maximise the accuracy and understanding of the results. It also demonstrates the widely accepted features of $A\beta$ aggregation, such as the formation of beta-sheets and the lag time before fibrils start to form. It is also clear more work must be done to discover the exact mechanisms surrounding the early stages of aggregation.

2. Methodology

2.1. Fluorescence

2.1.1. Fluorescence Introduction

Fluorescence is still to this day a widely used and growing technology amongst researchers, as new equipment and methods are created, which in turn leads to the lowering of costs to run the method. As discussed above, fluorescence can be used to probe Aβ peptides, as well as a number of other proteins, through the excitation of Tyr, Trp or Phe residues or even from Congo red or Thioflavin T label dyes. By probing these various fluorophores, it is possible to extract structural and dynamic information about a system. It is non-invasive and can even be used in living systems. This allows for the widespread use of fluorescence as a research tool for many different disciplines. It has high sensitivity and the ability to obtain information regarding the changes to a system's environment, as well as when these changes occur. These changes are sensitive to the nanometer scale, as changes to the local molecular environment will affect the fluorescence response [112] [139].

The environmental changes occurring on the nanoscale are caused by a number of characteristics such as temperature, pH and viscosity. These changes can be detected by fluorescence. Although this method cannot display a visual representation of these characteristics, it can reveal information about the characteristics, such as quantum yield, lifetime and polarisation which can be used to infer knowledge about the system [112] [139].

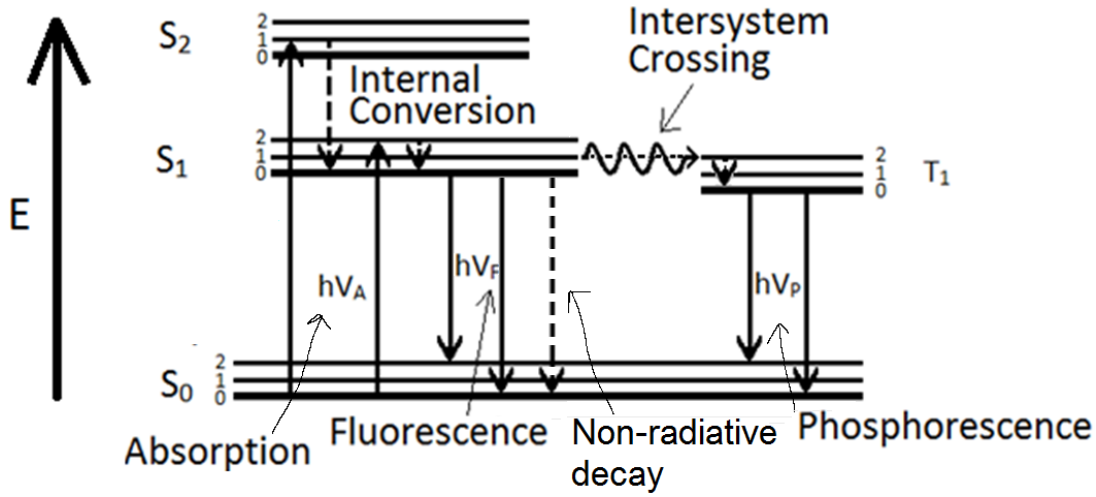

Figure 20 - Jablonski Diagram edited from Principles of Fluorescence Spectroscopy [112].

The Jablonski energy diagram in Figure 20 illustrates the absorption and emission of photons. S_0, S_1 and S_2 denote the singlet electronic states that are responsible for fluorescence (singlet/ triplet refers to the symmetry of the electronic wave function). A fluorophore can be in any of these electronic states, (though it should be noted that there are higher states available that have not been depicted in the diagram above). The first triplet state (T_1) is shown in the diagram above and is responsible for phosphorescence, which will be discussed in more detail below. The electronic states have vibrational energy levels that are denoted as 0, 1, 2… etc. The solid arrows depict the absorption (hV_A) and emission (hV_F and hV_P) of photons which can lead to two types of luminescence: fluorescence, which is relevant to the work presented here or phosphorescence. The dotted arrows show examples of vibrational relaxation [112] [139].

A fluorophore, such as Tyrosine (Tyr) at room temperature, will typically be in the lowest energy state available to it, which is denoted as the S_0 on the Jablonski diagram and will also likely be in the lowest vibrational state, 0. If the fluorophore absorbs a photon, it will now have a higher energy associated with it, and will move into one of the higher states and could reach any of the vibrational levels, such as S_1 in vibrational state 2, as shown by the second hV_A arrow in the diagram above. This is what is known as the “excited” state of a molecule. The singlet state and vibrational state that the molecule will reach is dependent on the energy of the photon that it has absorbed and only certain energy photons will be absorbed. This process occurs on a timescale of approximately 10^{-15} seconds which is extremely fast [112] [139].

Once in this excited state, if the molecule is not in the vibrational state 0, then it can relax through vibrational relaxation to the lowest vibrational state, usually within 10^{-12} seconds or less. This phenomenon occurs due to intermolecular collisions and due to the transition between electronic states of the same spin multiplicity through non-radiative means, known as internal conversion. The molecule is still in an excited state, and naturally wants to return to the ground state; however this transition, which occurs through internal conversion, takes a finite amount of time to occur. Once this state has persisted for an adequate length of time, the spontaneous emission of a photon can occur, bringing the system back down to the S_0. The emission of the photon is what causes fluorescence to occur (hV_A) [112] [139].

In some species, intersystem crossing can occur, which as shown in Figure 20 leads to the molecule entering the triplet state. As the molecule cannot transition to the ground state due to the fact that it is spin forbidden in the triple state as the states have different spin multiplicities; it takes a significantly longer time (in some cases minutes) to relax back into the ground state. This gives rise to the phenomenon known as phosphorescence [112] [139].

There are other ways for the system to return to the S_0 state through non-radiative means such as collisional quenching and and Försters resonance energy transfer (apparent in Dye fluorescence and known as FRET) [112] [139]. As there are multiple ways for the molecules in a system to decay back to ground state, equations involving both radiative and non-radiative means are required.

To calculate the quantum yield (Φ) of a system, the total number of photons emitted has to be compared to the total number of photons absorbed [112] [139]:

$$\Phi = \frac{\text{No. of emitted photons}}{\text{No. of absorbed photons}} \tag{2.1.1}$$

It can be concluded from this definition and the literature that Φ is related to the rates at which the excited states depopulate [112] [139]:

$$\Phi = \frac{K_F}{K_F + K_{NR}} \tag{2.1.2}$$

where, K_F is the spontaneous rate of emission of radiation (photons) and K_{NR} is the non-radiative rate constant, which takes into account anything that is not fluorescence.

This suggests that when K_{NR} is relatively small, the quantum yield will be close to 1 and when it is relatively large the quantum yield will be close to 0, which is intuitive as when the non-radiative processes are not the main driving force, then it will occur mostly due to fluorescence, and will thus have a high quantum yield. [112] [139].

The fluorophores excited state lifetime is determined by the amount of time spent in the excited state [112] [139]. This lifetime (τ) can be defined in the following way:

$$\tau = \frac{1}{K_F + K_{NR}} \quad (2.1.3)$$

When there are no non-radiative processes that are occurring, the natural or intrinsic fluorescence τ_n can be calculated by simply removed the K_F variable from the above equation [112] [139]. This can be used to calculate the fluorescence intensity of a system. Firstly, a system with a concentration N_0 fluorophores in an excited state must be considered. The rate at which they decay back to ground state can be described as follows:

$$\frac{d[N](t)}{dt} = -(K_F + K_{NR})[N](t) \quad (2.1.4)$$

Notice that both radiative and non radiative decay rates are considered here [112] [139]. This equation can then be integrated to take on the form of first order kinetics, which is what Fluorescence typically follows:

$$[N](t) = [N_0]e^{-(K_F + K_{NR})(t)} \quad (2.1.5)$$

Substituting Eqn. 2.1.3 and rearranging we get the equation:

$$[N](t) = [N_0]e^{(-t/\tau)} \quad (2.1.6)$$

As intensity is directly proportional to the concentration of the molecules still excited a further substitution can be made to create the final equation of fluorescence intensity, where I_0 is the intensity at t=0 when excitation has just occurred:

$$I(t) = I_0 e^{(-t/\tau)} \quad (2.1.7)$$

The fluorescence lifetime, as stated above, is the average time spent in the excited state; therefore this tells us how long the fluorophore has time to interact with its environment. During this time the interactions affect the fluorophore, and it is these interactions that affect the resulting fluorescence and allows us to monitor and observe information about the fluorophores environment. Aβ proteins have a single Tyr residue and three phenylalanine residues that can fluoresce; however by exciting a sample at a wavelength of 279nm, only the Tyr residue will be excited.

This simplifies the analysis as there is no interference from other fluorophores in the system.

These changes in the environment around the Tyr that affect the lifetimes, are phenomena such as collisional quenching caused by water. When aggregated, the water may not be able to reach the Tyr residue, causing less collisional quenching.

2.1.2. Fluorescence Spectroscopy

Time-correlated-single-photon-counting is the experimental method used in the work presented in this thesis. The information obtained through this method is superior as it gives more detailed results regarding various parameters such as: the rates and the kinetics, it also allows us to infer information regarding the structural parameters and the dynamics of fast phenomena that occur in the relevant time frame discussed above. The method works by firing pulses of light at the sample using an AlGaN light emitting diode, allowing the user to record intensity as a function of time after excitation [112] [139].

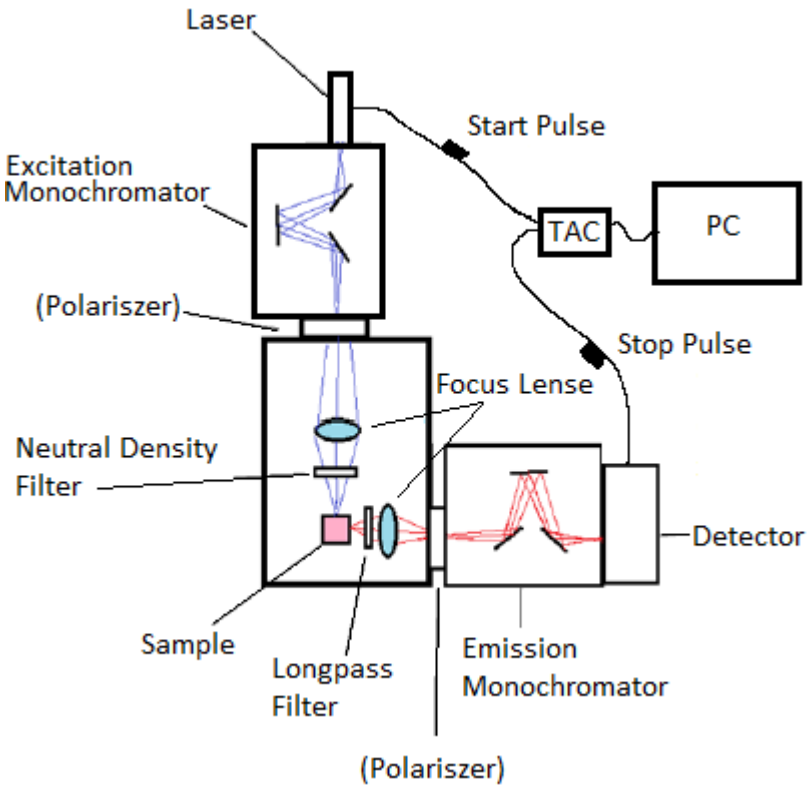

Figure 21 - Top-down view of single photon counting equipment in regular start-stop mode

Figure 21 illustrates the equipment set up for running a time resolved single photon counting experiment. A laser is fired into a monochromator into a sample holder,

where the laser is focused on the sample, exciting its fluorophores. Fluorescence then occurs in all directions as photons are emitted, some of which are sent through another monochromator and over to a detector. The right angle between the laser and the detector is to eliminate excitation light in the detection channel, which would otherwise make it difficult to obtain any results.

The fluorescence intensity is proportional to the probability of detecting a single photon emitted from an excited sample. This is the basic principle of how this method works and if done over a large number of photons a fluorescence decay curve can be created [139] [140] [141]. Normally, when a pulse of light is fired, the Time-to-Amplitude converter (TAC) would be turned on, which causes a voltage to linearly increase over time, when a photon activates the detector the stop pulse actives. The voltage is converted and stored as a comparable number on a PC using a program / software capable (known as a multichannel analyser or MCA).

By repeating the process, a histogram is formed of photons vs. time (where time is the period between a laser pulse being fired and detected) which is known as the intensity decay profile. Another setup for this experimental method involved reverse start-stop mode, which begins the voltage count when a fluorescence photon is detected and then stops when the laser emits a photon.

All experiments were done using a Horiba Jobin Yvon IBH Ltd (Glasgow, UK) Fluorocube fluorescence lifetime system, set up to execute time correlated single photon counting experiments. The TAC and MCA were handled by a computer running Datastation (DAS6) software, which was used to record and analyse the results. The laser used emitted light pulses at a wavelength of 279nm to excite the Tyr residues and the detector was used with a range of 185-650nm [142]. All experiments were carried out using $A\beta_{1\text{-}40}$ purchased from Sigma-Aldrich in powder form; all other chemicals used were also purchased here.

In order to ensure no aggregation occurred prior to all experimentation, the Aβ powder was dissolved in hexafluoroisopropanol (HFIP) at a concentration of 0.1μM. The resulting mixture was then placed in a sonicating bath for approximately 10 minutes, anticipating that this would break apart any aggregates, leaving only monomers. The mixture was then placed in a fume cupboard and allowed to evaporate and once dry the sample could then be stored at -20^{o}C until use. The

sample is now invisible to the naked eye; however, a simple test with a UV light indicates the presence of Tyr residues (and therefore the Aβ proteins) as fluorescence occurs [114] [143].

When the experiment was ready to be performed, the sample was allowed to heat up to room temperature naturally and then normally would be placed in a buffer, such as N-(2-hydroxyethyl)- piperazine-N'-(2-ethanesulfonic acid) (also known as HEPES buffer) at pH of 7.3 [143]. This buffer appeared to cause some issues with DLS experimentation and so other solvents were explored in order to aid DLS (see below). The resulting solution had a concentration of 50μM as this is was previously found to be an adequate concentration that allowed for aggregation to occur at a realistic rate for analysis [114].

The solution was then sonicated at body temperature (37^{o}C), the sample was then pipetted into a quartz cuvette (which was preheated to 37^{o}C) and placed in the lifetime measurement system's sample holder that was temperature controlled also. The laser then fired pulses of light at 279nm at a pulse duration of 50ps, exciting the Tyr residues, which then emitted photons that were detected in the range 300-360nm, using a TAC range of 50ns. By ensuring everything was at thermal equilibrium the results should be fair and unbiased.

The DAS software could then be used to do 1-4 exponential deconvolution calculations using the non-linear least square method, the goodness of the fit can be calculated from the χ^2 value, which is defined by the following formula from the Horiba Das6 user guide [144]:

$$\chi^2 = \sum_N \left[\frac{Y(i)-F_D(i)}{\sigma(i)}\right]^2 \qquad (2.1.8)$$

where, N is the number of channels selected for analysis, Y(i) is the fluorescence decay data, F_D(i) is the function that has been fit to said data, and σ(i) is the standard deviation of Y(i).

This means that $Y(i) - F_D(i)$ denotes the actual deviation from the fitting results, and is divided by the expected deviation due to noise (the standard deviation), with some degree of freedom, which is defined by subtracting the number of fitted parameters to the number of channels. It is standard practice to normalise this χ^2

value and therefore the result should be as close to 1 as possible. A value of above 1.2 is considered a poor fit, as the actual deviation is much higher than the expected deviation. In this case, a higher order exponential fit is required.

2.1.3. Fluorescence Anisotropy

Fluorescence anisotropy takes advantages of the unique differences in intensities along different axes of orientation, this occurs because fluorophores tend to have a preferred direction of excitation and emission [112] [145]. As shown in Figure 21, this is done using a similar setup to that used in spectroscopy, except the emission polariser now rotates between a horizontal and vertical position (the excitation polariser remains vertical throughout).

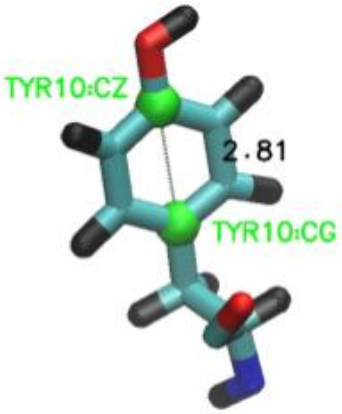

Figure 22 -The Tyr side-chain viewed using VMD [146], with transition moment highlighted. The carbon atoms used to identify the orientation of the transition moment across the aromatic ring are labelled [147]. The distance in between them measured in A.

The excitation monochromator has a vertical polariser placed in the path of the light, which ensures the light that passes through is polarised vertically, as depicted in Figure 23. This is a precaution as the laser light (though linearly polarised) may not be polarised perfectly. The polarised light will then excite Tyr residues whose transition moments, depicted in Figure 22 [147] are also orientated in this vertical direction. The likelihood of excitation is defined as $\cos^2(\theta)$, where θ is the difference in the angle between the transition moment of the Tyr residue and the polarised light [112].

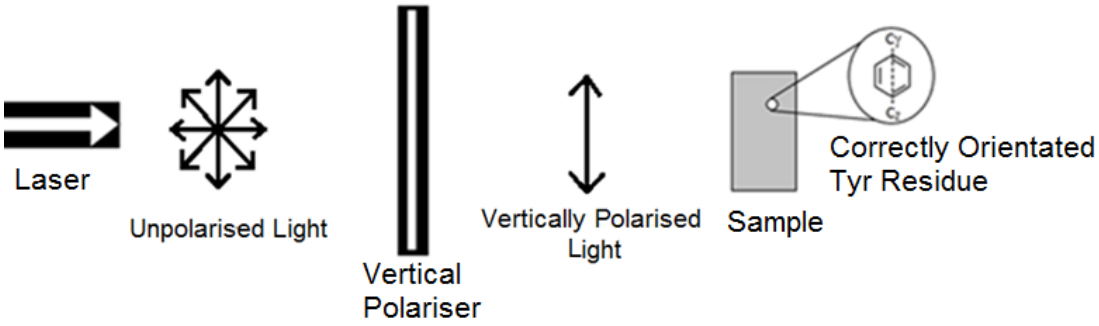

Figure 23 - Excitation of a correctly orientate Tyr using a Polariser. Photons travel Left to right.

The proteins will then rotate due to Brownian motion and sometime later the excited Tyr residues will return to ground state, releasing photons that are then filtered through a polariser, orientated vertically or horizontally (rotated 90^{o}). The photons oriented appropriately will then pass through and be picked up by the detector, as depicted in Figure 24. The process is repeated, alternating between the horizontal and vertical positions [112].

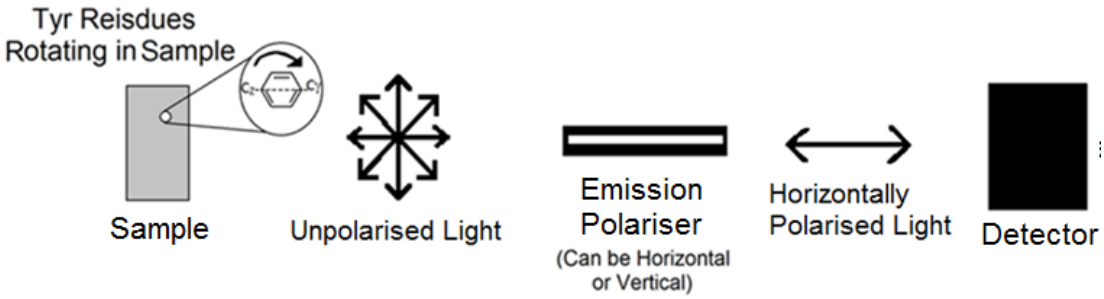

Figure 24 - Detection of a photon that is polarised correctly. Photons travel Left to right.

As is depicted in Figure 23 and Figure 24, there is a limited number of emission photons compared to the number of photons fired by the laser. This is because not all the excitation photons will be polarised correctly, and not all of those photons will excite a Tyr. Furthermore, after rotation of the proteins and emission of the photons from the Tyr residues, only a small number of those will pass through the detector.

This process is used to detect the lifetimes and rotational times of the proteins in the sample. This is because after excitation (time=0ns) almost all excited Tyr residues would be orientated vertically ($\sim\cos^2(\theta)$) and a short lived fluorescent lifetime would emit its photon quickly, suggesting that most of the residues should still be fairly ordered vertically [112]. At later times (for the longer lifetimes) the proteins are expected to have rotated to some degree and the distribution of photons being

emitted will be orientated with less order, some of which will be detected by passing through the polariser that is oriented horizontally. If the rotational times of the molecules are very fast, there will be no order to the system when the photons are released and no information can be extracted as the proteins will have rotated multiple times before emitting [112].

The two orientations of the emission polariser are used to create two separate histograms in a similar manner to what is described for Fluorescence Spectroscopy. As the vertically oriented Tyr transition moments will have a greater composition than that of the horizontal, a peak difference between the histograms will start to form and the experiment will end once a larger enough peak distance has been measured [112].

The anisotropy experiments were performed using the Horiba Jobin Yvon IBH Ltd (Glasgow, UK), modified with polarisers for anisotropy and the samples were prepared in the same way as described above. A peak difference of 10,000 was selected, and the polarisers would switch position every 60 seconds.

The two fluorescence decays were recorded in the detection channel as $I_{\parallel}(t)$ for the polariser in the vertical orientation, and $I_{\perp}(t)$ for this polariser in the horizontal orientation [112]. The anisotropy *r(t)* is then calculated by using Eqn. 2.1.9, below.

$$r(t) = \frac{I_{\parallel}(t) - I_{\perp}(t)}{I_{\parallel}(t) + 2I_{\perp}(t)} \qquad (2.1.9)$$

The factor of two seen in Eqn. 2.1.9 is due to the presence of two directions that are possible in the perpendicular orientation, but have identical characteristics. That is to say, if it is assumed that the vertical position is along the z-axis, then the perpendicular orientation will have two positions from the x and y axes [112]. The environment of the Tyr is responsible for the resulting lifetimes of this fluorescence process, which means that the response of an isolated Aβ monomer in solution will differ from an Aβ aggregate. Furthermore, larger aggregates will have slower dynamics associated with them because the rotational diffusion of the protein is dependent on the size of the aggregate, also creating differences in the rotational times (and therefore the resulting anisotropy graphs). This is how, in principle,

fluorescence anisotropy can be used to monitor the aggregation of Aβ proteins in solution.

The anisotropy decay detected at any time will be the superposition of the anisotropies of Aβ particles being in different states of aggregation. If there are only two different states of the proteins, each with its own rotational time T_i and fluorescence lifetime τ_i, then a theoretical model of associated fluorescence decays can be formed as seen in Eqn.'s 2.1.10 [112] [145]:

$$r_{exp}(t) = \frac{2}{5}\sum_{i=1}^{2} f_i(t).\, e^{-\frac{t}{T_{ri}}}, \qquad (2.1.10)$$

The components of the model are the anisotropy decays of two different states of the protein. The individual rates of the decays of the states determine the pre-exponential factor $f_i(t)$, switching the total anisotropy from being dominated initially by the fast decaying state to being dominated by the slow one.

The anisotropy is fit to the model equation:

$$r(t) = r_0 e^{-\frac{t}{T_{ri}}} + r_\infty \qquad (2.1.11)$$

where r_o is the initial anisotropy (2/5, i.e. 0.4), r_∞ is the final anisotropy, Tr_i is the rotational time (ns) and t is the time (ns). This model equation is developed for spherical fluorophores as real molecules tend to behave like spheres, which simplifies the equation as non-spherical systems are multi exponential.

This equation (2.1.11) can then be compared to the Stokes-Einstein equation in order to get the hydrodynamic volume (V) of the aggregate:

$$T_{r_i} = \frac{\eta V}{kT} \qquad (2.1.12)$$

where η is the viscosity of the solvent, k is the Boltzmann constant, T is the temperature.

For multi-species systems that have a fast and slow rotational time, a two exponential fit is required. DAS 6 software can be fit using the 2 exponential function with the form shown below in Eqn. 2.1.13:

$$r(t) = A + B_1 * \mathrm{e}^{-\frac{t}{\tau_1}} + B_2 * \mathrm{e}^{-\frac{t}{\tau_2}} \qquad (2.1.13)$$

where A is the anisotropy as the curve tends to infinity, t is the current time within the measurement timeframe, the τ values are the rotational times of the two species and the addition of the B values is equal to R_0.

This led to the creation of Eqn. 2.1.14, which is created by applying Eqn. 2.1.13 and Eqn. 2.3.3 (see below). This equation is used in the stochastic / annealing program shown below in the chapters that follow:

$$r(t) = \left(r_{\infty_F} + r_{\infty_S}\right) + \left(r_{0_F} - r_{\infty_F}\right)e^{-t/\mathrm{T}_F} + \left(r_{0_S} - r_{\infty_S}\right)e^{-t/\mathrm{T}_S} \qquad (2.1.14)$$

where r_{∞_F} and r_{∞_S} are the separated anisotropy's values of the fast and slow components as time tends to infinity, respectively. r_{0_F} and r_{0_S} are the initial anisotropy values of those components. T_F and T_S are the rotational times of the components and t is the current time within the anisotropy window.

MC and MD methods considered in this work will be used to provide independent estimates of the rotational times T_i which can significantly help interpretation of the experimental anisotropy data in terms of the model equations.

2.2. Dynamic Light Scattering

2.2.1. DLS Introduction

Brownian motion is the basis of how particles move around a system, which is caused by the constant bombardment of the particles from the molecules of the liquid surrounding it [148] [149]. The phenomenon was first studied by Robert Brown in 1828, where he studied how suspended pollen grains moved within a liquid. After the laser was invented, the technique named "dynamic light scattering" or DLS was possible, as well as many other light scattering techniques. The technique involves firing a narrow beam of light at particles suspended in a medium (such as a liquid), as these particles move into the path of the laser, the light will then bounce of the particle, scattering in different directions, often described as a flash of light. This

flash of light can be picked up by a detector and the flash of light has many properties that vary (such as intensity and duration of flash) [148].

2.2.2. Principles of DLS

Light scattering methods monitor the intensity of light scattered by a medium. DLS generally monitors the time-dependency of this intensity, I(t), which can change depending on a large number of factors, such as particle size or speed at which the particles move, which is related to viscosity of the medium. This means that properties based on particle motion, such as diffusion coefficients can be deduced [148] [149].

Detectors can measure the intensity of the light, and this intensity can be compared to the electric field of the scattered light:

$$I = |E|^2 \tag{2.2.1}$$

As discussed above, this intensity will fluctuate over time as shown in Figure 25a, and so can be converted into an intensity correlation function which can be defined by using the following function [148] [149]:

$$G_2(\tau) = \langle I(t)I(t+\tau)\rangle \tag{2.2.2}$$

This is done through the use of a digital correlator, attached to the equipment, which allows for useful information to be extracted and produces a graph similar to that shown in Figure 25b. This graph can then be normalised to start decaying at 1 and is defined by the equation shown below in Eqn. 2.2.3 [148] [149]:

$$\boldsymbol{g_2(\tau) = \frac{G_2(\tau)}{\langle I(t)\rangle^2} = \frac{\langle I(t)I(t+\tau)\rangle}{\langle I(t)\rangle^2}} \tag{2.2.3}$$

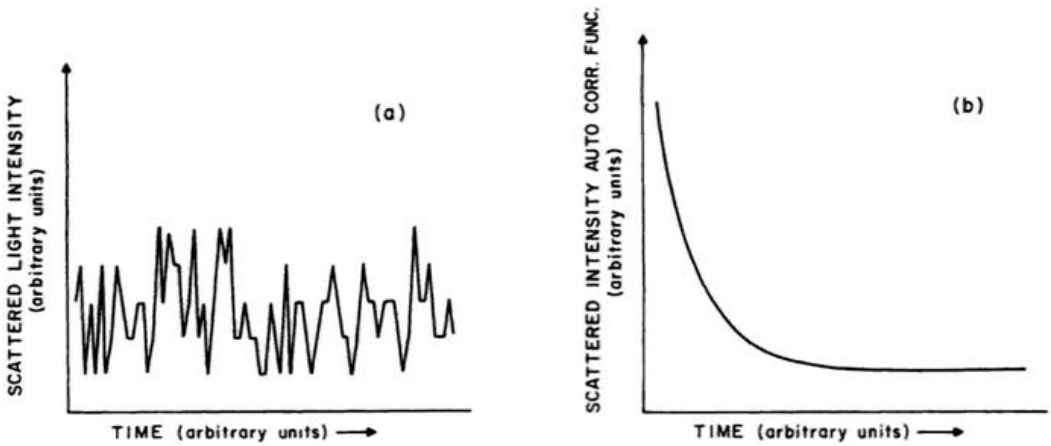

Figure 25 - (a) fluctuating intensity over time of an aqueous solution of polystyrene spheres of radius 1.01μm, (b) Intensity autocorrelation function, taken from Dynamic Light Scattering: With Applications to Chemistry, Biology, and Physics [150]

It should be noted that the graph shown in Figure 25b, has been edited to not include the initial stages of the measurement, which are seen as a delay in decay, the initial delay in decay is a sign of aggregation occurring, this is because smaller particles have higher diffusion coefficients. This will be visible in the results shown in this work.

Through the use of Seigert relation, the intensity correlation function equation, shown above, can be written in terms of the normalised electric field auto correlation function [151];

$$g_2(\tau) = 1 + \beta|g_1(\tau)|^2 \qquad (2.2.4)$$

Where b is an instrument response constant and $g_1(\tau) = e^{-\tau\Gamma}$, which can be plotted using the natural log to obtain a straight line relation with slope equal to the rate of decay (Γ) [148] [149].

$$\ln\big(g_1(\tau)\big) = -\tau\Gamma \qquad (2.2.5)$$

It should be noted that this only applies to mono-dispersed systems and a cumulant analysis is commonly carried out for small amounts of poly-dispersed particles. These cumulant analyses are simple and are not affected by background noise [151]. As these poly-dispersed particles do not have a linear relationship, they require fitting a polynomial to the natural log of $g_1(\tau)$ [151].

$$\ln\left(g_1(\tau)\right) = a + b\tau + c\tau^2 + d\tau^3 \quad (2.2.6)$$

Where, the magnitude of b is approximately equal to Γ.

A third order fit as shown in Eqn. 2.2.6 is considered to be the highest order fit feasible. This is because any results that require a higher order fit are deemed to have a lack of precision and such a high order fit will make other parameters less precise [151]. Γ can be used to gain information about the scattering vector, q:

$$\Gamma = Dq^2 \quad (2.2.7)$$

where, q is derived through trigonometric relations, with respect to the angle the detector is positioned, θ (see Figure 26) and the incident wavelength of the laser (λ):

$$q = \frac{4\pi n}{\lambda} sin\left(\frac{\theta}{2}\right) \quad (2.2.8)$$

The scattering vector is important for DLS analysis, as it is the difference in magnitude of the incidence and scattered light wave vectors. This allows the scattering vector to be used as a means to gain information regarding the length scale of the particles causing the most scattering, through the use of Eqn. 2.2.9 below.

$$L \approx \frac{2\pi}{q} \quad (2.2.9)$$

Furthermore, coefficient c in Eqn. 2.2.6 can be used as an indicator of the poly-dispersity of the system, known as the Poly-dispersity Index (PDI).

$$PDI = \frac{|c| \times 2!}{\Gamma^2} \quad (2.2.10)$$

The average hydrodynamic radius of the particles in a system can be calculated using the average diffusion coefficient and the Stokes-Einstein equation [151], which assumes the particles are spherical in shape in a viscous liquid.

$$R_h = \frac{k_B.T}{6.\pi.\eta.D} \quad (2.2.11)$$

This assumption does affect results seen for Aβ as they are rod-like in shape, rather than spherical, which is where noise can become apparent [120]. This means that using these methods would provide little information for Aβ and so more complex

methods such as “CONTIN” can be used to fit multiple exponentials to the data, which can extract multiple decay rates that are used to find particle sizes. These results can be used to establish size distributions [148] [149].

2.2.3. DLS Equipment used

As Aβ has a non-spherical aggregated shapes associated with it, which makes it hard to extract useful data from the results, except in the early stages. This created some challenging results that had to be tested on different experimental setups using different equipment in an attempt to discover more about the aggregation pathway that $A\beta_{1-40}$ takes, i.e. the evolving size distribution.

The basic setup for a DLS machine requires a laser, a sample and a detector which is positioned at some angle θ, as shown in Figure 26.

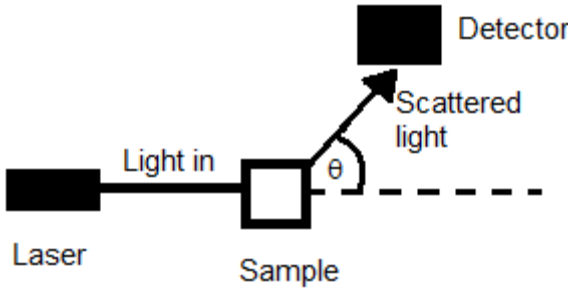

Figure 26 - Basic Setup for DLS experiment

The first experiments used two Malvern Zetasizers (Strathclyde University from the Chemical Engineering and Civil Engineering departments). They are both Non-invasive Backscattering equipment as they use a θ angle of 173^{o}. This angle is used because there could be interference detected if it was placed at exactly 180^{o}, which is why this method is preferred.

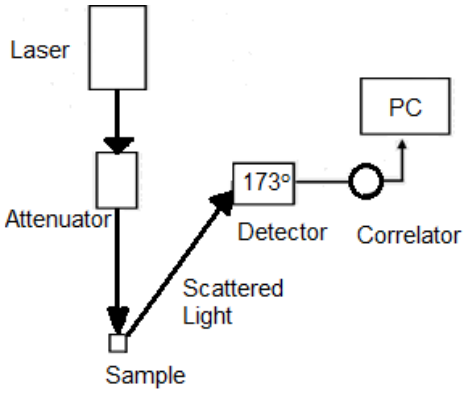

Figure 27 - Schematic of Malvern Zetasizer, based on schematic by Saha, Bhaskar et al. [152]

The attenuator shown in Figure 27 is used to reduce the intensity of the light to prevent detector overload, the correlator is used to calculate the graphs seen above using the equations above. The Zetasizer in the work shown here has a HeNe laser (3nW), which is then scattered and picked up by a detector (Avalanche photodiode) that could have its transmission changed between 0.0003% and 100%. It is then passed through the correlator which then goes to a PC for analysis. The lenses used to focus the laser are moved closer in low scattering samples and moved further away in higher scattering samples.

The other type of equipment used to gain a clearer understanding of the shape and growth pattern of $A\beta_{1\text{-}40}$ was the 3D-LS instrument. The instrument works using the same principles as above but instead has a beam splitter, causing two illumination light paths and using two detectors, one of which is setup at the desired θ angle, and one at a different angle all together.

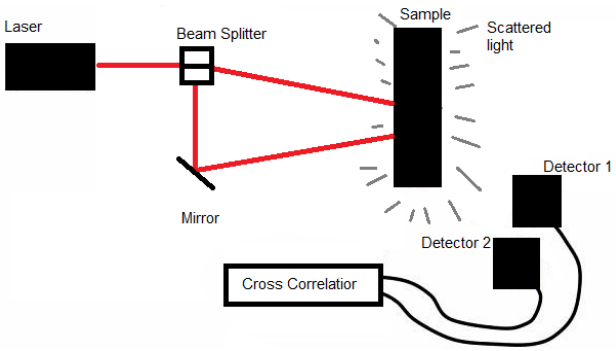

Figure 28 - 3D LS instrument schematic. This is based on LS Instruments website of the product [153].

This allows for accurate model fitting for low scattering samples. This makes its use limited for $A\beta$ aggregates, as there can be a lot of scatter in the system once

aggregates begin to form, which also means the lenses for the laser input for both the Backscattering and 3D DLS equipment must be moved accordingly.

All DLS samples were prepared in the same way as described for the Fluorescence experiments with the HCL and NaOH being filtered before addition of $A\beta_{1-40}$ to prevent any foreign particles from entering the system. The DLS equipment used is temperature controlled at 36.3^{o}C and had a detector angle of 90^{o} from the input laser.

2.3. Monte Carlo Simulations

2.3.1. Monte Carlo Introduction

The Monte Carlo (MC) method is another important way to gain information regarding Aβ. Unlike MD, MC simulations can be used to examine a system at a coarser scale, meaning the level of detail for the simulations is lower. This means that MC is generally nowhere near as resource heavy as MD. Subsequently, very large systems can be analysed on a much broader setting as they generally are not detailed to a molecular level, in the way MD is. The relatively low detail of the system means that little time is required to process the results.

However, as the system is modelled at such a low level of detail, it means that there will be no molecular scale interactions being modelled, which will cause some loss in accuracy as there is no way to model exactly what is going on. Despite this, the information that can be obtained through this method is still invaluable, as it allows for the implementation of different models and very large systems when compared to MD. The results could also lead to more exotic MD simulations, or perhaps further experimentation to complement the results found from the MC method.

The method was first developed at the end of World War II as a way to study the diffusion of neutrons in fissionable material. The extensive use of random numbers within the method led to the name “Monte Carlo” being coined in 1947 by Metropolis. This method works through random sampling of a system through the use of arithmetic and logical operations [154].

The basic principles of the MC method involve creating a system with inherent rules or known scenarios that can occur. These rules will occur based on some probability P, which is determined by the user. A random number is then selected by the

program which is then compared to the probabilities of these scenarios occurring. If the randomly selected number matches the parameters set by the probabilities then the algorithmic step can occur, which in turn changes the environment of the system in some way. If the random number does not adhere to the parameters of the probability then it does not occur. [154].

Regardless of the outcome, after all the scenarios have been checked with their appropriate random numbers, a counter is added to as shown by Eqn. 2.3.1 and the process is repeated (each repeat is known as a “pass”). The time taken for all of the scenarios to be given the chance to play out is called a MC time step (also known as a MC step or MCS). This counter portrays that MCS and can be as simple as adding an arbitrary number each step, or as complicated as calculating the real world time taken for these things to occur, based on experimental observation.

$$T_{new} = T_{old} + x \qquad (2.3.1)$$

Where; T_{new} is the new total time after the current pass has been completed, T_{old} is the previous total time before the current pass was completed and x is the time passed between this pass and the previous pass, which can always be the same. The x variable can also be drawn from Poisson distribution using the sum of event rates to determine the time constant.

The results from each pass can be stored in various ways, depending on the requirements of a simulation. This includes storing the results as a list, or in bins to create a Histogram. Due to the random nature of the MC method, results differ from simulation to simulation (assuming a different seed is used) and can be used to determine the time taken for a desired outcome, or how a system builds itself over time. [154].

2.3.2. Simulated MC Anisotropy

Experimental anisotropy is complicated; as Tyr residues explore their environments they have fast relaxation times, which is then combined with a slower rotational at time associated with the diffusion of the monomer/oligomer backbone (or “bulk”) that it is attached too. Simulated MC anisotropy has been used in this work as the basis to create results for a basic Aβ system and is used to explore the consequences of these timescales.

To simulate anisotropy, the motion of the transition moment over time is modelled by its orientation in terms of its angle to the backbone θ_T (see Figure 29). The backbone itself has orientation θ_B to the vertical, and a rotation of ϕ_B clockwise about the vertical axis to create a three dimensional system. On each MCS, these angles can change randomly. θ_B and θ_T are changed by angles selected randomly within the range $\pm d\theta_B$ and $\pm d\theta_T$ respectively; in general $d\theta_T > d\theta_B$. As spherical polar coordinates are used, ϕ_B changes by a random angle in the range $\pm {d\theta_B}/{\sin\theta_B}$.

As the backbone angle moves, the transition moment of the Tyr residue moves also; it represents the protein backbone carrying the Tyr. Furthermore, the Tyr cannot pass through its backbone and so the constraint $\frac{\pi}{2} - \theta_M < \theta_T < \frac{\pi}{2} + \theta_M$ is placed on the allowed values of θ_T. Here $\theta_M < \frac{\pi}{2}$, and MCS's that do not adhere to this condition are rejected and the process repeated, until a random valid value is found. These constraints mimic the accessible rotamer states of the Tyr residue in molecular scale models [44]. As an aggregate increases in size it will rotate more slowly and as more proteins aggregate closer together, the amount of movement available to a Tyr residue will generally be lower (see results section for MD simulations for examples of this). The backbone movements do not have the same constraints on them as the Tyr and have a larger freedom of movement comparative to the size of the protein being simulated.

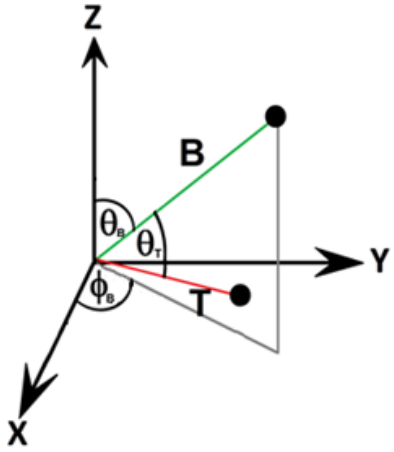

Figure 29 - Backbone and Tyr angles used in MC simulations

The fundamental anisotropy of a fluorophore is given by $r_0 = \frac{2}{5}\left(\frac{3cos^2\beta-1}{2}\right)$, where β is the angle between adsorption and emission [112]. The autocorrelation from the MC simulation can be measured:

$$r(t) = \frac{2}{5}\left\langle \frac{3(\underline{\beta}(t)\cdot\underline{\beta}(t+T))^2}{2} - \frac{1}{2}\right\rangle_T \qquad (2.3.2)$$

Here time t is measured in MCS's, $\underline{\beta}(t)$is the direction of the transition moment at time t, and the average is taken over a suitable range of T to observe the full $r(t)$ dynamics. For this model to work, it is assumed that the fluorescence lifetime of the Tyr side-chain is always the same throughout, and therefore does not affect the calculation of $r(t)$.

All simulated anisotropy data from Eqn. 2.3.2 is then fit to the following theoretical form:

$$r_{fit}(t) = \left(r_{\infty_T} + r_{\infty_B}\right) + \left(r_{0_T} - r_{\infty_T}\right)e^{-t/\mathrm{T_T}} + \left(r_{0_B} - r_{\infty_B}\right)e^{-t/\mathrm{T_B}} \qquad (2.3.3)$$

This equation is used for both MC and MD fits and makes the assumption that the Tyr residues transition moment will have a fast diffusion timescale T_T and the backbone a larger rotational timescale T_B. The values of the anisotropy at large times t are given by the respective 'infinity' values r_{∞_T} and r_{∞_B} , and the values at $t = 0$ are r_{0_T} and r_{0_B}. The constraint of $r_{0_T} + r_{0_B} = 0.4$ is also required by Eqn. 2.3.2. It should be noted that the pre-exponential factors of the two exponential terms in Eqn. 2.3.3 are not time-independent, unlike the factors $f_i(t)$ that appear in Eqn. 2.1.10; this means that Eqn. 2.3.3 is a special case of Eqn. 2.1.10.

We perform fits of Eqn. 2.3.3 to experimental, MC and MD data described below. The 5 independent parameters of the fit are found by a least square error search using stochastic methods.

A simplified list of instructions used to create this program is shown here (see Appendix 1 for full code):

1. Allow the backbone to rotate slowly once per MCS

1.1 Move Backbone angle position (θ_B and ϕ_B) by a randomly generated amount of degrees (both positive and negative rotation) in 3 Dimensional space

1.2 Move Tyr angle the same amount to simulate monomer/aggregate rotation

2. Move Tyr angle position (θ_B) by a random amount of degrees (separate and faster than previous movement) in 2 Dimensional space
3. Move angle position within boundary limits of backbone

3.1 Create conditional loop

3.2 Create a random angle movement for Tyr

3.3 if Tyr's new angle too big or too small with respect to backbone limits then undo movement

3.4 create new random angle movement for Tyr

3.5 repeat 3.2 and 3.3

3.6 end loop when condition is met (when tyrosine is within its limits)

2.4. Molecular Dynamics Simulations

2.4.1. Molecular Dynamics Introduction

Molecular Dynamics (MD) is a powerful computational method that is used here to simulate the early stages of aggregation. MD allows for an atomistic scale view of proteins and other structures; which allow the interactions between individual atoms to be viewed. MD simulations are obtained by the repeated calculation of Newton's equations of motion over time using a force field to create the potential energy of the system. The results are detailed, accurate and can be used as complementary information for experimental work, or can be used to inspire future experimental work. This is possible because MD can be used to track molecule orientation, bonds, structure and conformation, amongst other properties, which can reveal information about a system that would not be possible during experiments.

The early stages Aβ protein aggregation can be easily observed with MD as the relative size of an Aβ monomer is fairly small [44](c.f. Bovine serum albumin for example which is 585 residues in size [155]). This means significantly less processing power is used to study Aβ monomers and oligomers than some other proteins. However, as more proteins are added to the system, the amount of water required for the system becomes larger, creating more atoms and thus can become very CPU demanding systems. This means there is a limit to the number of proteins and simulations that can be done within realistic time frames.

The classical equations of motion must be solved for N molecules which are interacting through their potential, U. One method for doing this is by using one of the fundamental forms of the equation motion derived from the Hamiltonian $\mathcal{H}$ [156]

$$\mathcal{H} = \mathrm{E}_k + U \tag{2.4.1}$$

$$\dot{r}_i = \frac{\partial \mathcal{H}}{\partial p_i} \tag{2.4.2}$$

$$\dot{p}_i = -\frac{\partial \mathcal{H}}{\partial r_i} \tag{2.4.3}$$

Here E_k and U are the total kinetic energy and potential energy respectively of the system, $\dot{r}_i$ is the velocity of atom i, and p_i is the momentum of atom i [156]. The total kinetic energy can be written as:

$$\mathrm{E}_K = \frac{1}{2}\sum \frac{{p_i}^2}{m_i} \quad (2.4.4)$$

where m_i is the mass of atom i.

To compute the trajectories, the velocities must be calculated after some change in time δt. This is done using an algorithm such Euler (outdated) or SHAKE, which is used in the simulations in this work [157].

SHAKE is an algorithm used in order to constrain certain features of a molecule e.g. bond lengths. The SHAKE algorithm is used in conjunction with the Verlet algorithm [158]. The Verlet algorithm method uses positions r(t), accelerations a(t) and the previous positions, r(t-Δt) of each atom:

$$r(t + \Delta t) = 2r(t) - r(t - \Delta t) + \Delta t^2 \cdot a(t) \quad (2.4.5)$$

This form of the equation has no velocities as they are eliminated by the use of the equations obtained by the Taylor expansions [158].

$$r(t + \Delta t) = r(t) + \Delta t \cdot v(t) + 0.5 \cdot \Delta t^2 \cdot a(t) + \cdots$$

$$r(t - \Delta t) = r(t) - \Delta t \cdot v(t) + 0.5 \cdot \Delta t^2 \cdot a(t) - \cdots \quad (2.4.6)$$

Eqn. 2.4.5 allows for the calculation of the new positions which then allows for the velocities at the mid step to be calculated [158].

$$v(t + 0.5\Delta t) = v(t) + 0.5 \cdot \Delta t \cdot a(\mathrm{t}) \quad (2.4.7$$

The forces and accelerations can then be calculated at this new time, t+Δt [159].

For the use in SHAKE, the Verlet integrator for unconstrained atoms is obtained by doing a variable replacement of $a_i = \frac{f_i}{m_i}$.

$$r'_i(t + \Delta t) = 2r_i(t) - r_i(t - \Delta t) + \frac{\Delta t^2}{m_i} f_i \quad (2.4.8)$$

This is then constrained, meaning that the true positions are calculated using a constraint force [158]:

$$r_i(t + \Delta t) = 2r_i(t) - r_i(t - \Delta t) + \frac{\Delta t^2}{m_i} f_i - g_i \quad (2.4.9)$$

where g_i is the constraint force on atom i and can be a function of the particle coordinates or velocities and is used to hold certain variables at a constant value. An example of a fixed variable is the fixed bond length σ, shown in Eqn. 2.4.10:

$$g_i = \sum_{\alpha=1}^{M} \lambda_\alpha \left(\frac{\partial \sigma_\alpha}{\partial r_i}\right) \tag{2.4.10}$$

where, λ_α is the Lagrange multiplier, This means that bond length must remain constant throughout the simulation and so the following conditions must be satisfied,:

$$\begin{cases} \sigma_1(r) = 0 \\ \quad . \\ \quad . \\ \quad . \\ \sigma_M(r) = 0 \end{cases} \tag{2.4.11}$$

This means Eqn. 2.4.10 has λ selected so that the change in position of the atoms keeps σ constant [157] [158].

SHAKE goes through all the constraints adjusting positions step by step until all the constrained equations are satisfied to some margin of error [157] [158] [160].

2.4.2. MD Simulation Setup

There are three main types of systems that are discussed in this work; $A\beta_{1\text{-}40}$ simulations, $A\beta_{1\text{-}42}$ simulations – both allowing for amorphous aggregation – and pre-aggregated $A\beta_{1\text{-}42}$ fibril-like aggregate simulations. All of which are created with NAMD 2.6 [161], combined Charmm22 and Charmm 27 force field model and a TIP3P water model as was done previously. This force field and model were chosen for the work in this thesis, based on the previous work's trajectories success [44]; allowing for comparison and continuity between results. Furthermore, the parameters affecting the proteins in the latest version of the force field (Charmm33) are very similar to those in the force field used in this work and therefore, the minor alterations will not lead to significant changes. VMD is used to prepare the simulations and visualise the results.

The NMR structure of $A\beta_{1\text{-}42}$ was obtained by Crescenzi [46] (1iyt.pdb) and is available on the protein data bank (PDB). It has the most probable charge states at neutral pH7 for the ionisable residues. The initial simulation for a $A\beta_{1\text{-}42}$ monomer

began straightened out with approximate dimension 47.05Å x 25.29Å x 13.60Å. This monomer was allowed to reach a stable conformation with dimensions ~ 24.94Å x 23.58Å x 10.21Å and was used in all subsequent simulations.

The structure of $A\beta_{1-40}$ was obtained by taking the 1iyt.pdb model and removing residues Ile_{41} and Ala_{42} as was done in previous work [44]. As a monomer begins a simulation either straightened out with dimension ~48.06Å x 9.69Å x 26.21Å or in its preferred conformation occupied once a simulation has been ran long enough for it to become stable with dimensions ~34.16Å x 15.17Å x 23.69Å. When ions are present a monomer prefers to have dimensions ~25.31Å x 27.93Å x 2.84Å. $A\beta_{1-42}$ appears to be slightly smaller; however this is due to the rough approximations made for the sizes for the "straightened" out conformations. Despite this, once extra two hydrophobic residues will bury themselves away from the surface as much as possible and could potentially lead to a smaller over size. The structure was modelled in a *SDS micelle, aqueous trifluoroethanol* environment which, like water, is polar. Despite both environments being polar, the monomers were given time to become stable in the water during the initial stages of trajectories.

The proteins above are used to create the amorphous aggregate systems. The fibril-like aggregate trajectories are created using a hexamer beta-sheet conformation found by Waelti et al as discussed above [63]. The structure is what is assumed to be the basic building block of the protofibrils, it could also be compared to work done with metal ion mediated $A\beta$ aggregation, as similar shapes have been presented there (albeit with metal ions being part of the process [41] [42]). The various simulations related to this protofibril conformation are created by removing select proteins in the original fibril hexamer - found on the PDB (2NAO.pdb). The beta-sheet hexamer has dimensions~ 83.78Å x 51.91Å x 13.82Å and a single protein in that aggregate has dimensions ~59.94Å x 32.55Å x 4.86Å.

The number of proteins per simulation varies from one to six proteins, with variable distances between the proteins to increase or decrease chances of aggregation within the timeframe of the specific trajectory. The proteins are surrounded by a rectilinear waterbox which varies in size for each system and some systems had ions in them to mimic the ionic concentration of blood of approximately 0.250mMol/L [162], using Na^+ and Cl^- ions.

The size of the waterbox affects the concentration and therefore the likelihood of aggregation, however, if the waterbox is too small, it can potentially lead to proteins passing through the periodic boundary conditions (PBC) of the waterbox. As the trajectories have repeating boundary conditions, it can cause the protein to wrap around and begin interacting or aggregating with itself. This means that the systems were made with adequately sized waterboxes, unless stated otherwise.

Once the protein, waterbox and ions (if used) are set up, they are subjected to a water minimization stage (1000 steps) and are given 100ps for water equilibration. During this stage the Langevin piston control pressure is activated with group based pressure control, a piston temperature of 300K (310K) and the anisotropic cell fluctuations are not allowed based on previous work [44].

This is followed by a minimization phase for the whole system (10,000 steps) and then by 30ps of heating to 300K for amorphous systems or 310K (body temperature) for the fibril-like systems and 1atm pressure. Finally, 270ps are required for thermal equilibration with a timestep of 1fs.

Once preparation is complete, the production of trajectories can begin for various trajectory lengths (see below for details) all with a timestep of 2fs at 300K (or 310K) in the *NVT* ensemble and the SHAKE algorithm is used. Van der Waals interactions had a cut-off of 12 Å. Particle mesh Ewald (PME) is used for the electrostatic interactions.

2.4.3. MD Analysis Tools

The resulting trajectories are then analysed through various means, studying the changes in conformation over time or how the residues are interacting etc. However, one of the more important aspects of the work produced here is studying the Tyr residue. This includes its physical position within the aggregates/ peptides, its transition moment orientation (to simulate anisotropy) and the Tyr's rotamer states.

The rotamer states of the Tyr residue are the conformations that it likes to be in. In previous work it was found that the Tyr residue liked to rotate around the C_α–C_β and C_β–C_γ chemical bonds as shown in Figure 30 .

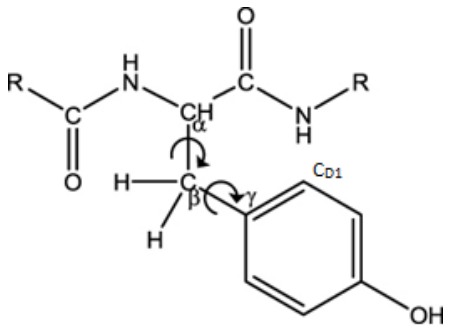

Figure 30 - Showing the freedom of movement of Tyr residue around C_α–C_β and C_β–C_γ edited from work by Amaro et al [44]

By using VMD the dihedral angles of both of these rotational points could be obtained. This was done by tracking the dihedral angles along atoms C-C_α-C_β-C_γ and C_α-C_β-C_γ-C_{D1} in VMD for each frame in the trajectory. These angles are exported to excel, and graphs are created showing the positions of these angles, and therefore the positions that the Tyr residue prefers to occupy as shown in Figure 13 [44]. Though it should be noted that for the work presented here, the angles X_1 and X_2 are fixed to fit on axes that range from 0-360, removing the negatives completely as the rotamer states seen at the top left are actually part of the rotamer in the top right. As can be seen from Figure 13, there are 4 general orientations (with variation) that the Tyr likes to occupy. Furthermore, in this work a simple program (see Appendix 2.1) was created to track the movements between these states, each zone was given a number to be identified by as shown in Figure 31. (Note we identify 6 rotamer states as explained below in the results).

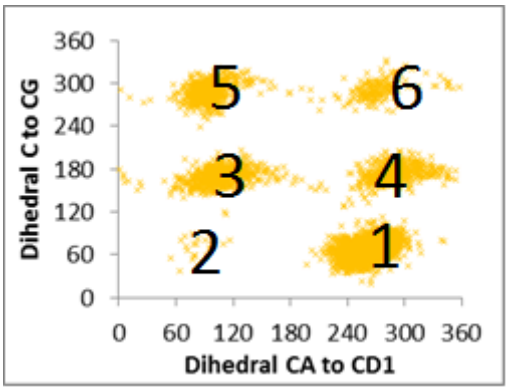

Figure 31 - Example of results, with rotamers numbered

The next interesting piece of information regarding the Tyr residue is tracking its transition movement in order to created simulated anisotropy curves. This was done

by tracking the C_γ and C_z atoms in the Tyr as shown in Figure 22, using a script which was then put through another program to create vectors between these two atoms and calculate the resulting anisotropy (see Appendix 2.2).

The Tyr fluorescence anisotropy response can be created using the assumption that the excited Tyr states can be represented by the ground state structure and interaction potentials. Echoing Eqn. 2.3.2, the autocorrelation for the normalised transition moment direction $\underline{\mu}(t)$ across the Tyr side-chain is calculated as

$$r(t) = \frac{2}{5}\left\langle \frac{3\left(\underline{\mu}(t+\tau)\cdot\underline{\mu}(t)\right)^2}{2} - \frac{1}{2} \right\rangle_\tau \qquad 2.4.12$$

Here $\underline{\mu}(t)$ is calculated from the coordinates of the relevant C atoms from the aromatic ring of the Tyr side-chain as discussed above. In the case of multiple proteins, each Tyr has its own autocorrelation, and these are averaged as appropriate (the experimental anisotropy is the average of a very large number of proteins). Experimental anisotropy cannot look at the individual responses of proteins; instead it takes in all the responses from all proteins at once, creating an average response. Simulated anisotropy allows for the study of single Tyr/protein responses which can be used to confirm, prove or demonstrate what is going on at a molecular level and show what causes the general responses seen experimentally.

3. Results and Discussion: Experimental

The experimental section of this thesis is presented here. The experiments undertaken for this thesis are mostly Fluorescence based, with some dynamic light scattering (DLS) used to help compliment the fluorescence results where possible, though limitations of the DLS method makes this difficult. All experiments were run for 3-4 days to ensure the important stages of aggregation had occurred [44].

Fluorescence spectroscopy uses a using a AlGaN light emitting diode laser to excite the tyrosine (Tyr) fluorophore found in both $A\beta_{1-40}$ and $A\beta_{1-42}$, which then release a photon of energy in order to return to ground state [142]. This emitted photon can then be potentially picked up by a detector, the time taken for this occur is known as the lifetime of the excited state and is the basic mechanism required for analysing the results from these experiments and reveals a typical decay curve as shown in Figure 32 [142]. In these fluorescence spectroscopy experiments, time-correlated-single-photon-counting was used to probe the Tyr environment by tracking the changing lifetimes of the systems, both in systems that do not aggregate and in those that do.

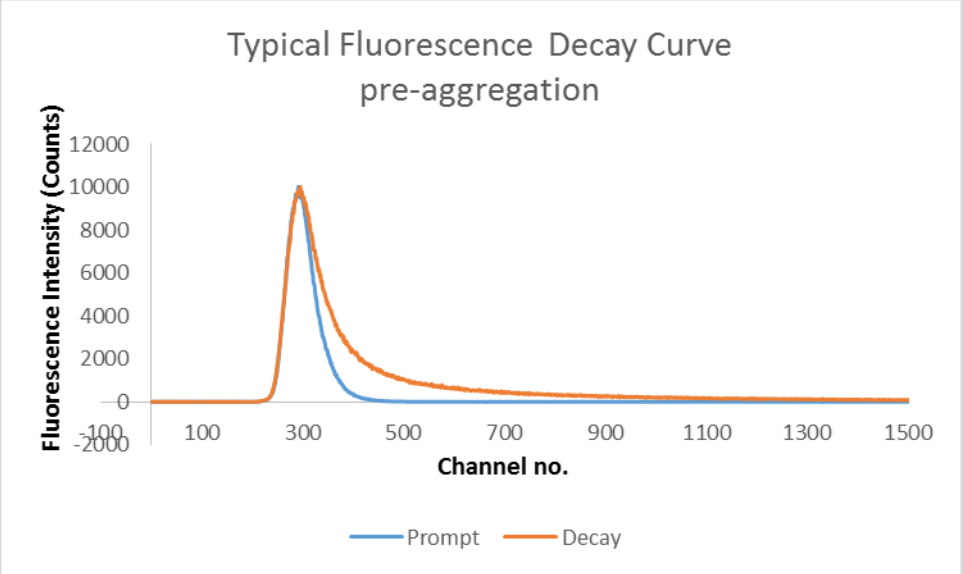

Figure 32 - Typical Fluorescence decay curve

As stated previously, the laser emitted light at a wavelength of 279nm, the detector had a detection range of 185-650nm [142], using a TAC range of 50ns and the $A\beta_{1-40}$ used in these experiments was purchased from Sigma-Aldrich in powder form.

Each experiment was set up in same manner for consistency, preparing the proteins to ensure no aggregation was present prior to the experiment and was kept at thermal equilibrium at a temperature of 37^{o}C to simulate body temperature [44]. The results could then be analysed to give lifetimes and lifetime contributions which is then used to infer information about the potential local Tyr environments with in the various experimental systems.

The next experimental method discussed in this chapter is the DLS, which uses the Brownian motion of the proteins in the systems and a laser to extract information about the radius of an aggregate. As the particles pass through the laser, it will cause a flash of light which can be identified by the detector, the bigger the molecule the longer this detection will last [148] [149].

The experiments were set up in the same way as the fluorescence experiments and also were maintained a constant temperature of 37^{o}C for consistency. Usually an autocorrelation is retrieved from these experiments which usually allows for the sizes of the particles in the system to be determined, however, this is proved difficult due to complications seen in the DLS results.

Finally, fluorescence anisotropy experiments were also undertaken in order to probe the sizes of the proteins which also proved difficult. This means that neither DLS nor anisotropy could be used to extract the sizes from the samples. Despite this, as anisotropy works using the same principles as spectroscopy, we can still gain invaluable information about the Tyr residues movements (as well as the aggregate it is part of) [112]. As discussed previously, fluorescence anisotropy works by taking polarised light from the AlGaN light emitting diode laser to excite appropriately oriented Tyr residues. They then emit their photons, which are then passed through an emission polariser (orientated horizontally or vertically) only allowing correctly orientated photons through, the difference in results found for the horizontal and vertical orientations can be used to create the anisotropy graph which can then be analysed [112].

3.1. Fluorescence Spectroscopy

In a previous project undertaken by another researcher at Strathclyde, attempts had been made to create size distributions of Aβ aggregation using DLS, which failed due to intense scattering, making the results too noisy to obtain any valuable

information. As discussed above, this could be caused by the aggregation process (multi-distribution of various sized aggregates), dust or other foreign objects, or even the shape of the fibrils themselves.

To ensure that this scattering was not a product of the HEPES buffer solution, an alternative was required. This lead to the following experiments where HEPES buffer was replaced with water, hydrochloric acid (HCl) and sodium hydroxide (NaOH). All fits have an acceptable χ^2 (between 0.9-1.2) [163], unless otherwise stated and are given in Appendix 3.1a. The most significant results for the lifetimes are shown in Table 1 and Table 2 below.

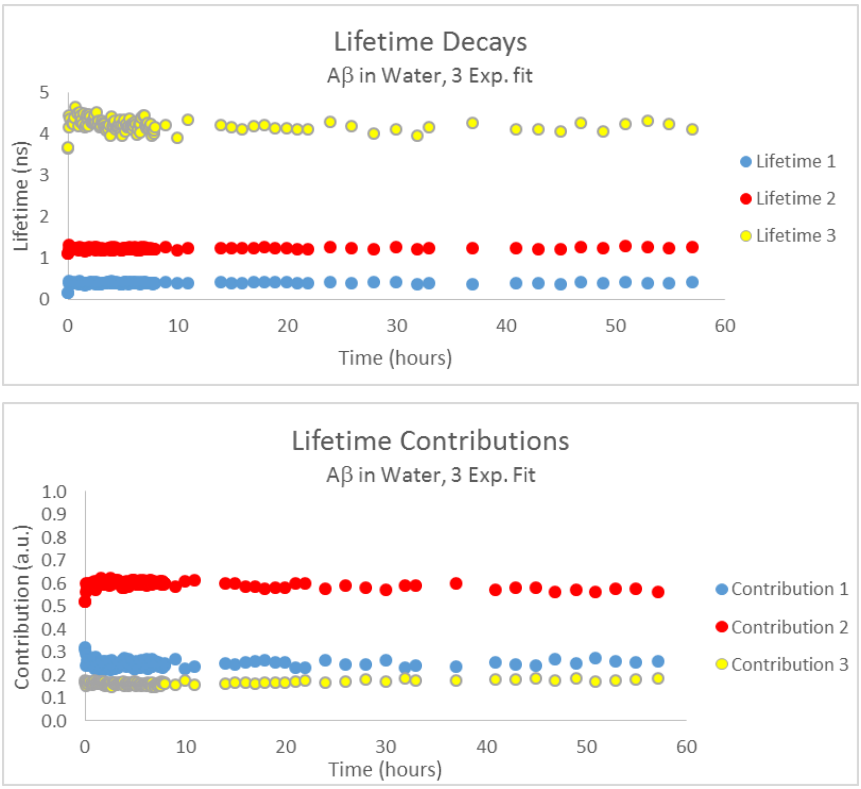

Figure 33 - Fluorescence spectroscopy results of Aβ in deionized water. Top graph shows lifetime decays. Bottom shows contributions of those lifetimes. (χ^2 = 0.9-1.2)

Deionized water at neutral pH 7 is the first experiment discussed here as shown by the results in Figure 33. Unfortunately, the results show that the lifetimes do not change by any significant amount during the course of the experiment, all remaining approximately at their initial values. The first lifetime in blue is ~0.40ns, the second in red is ~1.22ns and the third in yellow is ~4.22ns. Furthermore, the contributions of those lifetimes remain relatively steady, with some initial movement within the first

6min of the experiment. The initial contributions from the first, second and third lifetimes are 0.31, 0.52 and 0.17 (respectively) and then after 6min become approximately 0.24, 0.59 and 0.16 respectively, which we do not consider to be significant changes relative to previous results [44]. The χ^2 for these lifetimes are acceptable and the majority are close to 1 (see Appendix 3.1a).

This suggests that there is some initial movement but it is insignificant and does not indicate any significant change to the Tyr residue environments. As the environments are not changing throughout the three days of the experiment, no aggregation is likely to be occurring [43] [112]. Therefore, deionized water is not a suitable replacement for the DLS experiments.

Though no aggregation occurs, this experiment still provides relevant information. The results were fitted to 3exp, giving three lifetimes for the Tyr residues; this is what is expected from previous results [44], the lifetimes have been suggested to be caused by three different local environments that the Tyr experiences. Though there are three environments that are picked up by fluorescence, there could be more environments that that are quenched (as seen by the presence of four rotamer states in MD simulations [44]) and do not appear in the measured results. This is hard to determine as there are not many techniques that can probe the Tyr local environment to the same degree as fluorescence. The MD simulations shown in later chapters can help reveal information about the different environments.

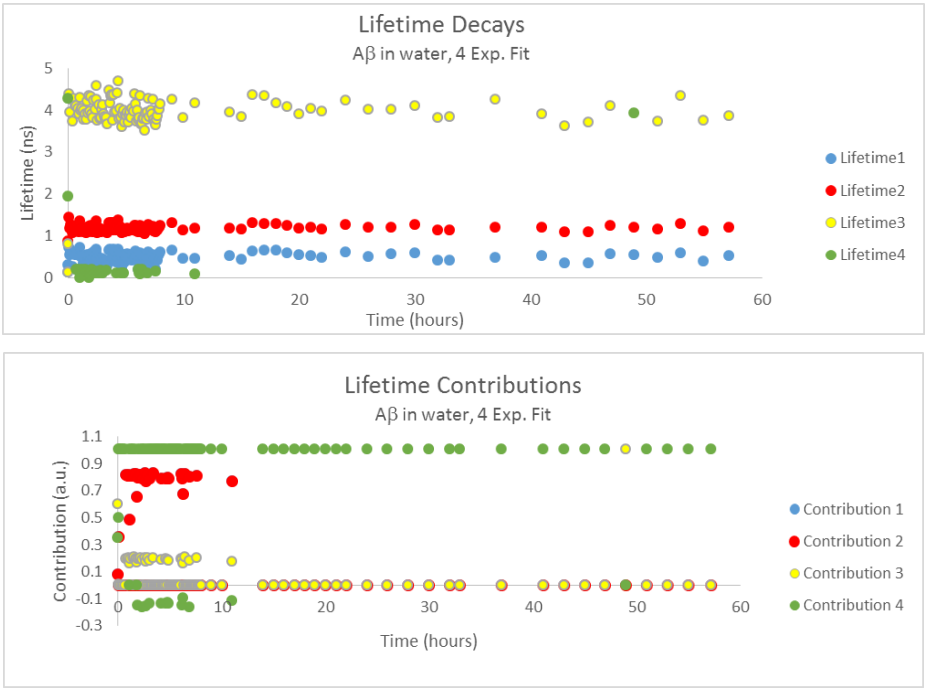

Figure 34 - Fluorescence spectroscopy results of Aβ in deionized water with 4 exp. fit. Each colour corresponds to a specific lifetime and the graphs show the evolution of the lifetimes over time in the top graph and the contributions from each lifetime in the bottom graph. (χ^2 = 0.9-1.2)

We investigate a 4exp fit in in Figure 34 in order to ensure that a four fluorescent environment does not exist for the Tyr residues. Despite the fact that the χ^2 for these fits are an improvement on the χ^2 of 3 exponential fits, the results here are erratic and have three near-zero contributing lifetimes and one that shows a contribution of above 1 (100% contribution). This would suggest that there is a lifetime that is impossibly long and does not even appear within the limits of the lifetime graph and even shows negative contributions near the beginning. These results are meaningless, which suggest that the three exponential fit is likely to be correct.

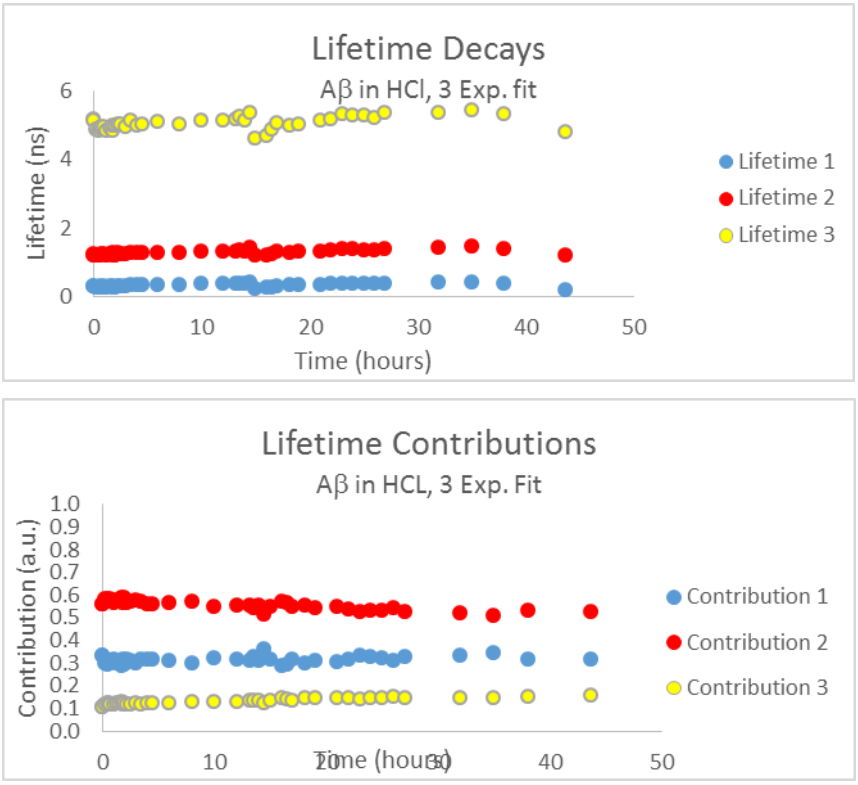

Figure 35 - Fluorescence spectroscopy results of Aβ in HCL with 3 exp. fit. Each colour corresponds to a specific lifetime and the graphs show the evolution of the lifetimes over time in the top graph and the contributions from each lifetime in the bottom graph. (χ^2 = 0.9-1.2)

The next type of experiment undertaken involves HCl, diluted with water to a pH of 5.5, which is close to the isoelectric point of Aβ. At this pH the proteins will carry no net electrical charge [164]. Shown in Figure 35, it has similar characteristics as when water is used; the lifetimes and contributions do not change in any significant way, suggesting that there is no aggregation.

The lifetimes approximately remain at 0.33ns, 1.29ns and 5.1ns for the first, second and third lifetimes respectively, which is similar to the initial positions of the sample with water in it. Their contributions are 0.31 0.56 and 0.13 which again, are similar to the initial contributions from the water sample. This further suggests that there are some movements and interactions that occur in the first 6 minutes for the sample containing water, but aggregation does not occur regardless.

Furthermore, a four exponential fit for this system, proved to be erratic with lifetimes as slow as 10^{-4}ns, which are unacceptable and the fit, therefore, unusable (see Appendix 3.2a). This further suggests that the system being probed here has only monomers in it and the system containing water also has monomers (and potentially

small amorphous aggregates present). It also appears that these kinds of systems have three lifetimes associated with them; which is an indication of three separate local Tyr environments (chapter 7.10) [44].

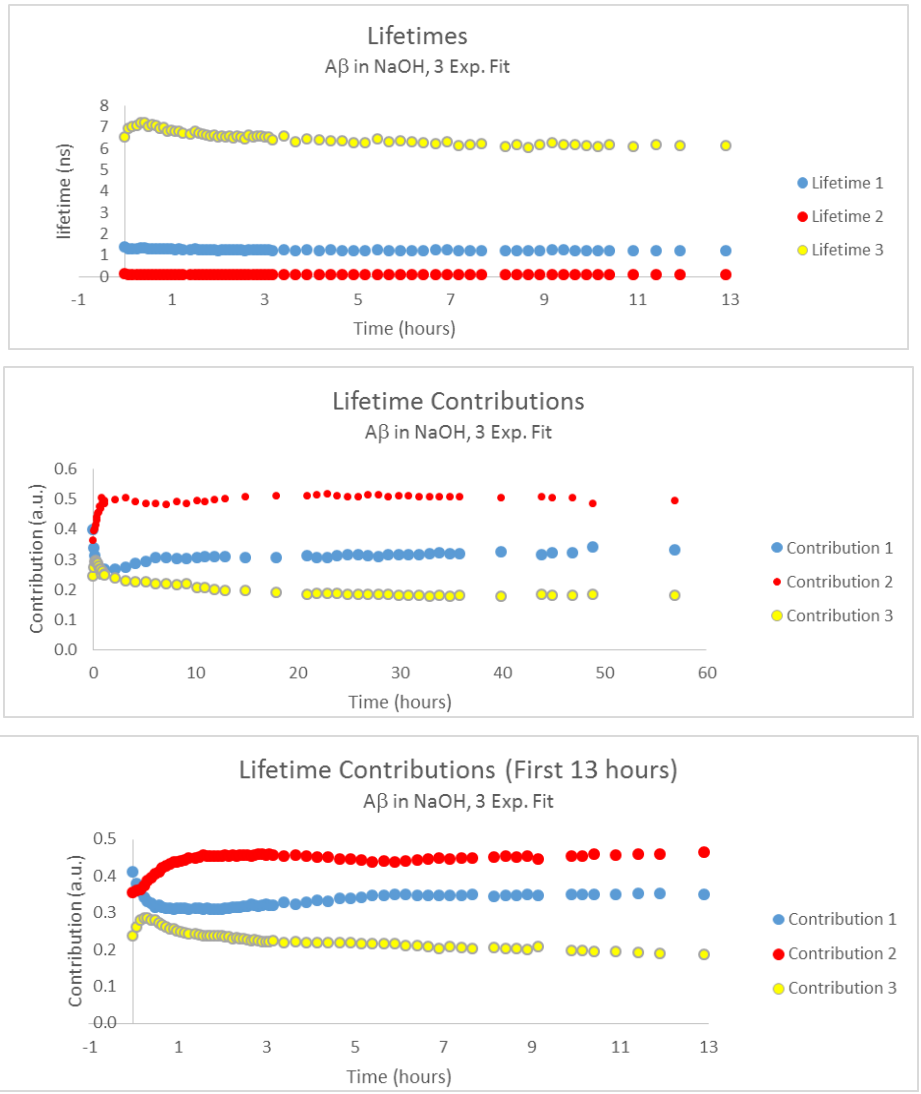

Figure 36 - Fluorescence spectroscopy results of Aβ in NaOH with 3 exp. fit. Top graph shows Tyr lifetime decays. Bottom shows contributions of those lifetimes.

The final type of experiment has Aβ in dilute NaOH, (with deionized water) with a pH of approximately 7.3, which is used to mimic similar conditions to HEPES buffer, an environment Aβ is known to aggregate in [44]. This system shows improved results as the changing lifetime contributions suggests that aggregation does occur, as shown in Figure 36 and are similar to what has been seen in HEPES buffer [44].

Figure 36 shows that the starting contributions for the three lifetimes are 0.41, 0.35 and 0.24 for each sequentially. After this the contribution from the first lifetime decays quite rapidly (becoming less of a contribution than the second lifetime), before slowly increasing again to a value of ~0.32. The second lifetime has a sharp increase to 0.51 and the third decays has an initial steep increase followed immediately by a sharp decrease (mirroring the second lifetimes increase) and then a more shallow decay which mirrors the first decays increasing contribution, ending at a contribution value of ~0.18. The lifetimes remain steady at approximate values of 1.14ns, 0.05ns and 5.38ns sequentially.

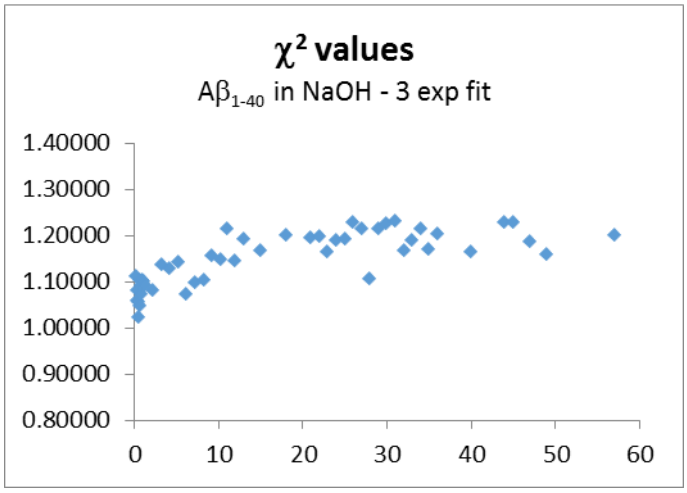

Figure 37 - χ^2 values of the three exponential fit of $A\beta_{1-40}$ in NaOH

However, the χ^2 values of the fits are not always within the acceptable range as shown in Figure 37 (ranging from 1 to above 1.2), suggesting that there is a more complicated lifetime system for this kind of sample. This is complemented by the fact that the third lifetime has such an unusual initial contribution change. As the fits for the system are not always reasonable a four exponential fit for this system is viable, suggesting that there are at least four different environments that the Tyr residues occupy during the course of the aggregation [112]. This could be due to proteins interacting closely as they aggregate, affecting the environments and positions of the Tyr residues.

Sample (3 Exp. Fits)	Tr_1 (ns)	Tr_2 (ns)	Tr_3 (ns)	Contr. 1	Contr. 2	Contr. 3
(Average): $A\beta_{1-40}$ in water	0.40(5)	1.22(4)	4.22(32)	0.24	0.59	0.16
(Average): $A\beta_{1-40}$ in HCL	0.331(9)	1.289(7)	5.08(3)	0.31	0.56	0.13
T=0hr: $A\beta_{1-40}$ in NaOH	0.109(4)	1.38(1)	6.53(4)	0.35	0.41	0.24
T=0.58hr: $A\beta_{1-40}$ in NaOH	0.083(3)	1.30(1)	7.11(4)	0. 41	0.32	0.27
T=39.92hr: $A\beta_{1-40}$ in NaOH	0.093(3)	1.20(1)	5.85(3)	0.47	0.36	0.17

Table 1 - Lifetimes of various 3 exponential fits. Average lifetimes shown for water and HCl samples and specific times (Initial value, mid-agrgegation value and post aggregation value) for sample containing NaOH. The uncertainties associated with the last digit(s) are in brackets. The water errors have been estimated from the average value of Figure 33.

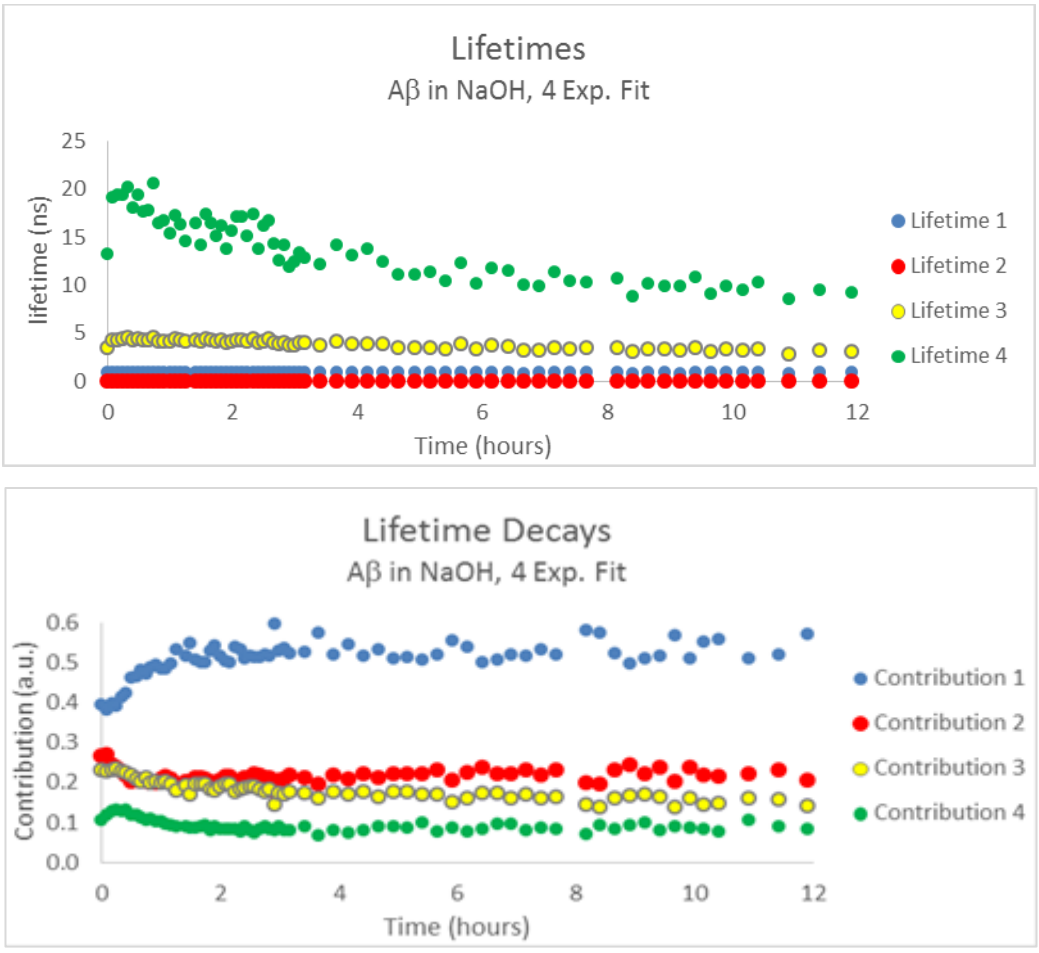

Figure 38 - Fluorescence spectroscopy results of Aβ in NaOH with 4 exp. fit. Top graph shows Tyr lifetime decays. Bottom shows contributions of those lifetimes.

In Figure 38 the initial stages of the experiment are shown for the four lifetimes, this is because after 12 hours there are no significant changes to the lifetimes or their contributions. For the full experiment time frame please see Appendix 3.2b. The resulting fits also have χ^2 values that remain satisfactory throughout the experiment (except one measurement) in Figure 39 below.

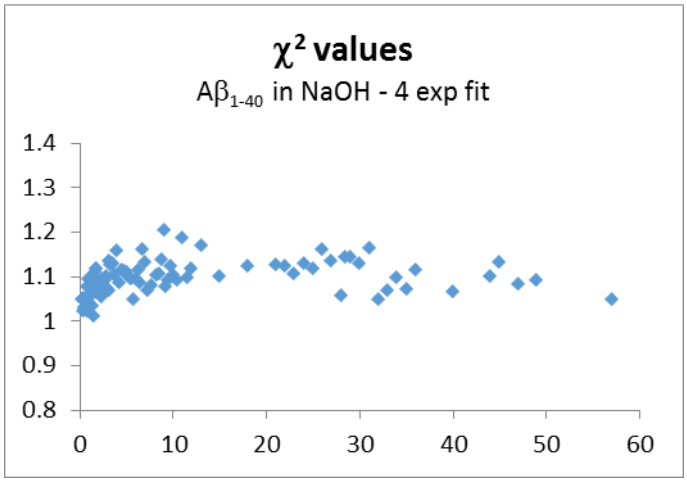

Figure 39 - χ^2 values of the four exponential fit of $A\beta_{1-40}$ in NaOH

The fourth lifetime (in green) was not present before and the other three lifetimes have been affected by the aggregation as the values obtained are different from that found in previous experiments and fits. This is expected from aggregating proteins as the surroundings of Tyr residues would be vastly different from those of monomers. The fact that these lifetimes are instantly affected implies aggregation began before the first measurement was taken [112].

The reason that a three exponential fit works well in the non-aggregating samples could be due to the fact certain Tyr orientations/environments are not favourable or are being quenched (see chapter 7.10 for more information). It should be noted that one of the lifetimes is very short lived (30ps) and the time calibration is 13.5ps/channel. This means that this fourth lifetime could be background noise but could still actually be a short lived lifetime associated with the Tyr's environments [163].

The average lifetime values of the faster responses are 0.02ns, 0.95ns and 3.56ns with almost no change in the first two, but some initial variation in the third lifetime. The new lifetime response is significantly slower, at an initial value of ~20ns (this seems a little too large, however as the aggregation continues, the lifetime begins

descending to a value of 10ns). The contributions are also shifting for all four lifetimes, as they are initially 0.34, 0.29, 0.23 and 0.11 for the four (1 to 4 sequentially) but end at 0.22, 0.15, 0.10 and 0.53. A potential reason for the appearance of a fourth lifetime is discussed further in chapter 7.10.

Our results indicate that dilute NaOH allows for Aβ aggregation and show a similar aggregation pattern as in HEPES buffer [44] [165], although the aggregation seems to be to a lesser degree and the contribution changes are less significant. Regardless, it is a potential replacement for HEPES buffer in DLS experiments in an attempt to reduce scattering. Unfortunately, the DLS experiments still proved difficult, as will be discussed in chapter 3.3.

Sample (4 Exp.)	Tr_1(ns)	Tr_2 (ns)	Tr_3(ns)	Tr_4(ns)	C. 1	C. 2	C. 3	C. 4
T=0hr: $A\beta_{1\text{-}40}$ in NaOH	1.00(2)	0.032(3)	3.45(6)	13.2(3)	0.39	0.27	0.23	0.11
T=0.58hr: $A\beta_{1\text{-}40}$ in NaOH	1.01(2)	0.0243(3)	4.36(7)	17.65(4)	0.47	0.21	0.21	0.12
T=39.92hr: $A\beta_{1\text{-}40}$ in NaOH	0.87(3)	0.027(3)	2.41(7)	7.29(8)	0.53	0.22	0.14	0.10

Table 2 – The lifetimes of 4 exponential fits. Lifetimes (Tr) and contributions (C.) Initial value, mid-agrgegation value and post aggregation value for sample containing NaOH. The uncertainties associated with the last digit(s) are in brackets.

3.2. Dynamic Light Scattering

The effect of pH on $A\beta_{1-40}$ is investigated here using DLS equipment. Test samples were analysed on the Zetasizer “Nano” in the department of Civil Engineering at Strathclyde to see how significant the scattering is for the HCl and NaOH samples. As there are limited changes to the environment seen in the fluorescence experiments for HCl, an extended analysis was not required. For these tests, the samples are studied over a 10 second time window. Standards are run to ensure the reliability of the equipment, multiple measurements were taken and some measurements of BSA in various buffers were taken in collaboration with Ben Russell. This is useful as BSA has a consistent particle size at a pH of 7.4, which can give reliable correlation results (see Appendix 3.3a) that can be analysed.

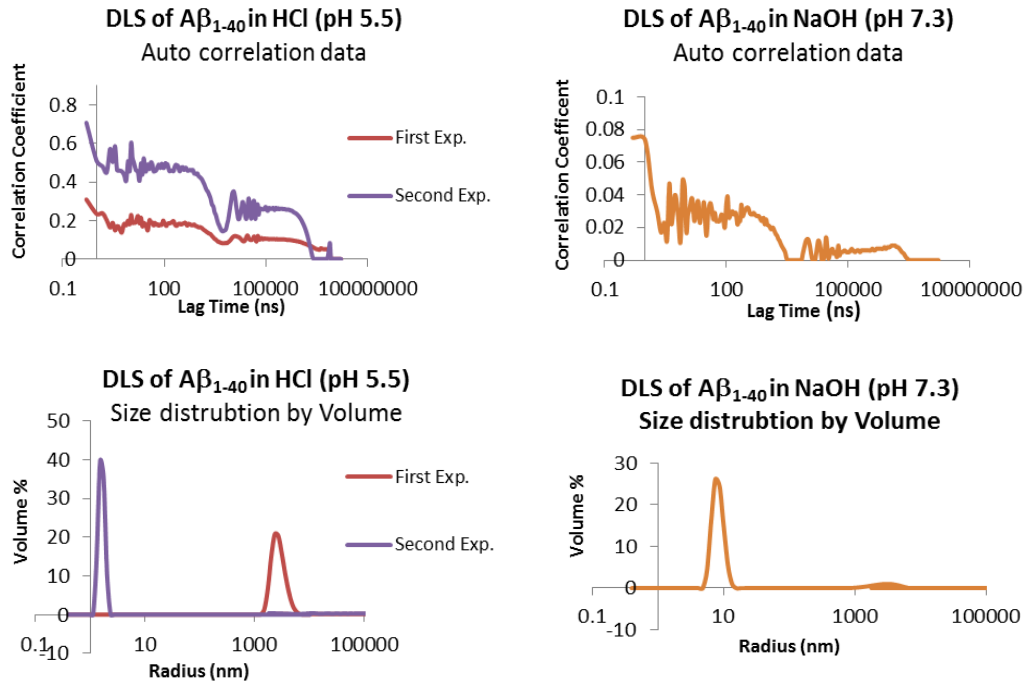

Figure 40 - Autocorrelations and size distributions from Zetasizer of samples containing NaOH and HCl

The resulting autocorrelation data from the experiments shown in Figure 40 are erratic and have decays that are not acceptable for size distributions. Despite this they show the presence of monomers and a single large population, unlike what has been seen in the literature [84]. This is an indication that there is either some foreign particle (e.g. dust) or a single large population is present in the system. A population this large should not be present as the measurements are taken as soon as possible after preparation is complete and the polydispersity index being 1, suggesting many different sized aggregates should be present. As the necessary precautions (such as filtration) are taken to ensure minimum exposure to dust particles, this is unlikely to be the issue [148] [149]. Furthermore, when all DLS results in Appendix 3.3b are viewed, the apparent sizes are completely random and show a different sized species with no regard to time, as well as some negative sizes. Despite the extremely large aggregate seen in the NaOH sample, the potential reason for the presence of the 9nm radius particle could be due to the initial aggregation forming oligomers or protofibrils. The large population could also be large amorphous clusters of proteins [148]. However, this is speculation as the correlations are poor and is related to either the equipment used or the samples' polydispersity.

All the results have high cumulative error and a polydispersity index of 1 - above 0.7 is considered an unsuitable sample for DLS as there are multiple species in the sample, making the results unreliable and non-repeatable[[151].

BSA samples in various buffers (including HEPES) give significantly more reasonable results. HEPES buffer has a slightly more unfavourable correlation decay when compared to PBS but is still more reasonable than what is seen for the HCl and NaOH samples above (see Appendix 3.3a and Appendix 3.3b).Therefore, as HEPES buffer is not seen to be an issue a sample containing $A\beta_{1-40}$ in said buffer was prepared and DLS measurements were made using the 3D DLS equipment. The measurements are taken every five minutes (for a total of three days) in an attempt to track the aggregation of the $A\beta_{1-40}$ sample using a 30 second time window for each measurement. Sample results from this experiment in Figure 41 demonstrate the poor autocorrelation [148] functions seen throughout the three day experiment.

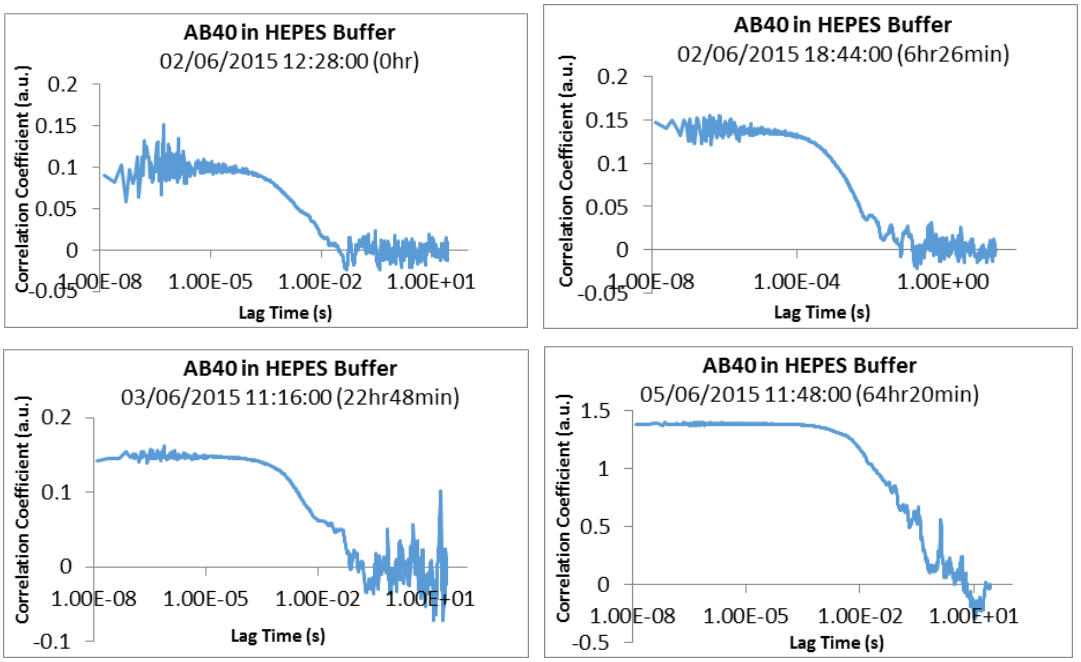

Figure 41 - Autocorrelations of $A\beta_{1-40}$ in HEPES buffer at T = 0hr, 6hr26min, 22hr48min and 64hr20min

The polydispersity index of 1 and high cumulative error of these samples suggest that any size analysis for these systems would not produce justifiable results as seen above [148] [151]. It should also be noted that despite HEPES buffer scattering, the result here show significantly worse scattering and cannot be fit for

size distributions at all which suggests that the Aβ proteins or the equipment used is the reason for the issue and not the buffer itself.

Despite this, the scattered light intensity (I) of these results can be used to show the presence of aggregation. The scattered light intensity corresponds to the mean count rate and is proportional to the number concentration of the scattering objects (particles, clusters etc.) This means that the scattered light intensity will increase when the particle cluster (aggregate) size increases. It will also increase due to changes in the optical contrast between the aggregate and its surrounding medium (HEPES buffer) i.e. when there are more aggregates in the medium. The resulting time distribution of these scattered light intensities is shown in Figure 42.

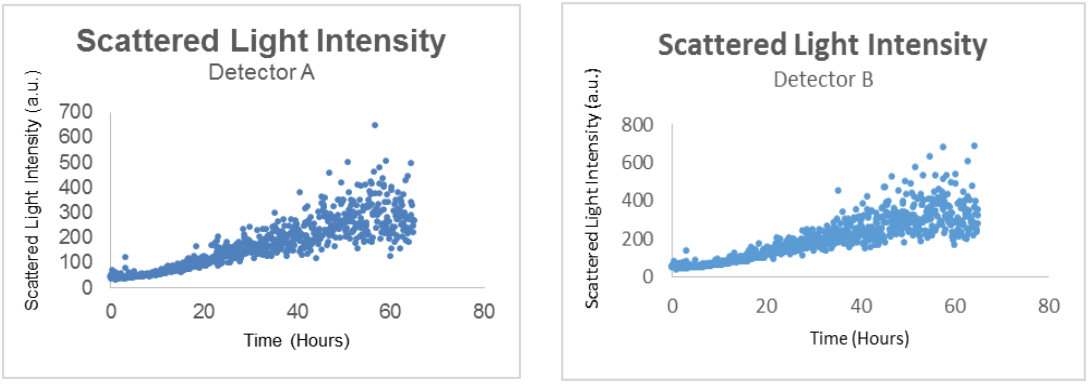

Figure 42 - Increase in "scattered light Intensity" for detector A and B over three day period

The increase in intensity is an indication of aggregation, though it is not certain if it is caused by a larger number of aggregates being formed, or from the aggregate sizes becoming larger. The graphs in Figure 42 show clear signs of aggregation, continuing over the three days of measurements. Initially this increase is relatively slow, but after approximately 5 hours, the increase becomes sharper and the variation in the photon count becomes larger. After 30 hours there is still a visible increase in intensity, however the variation is more rapid and makes it difficult to determine how steep the true increase is in the intensity.

These results combined with the fluorescence results seen previously, suggests that there are some early changes to the environment as the Aβ proteins begin to aggregate together to create oligomers, which causes no notable increase in the intensity graphs (but is still affecting the correlations) [112] [148]. After these have formed their pre-protofilament conformation where the beta-sheets begin to form,

they begin stacking rapidly creating large aggregates [50]. Though it is unclear if it is multiple aggregates or a single aggregate from these intensity results, the polydispersity seen from the measurements suggests that it must be many different sized aggregates [148] [151].

3.3. Fluorescence Anisotropy

The first experiment shown below in Figure 43 is a sample of $A\beta_{1-40}$ in HEPES Buffer, done in collaboration with Thorben Wellbrock. The anisotropy experiments proved to be challenging. This is because the equipment used is optimised for fluorescence in the IR spectrum, however Tyr fluoresces in the ultraviolet region (~300nm) [166]. This greatly affects the quantum yield of the measurements, which means the photon count detected will be lower than expected [112]. Furthermore, this is compounded by the experimental setup used in anisotropy.

The first issue is the fact that the excitation monochromator has a polarizer attached to it. This may prevent some of the laser's photons from entering the sample holder if they are not perfectly polarised to begin with. In addition to this, only Tyr residues whose transition moments are parallel to the polarised light will actually be excited, further lowering the amount of photons from the laser that will successfully excite Tyr residues [112] [147]. Furthermore, these excited Tyr residues will then rotate randomly and will emit a photon in various orientations. Only the appropriately orientated photons will pass through the emission polariser which will then be detected [112] [147]. The accumulation of these effects creates a much lower proportion of detected photons in comparison to photons fired by the laser, resulting in a low detection rate.

This greatly increases the time taken to reach the required peak difference for anisotropy, limiting the number of measurements that can be taken per experiment. Moreover, the photon count lowers and the noise become more severe due quenching when the Aβ peptides become tightly aggregated. When aggregated tightly together, the closeness of the Tyr residues causes the photons that are emitted to be reabsorbed by other nearby Tyr residues. This effect is demonstrated in chapter 7.

Obtaining useful data from the anisotropy curves is difficult due to the noise, which is seen in all measurements and shown in Figure 43. The noise is apparent from

around 5ns and becomes more pronounced as the aggregate size increases. The noise becomes overwhelming in the later stages and so the best fit lines can only be produced over a narrow region of the time window for both the one exponential and two exponential fits. The fits for the anisotropy measurement recorded at 43hr 50min are created between approximately 1.49ns and 29.87ns of the analysis window with some variation between the DAS 6 fit and the annealing fit. Note that the analysis window is the correlation time for the measurement in question, which is the timescale seen in the anisotropy graphs. These should not be confused with fluorescence lifetimes which are the time spent in the excited state. At 78hr 23min the noise is so severe that the time window is only between 13.43ns and 20.59ns for the DAS and between 14.26ns and 20.59ns for the annealing program.

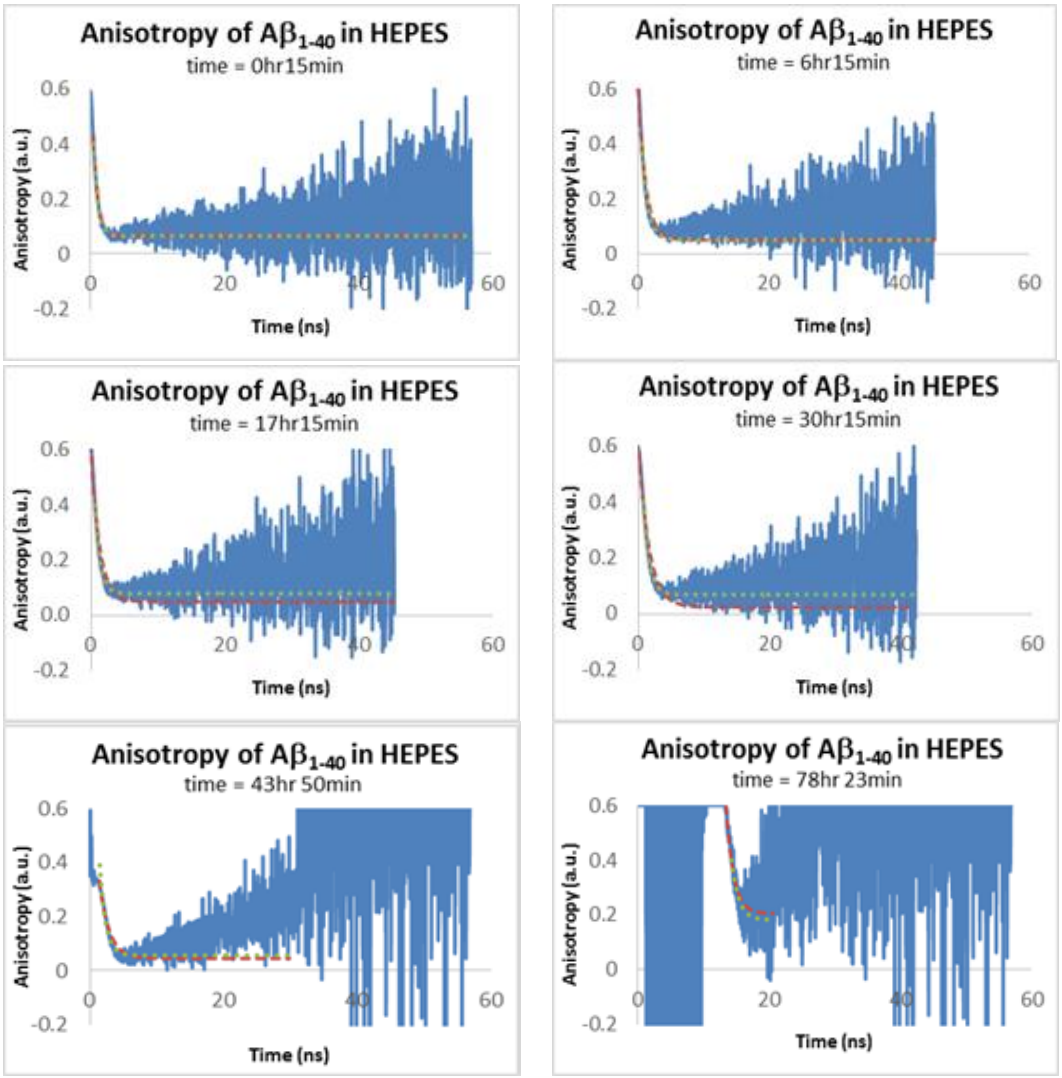

Figure 43 – 1 Exp. fit of Fluorescence Anisotropy of $A\beta_{1-40}$ in HEPES buffer over the course of 78 hours. The measured anisotropy in blue with the DAS 6 software's 1 exponential fit denoted as a dashed red line [163] and the fits from annealing program denoted by a dotted green line. The x axis is analysis time window (Time in ns) and should not be confused with the time (in hours and minutes) the measurement is initiated at.

Despite the noise, there is a visible rise in the anisotropy decay, which should not occur in a mono-dispersed system. This is sensible as the results of the DLS measurements also indicated a high polydispersity of the samples. The initial decay seen in Figure 43 is due to a species that has an initial high contribution [167]. The rise in decay is due to a species, which initially has a lower contribution. This rise occurs because the low contributing species has a longer lifetime and becomes dominant once the initial shorter lifetime is no longer detected [167]. Once the

shorter lifetime is no longer being detected, the response from the longer lifetime is all that is left, and as such a rise in anisotropy can be observed. If the anisotropy decay window could be larger and there was less noise present, we would expect there to be a secondary decay visible [167].

The fits seen in the above graph are visibly poor as they are one exponential equations and subsequently do not include the rise in anisotropy. The longer lifetime response will not be included in the model equation as a two exponential equation is required to capture them and are presented below in Figure 44. Nonetheless, all the graphs have fits created using DAS 6's in built software [163], shown in red and the green lines are fits created using a stochastic / annealing optimisation program that was coded in house (see Appendix 3.4), which will be used later in the MD chapter. These annealing fits are included here as a comparison and check of validity for use in the MD section. The correlations between the measured results and the fitted results are calculated using their covariance and standard deviations and shown below in Table 3 [168] (see Appendix 3.5 for sample calculation).

Day/Time	Fit	5ns fit	10ns fit	20ns fit	40ns fit	Total Fit
Day 1	DAS 6	0.992	0.955	0.788	0.409	0.288
15m	Annealing Program	0.992	0.949	0.764	0.377	0.263
Day 1	DAS 6	0.987	0.965	0.883	0.581	0.480
6h15m	Annealing Program	0.979	0.911	0.67	0.270	0.205
Day 2	DAS 6	0.982	0.951	0.838	0.441	0.360
17h15m	Annealing Program	0.986	0.930	0.671	0.233	0.177
Day 2	DAS 6	0.985	0.960	0.885	0.540	0.496
30h00m	Annealing Program	0.991	0.948	0.745	0.281	0.248
Day 3	DAS 6	0.982	0.900	0.500	-	-
43h35m	Annealing Program	0.976	0.927	0.553	-	-
Day 4	DAS 6	0.838	-	-	-	-
78h23m	Annealing Program	0.429	-	-	-	-

Table 3 – Correlations calculated for various times for the 1 exponential fits from DAS 6 software and annealing program.

Table 3 reveals that when the entire timeframe window of the anisotropy data is correlated, the results are poor and cannot be considered useful. In contrast, when

only the early stages are correlated the fits become more reasonable. This is due to the fact that there is less noise in the early stages of the graphs and the rise caused by the secondary decay will not be included [167]. The noise in the later stages of the aggregation process is so severe that the results in days 3 and 4 can only be fitted for a 20ns and 10ns window respectively. These results validate the annealing programs fitting parameters as being adequate and comparable to the DAS 6 fitting parameters [163].

In Figure 43, the longer lifetime species become dominant earlier in the decay as the experiment progresses, insinuating that there is significantly less involvement from the shorter lifetime species. This potentially suggests that the environments have changed causing the dominant species to change due to quenching of the aggregates [167]. Due to the increasing r_∞ value, it is also reasonable to conclude that there are a higher population of large slow moving aggregates and a low population of the fast moving species as will be shown below in the 2exp fits, which require negative pre-exponential factors in order to create the rising anisotropy [112] [167]. These results, combined with the DLS measurements, demonstrate that Aβ quickly becomes a multispecies system with monomers, oligomers and smaller protofibrils present. Unfortunately the sizes cannot be extracted due to the noise. If it had been possible to collect the sizes, this information would have been invaluable in understanding what types of species are present during the various stages of the aggregation process. It can be concluded from the combination of the DLS results and the anisotropy results that the various species are present from before the first measurement is taken and the population slowly shifts from smaller species to large mature fibrils over the course of the experiment. It is also conclusive that these measurements must be fit to two exponential functions using Eqn.'s 2.1.13 and 2.1.14, as the single exponential fit does not capture all the characteristics of the graphs.

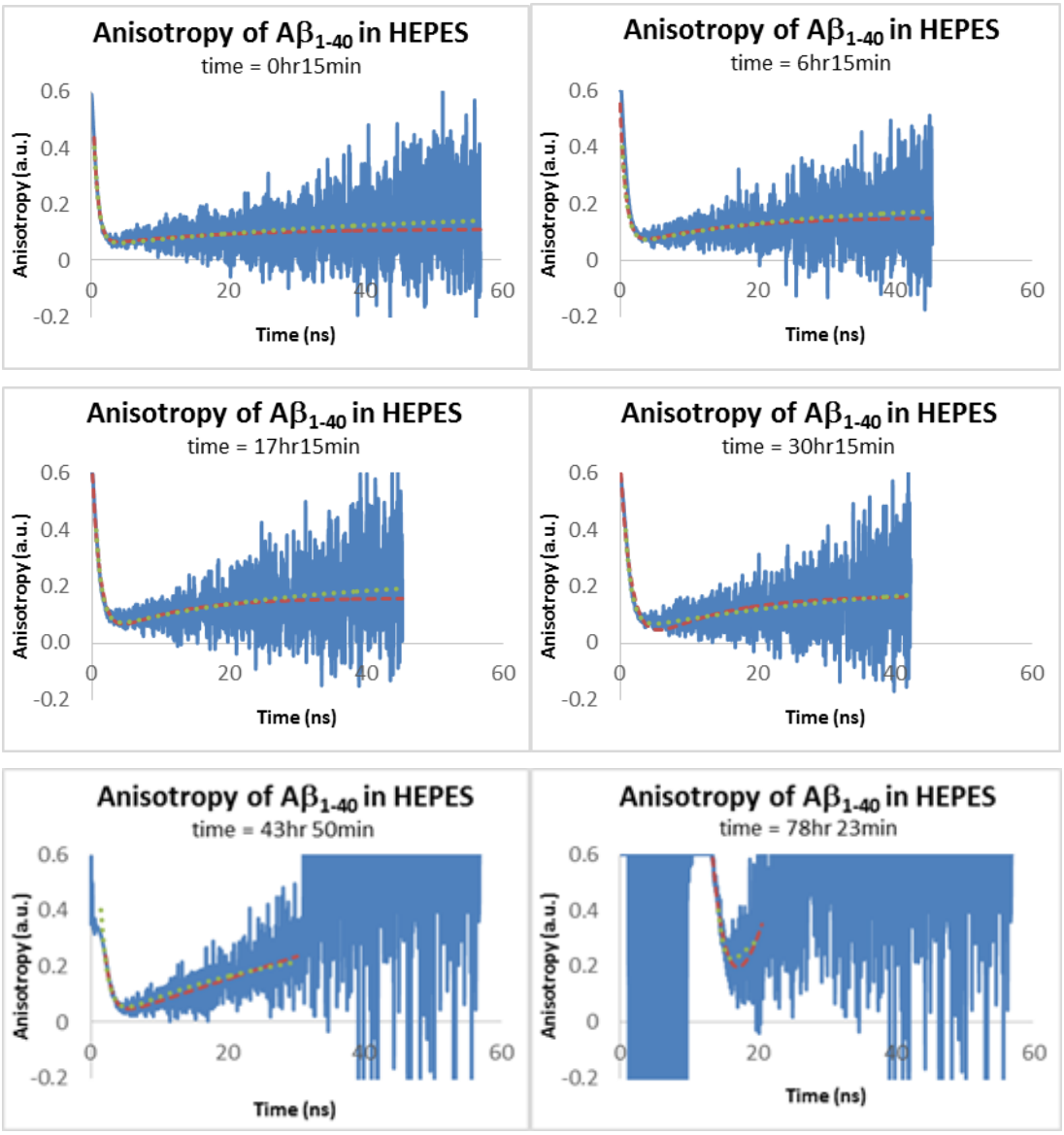

Figure 44 - 2 Exp. fit of Fluorescence Anisotropy of $A\beta_{1-40}$ in HEPES buffer over the course of 78 hours. The measured anisotropy in blue with the DAS 6 software's best fit denoted as a dashed red line and the fits from annealing program denoted as a dotted green line. The x axis is analysis time window (Time in ns) and should not be confused with the time (in hours and minutes) the measurement is initiated at.

Figure 44 and Table 4 shows visible improvement in the fits due to the inclusion of a second set of fitting parameters. The noise is so severe that it is unclear if a two or three exponential function is adequate, as a three exponential fit could potentially cause over fitting of the results, despite good χ^2 values or better correlations.

Day/Time	Fit	5ns fit	10ns fit	20ns fit	40ns fit	Total Fit
Day 1	DAS 6	0.994	0.964	0.794	0.455	0.360
15m	Annealing Program	0.992	0.954	0.760	0.428	0.360
Day 1	DAS 6	0.996	0.977	0.871	0.554	0.486
6h15m	Annealing Program	0.990	0.947	0.748	0.445	0.414
Day 2	DAS 6	0.992	0.978	0.882	0.560	0.503
17h15m	Annealing Program	0.984	0.938	0.707	0.416	0.412
Day 2	DAS 6	0.990	0.980	0.920	0.637	0.601
30h00m	Annealing Program	0.991	0.954	0.780	0.440	0.420
Day 3	DAS 6	0.965	0.858	0.737	-	-
43h35m	Annealing Program	0.978	0.943	0.800	-	-
Day 4	DAS 6	0.83775	-	-	-	-
78h23m	Annealing Program	0.521412	-	-	-	-

Table 4 - Correlations calculated for various times for the 2 exponential fits from DAS 6 software and annealing program.

Although the two exponential fits generally show better correlations, they are still only within acceptable ranges when correlated within the first 10 ns or so. This shows that the noise creates a large problem that must be overcome if any useful data can be extracted from Aβ samples (Table 5a) shows the resulting timescales and χ^2 values for all results in this experiment). Nonetheless, both the DLS measurements and these anisotropy measurements have shown signs of aggregation. When combined with the fluorescence results, we can speculate that the initial stages of the experiment contain monomers and small aggregates that are in the process of forming (the change in lifetimes), followed by the rapid growth of the protofibrils into protofilaments and mature fibrils (the changes in anisotropy/ DLS). The DAS 6 software was fit using the 2 exponential functions in order to extract a second, longer timescale [163]. However, the resulting times are random and appear to grow and shrink over time, which is also seen in Table 5b via the annealing program fits.

In an attempt to get more consistent results, the fitting window for the DAS 6 fits were manipulated to obtain fits with good χ^2 values and consistent timescales. However, this required fitting the equation to very small sections of the measured data and result in times that are outside the analysis window (see Appendix 3.6b).

(A)

Day	Clock	Time	Slow T_1 (ns)	Fast T_2 (ns)	B_1	B_2	A	χ^2
1	1600	15m	16.76	0.69	-0.059	0.384	0.111	1.09
1	2200	6h15m	13.55	0.84	-0.109	0.509	0.152	1.16
2	0900	17h15m	9.76	1.16	-0.165	0.656	0.160	1.72
2	2200	30h00m	10.58	1.60	-0.243	0.726	0.169	3.59
3	1135	43h35m	2589.37	1.06	-20.75	0.226	20.765	1.17
4	2223	78h23m	1191.21	2.88	-124.58	1.07	124.099	1.00

(B)

Day	Clock	Time	Slow T_1 (ns)	Fast T_2 (ns)	$R_{0_1}-R_{\infty_1}$	$R_{0_2}-R_{\infty_2}$	$R_{\infty_1}+R_{\infty_2}$
1	1600	15m	43.39	0.72	-0.125	0.351	0.17
1	2200	6h15m	24.01	0.82	-0.146	0.351	0.20
2	0900	17h15m	27.10	0.91	-0.185	0.356	0.23
2	2200	30h00m	39.64	0.95	-0.192	0.354	0.24
3	1135	43h35m	27.82	1.10	-0.32	0.40	0.33
4	2223	78h23m	4.56	1.05	-0.31	0.33	0.37

Table 5- Rotational times of fit parameters. (A) is the table for DAS 6 parameters, (B) is the results from Annealing. The fitting parameters B_i are the pre-exponentials and the fitting parameter A is comparable to the r_∞ (Eqn. 2.1.10 and 2.1.13)

Although the DAS 6 results have generally good χ^2 values in Table 5, they are still unreliable as can be seen by the drastic changes in value in the later stages. The results for the annealing program are slightly more consistent; however they are still unreliable as noted by their correlations and no information can be extracted from the seemingly random changes to the timescales (T_i) over time. Furthermore, the resulting response for day 4 is due to a small analysis window being used and is not a useful result. However, the results do appear to have a growing r_∞ value, which is indicative of a system which is aggregating, this pattern of growth is also seen for

the annealing program. This suggests use in the MD simulations of the annealing program is adequate as results given are similar.

A second experiment with the filters removed was also undertaken. The lack of filters allows a larger quantity of photons from the light source to enter the system, which increases the quantum yield [112]. This improves the time taken for each measurement and therefore improves the noises levels of the results. The experiment is done using NaOH instead of HEPES buffer and despite the presence of less noise, they still requires 2 hours to complete each measurement as the detection rate is still very low. The measurements also need to be fitted for three exponentials, suggesting that there are potentially three subsystems (i.e. three species in the system with unique pairs of rotational times and lifetimes) within the sample [167]. As the annealing program has not been optimised for three exponentials it has not been included in this analysis.

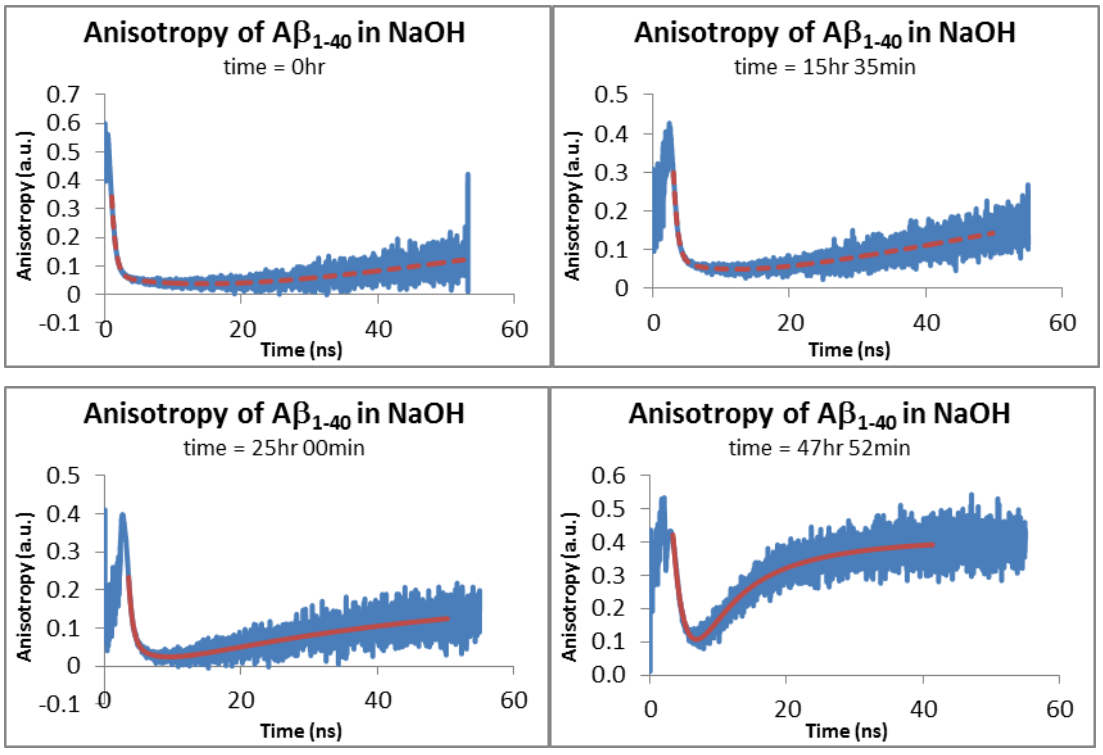

Figure 45 – 3 Exp. fit of Fluorescence Anisotropy of $A\beta_{1-40}$ in NaOH over the course of 78 hours. The measured anisotropy in blue with the DAS 6 software's best fit denoted as a dashed red line. The x axis is analysis time window (Time in ns) and should not be confused with the time (in hours and minutes) the measurement is initiated at.

As with $A\beta_{1-40}$ in HEPES buffer, there is a rising decay, suggestive of a multi species system. There is also a clear indication of aggregation occurring, as the rotational times and lifetimes of the systems are changing as the experiment progresses [112] [167]. Despite the limits of useful information that can be extracted from the measurements, the fits have strong correlations with the measured data for the first 20ns-30ns of the analysis window, as expected from a three exponential fit (see Table 6). The resulting timescales are also questionable and are to be ignored (see Appendix 3.7).

Day	Time	5ns fit	10ns fit	20ns fit	40ns fit	Total Fit
1	1200	0.999	0.996	0.979	0.884	0.853
2	0335	0.998039	0.993721	0.97091	0.892746	0.89447
2	1300	0.993379	0.977773	0.900774	0.845862	0.845935
3	1152	0.989248	0.967099	0.961242	0.948115	-

Table 6 - Correlations values of anisotropy fitting paramters for $A\beta_{1-40}$ in NaOH.

These results cannot be assumed to be accurate as there are too many factors to be considered in a three exponential system. The three subspecies that are observed must have some lifetime and rotational time associated with them [112] [167], which the fitting parameters for the DAS 6 software (and annealing program) do not include [163]. However, if there are three subspecies, they will all have a unique lifetime-rotational time pair, which cannot be determined [112] [167]. What can be determined is that the changes to the anisotropy curves over time (e.g. the increasing height of r_∞ which can be seen to some degree in Appendix 3.7.) As lifetimes stop changing after the first 10 hours of the experiment, we speculate that the changes in anisotropy after these times must be associated with rotational times and not lifetimes. This implies that the aggregates are getting larger over time.

3.4. Experimental Conclusions

In conclusion, it is clear that within the scope of these experiments that HEPES buffer is still the best environment to be used for Aβ aggregation. Despite this, a potential alternative that shows acceptable results (NaOH) was found and used in many of the experiments. However, the use of NaOH in the DLS results did not allow for the size distributions associated with the samples to be correctly establish.

The spectroscopy results showed that there are no Tyr residue environmental changes, when the samples used water or dilute hydrochloric acid, resulting in a three lifetime system (with no possibility of a fourth), that remained the same throughout all the experiments. This suggests aggregation did not occur in these samples, as there are no changes to the Tyr lifetimes and as such no changes to the environment surrounding them, which is unlikely to happen during aggregation [112]. In contrast, it is clear that NaOH shows signs of aggregation as there are changes to the lifetimes, similar to those seen for samples in HEPES buffer [44]. Furthermore, there is apparently an appearance of a potential fourth lifetime, which could be due to background noise, but is also potentially a new lifetime environment being observed that was previously being quenched or did not exist. This would be explained by local interactions forcing the Tyr to take on a different orientation within the system (similar to the rotamer states found in the MD simulations) which would change the environment [112].

The DLS results did not reveal any significant information. The size distributions were found to be impossible to extract from the results of the experiments, despite the use of a different solvent. This suggests that the polydispersity seen in the DLS results is due to the $A\beta_{1-40}$ proteins themselves rather than the buffer. The graphs of the intensities show the clear presence of aggregation over time, but the large polydispersity index of 1 prevents accurate size distributions from being obtained for the $A\beta$ [151] . Though the scattering was initially suggested to be caused by HEPES buffer, the removal of the buffer does not appear to improve the situation significantly. As BSA does not aggregate it has improved correlations in HEPES buffer (though not perfect), which suggests the complexity for $A\beta$ is fundamentally due to the multiple sizes of species in the system. This implies that there is early aggregation occurring before the first measurement is even taken (as was also seen in chapter 2.2). Therefore, the experimental setup used here is not adequate for $A\beta$ size analysis. Additionally, the intensity graphs reveal that the proteins continue to form larger aggregates, even after the Tyr residue environments stop evolving (as shown by the fluorescence lifetime changes in this chapter). This suggests that the early stages of aggregation (oligomer and protofibril formation) are responsible for the changes in lifetimes and initially do not rapidly aggregate together, but after some time these oligomers begin to stack. This result could lead to better insight into the aggregation pathway in the future.

Finally, the results for the fluorescence anisotropy experiments suggested that the current experimental setups available do not allow for accurate measurements of Aβ systems. The low quantum yield causes extremely long measurement times to occur, which is insufficient for Aβ measurements as information regarding the intermediate species (oligomers and protofibril formation) will be lost due to the rapid aggregation which occurs [169]. The resulting parameters are therefore questionable, but do show some general aggregating trends in the r_∞ values of both experiments [112]. Furthermore, some common features could be seen in the systems, such as a clear presence of aggregation and the clear presence of dipping and rising decays. This dip and rise suggests a multi species system, which seems likely based on DLS results and literature for the early stages of aggregation. This dip and rise is also indicative of species that have varying contributions and lifetimes [112] [167]. Some of the characteristics of the anisotropy curves could be due to the changes in lifetimes (from environmental differences seen in spectroscopy). However, as the lifetimes stop changing after 10 hours it could suggest that the changes in anisotropy seen after this point are purely due to rotational time increases. Regardless, the results are indicative of the presence of multiple subspecies, each with a unique pair of lifetimes and rotational times [167]. Though no results were obtained regarding size distributions, the successful use of the annealing program allows for a direct comparison between the fits seen here and the fits seen below in the computational work.

4. Results and Discussions: Monte Carlo Simulations

Monte Carlo (MC) simulations allow for the examination of systems at a coarser scale than molecular dynamics (MD) simulations. As the level of detail is significantly less than with MD simulations, it allows for significantly larger systems to be analysed for significantly longer time scales, without requiring as much processing power [154]. The simulations are created by using a set of rules and known scenarios set out in the programming code which then are allowed to happen based on probabilities of that specific event occurring. They also do not account for molecular scale interactions and so there is a distinct loss in accuracy of what is truly going on in these systems [154].

As discussed previously, experimental anisotropy is complicated and so a simplified variation was created for the MC simulations that did not account for the excitation and emission of photons, assuming that any changes caused by this process would be insignificant at the scale we are examining. The rules of these simulations begin with the rotation of the backbone (i.e. the entire protein in the case of a monomer or the entire aggregate in the case of an aggregate). The backbone was allowed to rotate in 3D space dictated by the θ_B and ϕ_B angles. They would be moved by a random amount within the limits of what the rules dictate; for example a large limitation is placed on the movement when part of a large aggregate to simulate the slow rotation of large aggregate and a monomer would have a relatively low limitation associated with it [44] [112]. Once this movement was completed, the program then ensures the Tyr residue has moved by the same amount. The Tyr residue is then allowed to move (portraying a simplistic version of the rotamer states seen in the MD section) at a fairly fast rate, but with significantly larger limitations on it (as it cannot pass through the backbone). These limitations are more sever when it is part of an aggregate, as suggested by the fluorescence results. This Tyr residue can then be tracked along its dipole moment [147] and then analysed using the in-house autocorrelation function to determine anisotropy parameters which can be indirectly compared to the results seen in both the MD and experimental anisotropy sections.

4.1. Monte Carlo Simulated Anisotropy

MC simulations are performed here to create a better understanding of fluorescence anisotropy; these will be compared to the experimental anisotropy data above and

used to aid understanding and interpretation of the MD anisotropy data presented below. These MC simulations require the input of three parameters, which are the maximum angular step size $\boldsymbol{d\theta_B}$ and $\boldsymbol{d\theta_T}$ for the backbone and transition moment respectively, and the maximum allowed angle $\boldsymbol{\theta_M}$ between the normal to the backbone and the transition moment. These parameters can be related to the rotamer states associated with real beta amyloid systems. When a Tyr residue is trapped in one rotamer state, it is comparable to having a small $\boldsymbol{\theta_M}$ value. This is usually considered to be an aggregate state, as the surrounding environment is holding the Tyr in place by limiting its movement due to the close proximity of the other protein backbones in the aggregate [63], see section 7.9 for more information. When the Tyr can move freely it is indicative of a larger $\boldsymbol{\theta_M}$, which is usually related to a monomer system or Tyr residues with a lot of freedom. The frequency it flips between the states is created within the simulation through the use of the $\boldsymbol{d\theta_T}$ variable. Furthermore, the Tyr residues themselves can allow local rotations due to the flexing of the backbone, which lead to the creation of the simplified MC simulation model.

Species	$d\theta_B$	$d\theta_T$	θ_M
Monomer	1°	5°	65°
Oligomer	0.5°	5°	25°

Table 7 - MC parameters used to mimic the behaviour of a monomer and protein aggregate.

By altering these parameters, it is possible to mimic the behaviour of an isolated monomer. A monomer with no external interactions will have a Tyr side-chain transition moment that moves more rapidly than the backbone and is relatively unrestricted [126], and values we use here are given in Table 7. In contrast the anticipated behaviour for an oligomer of aggregated protein will have a slower backbone rotation and a more restricted Tyr side-chain transition moment [89] [147], which are also shown in Table 7.

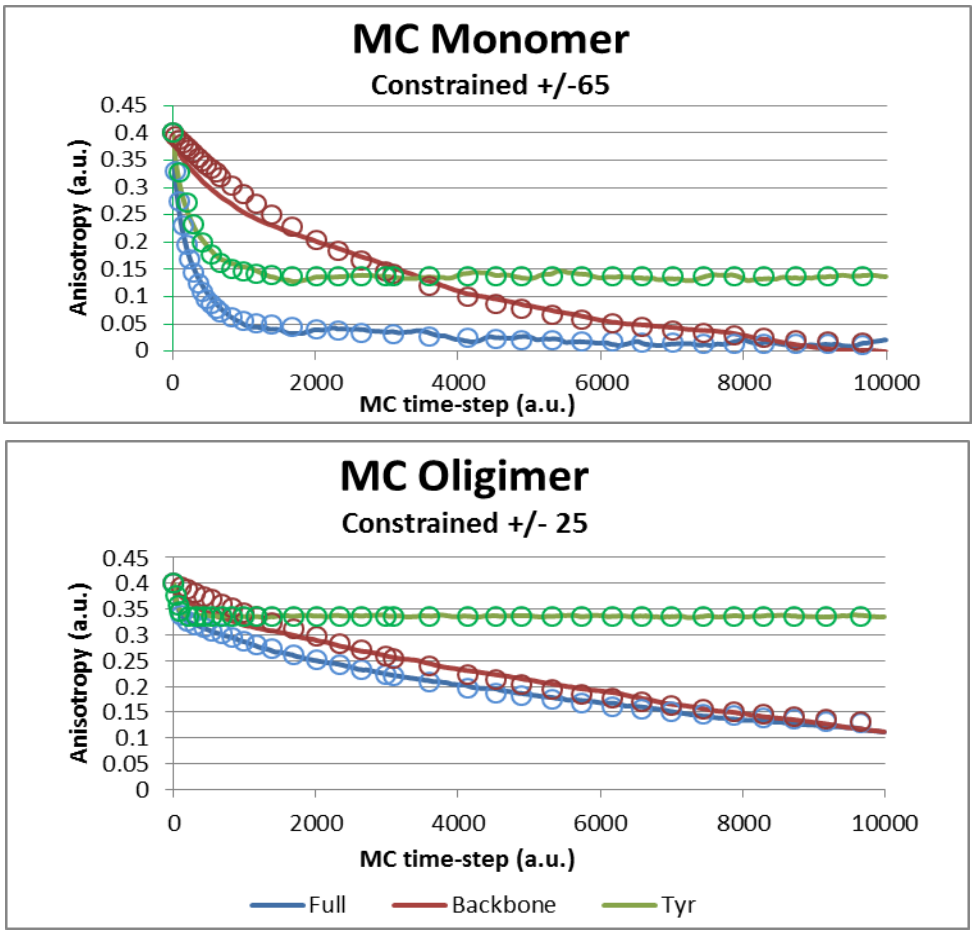

Figure 46 – The expected Anisotropy Curves for Monte Carlo Simulation. The anisotropy with both backbone and Tyr movements is shown as a solid blue line, the Tyr transition moment is shown by the green line, and the backbone is shown as a red line. The top graph depicts a monomer, the bottom an oligomer. The circles depict the best fit graphs created using the variables in Table 7 below.

The results of the MC simulations are displayed in Figure 46. The green lines shown in these graphs are the Tyr response when the backbone is held in place. For the monomer simulation the anisotropy curve rapidly decays for approximately the first 1000 MC steps from its initial value of 0.4 and plateau's at r_∞ ~0.14. The reason for this plateau value is due to the constraint placed on the angular movement of the transition moment, which is $\theta_M = 65°$. As the backbone is frozen, the extent to which the transition moment can diffuse from its position at time τ to that of a later time $\tau + t$ is limited. Therefore, the resulting green line shows to what degree the Tyr side chain has been constrained, which explains the reason for nonzero fluorescence anisotropy decays. In the oligomer anisotropy decay, the Tyr movements have been

constrained further where $\theta_M = 25°$. When the backbone is frozen here, the Tyr shows a significantly smaller initial decay in the anisotropy (to ~0.34).

In contrast, when the backbone is analysed individually with the Tyr movements frozen (shown in red in Figure 46), the anisotropy decays to approximately zero for the monomer. However, when both the Tyr side-chain and the backbone are allowed to move, the resulting anisotropy is a combination of both effects. There is a rapid decay in the anisotropy initially, which is limited by the constraint imposed by θ_M, added to the slow decay of the backbone. For the oligomer, however, the backbone movements are slow compared to the sampling window of the anisotropy, which results in an apparent nonzero long-time anisotropy. These changes in the characteristics suggest that both the initial decay and the r_∞ values can give information regarding the aggregate size.

The circles that follow the various decays in Figure 46 are the results of fitting Eqn. 2.3.3 to the MC data, and Table 7 displays the parameters of each fit. The resulting r_∞ value (from fitting parameters $r_{i_T} + r_{i_B}$) for the monomer's Tyr response is 0.14. The time-scale required for the Tyr side-chains response to decay to its plateau is an order of magnitude shorter than that of the backbone, whether the movement of both or just the backbone are included. This is because the Tyr side-chain can explore its constraints ($\pm 65°$) in approximately 1000 or so random MC steps due to its $d\theta_T$ value of 5°. In contrast, the backbone will take up to roughly 10,000 random steps to explore the constraints of $\pm 90°$ with a $d\theta_B$value of 1° order to reduce its autocorrelation to zero.

Curve	$r_{\infty_T} + r_{\infty_B}$	$r_{0_T} - r_{\infty_T}$	T_T	$r_{0_B} - r_{\infty_B}$	T_B
Monomer-backbone	0.00	0.00	-	0.40	3000
Monomer-transition moment	0.14	0.26	300	0.00	-
Monomer-both	0.01	0.33	200	0.06	2900
Oligomer-backbone	0.11	0.00	-	0.29	4200
Oligomer-transition moment	0.33	0.07	59	0.00	-
Oligomer-both	0.11	0.06	35	0.23	4100

Table 8 - Parameters from fit of Eqn. 2.3.3 to the MC anisotropy curves of Figure 46
The times T_T and T_B are given in units of MC steps.

The oligomer simulation parameters follow the same pattern. The relaxation time $\mathrm{T}_B \approx 4000$ is larger than for the monomer system. This is because the maximum

step size is half the value it had for the monomer simulation ($d\theta_B = 0.5°$.) The smaller value of $T_T \sim 50$ reflects the smaller parameter space ($\pm 25°$) that the Tyr side-chain can explore. This Tyr response has a small contribution to the anisotropy of the full simulation with both transition moment and backbone movements.

4.2. Monte Carlo Simulated Anisotropy Conclusions

In conclusion, these simulations have successfully demonstrated that movement limitations and restrictions on the Tyr residue and the backbone can have dramatic effects on the resulting anisotropy graphs [112], which can be related to what is seen in the experimental results in previous chapters. The resulting graphs are promising, showing very similar results to what can be found in anisotropy experiments [170].

These simulations reveal that the rapid movement of the Tyr side-chain transition moment can be characterised by the initial rapid decay in the anisotropy [112]. The plateau value for the decay in question can be determined by the level of constraint placed on the movement with respect to the backbone. The slower backbone movement can be observed in the longer time relaxation of the anisotropy [112].

Finally, these simulations also reveal that for a nonzero plateau value to occur after very long times, the slow relaxation time of the backbone must either be beyond the measurement window (be that experimental or from simulation), or the backbone itself might be constrained [112]. In the following sections we use the perspective these conclusions provide to discuss the MD simulation results.

5. Results and Discussion: MD Amorph. Aggregation of $A\beta_{1-40}$

Molecular Dynamics (MD) is used throughout the next three chapters to study the early stages of aggregation. The first chapter pertaining to the MD results shows the atomistic results of the trajectories of $A\beta_{1-40}$, which allows us to gain information regarding structural changes of the proteins, the Tyr residue position and overall shape of the aggregate forming in each trajectory. Each simulation in this section was allowed to run for a minimum of 50ns.

The structure used for these simulations was taken from work by Crescenzi et al (1iyt.pdb) [46]. This has 42 residues and so, the last two residues were removed as discussed previously [44]. The Charmm22 and Charm27 hybrid forcefield and TIP3P water model used here are satisfactory as discussed in chapter 2.4.2 [44]. The visualisation of each of the simulations was done using VMD [146].

The trajectories will be study by initially discussing how the proteins move during the whole simulation, noting aggregation conformational changes, or any other interesting features (such as a trapped or free moving Tyr residue). The Tyr can be then tracked more accurately using its dihedral angles, as discussed previously, to reveal which position or rotamer state it is currently in, which can reveal useful information about the Tyr's surroundings and could be potentially linked to the fluorescence experiments. This is then further complimented by the simulated anisotropy models, which were creating by tracking the Tyr residues transition moment as discussed above [147]. Although the simulated anisotropy does not allow for excitation and emission of photons, they can still be compared to the fluorescence anisotropy experiments, revealing an atomistic reasoning behind fluorescence anisotropy results.

5.1. One Protein System (No Ions)

The trajectory of a single $A\beta_{1-40}$ protein in a waterbox is illustrated by the snapshots in Figure 47. The box is large enough to prevent any artificial protein-protein interactions caused by the use of periodic boundary conditions as the monomers dimensions are ~(34Å,15Å, 24Å) and the waterbox dimensions are ~(91Å,78Å,103Å). There are no ions present in this system, which allows the protein to move freely in a simple waterbox.

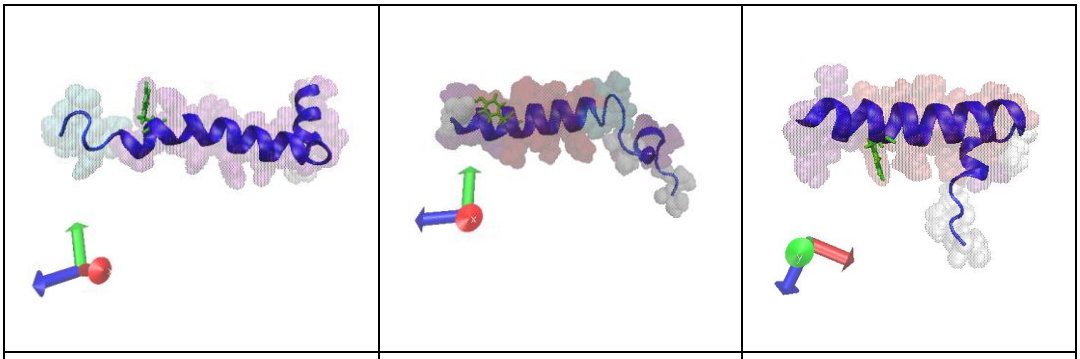

T=0ns	T=25ns	T=50ns

Figure 47 – Single Protein. The first panel shows the starting position of the protein at T=0ns. The blue line indicates protein A in the system, with the Tyr side-chain highlighted in green and the VDW interactions are indicated by the transpaernt spheres. Purple denotes alpha helix structure, red denotes pi-helix, white denotes a coil and cyan denotes a beta turn (similar to a alpha helix).The middle panel shows the trajectory at 25ns and the right panel shows the system at the end of the trajectory at a time of 50ns.

During the first 10ns of the trajectory (see Figure 47) the tail of the protein begins to unravel becoming straighter between residues 27 and 30. The backbone remains straight and has a distinct bend at residue 37 throughout the rest of the trajectory with the tail (residues 37-40) curving more towards the midsection of the protein. It is shown through the transparent VDW forces that the structure is primarily dominated by an alpha-helix secondary structure, but quickly gains a pi-helix (a less stable helix structure [171]) structure (in red) in the middle and a more pronounced coil (in white). This stabilises the protein by hiding the hydrophobic sections away from the surrounding water (see Figure 48) [122]. The tail unravelling is partly due to the hydrophobic residues having nowhere to bury themselves and are straightening out in order to help stabilise the system and would potentially continue to happen if the trajectory was longer, revealing a less ordered structure [172]. This structure seems fairly ordered due the helical structure, with the head of the backbone being unravelled with minimal structuring, as it does not lose much of its shape, it is still comparable to the initial structure.

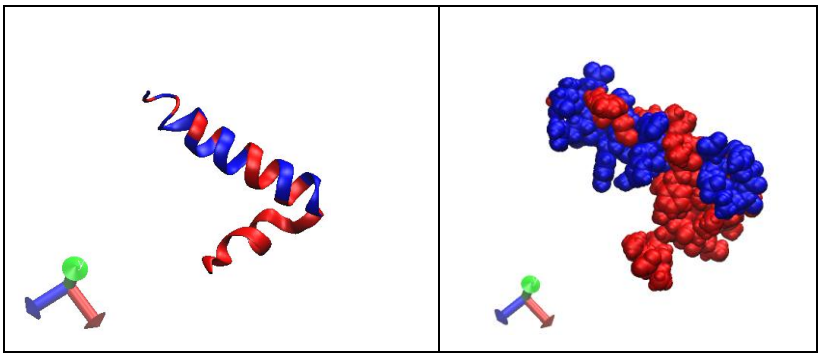

Figure 48 - $A\beta_{1-40}$ Monomer at equilibrium with hydrophobic sections highlighted in Red. Proteins A shown at 50ns. The hydrophilic residues are shown in blue. The image on the left uses VMD's cartoon representation, and on the right the structure is shown using VDW spheres.

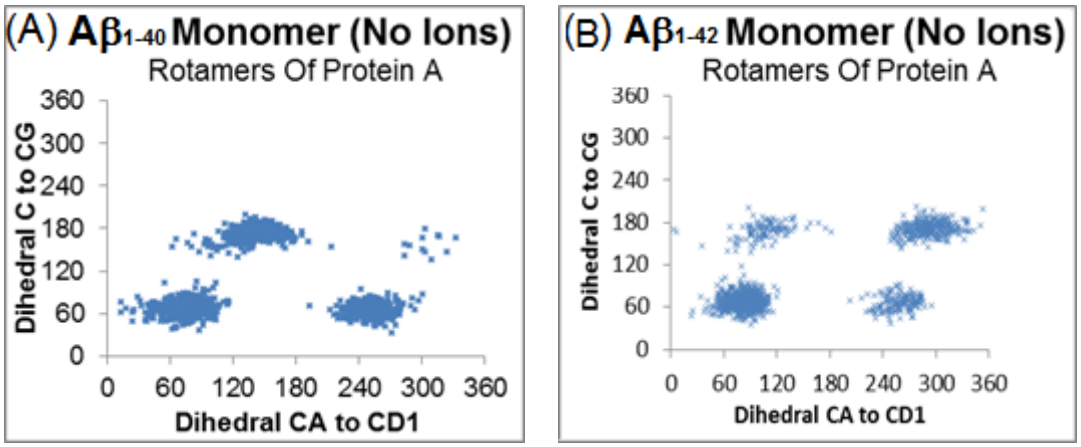

Figure 49 – Comparison of Tyr Rotamer States of an (A) $A\beta_{1-40}$ Monomer and (B) $A\beta_{1-42}$ Monomer, both without Ions. The graphs depict the orientations that the Tyr side-chain of a monomer favours during the 50ns trajectory. The centre for each is approximately (65,60), (250,60), (140,180), (310,170) for Tyr A.

Figure 49 shows the resulting rotamer states for an $A\beta_{1-40}$ and $A\beta_{1-42}$ monomer, with the x-axis as the dihdreal angle created between the C_α, C_β, C_γ and C_{D1} atoms in the tyorisne. The y-axis is the dihdreal angle between C, C_α, C_β, C_γ atoms in the Tyr. This creates zones that the Tyr prefers to orientate itself in. The Tyr side-chain takes on the four classic rotamer states seen both in previous work and in many of the trajectories discussed here [44]. Figure 49A shows an equal preference between states 1, 2 and 3 with some brief occupation of state 4. These state occupations show that non aggregated systems tend to prefer states 1 and 2 rather than states 3 and 4, due to the open environment around the Tyr. This is discussed below in Figure 149 to Figure 151 , where it is found that states 3 and 4 tend to be more occupied when the Tyr is influenced into twisting along the C to $C\gamma$ angle. Figure

49B shows similar results for an $A\beta_{1-42}$ monomer, though there is a more even distribution among the 4 states. The variation here can be attributed to the random nature of simulations and so show similar results with expected variation [173]. Figure 48B is discussed in more detail in Chapter 6.2 and is only shown here for direct comparison.

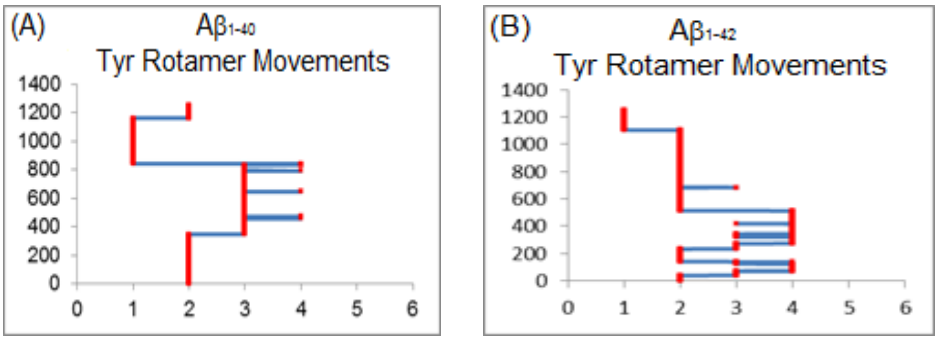

Figure 50 – Comparison of Tyr movement Between States of an (A) $A\beta_{1-40}$ Monomer and (B) $A\beta_{1-42}$ Monomer. This graph shows the Tyr side-chain movements between the different states over the course of the trajectory with the x axis showing the different states and the y axis showing the frame within the trajectory.

The graphs in Figure 50 show how the Tyr side-chains occupy the different rotamer states over the course of the trajectory with respect to its frame number. Every 100th frame of the original trajectory is depicted for all the rotamer state movements and each of the new frames is 0.04ns in length. As discussed previously, the transition between the states is created by using the dihedral angles associated with the Tyr movements and giving a number (state) to each region (Table 9) seen in graphs, such as Figure 49 [44].

	C_α-C_{D1}	C-C_γ
State 1	181-360	0-120
State 2	0-180	0-120
State 3	0-180	121-240
State 4	181-360	121-240
State 5	0-180	241-360
State 6	181-360	241-360

Table 9 - State Numbering Rules.

For the $A\beta_{1-40}$ monomer, the Tyr side-chain begins in state two and remains there for over 300 frames (12ns) of the trajectory, before moving into state 3 where it jumps between states 3 and 4 with a preference towards state 3 for about 400 frames

(16ns.) After the Tyr moves from state 4 into state 1 and ends the trajectory in state 2. Though it doesn't move between states often due to the lack of surrounding interactions, it still moves regularly within the states as seen by the population densities in Figure 49. Furthermore, it should be noted that the Tyr side-chains have a tendency to only move from state 1 to 2, 2 to 3, 3 to 4 and 4 to 1, implying that the Tyr has a preferred order that it moves through its dihedral angles. This pattern is seen throughout all the trajectories described below (with a few exceptions as discussed). The $A\beta_{1-42}$ monomer shows different movements, as it starts with erratically moving between the four states which can be attributed to the random nature of these simulations, the relaxation time and also the slightly different starting environment (see Figure 93). Regardless, they have the same affinity for states 1 and 2 once they have reached equilibrium, showing minimal differences.

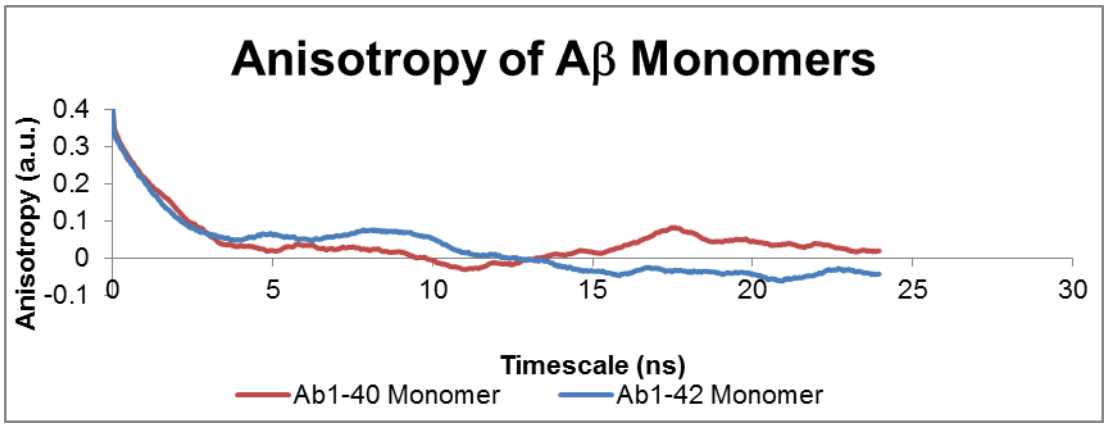

Figure 51 - Simulated Anisotropy of $A\beta_{1-40}$ and $A\beta_{1-42}$ Monomer. This graph shows the simulated anisotropy of Monomer A (blue line).

As expected for a $A\beta_{1-40}$ monomer, the anisotropy shown in Figure 51 decays rapidly to 0 within 4ns of the correlation time and remains at approximately 0 for the rest of the trajectory. This is because the protein can move freely, allowing the system to decay to 0; the Tyr side-chain has minimal restrictions on it as shown by the density populations in Figure 51. The $A\beta_{1-42}$ monomer has a very similar decay with only some inconsequential variance caused by the random nature of the simulations, which would not be seen when studying a real sample which has a larger population of proteins present.

5.1.1. Best Fits

The best fit variables and graph for the $A\beta_{1-40}$ monomer's anisotropy curve (with no ions) and all other $A\beta_{1-40}$ graphs can be seen below in Figure 85 and Table 10, where the data is compiled to ease comparisons and $A\beta_{1-42}$ results for monomers can also be found in Figure 110 and Table 11. The variables associated with the first fit seen in Table 10 for the monomer is a two exponential fit that shows almost no contribution from its slower rotational time (τ_r) and as such the other variables are redundant. This is because an insignificant contribution from one of the mechanisms implies that a single exponential fit should be used instead. This is further proven as this slow τ_r value is unrealistic as it implies that this free moving monomer has a 20ns τ_r value.

As such the single exponential variables for this monomer show a τ_r value of 1.43ns which is slightly faster than the $A\beta_{1-42}$ monomers seen below in chapter 6.6 (ranging from 2-3ns) which is logical as $A\beta_{1-40}$ is smaller than $A\beta_{1-42.}$ The plateau value is slightly above 0 due to the fluctuations at the end of the anisotropy decay but is still an acceptable result for a monomer.

This single exponential fit also has a smaller error associated with it, as its correlation is 0.93 as opposed to the 0.91 correlation seen for the two exponential fit. Though 0.93 is still not a strong correlation it is still reasonable and the resulting graph and variables are suitable for a single $A\beta_{1-40}$ monomer.

A single exponential fit was also made for $A\beta_{1-42}$ monomer (the nearby dimer should have minimal effect on it). Due to the secondary decay seen for this $A\beta_{1-42}$ monomer it is more difficult to get an appropriate fit for it however, when fit to both the first and secondary decay, the resulting rotational times stayed at around 2ns-3ns. This increase could be due to the other monomers/ aggregates in the system slowing down the bulk rotation. When a single $A\beta_{1-42}$ monomer system is looked at the rotational times vary between approximately 1.7ns-2ns, showing that there is a slightly increase in rotational times though if there are surrounding monomers it can have an effect.

5.2. One Protein System (Ions)

The next trajectory studied in Figure 52 has is a single $A\beta_{1\text{-}40}$ protein in a waterbox which has ions in it that simulated the ionic concentration of blood at 0.250mMol/L [162]. This simulation was created to examine what effect ions have on the system.

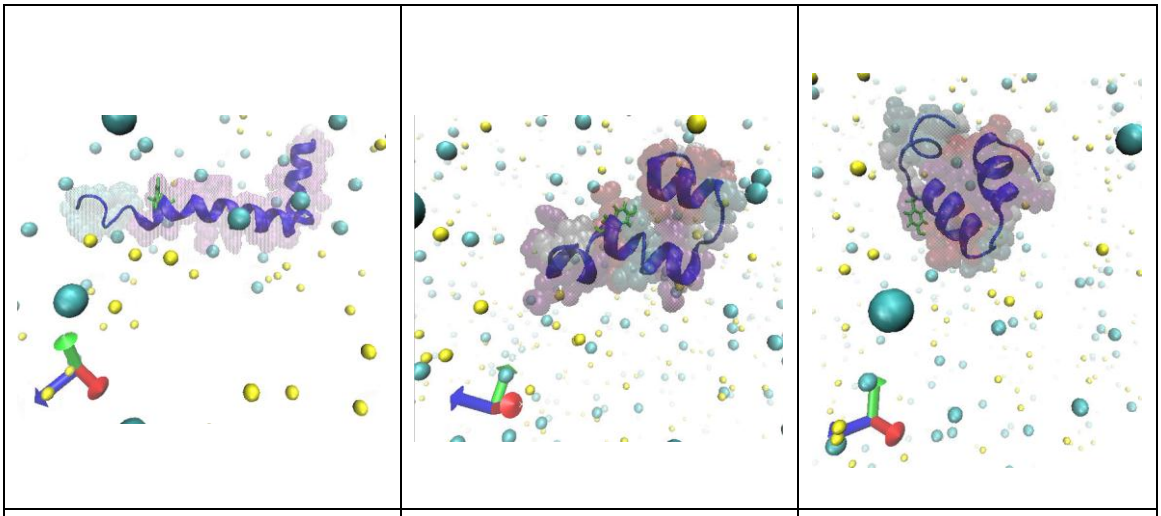

T=0ns	T=25ns	T=50ns

Figure 52 – Single Protein with ions. The blue line indicates protein A in the system with Tyr side-chain shown in green and the VDW interactions are indicated by the transpaernt spheres. Purple denotes alpha helix structure, red denotes pi-helix, white denotes a coil and cyan denotes a beta turn. The ions are show as the yellow and teal spheres. The first panel shows the starting position of the protien at T=0ns. The middle panel shows the trajectory at 25ns and the right panel shows the system at the end fo the trajectory at a time of 50ns.

In Figure 52 the trajectory for the monomer with ions is seen. In a similar manner to the monomer without ions, the initial structure is almost fully alpha helical (in purple) but very quickly changes shape, to have a coil form at the tail section of the protein and a pi-helix structure in the middle at around residues 11 to 14. This quickly changes again and ends on a structure that is balled up containing a pi helix, an alpha helix, a beta turn and a coil [171]. It contains the same characteristics but in a different configuration without ions and is closer to the unravelled shape seen in literature [172].

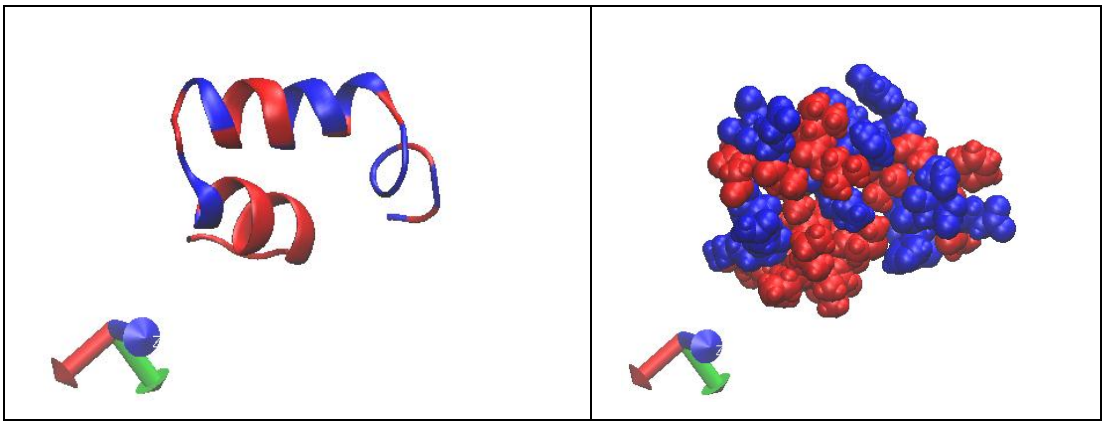

Figure 53 - Hydrophobic Sections of an $A\beta_{1-40}$ Monomer in Ions. Both pictures are taken at 50ns with the left panel showing the shape of the protein and the right panel showing the VDW spheres. The hydrophobic residues (in red) are shown against the hydrophilic (blue) sections on the right.

As the trajectory begins, the protein bends at residues 22 and at residue 26 creating a “U” or horseshoe shape. This is similar to the hairpin or horseshoe misfolded beta-sheet motif required for the formation of oligomers and could be the start of it forming [63]. This shape persists throughout the trajectory and is only slightly different from the shape seen above without ions (Figure 47). This is due to the stabilisation process as discussed above, where the hydrophobic sections will attempt to bury themselves (see Figure 53) [122]. The presence of the ions can cause long range screening effects, which prevent long range interactions from occurring between residues / backbone of the protein. This effect appears to allow for a more rigid beta-sheet hairpin structure to form as the residues cannot affect each other from the longer ranges [174] [175].

This “U” shape could lead to the subsequent aggregation of proteins creating an $A\beta_{1-40}$ protofibril (see Figure 112 for $A\beta_{1-42}$ equivalent structure) This protein does seem a little more stable than its counterpart with no ions, as more of the hydrophobic sections are buried though both are stable regardless.

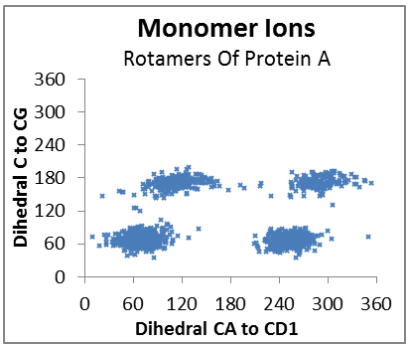

Figure 54 – Tyr Rotamer states of an Aβ1-40 Monomer with/ Ions. The graph depicts the orientations that the Tyr side-chain of monomer A favours during the 50ns trajectory. The centre for each is approximately (65,65), (250,65), (115,175), (290,170) for Tyr A.

Much like the $A\beta_{1\text{-}40}$ monomer without ions, the Tyr in this system shows four rotamer states as expected. Figure 54 also shows an even spread between the states with a slight preference towards states 1 and 2. The Tyr side-chain are potentially influenced by the surroudning ions creating a higher probabilty of states 3 and 4 to be occupied, which (from the results of this work) appears to be more common in aggregates.

As explained below in Figure 149 to Figure 151, the Tyr side-chain will begin to move due to its proximity to other residues/ions/aggregates in an attempt to find a stable configuration. This external influence may be required to enter states 3 and 4 and the surrounding environment of the Tyr in Figure 52 could cause the change in conformation due to the hydrophobic sections becoming more buried.

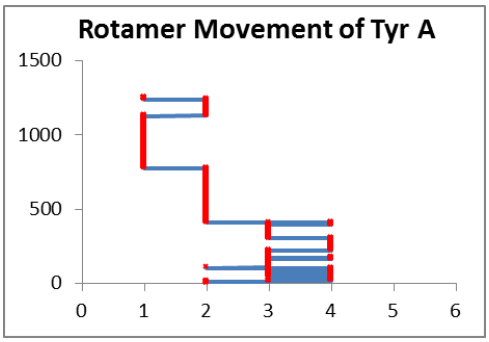

Figure 55 - Rotamer Movement between States of an Aβ1-40 monomer w/ Ions. This graph shows the Tyr side-chain movements between the different states over the course of the trajectory with the x axis showing the different states and the y axis showing the frame within the trajectory.

Figure 55 shows that the Tyr side-chain begins by moving erratically between states 3 and 4 before occupying and holding states 1 and 2 for longer periods. States 3

and 4 appear during the stabilisation process, which is likely due to the proximity of the ions in the system before a stable position for the system is found.

This explains why the Tyr does not naturally prefer to occupy states 1 and 2. If this trajectory could be continued, it would likely show that states 1 and 2 are preferred post stabilisation, based on the Tyr residue's final position in Figure 52. Regardless, despite the ions and different final conformation, the Tyr side-chain still moves between the four rotamer states in the expected pattern.

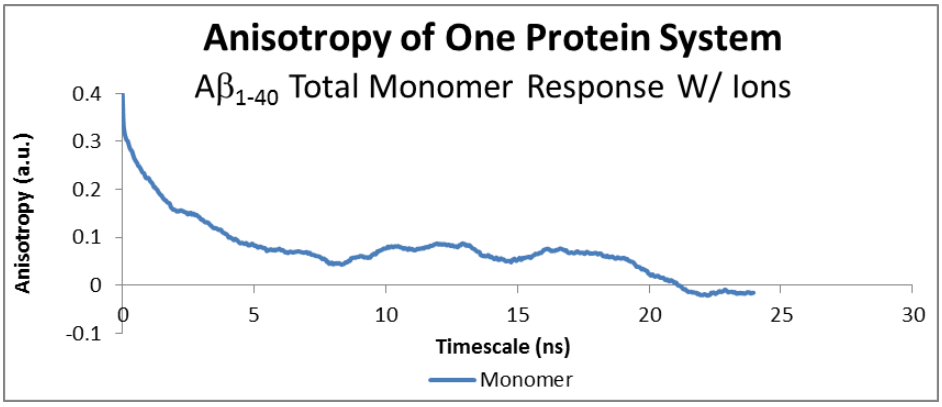

Figure 56 - Simulated Anisotropy of an $A\beta_{1-40}$ Monomer with ions. This graph shows the simulated anisotropy of Monomer A (blue).

Figure 56 depicts the anisotropy curve of the monomer with ions, which shares characteristics with the monomer without ions. However, the initial drop is sharper as the Tyr moves more often (Figure 55) and possibly also has a higher plateau value associated with it. The changes in the protein structure could potentially be responsible for the change in anisotropy; however this is impossible to determine as there are many factors affecting the two systems in different manners due to the random aspect of the simulations, the ions addition of the ions and the change in structure itself. Nonetheless both systems show similar responses that appear to be associated with monomers.

5.2.1. Best Fits

The best fit graph and variables are shown below in Figure 85 and Table 10, where it can be seen that the monomer with ions requires a single exponential fit due to lack of contribution from the second mechanism (0.041) which if not ignored would suggest that the system has an exceptionally slow τ_r value of 37.31ns. As such, the resulting τ_r value for the system is 1.82ns which is fractionally slower than the

monomer without ions (1.43ns). As expected the fitted r_∞ value is slightly higher than the no ion system (0.049 and 0.022 respectively).

Both the 2 exponential and 1 exponential fits have poor correlations associated with them (0.89 and 0.88 respectively). This is due to the complex decay seen between the time values of 8ns and 16ns as well as the second rapid decay at 19ns. This behaviour is likely due to the initial stabilisation process induced by the ions; It is possible that a longer trajectory not including this stabilisation would help create a more smooth decay, although we did not test this idea.

Despite this, the single exponential fit gives reasonable results for a monomer with the ions, despite the poor correlation. This suggests that the complications created in the decay by the stabilisation process do not affect the anisotropy significantly (at least for a monomer.) These results further reflect those seen in the MC anisotropy results.

5.3. Two Protein System (Monomers)

The first two protein system for the $A\beta_{1\text{-}40}$ results has a sufficiently sized waterbox with dimensions ~86Åx93Åx98Å (recall protein dimensions ~48.06Å x 9.69Å x 26.21Å) which gives ample room for the proteins to move. No aggregation occurs and as such, this system was studied as a monomer system to see how two monomers interact in close proximity.

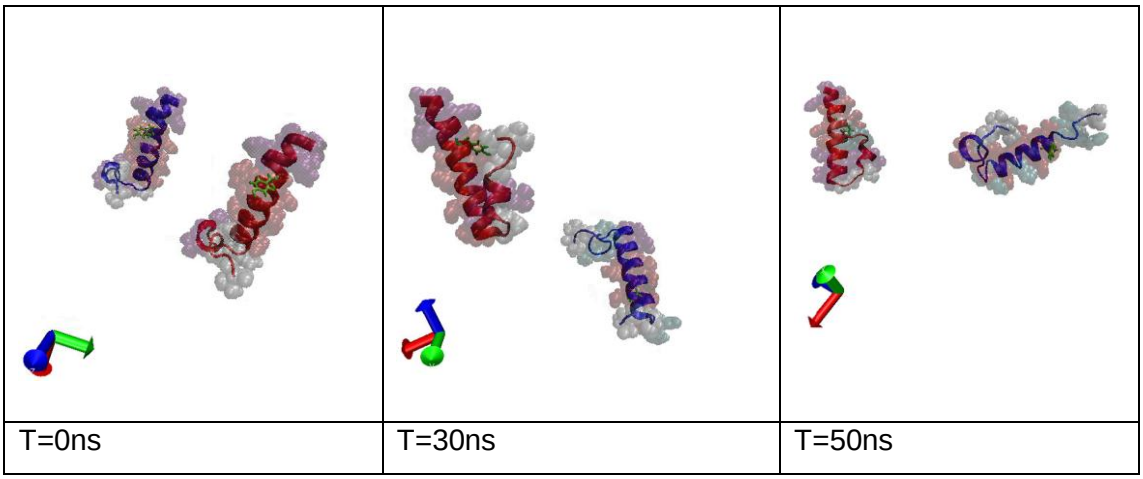

Figure 57 – Two Monomer System. The panels shows proteins A (blue) and B (red) with the Tyr side-chains highlighted (green) and the VDW interactions indicated by the transparent spheres: Purple denotes alpha helix structure, red denotes pi-helix, white denotes a coil and cyan denotes a beta turn. The first panel shows the starting postion of the proteins. The middle panel shows the trajectory at 30ns and the right panel shows the system at the end of the trajectory at a time of 50ns.

Figure 57 shows that the two monomers never interact but also the monomers do not seem to move much though they do move into more stable configurations. Monomer B ends the trajectory with the tail tucked into the backbone to help bury the hydrophobic sections [122], but monomer A does not move much from its starting position, leaving the tail slightly more exposed to the water. Without the ions present, it appears the fold for the beta-sheet occurs lower down the tail, but is still similar to the U shape. The trajectory begins with almost fully helical structures (depicted as red) and then the two begin to stabilize into two different configurations with some similarities. Both the tails have a beta turn (in cyan) and coil (in white), but monomer A shows a pi-helix (in red) structure in the middle, and monomer B shows an alpha-helix structure x (purple) in the middle [171]. Overall monomer B shows a much more prominent alpha helix structure by the end.

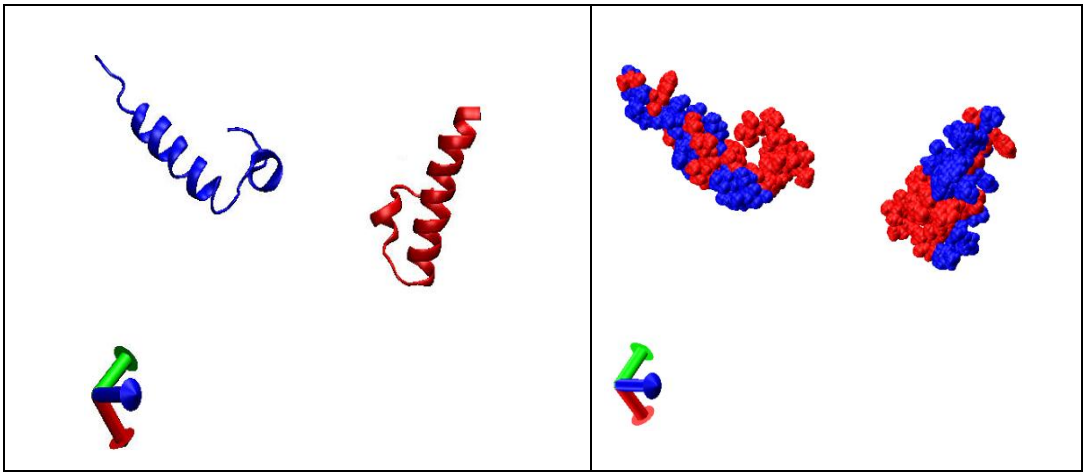

Figure 58 - Hydrophobic Sections of two $A\beta_{1-40}$ Monomers. Both pictures are taken at 50ns with the left panel showing the shape of the proteins (A and B; blue and red respective) and the right panel showing the VDW spheres with the hydrophobic sections (red) against the hydrophilic sections (blue) on the right.

As explained above, Figure 58 depicts how monomer A does not hide the hydrophobic sections as effectively as monomer B. This could be caused by some unique interactions caused by the size of the waterbox and interactions with protein B which causes protein A to fold incorrectly. The trajectory may also require being ran for a longer time to allow them to fold correctly, as Ab1-40 appears to be partially unfolded in water with only an alpha helix in the central region of the backbone [172]. This could also explain why the system does not aggregate, assuming that misfolding is an important part of the aggregation process rather than metal ion binding for example [41] [42].

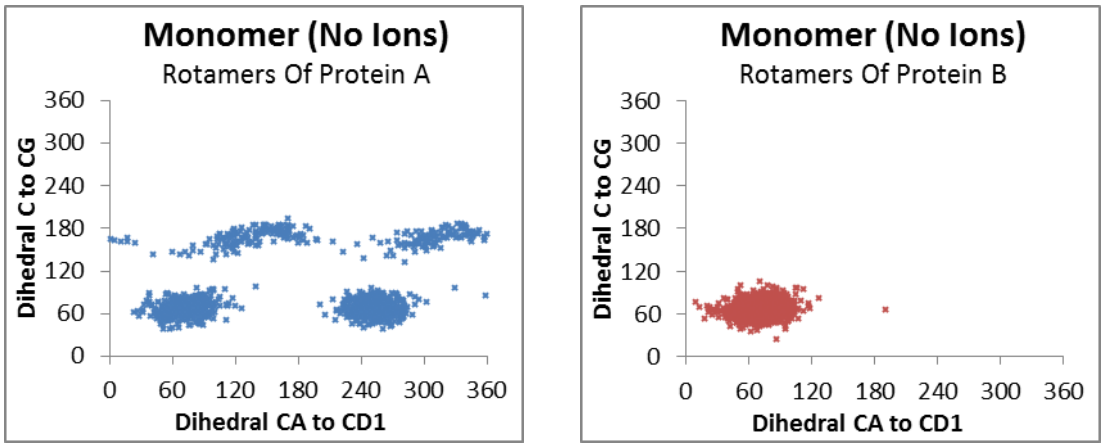

Figure 59 – Tyr Rotamer states of two Aβ1-40 Monomers. The graph depicts the orientations that the Tyr side-chain of monomers A and B favour during the 50ns trajectory. The centre of each state for Tyr A is approximately (65,65), (250,65), (130,170), (310,165). For Tyr B only state 2 (65,65) is present with a single instance of state 1 at (190,65).

Again, monomer A shows occupation of the four rotamer states, whereas monomer B shows occupation of only state 2. These results are acceptable, as a monomer should favour states 1 and 2, with some occupation of states 3 and 4 as shown for monomer A. Tyr B is trapped in state 2, which could be due to the length of the trajectory or created due to the surroundings (the tail touches the Tyr, holding it in position.)

If this trajectory was longer there would likely be a preferred occupation of states 1 and 2 with some occupation of states 3 and 4 as expected. Nevertheless, Tyr A shows the acceptable responses of a monomer (with respect to other results) and Tyr B does show a prefference towards the least twisted states 1 and 2.

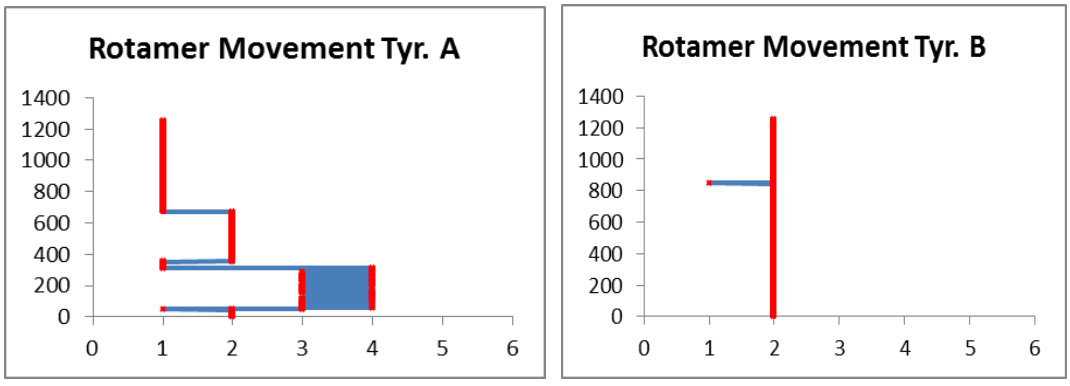

Figure 60 - Tyr movement between States of two Aβ1-40 monomers. This graph shows the Tyr side-chain movements between the different states over the course of the trajectory with the x axis showing the different states and the y axis showing the frame within the trajectory.

Figure 60 shows that the movements of both Tyr side-chains move between the states in the expected manner and have a preference towards states 1 and 2 over states 3 and 4, which as stated previously is the correct response from monomers. As monomer A does not bury the hydrophobic tail, the Tyr side-chain has fewer influences from its surroundings as it is part of the head of the protein. In contrast, Tyr B is hydrophilic and is interacting directly with the hydrophobic tail (Figure 57.) This explains the lack of movement from Tyr B as it is being pulled (and straightened) towards the tail.

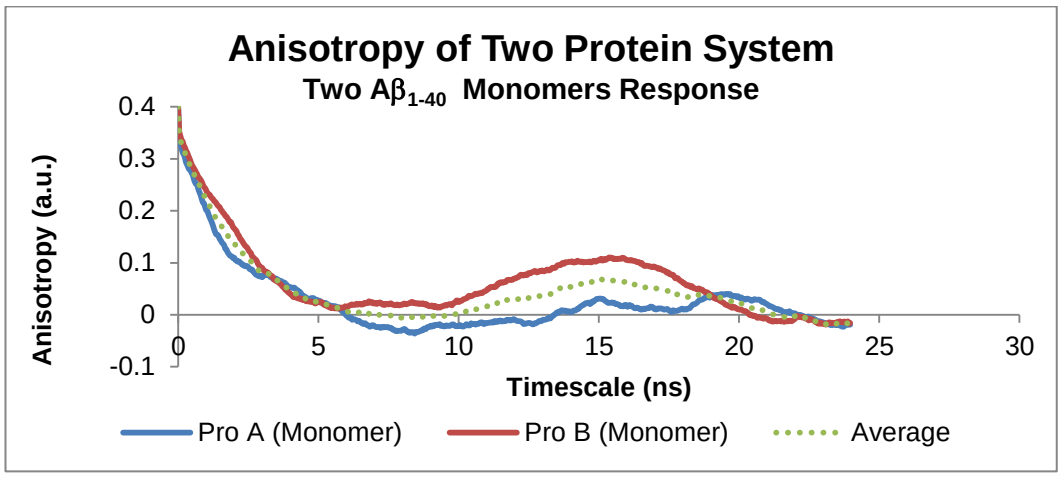

Figure 61 - Simulated Anisotropy of two $A\beta_{1-40}$ Monomers. This graph shows the simulated anisotropy of Monomer A (blue), Monomer B (red) and the average of the two (dotted green line).

The anisotropy of both monomers shown in Figure 61 decay rapidly to 0 within the first 5ns of the correlation time, as seen previously in the monomer without ions. The difference in in the initial decay will be related to the subtle difference in the Tyr movements, as Tyr A moves more than Tyr B (Figure 60.) The rise seen in monomer B at around 10ns could potentially be due to the extreme lack of movement from the Tyr, though it is difficult to determine as there is a finite sample in the trajectory. Despite this, the average anisotropy of these two graphs does show a monomeric response as the plateau value can assumed to be approximately 0. Despite the fact there are two monomers interacting in this waterbox, the overall response is more or less unaffected.

5.3.1. Best Fits

As with the previous examples and shown in Figure 85 and Table 10, the slow mechanism with a τ_r value of 25.22ns has very little contribution to the fit (a 0.37

contribution from the fast mechanism and 0.03 for the slow.) Which means a single exponential is used in this example as well. The resulting τ_r value for the single exponential fit is 1.54ns, which is an expected time for a monomer as seen in previous examples. It also has a low r_∞ value of 0.02 which is a reasonable decay close to 0 for a monomer system. These sharp initial decays and plateau values of approximately 0 are reflections of the MC results

5.4. Two Protein System (Dimer with Big Waterbox)

This two protein system is similar to the previous trajectory, except they begin closer together with a larger waterbox (~87Åx104Åx100Å). Due to random interactions, despite being a lower concentration this system aggregates into a dimer.

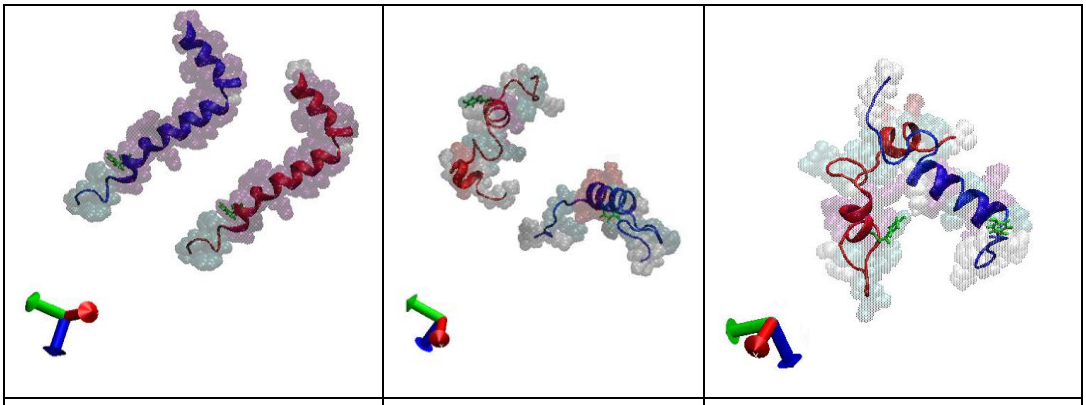

Figure 62 – Dimer system with a big waterbox. The panels shows the starting position of proteins A (blue) and B (red) with Tyr side-chains highlighted (green) at T=0ns with the VDW interactions indicated by the transparent spheres: Purple denotes alpha helix structure, red denotes pi-helix, white denotes a coil and cyan denotes a beta turn. The first panel shows the starting postion of the proteins. The middle panel shows the trajectory at 20ns and the right panel shows the system at the end fo the trajectory at a time of 50ns.

The trajectory begins with the two proteins moving away from each other and start to uncoil and by the first 20ns they contain significantly less helical structures in both, consisting of predominantly coils and beta turns. They then start interacting and aggregate and by the end. After the 20ns they begin to get closer and form a dimer by interacting at the tails. They then continue to stabilise as a dimer throughout the rest of the trajectory and by the end are configured with large portions of the protein being ordered as a beta turn. They appear to misfold in a different way from what has been seen previously but resemble the literature and also aggregate [172].

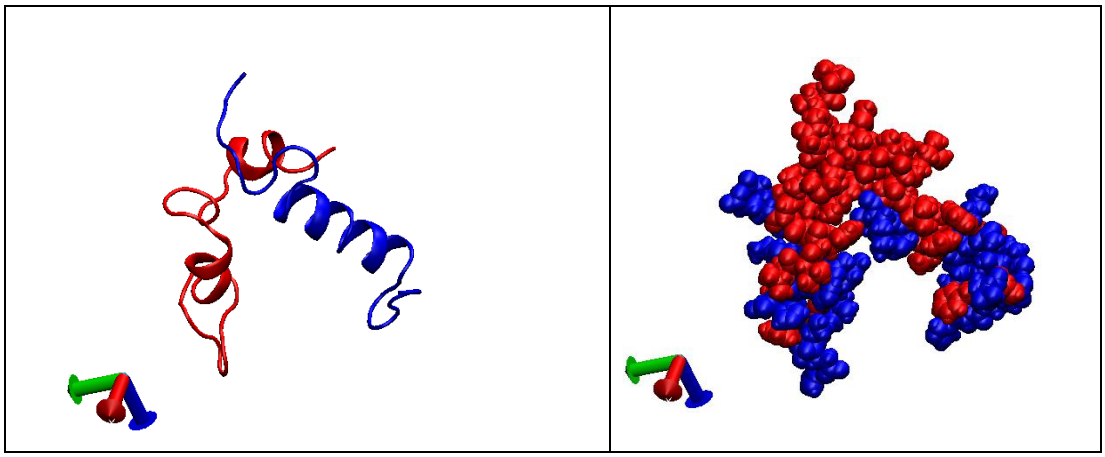

Figure 63 - Hydrophobic Sections of an $A\beta_{1-40}$ Dimer. Both pictures are taken at 50ns with the left panel showing the shape of the proteins (A and B; blue and red respective) and the right panel showing the VDW spheres with the hydrophobic sections (red) against the hydrophilic sections (blue) on the right.

As can be seen in Figure 63, the tails begin interacting due to their hydrophobic nature, aggregating together to help bury as much of these sections as possible. The hydrophobic tales of both proteins are interacting very closely [122], the residues from protein A that are in direct contact with B are: GLY_{25}- $GLY_{37.}$ Those from protein B that are in contact with A are: PHE_{20}-GLY_{29}, ILE_{31}-GLY_{33}, GLY_{37}-VAL_{40}.

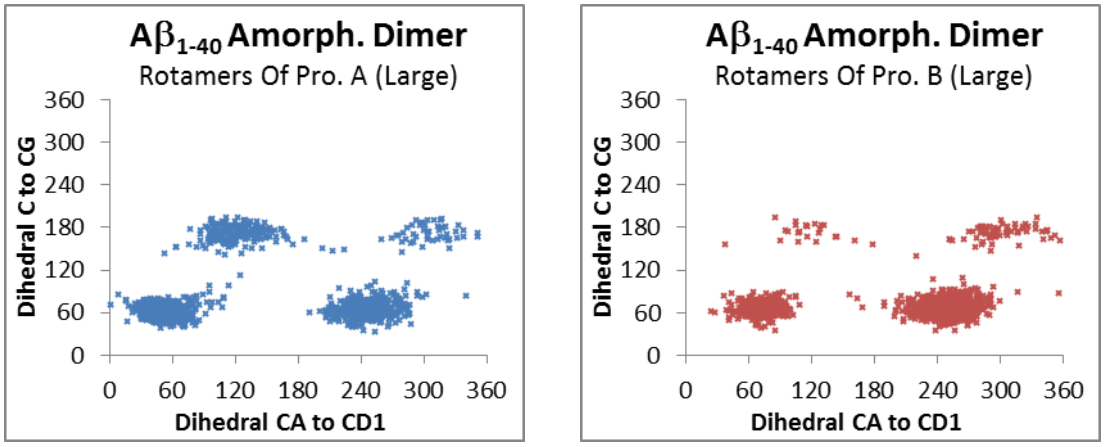

Figure 64 – Tyr Rotamer states of an Aβ1-40 Dimer. The graph depicts the orientations that the Tyr side-chain of monomers A and B favour during the 50ns trajectory. The centre of each state for Tyr A is approximately (55,60), (245,60), (120,170), (310,170). For Tyr B there are (65,60), (245,65), (110,170), (305,165).

Figure 64 shows that the Tyr side-chains have a preference for the four classic rotamer states with a preference to states 1 and 2, which is due to their position

within the aggregate, being fairly free to move with minimal external influences affecting them (Figure 62.) Due to their proximity to the backbone and freedom to move these are the expected results for Tyr side-chains which are part of an amorphous aggregate (see Figure 149 to Figure 151 below.)

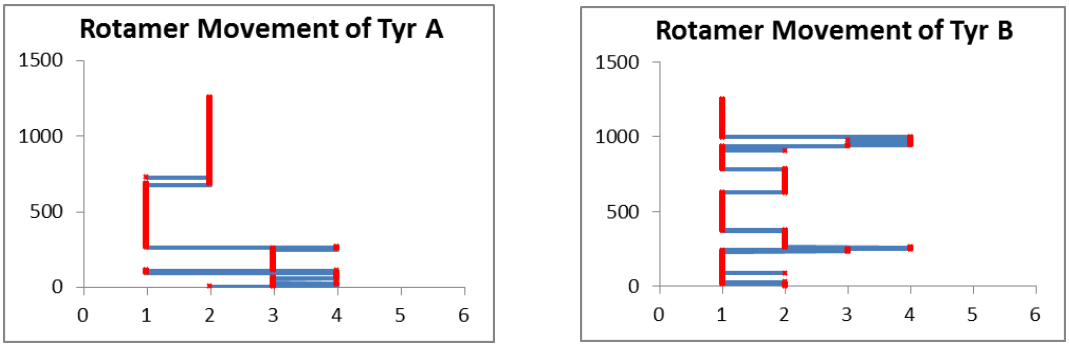

Figure 65 - Tyr movement Between States of an Aβ1-40 Dimer. This graph shows the Tyr side-chain movements between the different states over the course of the trajectory with the x axis showing the different states and the y axis showing the frame within the trajectory.

The rotamer movements for the Tyr side-chains also adhere to the expected outcomes (Figure 65). Tyr A shows a preference to states 3 and 4 to begin with, which will be due to its own interactions as it is not part of an aggregate yet. After aggregating, Tyr A has no interaction with the aggregate backbone allowing the Tyr to move freely, which explains why Tyr A prefers to occupy states 1 and 2; however, it appears to be held in place by its own backbone, which is reflected in the long term occupations of the states.

On the other hand, Tyr B shows a preference towards states 1 and 2 throughout the trajectory, with a short lived occupation of states 3 and 4 post aggregation. This is due to the degree of freedom for this Tyr side-chain as it is close enough to the aggregate backbone that it would influence it to prefer states 3 and 4 temporarily (as it interacts closely only briefly). These unique movements for both Tyr side-chains still adhere to the movement patterns discussed previously.

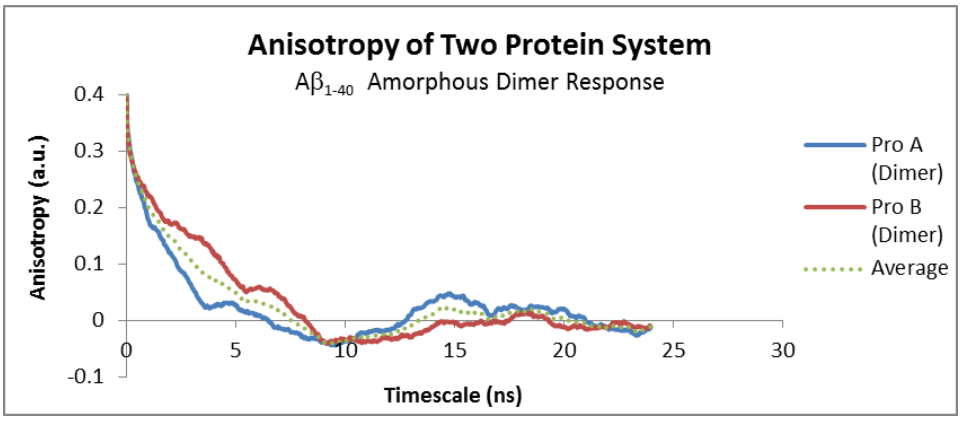

Figure 66 - Simulated Anisotropy of an $A\beta_{1-40}$ Dimer. This graph shows the simulated anisotropy of Monomer A (blue), Monomer B (red) and the average of the two (dotted green line).

The anisotropy of this dimer is similar to that of a monomer (Figure 66) with a slightly shallower initial decay. Protein B (which as shown in Figure 62 does not move as erratically initially) has a longer relaxation time than a monomer, as expected from a dimer. Protein A has a monomer-like response.

The reason these results are similar to that of a monomer is due to the large waterbox and the fact that for the first 20ns of the trajectory they are monomers. The erratic decays and the increasing anisotropies are likely a combination of the three separate states the proteins are in as pre-aggregation, aggregation and post-aggregation are included in the analysis window. Nevertheless, the average decay is slightly slower than a monomer response.

5.4.1. Best fits

The variable fits in Table 10 for this graph show contributions of 0.12 and 0.29 for the fast and slow mechanisms respectively, which means a single exponential fit is not required for this system. The r_∞ values are negative which is not ideal, but forcing the fit to 0 has no effect on the values (See Appendix 4.4b for fits not included in the graph). The τ_r values for the system are 0.13ns for the Tyr movements and 2.6ns for the bulk aggregate rotation, which are responsible for the initial decay and the long relaxation time respectively, as stated in the results for the MC simulations. The results are reasonable as the Tyr side-chains can move freely and the dimer rotates more slowly than a monomer due to the increase in aggregate size.

5.5. Two Protein System (Dimer with Small Waterbox)

Another Dimer simulation was created with a smaller waterbox, to see how the high concentration affects the aggregation process. The waterbox is smaller than the previous simulation and forces aggregation to occur immediately as it has dimensions ~82Åx74Åx80Å.

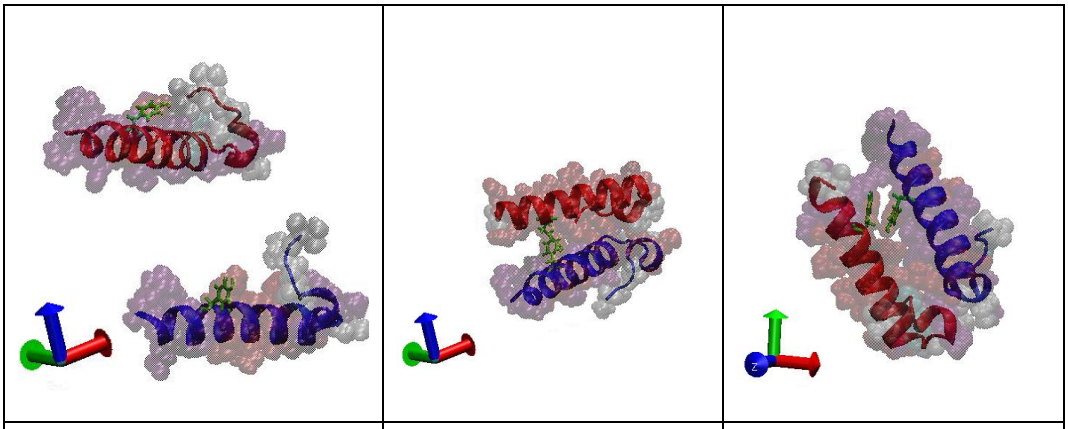

T=0ns	T=40ns	T=100ns

Figure 67 – Dimer system with a small. The panels shows the position of proteins A (blue) and B (red) with Tyr side-chains highlighted (green)with the VDW interactions indicated by the transparent spheres: Purple denotes alpha helix structure, red denotes pi-helix, white denotes a coil and cyan denotes a beta turn. The first panel shows the starting postion of the proteins. The middle panel shows the trajectory at 40ns and the right panel shows the system at the end fo the trajectory at a time of 100ns.

As the trajectory begins, the two proteins remain far apart, but at 12ns they start interacting at their tails as seen previously (see Appendix 4.5a for hydrophobic positons [122]. They then begin aggregating more closely together, eventually agrgegating side-by-side in a mirrored fasion, allowing the Tyr resides to face each other (see Figure 67, Time = 40ns). This configuration does not move signficantly throughout the rest of the trajectory, except some movements from the bulk aggregate and the Tyr side-chains. The proteins also remain predominantly helical throughout the entire 100ns trajectory shown by the purple and red in the figure, unlike what has been seen in 5.4 and in literature [172]. It should be noted that the Tyr side-chains have very little freedom to move. They also both appear to have a slight hairpin motif forming at their tales, which could be the proteins beginning to disorder like the literature [172].

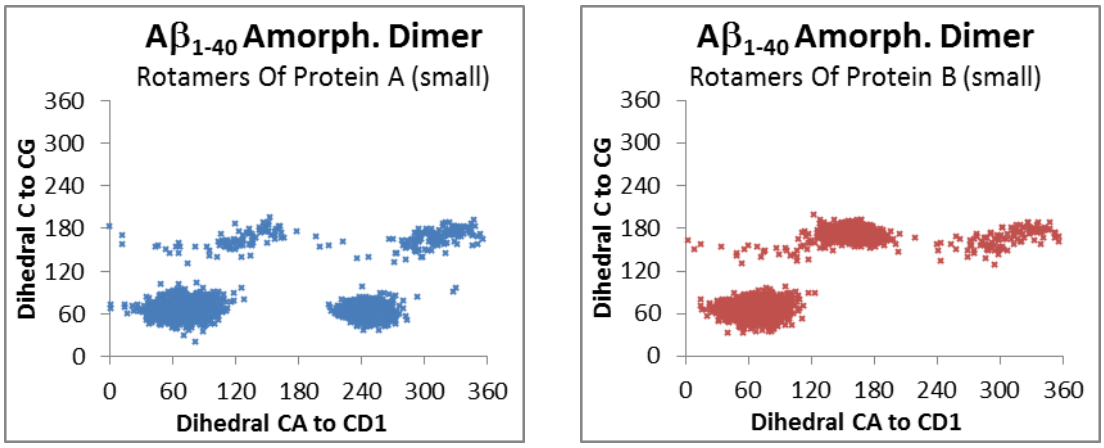

Figure 68 – Tyr Rotamer states of an Aβ1-40 Dimer with a small waterbox. The graph depicts the orientations that the Tyr side-chain of monomers A and B favour during the 100ns trajectory. The centre of each state for Tyr A is approximately (65,60), (245,60), (120,170), (310,170). For Tyr B there are (65,60), (170,180), (305,165).

As expected for an amorphous dimer, the resulting rotamer state distributions (in Figure 68) show the four lower states with Tyr A showing a preference towards states 1 and 2, and Tyr B having a preference for states 3 and 4. As they are aggregated and the Tyr side-chains are very close to each other and to the backbones, they are expected to have a preference towards states 3 and 4.

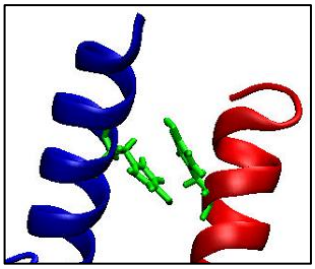

Figure 69 - Interactions between Tyr side-chains for a Dimer

Tyr A does not have this preference as the alignment of the aggregate in Figure 67 shows that Tyr A is below Tyr B. This means that Tyr A is likely influencing Tyr B by forcing it into states 3 and 4, but Tyr A in contrast is forced to remain in states 1 and 2 (see Figure 69.).

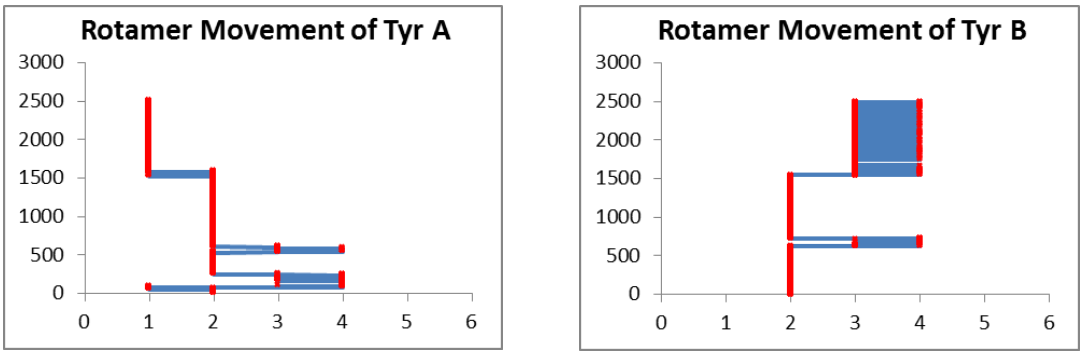

Figure 70 - Tyr movement between states of an Aβ1-40 dimer with a small waterbox. This graph shows the Tyr side-chain movements between the different states over the course of the trajectory with the x axis showing the different states and the y axis showing the frame within the trajectory.

As discussed above, due to the orientation of the Tyr side-chains within the aggregate it is clear when aggregation has occurred, Tyr A is being forced into states 1 and 2 and Tyr B is forced into states 3 and 4 (see Figure 70). Despite these strange interactions, the resulting movements between the states still adhere to the rules discussed previously, and the rotamer state distributions are sensible for a dimer with this configuration.

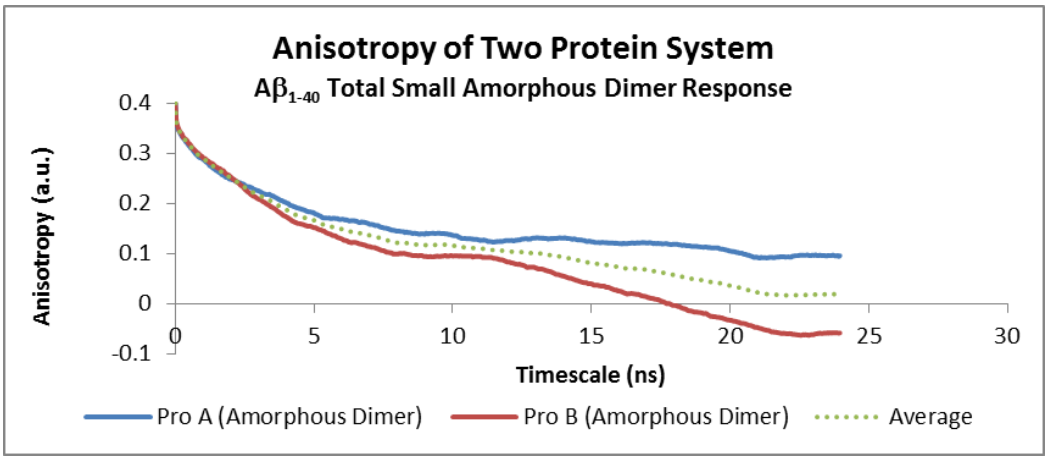

Figure 71 - Simulated Anisotropy of an $A\beta_{1-40}$ Dimer in a small waterbox. This graph shows the simulated anisotropy of Monomer A (blue), Monomer B (red) and the average of the two (dotted green line).

As this dimer has such a small waterbox, the expected rotational time for this aggregate would be quite large as it could interact with itself through the periodic boundaries. Figure 71 displays short lived initial decays, which are due to the Tyrs movements (with Tyr A moving less than Tyr B as seen in Figure 70) and a long relaxation period from the bulk aggregate rotation. This is logical as the aggregate

itself does not move, and the Tyr side-chains have limited movement too. Protein A decays to a plateau value of approximately 0.1 and protein B initially follows a similar decay but has a second rapid decay at a correlation time of 11ns that allows it to decay too (and past) 0. This is a reasonable result for a dimer with restricted movement, comparable to the $A\beta_{1-42}$ dimer seen below in Table 11. The reason for protein B having a faster decay towards 0 is because it moves significantly during the course of the simulation, whereas protein A remains stationary throughout. The results also adhere to what is expected, as established by the MC simulations.

As stabilisation occurs during the trajectory a second simulation was created to see the effects of the process on the anisotropy. The new system is created by taking the last frame of the trajectory and another simulation with a similarly sized waterbox. This system moved around freely as a dimer and the effects are seen below in Figure 72.

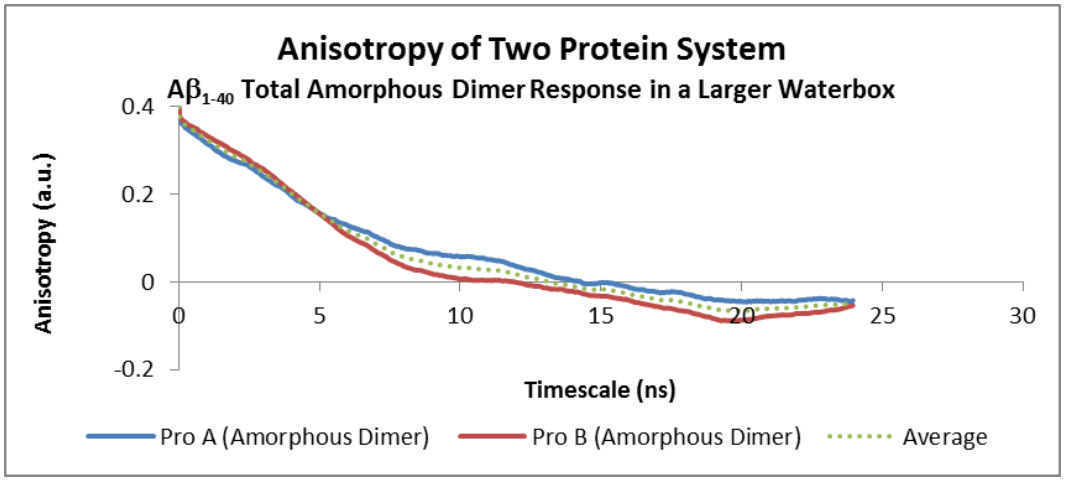

Figure 72 - Simulated Anisotropy of an $A\beta_{1-40}$ Dimer in a large waterbox. This graph shows the simulated anisotropy of Monomer A (blue), Monomer B (red) and the average of the two (dotted green line).

As is expected, due to the lack of movement from the Tyr side-chains which are trapped, the initial decay is almost non-existent. This differs from the first trajectory for this system slightly, as the Tyrs had room to manoeuvre initially. This strengthens the finding in Figure 46. There is then a fairly rapid relaxation period as expected as the dimer is fairly small and will have more movement than the two separated monomers (prior to aggregation) in the first trajectory. As such, both proteins have almost identical responses as the proteins mirror each other in this

trajectory, unlike the previous trajectory where protein A barely moved. It should also be noted that the new rotamer states below in Figure 73 continue to have the same limitations as seen near the end of the original simulation. There is also significantly less movement between the states as expected from this system as it is unable to move. Furthermore, it is clear that when in states 3 and 4 the jumps are more erratic, a characteristic seen throughout most of the amorphous aggregate simulations.

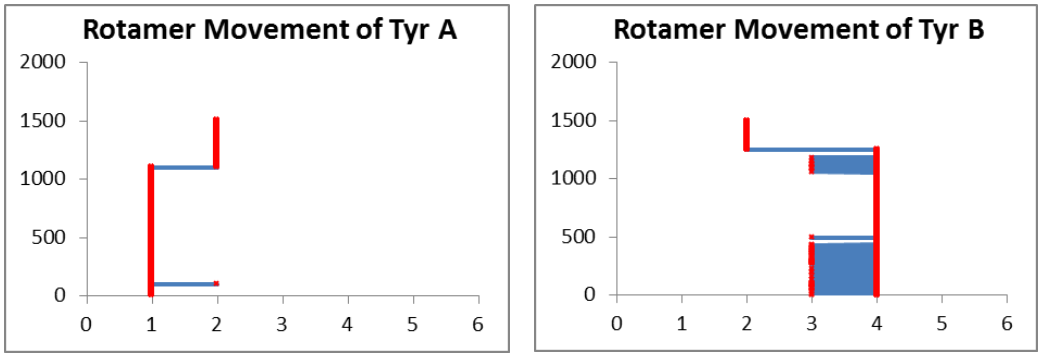

Figure 73 - Tyr movement between states of an Aβ1-40 dimer with a small waterbox. This graph shows movements for the second simulation involving these two proteins in a larger waterbox.

5.5.1. Best Fits

The variable fits in Table 10 for the original system show contributions of 0.13 and 0.26 for the fast and slow mechanisms respectively. They show τ_r values of 0.91ns for the Tyr side-chains and 9.64ns for the bulk aggregate. These results are reasonable results as there will be some movement from the Tyr side-chains despite their positions in the aggregate, due to the pre aggregation period. Furthermore, the bulk aggregate will rotate slowly due to the aggregate size, but also rotates slower than the slightly larger $A\beta_{1\text{-}42}$ amorphous dimer, likely because of space restrictions. As such, the second trajectory was created in a larger waterbox, using the final stabilised form of the aggregate to check what effect a larger waterbox has on the system.

The second trajectory has an overwhelming contribution from the bulk rotation (which is 5.42ns.) This rotational time is acceptable for this aggregate and the contribution is sensible as the Tyrs do not move, implying that they play a very small role in the decay curve. This means a single exponential could potentially be used, which gives a resulting 6.58ns rotational time which is still reasonable for this system. The rotational time is slower than that seen for the dimers above, which is

likely due to the fact it spends all its time aggregated, whereas the dimer above has a monomer responses too. We will find that it also has a slower rotation than an $A\beta_{1-42}$ stacked dimer (see Figure 117 below) as it is not as tightly aggregated.

5.6. Three Protein System (Dimer and Monomer)

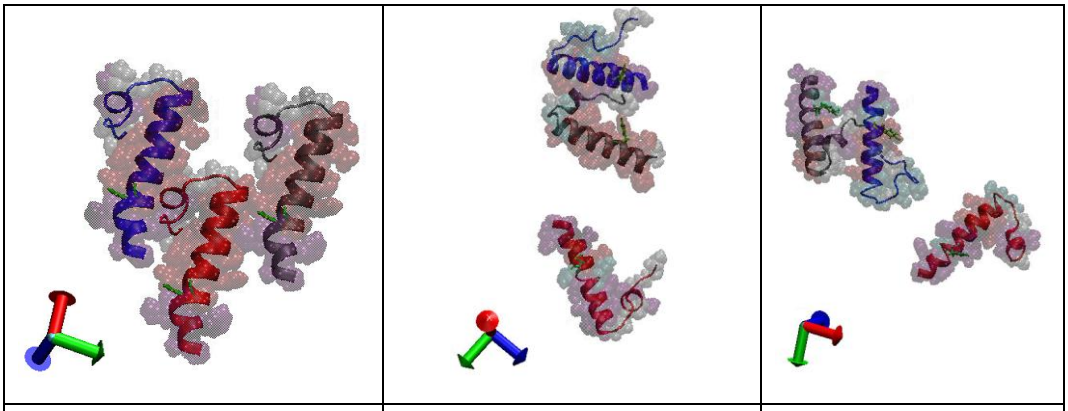

T=0ns	T=20ns	T=50ns

Figure 74 - Dimer & Monomer system with a small waterbox. The panels shows the position of proteins A (blue), B (red) and C (grey) with Tyr side-chains highlighted (green) at T=0ns with the VDW interactions indicated by the transparent spheres: Purple denotes alpha helix structure, red denotes pi-helix, white denotes a coil and cyan denotes a beta turn. The first panel shows the starting postion of the proteins. The middle panel shows the trajectory at 20ns and the right panel shows the system at the end fo the trajectory at a time of 50ns.

The next trajectory shown in Figure 74 involves three monomers interacting with each other in a waterbox of dimensions 85Åx75Åx85Å (similar to the waterbox in chapter 5.5). Proteins A and C start interacting almost instantaneously and fold more than protein B and begin aggregating by 10ns, lining up in a parallel manner. As is seen at 50ns, the aggregate is never fully formed with both Tyr side-chains having significant freedom to move. As the trajectory progresses both the dimer and monomer (protein B) have freedom to move with minimal external interactions affecting their ability to rotate, ensuring a more accurate indication of their rotational times. The proteins also maintain their helix structures throughout the entire trajectory and do not misfold as seen in other trajectories [171] [172] [174], yet two still begin to aggregate.

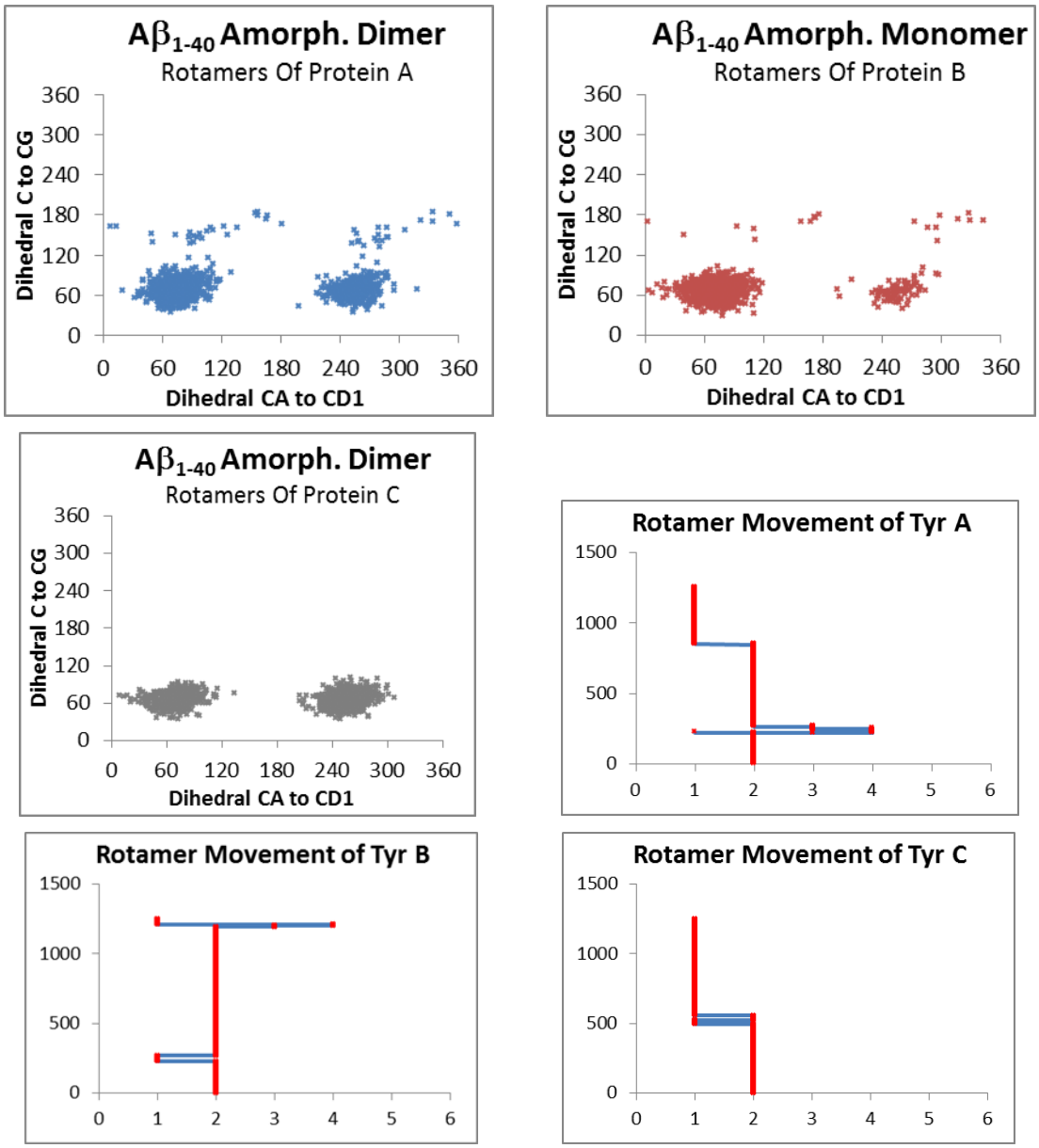

Figure 75 – Tyr Rotamer states of Aβ1-40 Dimer and isolated monomer. The graph depicts the orientations that the Tyr side-chain of monomers A, B and C favour during the 50ns trajectory. The centre of each state for Tyr A is approximately (70,65) and (250,65). For Tyr B they are (65,60) and (250,60). Both have minor occupation of states 3 and 4. For Tyr C the centres are (65,60) and (250,60). The movements between these states are also shown here.

The Tyr side-chains in this trajectory occupy states 1 and 2 similar to the monomers. This is because Tyrs A and B have minal interactions from their own backbones that seem to only be subtly influencing their occupation away from states 3 and 4. Tyr C on the other hand has minimal movement due to being forced to hold states 1 and 2

for extended periods (see Figure 75.) The resulting movement between rotamer states follow the expected movement patterns, despite differing environments.

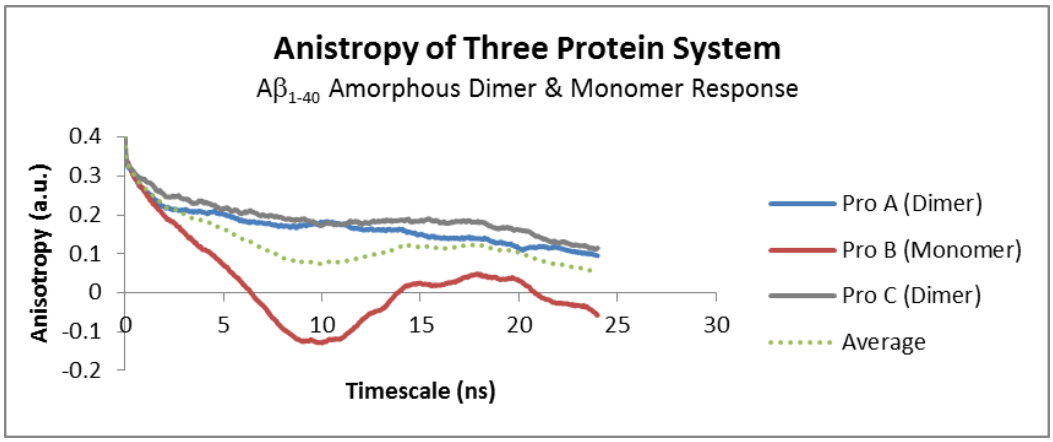

Figure 76 - Simulated Anisotropy of an $A\beta_{1-40}$ Dimer and monomer. This graph shows the simulated anisotropy of Protein A (blue), protein B (red), protein C and the average of the two (dotted green line).

The dimer anisotropy decay response of Proteins A and C are similar to that of the dimer seen above with a short lived initial decay, which is related to the lack of movement from the Tyrs as Figure 75 depicts. Tyr A has a longer and faster initial decay than C as it has more freedom to move. It also has a slow relaxation that ends at a value of 0.1, and would likely to continue to fall to a nonzero plateau value as expected from an aggregate.

Protein B has a faster decay to 0 at a correlation time of 6ns; the decay is comparable to a monomer with an unmoving Tyr, as the r_∞ value can be considered 0.

5.6.1. Best Fits

These results reflect characteristics discussed in the MC simulations. However, due to the complication created by the monomer response, it is hard to determine the best fit for the average decay of the system, as such, when analysing this curve the program only fits to the first half of the trajectory in order to ignore the increasing anisotropy (which cannot be fit accurately.) This gives a reasonable overall fit with a correlation of 0.93 and τ_r values of 1.3ns for the Tyr side-chains and 7.4ns for the bulk aggregate with equal contribution from both mechanisms, which are reasonable results and are comparable to the $A\beta_{1-42}$ amorphous dimer seen below Table 11.

5.7. Three Protein System (Trimer with ions)

The next trajectory is a three protein system ion a very small waterbox (dimension ~52Åx53Åx67Å) with ions (0.250mMol/L [162]) to attempt to force an amorphous trimer to form. As with previous examples, the amount of ions does not change, it is just the repeating boundary conditions.

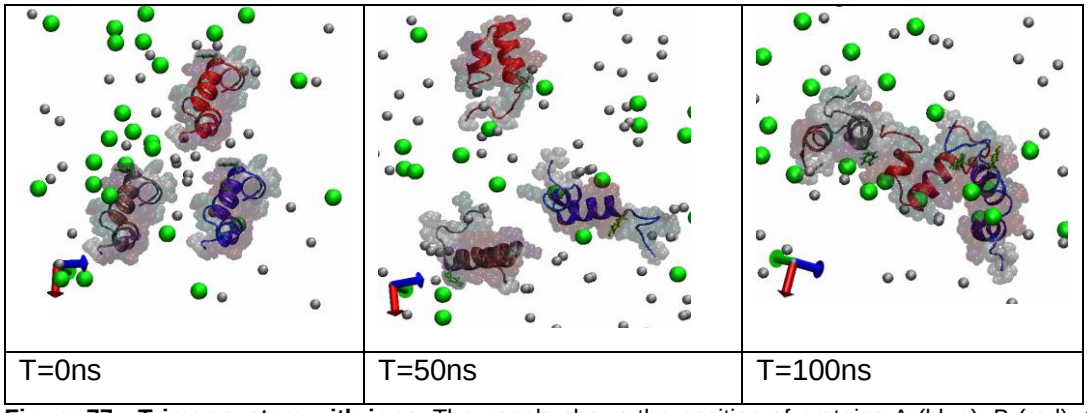

Figure 77 - Trimer system with ions. The panels shows the position of proteins A (blue), B (red), C (grey), ions are shown as green and grey spheres. and Tyr side-chains highlighted (green) with the VDW interactions indicated by the transparent spheres: Purple denotes alpha helix structure, red denotes pi-helix, white denotes a coil and cyan denotes a beta turn. The first panel shows the starting postion of the proteins. The middle panel shows the trajectory at 50ns and the right panel shows the system at the end fo the trajectory at a time of 100ns.

As soon as the trajectory begins all three proteins begin to misfold into the horseshoe shape discussed previously, with what appears to be the presence of 2 loops and three anti-paralell beta-sheet sections, which is similar to that seen in the literature [172]. They do not immediately aggregate despite the small waterbox.They evnetually aggregate together at around 64ns. The proteins all have the same characteristic of two alpha helix seen between residue 28 and 36 and between 11 and 22 intially, but their conformations constantly change throughout the trajectory, with the length of the alpha helix becoming smaller and their being more instances of coils and turns [171] [174]. Once they have aggregated, there are small portions of the system which are still helical, however it has mostly unraveled, as seen in literature [172].

All three Tyr side-chains have a fair degree of freedom with some minor interactions with their own backbones (specifically for Tyrs A and B.) This could potentially suggest that this shape is the beginning of the misfolding process.

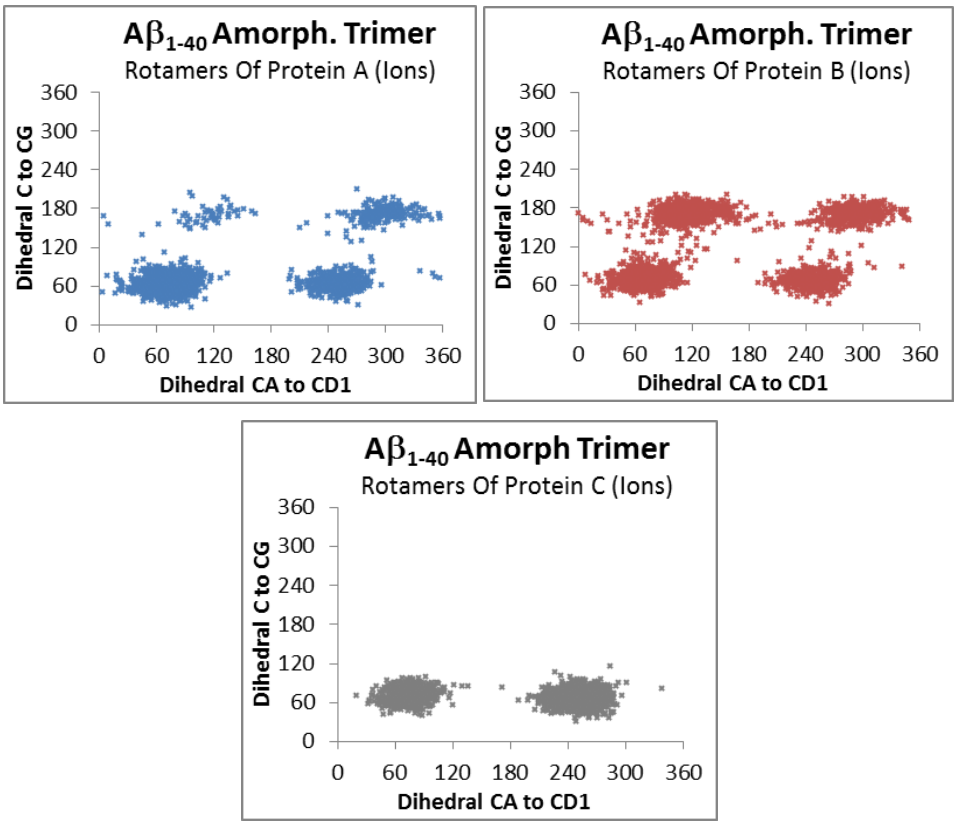

Figure 78 – Tyr Rotamer States of an Aβ1-40 Trimer with Ions. The graph depicts the orientations that the Tyr side-chain of monomers A, B and C favour during the 50ns trajectory. The centre of each state for Tyr A is approximately (70,60), (245,60), (110,175) and (290,175). For Tyr B they are (65,60), (250,60), (110,175) and (290,175). For Tyr C the centres are (75,65) and (245,60).

Figure 78 shows the rotamer states of this amorphous trimer, with Tyr A showing all four rotamer states and a preference towards states 1 and 2. Tyr B shows equal preference to both the least twisted states (1 and 2) and the slightly more twisted states (3 and 4.) Tyr C only shows occupation of states 1 and 2 due to its postion within the aggreate possibly holding it in place.

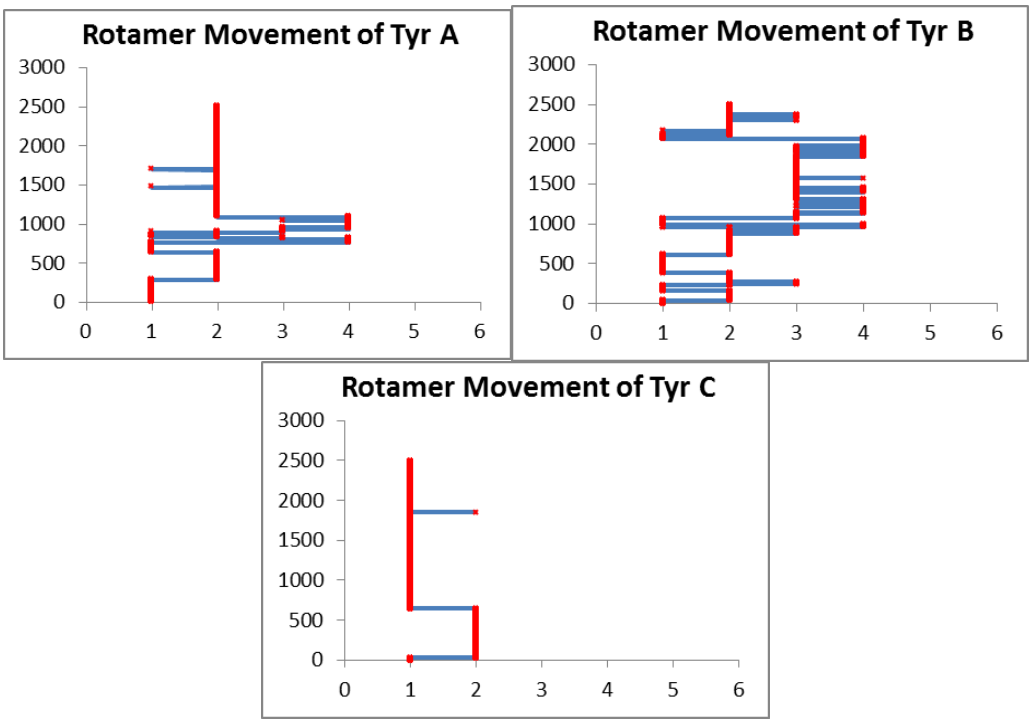

Figure 79 - Tyr movement between states of an Aβ1-40 trimer with ions. This graph shows the Tyr side-chain movements between the different states over the course of the trajectory with the x axis showing the different states and the y axis showing the frame within the trajectory.

Figure 79 shows the Tyr side-chain movements for the trimer system. Tyr A has rotamer state occupations similar to a monomer's due to the freedom and lack of external interactions from the aggregate backbone as it has a preference towards states 1 and 2 but does not get stuck for long periods. Tyr B, on the other hand has signficant interactions from its own backbone in the second half of the trajectory, which influences the Tyr into occupying states 3 and 4 exclusively in the second half of the trajectory. Considering the shape of this aggregate, these results are sensible. Tyr C must have some external influence from its own backbone pushing it into states 1 and 2 as shown by the lack of movement.

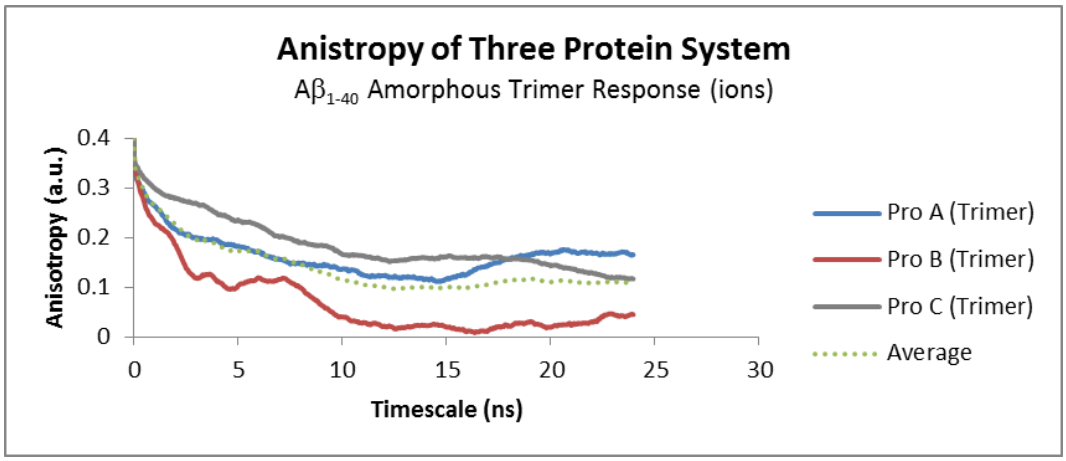

Figure 80 - Simulated Anisotropy of an $A\beta_{1-40}$ Trimer in a small waterbox. This graph shows the simulated anisotropy of protein A (blue), protein B (red), protein C (grey) and the average of the three (dotted green line).

The anisotropy results for this trimer system (Figure 80), share similar characteristics to the dimer/monomer system seen in Figure 76. Tyrs A and C have a slow initial decay due to their Tyr movements, with protein A having a faster initial decay than C as it has more movement as seen in Figure 79 and protein B has a faster initial decay due to the Tyr's erratic movements. Tyrs A and C both have slower decays with higher plateau values of 0.18 and 0.11 respectively when compared to a dimer. Tyr B has a complex decay, with an initial decay to 0.1 at a correlation time of 7ns, followed by a second sharp decay to a plateau value of approximately 0.02.

These results are sensible as the slower relaxation of all the proteins are caused by the slower rotation of a trimer as it is larger than a dimer and the sharp initial decay is due to their freedom to move, with some constraints created from the aggregation and the ions. These results all parallel what was discussed in the MC simulations.

5.7.1. Best Fits

Table 10 has two fits for this system because the first fit has a bulk aggregate τ_r value of 5.4ns which is fast for a trimer (compared to previous dimers seen) and has a strong correlation of 0.971, with comparable contributions from both the slow and fast mechanisms. The second fit has a slightly better correlation of 0.981 with similar contributions with slightly slower τ_r value of 0.51ns for the Tyr side-chains (compared to the 0.42 for the first fit) and a faster bulk aggregate rotation of 4.93.

Both of these seem fast for this system, as the tightly aggregated dimer with the trapped Tyrs has a rotational time of 9.64ns. This is simply due to the fact that the first fit was in a small waterbox, slowing down the rotations and the other two fits are post stabilisation fits, which causes a slower rotation as no monomers were present at any point.

Therefore, this fit has to be compared to the dimer in the large waterbox that also includes stabilisation, which has a rotational time of 2.64. This makes the results more reasonable and the 4.93ns rotation can be considered correct as it has the better correlation.

These results suggest that all the systems would benefit from post stabilisation analysis. However, limitation in computing power made this impossible within the scope of this work.

5.8. Four Protein System (Tetramer)

The final $A\beta_{1-40}$ amorphous aggregate is a four protein system and has a 100ns trajectory (Figure 81). As this system is relatively large and long, a small waterbox is used due to the limitations in the computing power and storage space available. The dimensions are ~83Åx76Åx110Å, which is small considering the number of proteins contained within it. Despite this, useful information can still be extracted from this system.

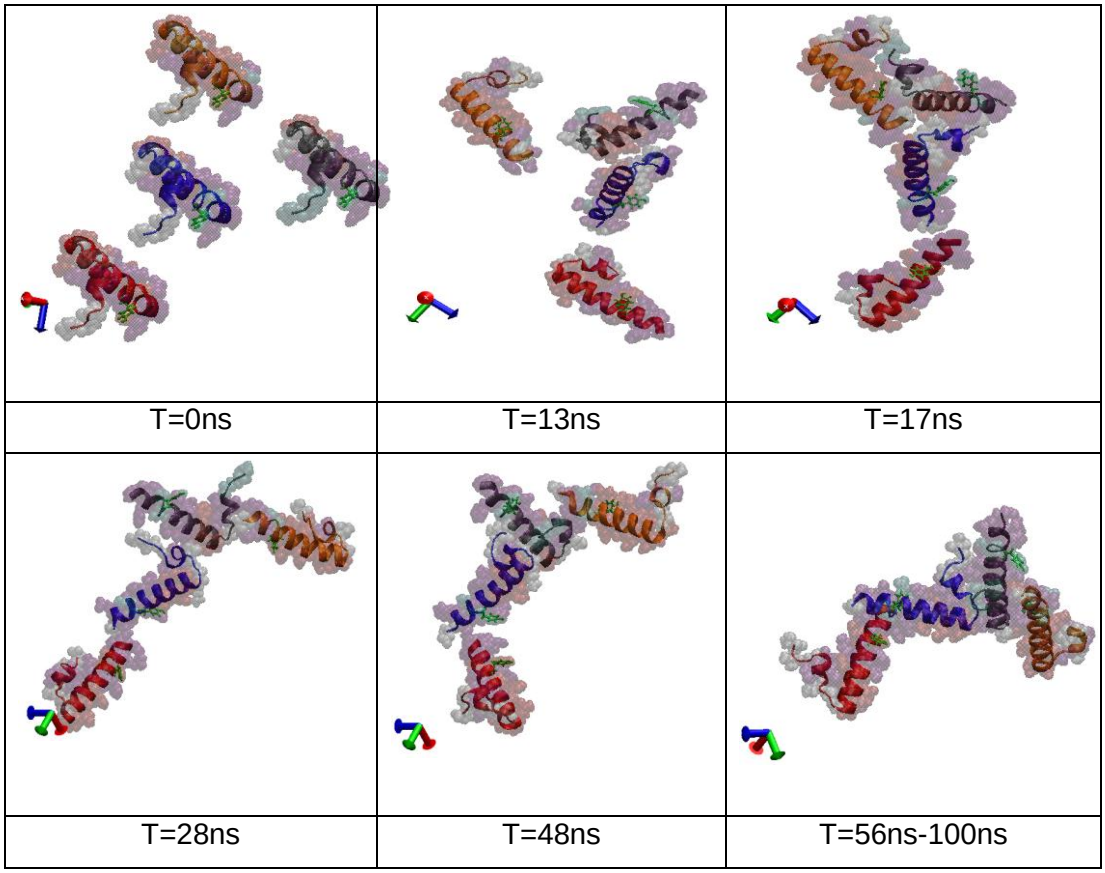

Figure 81 - Tetramer system. The panels shows the position of protiens A (blue), B (red), C (grey) and D (Orange) with Tyr side-chains highlighted (green) with the The VDW interactions indicated by the transparent spheres: Purple denotes alpha helix structure, red denotes pi-helix, white denotes a coil and cyan denotes a beta turn. The panels shows the progression of the proteins during the trajectory from 0ns to 100ns.

The proteins begin approximately 1nm apart and diffuse freely, slowly coming closer together and interacting with one another and within 20ns an amorphous tetramer starts to form but quickly breaks apart. The presence of the beta-sheet U-shape motif is minimal [172], and appears to show minimal interactions between the proteins. Interestingly, the two monomers that form a dimer at 48ns are not the pair

that formed the initial dimer at 13ns (A blue and C grey). This early dimer formed a trimer with monomer D (orange) at 17ns, and yet the aggregate still dissociated implying that there is a preferred mode of interaction to form stable aggregates. The preference seems to be for alignment of neighbouring alpha-helix structures (despite the more disordered structure seen in literature [172]), although further analysis is required in future work. After several attempts to aggregate into a stable tetramer, it eventually forms one at 56ns. This aggregate then continues to compact into the tighter oligomer observed at 100ns.

When the aggregate has fully formed, the Tyr side-chain of protein A has its movements somewhat constrained by protein B's backbone. Protein B's Tyr is also facing protein A's backbone but with minimal interactions. However, protein B is aggregated at only one end of its alpha-helix, allowing some freedom for the backbone to move and pivot. Protein C holds protein A in position, and also interacts with protein D. Protein C's Tyr side-chain has a lot of freedom throughout the simulation; it repeatedly opens out to the surrounding water before retracting to the protein surface. Protein C's backbone is restricted by its interactions with two other proteins from either side. Protein D is similar to C but its Tyr side-chain does not possess the same freedom of movement.

It appears that this system is so concentrated that the proteins do not have time to unravel, maintaining a long helical section throughout [46], seen between residues 1 and 27 and another small section between residues 32 and 35. This is different from what is seen previously, as the coil tends to unravel before aggregation [172]; however this shows it is possible for the aggregation to occur first.

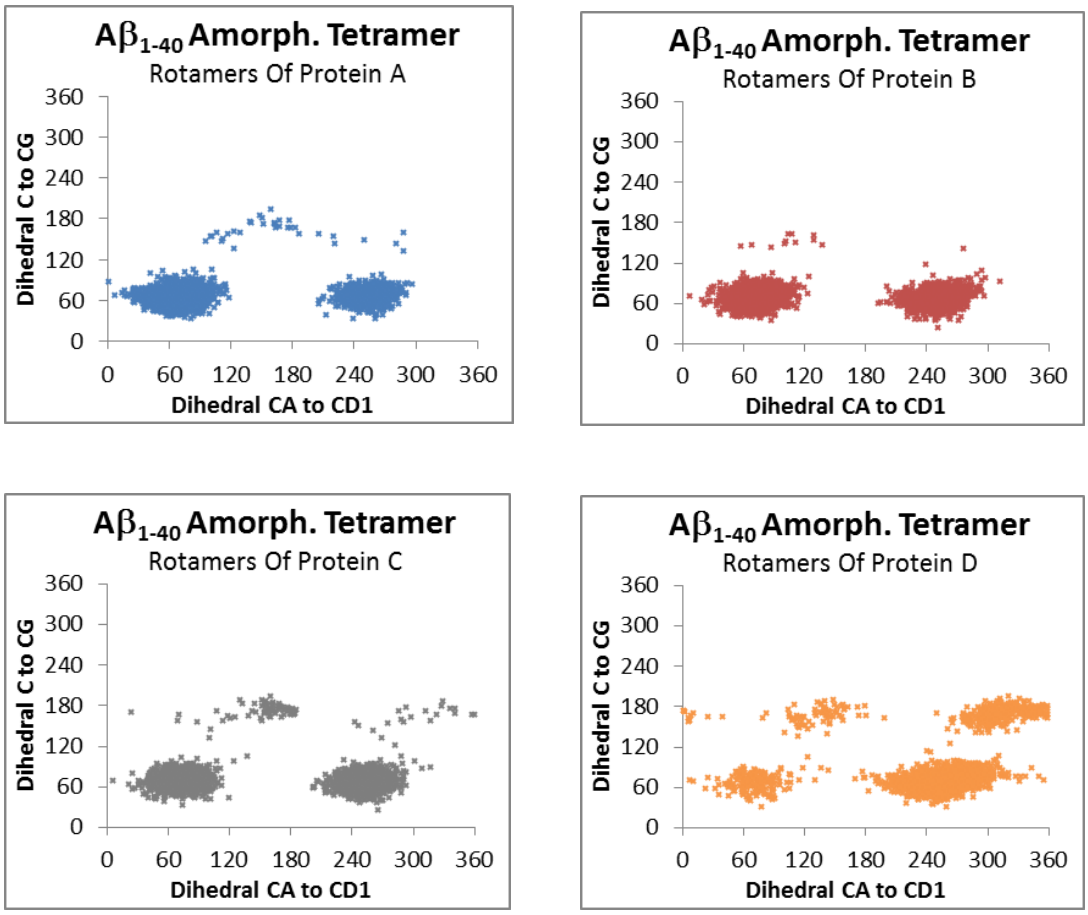

Figure 82 – Tyr Rotamer States of an Aβ1-40 Tetramer. The graph depicts the orientations that the Tyr side-chain of monomers A, B, C and D favour during the 100ns trajectory. The centre of each state for Tyr A is approximately (70,65), (250,65), (140,180) and some minor occupation of state 4. For Tyr B they are (70,65), (250,60), and some brief occupation of state 3. For Tyr C the centres are (75,65), (250,60), (140,175) and some minor occupation of state 4 . Tyr D shows occupation centres at (70,65), (250,65), (130,170) and (315,170)

As described above, proteins A's Tyr side-chain has fair restriction on it throughout the trajectory and as such prefers to occupy states 1 and 2 with some movement into states 3 and 4 due to the minor interactions with the other protein backbone (see Figure 82 and Figure 83). Tyr B has interactions affecting its movements as this is reflected in its preference towards states 1 and 2 with lack of movements into states 3 and 4.

Tyr C is has a fair amount of freedom throughout the trajectory but constantly comes into contact with the other protein backbones. In contrast, Tyr D has a more dense occupation of states 3 and 4 relative to the other three proteins, which is due othe external influences pushing it into the states (see Figure 150.)

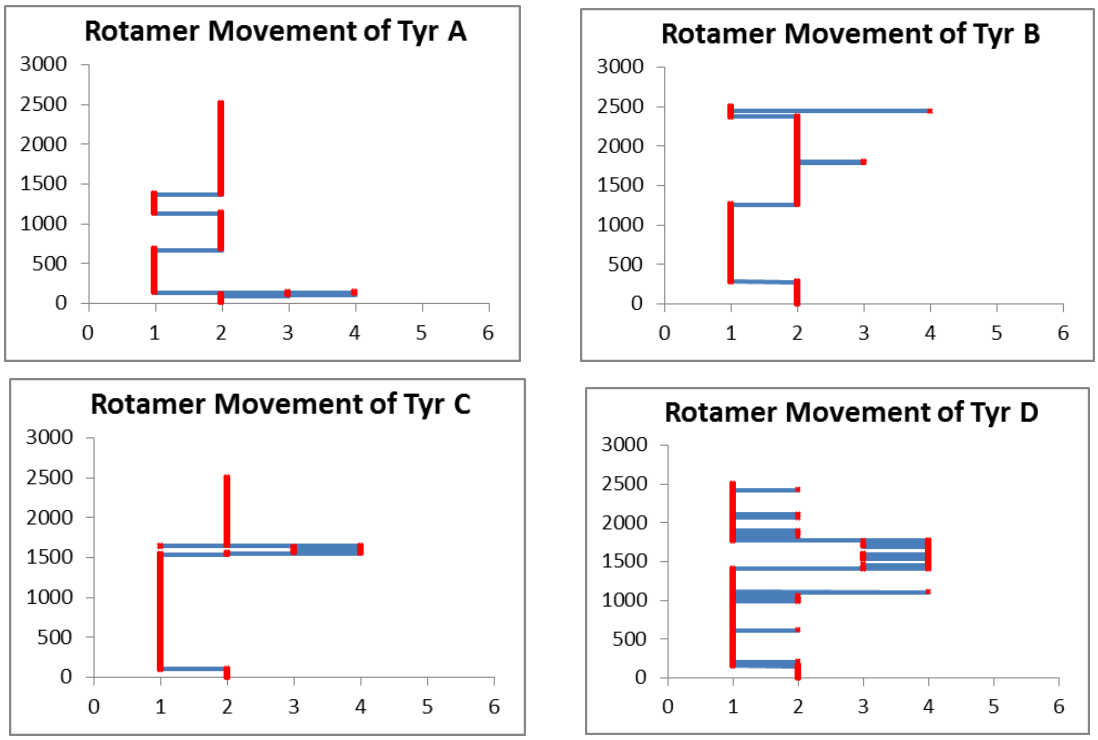

Figure 83 - Tyr movement between states of an Aβ1-40 tetramer. This graph shows the Tyr side-chain movements between the different states over the course of the trajectory with the x axis showing the different states and the y axis showing the frame within the trajectory.

As expected, Tyr's A, B and C all have movements between states 1 and 2 with some minor movements into states 3 and 4 but have limited transitions between states due to their restricted movements. These movements into states 3 and 4 are due to their interactions with both their own backbones, and the aggregate backbone. The aggregate backbone clearly affects Tyrs B and C as they have late movements into states 3 and 4 after aggregation. Similarly, Tyr D spends significant time in states 3 and 4 post aggregation but is free throughout the trajectory and is reflected in its erratic movements. This confirms that these movements between states are related to the Tyr surroundings (see Figure 150).

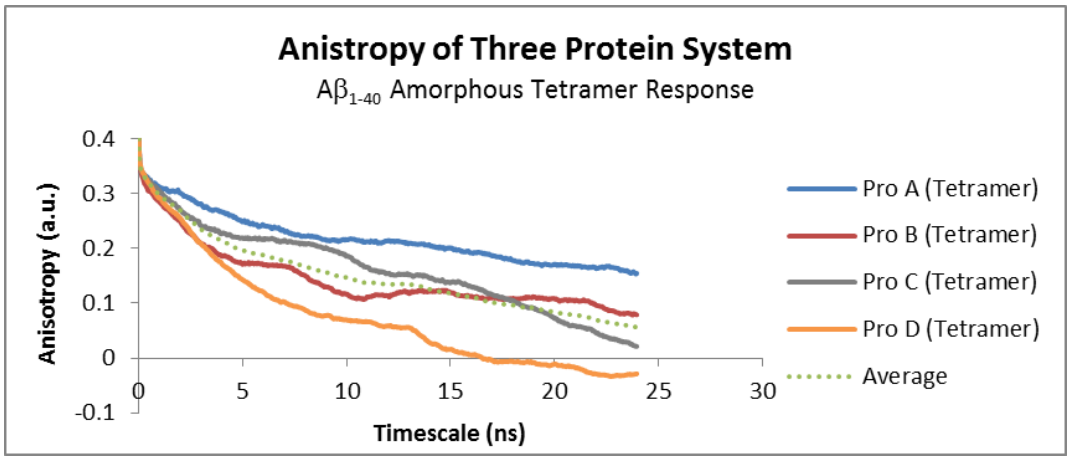

Figure 84 - Simulated Anisotropy of an $A\beta_{1-40}$ Tetramer. This graph shows the simulated anisotropy of protein A (blue), protein B (red), protein C (grey), protein D(orange) and the average of the two (dotted green line).

The anisotropy results for this tetramer system show clear signs of aggregation as the proteins have a short lived initial rapid decay followed by a slow relaxation to 0 at a correlation time of approximately 6ns. Protein D has the most freedom to move as it is on the end of the amorphous aggregate. This is reflected in the relaxation period being more rapid than the two proteins (A and C) in the middle of the aggregate, as they will have even less movement. The sharp initial decay of Protein D is related to the Tyrs ability to move more freely throughout the trajectory. Protein B shows a shorter lived initial decay due to the lack of movement from the Tyr, but does have a faster relaxation time, due to being on the other end of the aggregate.

As such, the overall (average) decay shows clear signs of aggregation and has a nonzero decay time that takes longer to plateau than previous aggregates. This is a characteristic of a larger aggregate. The initial decay is also indicative of restricted Tyr residues.

5.8.1. Best Fits

These results are confirmed by the fit parameters used for the variables in the best fit graph for the average tetramer decay. The τ_r values for the two mechanisms are 0.21ns and 10.11ns for the Tyr side-chains and the bulk aggregate rotation respectively, which is a logical growth in the size based on the previous results for the smaller aggregates (Table 10) when you consider that this aggregate is aggregated tip to tail, creating a very long thin aggregate. This odd aggregate shape

is not as tightly packed, possibly due to no misfolding being present, and has limited movement available to it. Despite these complications the results are still logical.

5.9. Aβ1-40 Amorphous Aggregates Comparative results

Simulation	$r_{\infty T} + r_{\infty B}$	r_{0T}-$r_{\infty T}$	T_T	r_{0B}-$r_{\infty B}$	T_B	Correl.
Monomer	0.00	0.37	1.36	0.03	20.61	0.919
1exp	0.02	0.38	1.43	-	-	0.931
Monomer (Ions)	0.03	0.33	1.60	0.04	37.31	0.894
1exp	0.05	0.35	1.82	-	-	0.882
2 Monomers	0.00	0.37	1.45	0.03	25.22	0.932
1exp	0.02	0.38	1.54	-	-	0.936
Dimer (Large WB.)	0.00	0.11	0.13	0.29	2.64	0.966
Dimer (Small WB.)	0.02	0.13	0.91	0.26	9.64	0.987
Stabilised fit:	-0.06	-0.09	1.98	0.54	5.42	0.996
Stabilised fit 1exp:	-0.07	-	-	0.47	6.58	0.996
Dimer + Monomer	0.08	0.19	1.28	0.13	7.44	0.930
Trimer (Ions)	0.09	0.13	0.42	0.18	6.29	0.977
Trimer (Ions)	0.10	0.12	0.51	0.19	4.93	0.981
Tetramer	0.05	0.09	0.21	0.26	10.11	0.993

Table 10 - $A\beta_{1\text{-}40}$ Amorphous Aggregates Anisotropy Best Fits Variables

Table 10 shows the resulting variables for the best fits of the average decays from each of the systems analysed above based on fluorescence equations [112]. The correlations are a show of how well the fits match the data [168]. The data above are the variables attained from the stochastic optimiser from Eqn. 2.3.3

In general, there is an increasing r_∞ value as the aggregates get larger, except for the tetramer, which has a lower value likely due to the amount of movement during the aggregation process and the fact that the proteins are not as tightly aggregated as some of the other systems seen below. This is sensible based on the theory, as the bigger the aggregate, the less freedom it will have to move and so will have a larger r_∞ value [112].

The ratio of the contributions from the two mechanisms become more even after aggregation occurs, this is potentially due to the monomers rotating so quickly that the Tyr side-chain movements are not being pick up. By analysing the general trend of increasing rotational times it can be concluded that the single exponentials for the monomers and dimer are likely the backbone rotation and not the Tyr itself. If true, once the proteins start aggregating, they slow down and the contribution from the Tyr becomes more apparent, this is also visible in the graphs as the decays and characteristics differ when aggregation has occurred. This could also be due to the complications created from the system aggregating during the analyses window as seen for the one exponential fit for the stabilised dimer.

The τ_T values do show a general trend with respect to the systems rotamer state movements r_∞. The first three systems show limited rotamer movement and as such all show τ_T values ~1.5ns. The fourth simulation, “Dimer (Large WB.)”, showed significantly more rotamer movement and has a 0.13ns rotational time, which is most likely too fast but still adheres to the general trend. The fifth system, “Dimer (Small WB.)”, has a fair bit of movement in but is mostly limited, giving a resulting τ_T value 0.91ns. It also has a second simulation associated with it that has a much slower rotational time, and also has limited rotamer movements due to its position. The sixth system, “Dimer + Monomer”, has limited rotamer movements from all its Tyr residues, and as such has an average τ_T value 1.28ns. The final two simulations show a great deal of movement from their rotamer states and τ_T values 0.42ns and 0.21ns respectively. This further suggests that these fast time scales for the Tyr residues are logical within these simulations [112].

There is a large variation among the aggregates for their rotational times (and therefore their aggregate sizes) due to how quickly they aggregate and the shape of the various aggregates themselves. It does appear that certain monomer shapes that can form more readily aggregate than others, suggesting the misfolding process places a part in the aggregation [172]. This makes it difficult to determine a clear pattern in the increasing sizes of the aggregates. Despite this, there is still a clear indication that as the aggregates grow, their rotational times become slower [112]. One potential pattern, that can be seen in these results, is monomers at a rotational time of 1.5ns, dimers at 2.6ns, trimers at 4.9ns and tetramer at 10ns, as they all include pre and post aggregation.

The most trustworthy result here is the result for the stable Dimer that was analysed solely post-aggregation which has a resulting τ_r value of 6.52. This is much higher than the rest of the dimers as it spends no time as a monomer. This result can be compared to the dimers below that begin the simulation aggregated (Table 13 below), although there is still time required for the structure itself to stabilize.

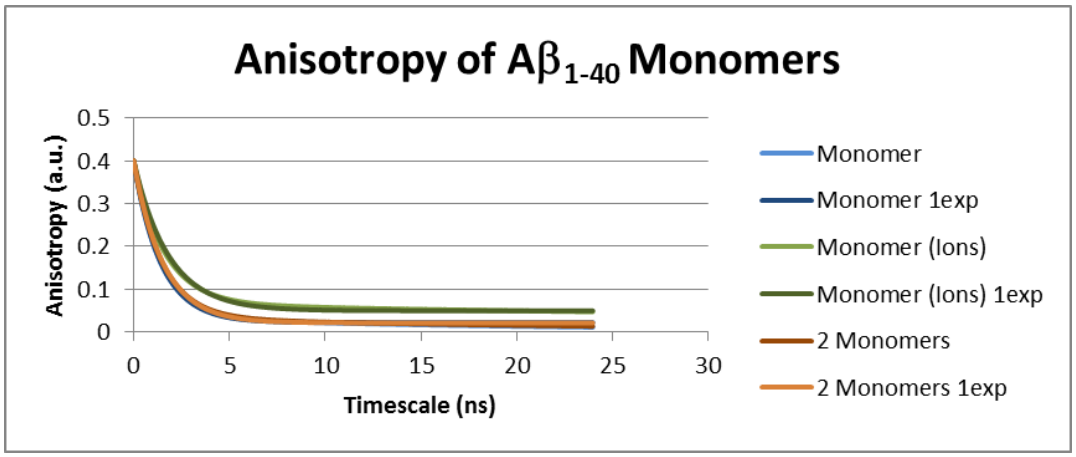

Figure 85 – $A\beta_{1-40}$ Monomer Anisotropy Best Fit Graphs – Colour coordinated, with the three colours (Blue, Green and Orange) depict a fit that was created from the same system.

The best fit graphs shown in Figure 85 show the different monomer responses. There are six monomer systems overall. The systems without ions all show near identical responses, with a sharp initial decay to 0. This is what is expected for a monomer based on fluorescence anisotropy theory as the monomers are very small and their Tyr side-chains will have minimal external influences [112]. The presence of multiple monomers in a system with adequate room to move shows no apparent changes to the results.

The system with ions, in contrast, shows a slightly higher plateau value, but still has a very sharp initial decay and can still be considered a monomer. The reason for this higher plateau value is due to the ions affecting the movements of both the Tyr side-chains and the bulk aggregate, which is reflected in the table for their τ_r values. These monomer results adhere to the findings in the MC simulations, the Tyr side-chain movements between rotamer states is seen to be free moving, which is comparable to the lack of restriction on the put on the MC variable. Furthermore, the secondary mechanism, explained in the MC simulation, can be compared to the slower moving backbone. These graphs adhere to what is expected from the theory,

having a sharp initial decay, followed by a long relaxation period [112]. Though it should be noted that these fits give contributions that require only one exponential fit, suggesting they can be treated as spherical [112].

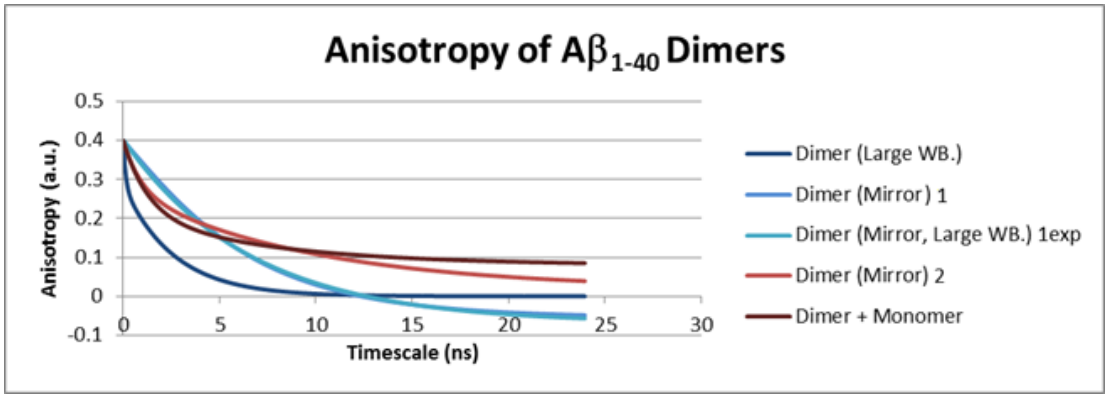

Figure 86 – $A\beta_{1-40}$ Dimer Anisotropy Best Fit Graphs

The dimers have been colour coded in Figure 86; the blue curves represent dimer systems with large waterboxes, and the red curves depict systems with small waterboxes. The dimer with the large waterbox and free moving Tyr side-chain (dark blue) has a sharp initial decay and a relatively fast relaxation time, slightly slower than a monomer. The results from each of the systems analysed show that the sharp initial decay is due to the fast movements of the Tyr side-chains. Furthermore, the relatively fast relaxation time and decay to 0 is due to the aggregation occurring during the analysis window which speeds up the rotational speed associated with the aggregate.

The red decay curved titled “Dimer (Mirror) 2”, is the next trajectory analysed. It has a small waterbox relative to the proteins and they initially do not move much, once aggregated they mirror each other. The Tyr side-chains are trapped against each other, causing them to remain stationary. As such, the resulting decay has a shorter lived initial drop followed by a slower relaxation period. This aggregate is then placed in another similarly sized waterbox but has relatively more room to manoeuvre due to the closeness of the two proteins, creating the two near-identical light blue curves. There is a similar short lived decay initially as the Tyr residues are still trapped, but they have a significantly faster relaxation period as they rotate more freely.

The final system discussed in Figure 86 is a relatively high concentration system with a dimer and monomer present. This creates slow moving particles as is seen by the slow relaxation period, plateauing at the highest of the five graphs at 0.09. The initial drop is also slightly faster than the “mirror” system responses as the Tyr residues are not as trapped. However, the drop is significantly slower than the dark blue curve due to the fact that the Tyr side-chains are restricted in the dimer, whereas the dimer that gives the dark blue curve has full freedom to move. These changes to the curves are reasonable as there are distinct physical reasons for why these systems have varying initial drops and relaxation periods [112].

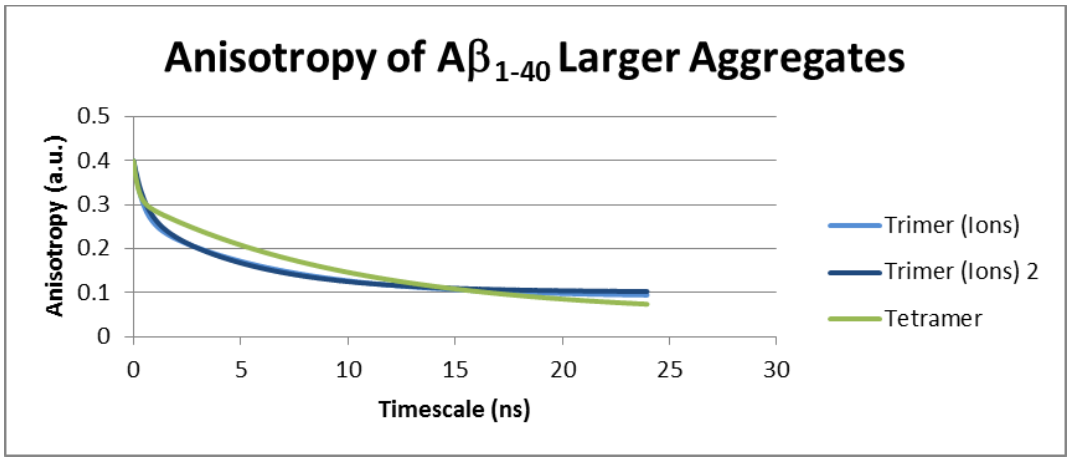

Figure 87 – $A\beta_{1-40}$ Aggregate Anisotropy Best Fit Graphs

Figure 87 demonstrates that as the aggregate gets larger the plateau levels continue to increase and the relaxation periods become slower [112]. The curves related to the trimer are from the same average fit and have nearly identical characteristics; the subtle changes here are what effect the rotational times given to the variables, seen in Table 10. The tetramer fit has a similar plateau value with what seems to be a faster relaxation period as this system has more movement associated with it due to how the proteins aggregate. The initial drop for the tetramer is also shorter lived than the trimer response, as the Tyr residues have less movements associated with them.

These results prove that characteristics can be gained not only through the plateau values but also through analysis of the initial stages of an anisotropy graph [112]. They also further strengthen the results seen in the MC simulation, which have allowed for a more in depth understanding of the subtle changes that can occur in

the MD anisotropy curves. There are also signs that aggregation can only occur once misfolding has occurred [172]. There is a slight change in conformation when ions are present that could potentially affect aggregation [175], though it appears that amorphous aggregation can occur in these simulations with or without ions.

5.10. $A\beta_{1-40}$ Monomers and Aggregation Conclusions

In summation, these anisotropy results show that as aggregates grow, their rotational times generally decrease and have r_∞ values that also increase [112]. This can be seen visually in the graphs as monomers decay to 0 (r_∞ =0) very rapidly and have almost identical decays, due to the lack of variation seen between the systems. As the aggregates get bigger the plateau values also become higher [112], with the most variation occurring in the dimer structures.

The differences in the simulations are significant, as can be seen by the large variation in the dimers; however an experimental sample would contain significantly more proteins, which should mask some of the effects we see here, giving a more uniform result [112]. Though the differences in these anisotropy curves could perhaps be used to tell which species is most prominent in an experimental sample. The differences in these characteristics are due to the bulk aggregate taking more time to rotate and the initial decay is directly related to the amount of movement associated with the Tyr, which can become increasingly more restricted as the aggregate gets larger [112]. A reason for the high degree of variation between the dimers is due to the variously shaped aggregates that have formed as they are all have unique conformations. The variation seen in the dimers may also be apparent in larger amorphous aggregates.

Furthermore, the structural changes seen throughout most of the trajectories, shows that $A\beta_{1-40}$ does not have a stable conformation, and instead changes frequently [172]. There is also a general trend of unravelling the alpha helix before aggregation, which is most prominent when ions are present. In the one case where the alpha helix does not unravel (tetramer system) the aggregation sites appear loose and split into two dimers at two points during the trajectory suggesting the unravelling is needed to allow aggregation to occur properly [171] [174]. Although perhaps in high concentrations amorphous aggregates can form first (as seen with the tetramer) and the assembly of the proteins occurs after. Unfortunately this is outside the scope of these simulations.

6. Results and Discussion: MD Amorph. Aggregation $A\beta_{1-42}$

This chapter shows the MD results of the trajectories of $A\beta_{1-42}$. Much like chapter 5, MD and VMD are used here to reveal information regarding structural changes, Tyr residue position and overall aggregate shape. Each simulation in this section was allowed to run for a minimum of 50ns, except the six protein system, which only has a 30ns trajectory due to the size of the system.

The structure used for these simulations was taken from work by Crescenzi et al (1iyt.pdb) [46]. This has 42 residues and was found to be the stable form for this protein [46]. As with chapter 5 and previous work [44], Charmm22 and Charm27 hybrid forcefield and TIP3P water model were used [124] [125] and VMD was used for the visualisation of the simulations [146].

As stated in chapter 5, the trajectories will be used to discuss how the proteins move throughout the trajectory, noting monomer and aggregation conformational changes, or any other interesting features (such as a trapped or free moving Tyr residue). The Tyr dihedral angles are, again, used to reveal which rotamer state it is currently occupying. The combination of this information and the conformational changes can reveal important information about the Tyr's surroundings and can be potentially linked to experimental work [44] [112]. Simulated anisotropy models are then created and compare to both the experimental work and the $A\beta_{1-40}$ simulated anisotropy results by tracking the Tyr transition moment [147]. These two chapter combined will allow for a detailed study of how the very early stages of $A\beta_{1-40}$ and $A\beta_{1-42}$ aggregation may begin to occur (prior to beta-sheet formation), revealing some information regarding their differences and propensity for aggregation.

6.1. Three Protein System (No Aggregation, no ions)

The first amorphous $A\beta_{1-42}$ aggregate trajectory follows another three monomer system that does not aggregates; it has a waterbox with dimensions ~98Åx101Åx67Å, giving the proteins significantly more freedom than other $A\beta_{1-42}$ systems possibly suggesting that the concentration is too low to promote aggregation on the timescale of the simulation. If misfolding does cause the aggregation process to begin, this could also be the reason for the lack of aggregation. Furthermore, it also has 100ns to allow more time for aggregation

rather than the normal 50ns. Regardless, this particular simulation did not show aggregation, reflecting the stochastic nature of diffusion.

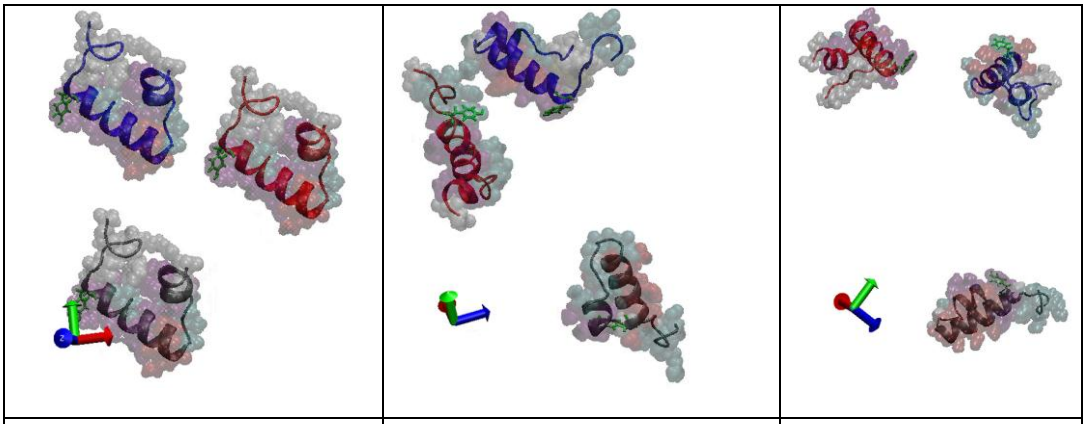

T=0ns	T=50ns	T=100ns

Figure 88 – Three Proteins Monomer Stabilization at time = 0ns, 50ns, 100ns with protein A shown in blue, protein B shown in red and protein C shown in grey. The VDW interactions indicated by the transparent spheres: Purple denotes alpha helix structure, red denotes pi-helix, white denotes a coil and cyan denotes a beta turn. The panels show the proteins positions at the beginning of the trajecotry, 50ns and 100ns

As the trajectory progresses, Monomer A and B initially come close together and begin to interact between 20ns and 50ns. After 50ns they break apart and the three monomers spread out throughout the waterbox and do not interact through the periodic boundaries. This creates a monomer system that can be easily analysed. They do not appear to have misfolded in the same way as seen previously [172]. Furthermore, as with the $A\beta_{1\text{-}40}$ simulations, the initial three proteins all contain a helix dominated structure which is present throughout and none of the proteins really change shape. However, during the brief period where the monomers interact, protein A temporarily forms an anti-parallel beta-sheet His_6 and $Ile_{41.}$ The protein quickly returns to the initial conformation seen for all at the end, which contains predominantly an alpha-helix / pi-helix between residues 13-25 and another between 33-36, and some coiling and turns at the heads and tails [171] [174].

.

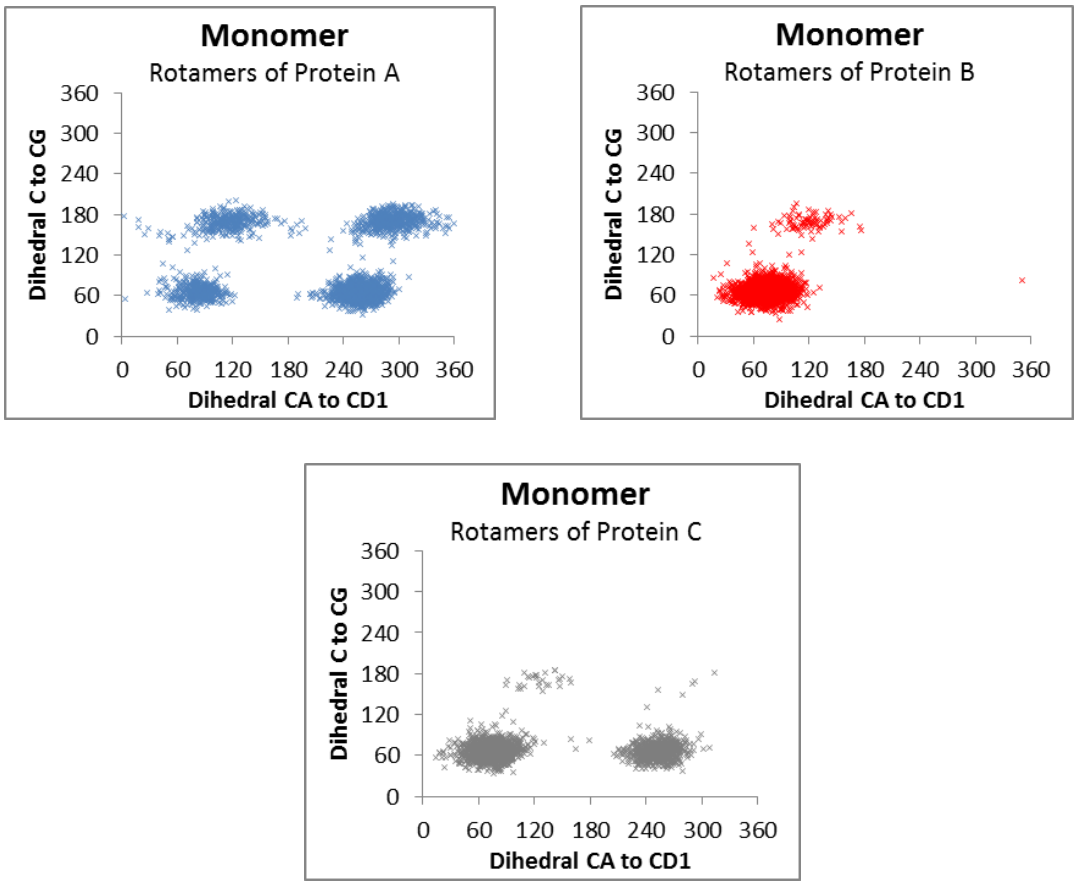

Figure 89 – Three Monomer System Rotamer Response. The centre for each is approximately (70,65), (260,60),(110,170) and (290,170) for Tyr A. Tyr B has only one largely favoured rotomer state and one less favoured at (70,65) and (110,170) respectively. Tyr C has two distinct rotamers at (70,65) and (260,60), as well as two unfavoured rotamers at (110,170) and (290,170).

The results for the above trajectory are interesting as they show strange behaviour for the Tyr rotamer occupation (Figure 89), when compared to results seen in this work and previous work [44]. Protein A shows the common responses that have been present for the majority of monomers, occupying the four states but has a mild preference to states 3 and 4 which is normally associated with aggregated systems as discussed previously. Similarly, protein C also shows the common responses, with a preference towards states 1 and 2 as expected for a monomer. Tyr B has very little movement and only occupies states 1 (a rotamer state usually associated with a monomer) and state 2 (a state associated with aggregates.)

Tyr A's preference to the states associated with aggregate (states 3 and 4) is likely due to the interactions between proteins A and B during the first half of the trajectory (Figure 90) as they appear to start aggregating, making Tyr A's surrounding

environment affect its C to C_G dihedral angle. Tyr B has a preference towards the second state as expected from a monomer but its lack of movement will be due to the fact it begins interacting with protein A restricting its movements. These interactions from proteins A's backbone are affecting Tyr B's movements allowing it to occupy the more twisted states seen with aggregates. If the trajectory was continued, perhaps Tyr B would start occupying a more natural pattern of preferring to move between states 1 and 2, once the other monomers were no longer influencing it.

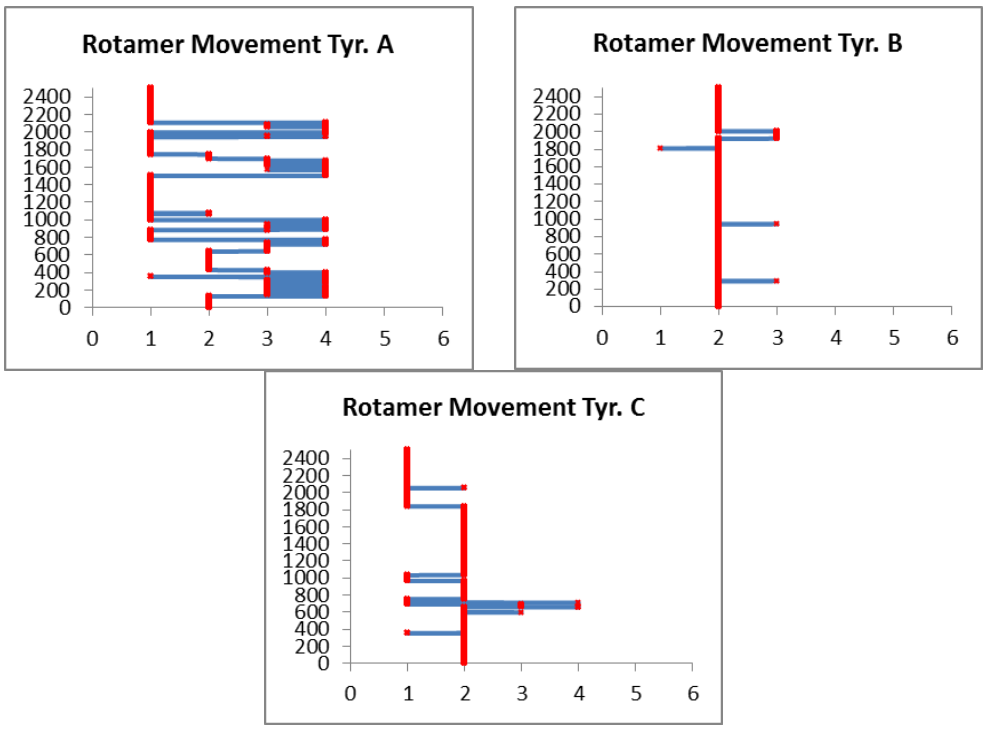

Figure 90 - Time Lapse Rotamer Responses of Monomers without ions.

As can be seen in Figure 90, Tyr A has no movement restrictions, moving freely between all its rotomer states having a preference to states 3 and 4 mostly during the period where it is interacting closely with monomer B. Tyr C has a preference to the first two states with some minor movements into the slightly more twisted states 3 and 4, never the less, they both show acceptable monomer responses. Contrastingly, Tyr B has minimal movements, likely due to the interactions with Tyr A, as seen at 20-50ns in Figure 88. It appears these interactions allow the Tyr to find a favourable conformation that is stable against rotamer fluctuations, at least on the timescale of the simulation. It is known that the energy landscape of proteins is very

rugged, and this is probably an example of a protein visiting a metastable state. Longer duration simulations would be required to explore this idea further.

Despite these unique behaviours, the Tyr side-chains adhere to the usual movements through the rotamer states except a few uncommon movements through 2 to 4 and 1 to 3. These movements are likely due to truncation as these uncommon movement patterns only happen for a single frame.

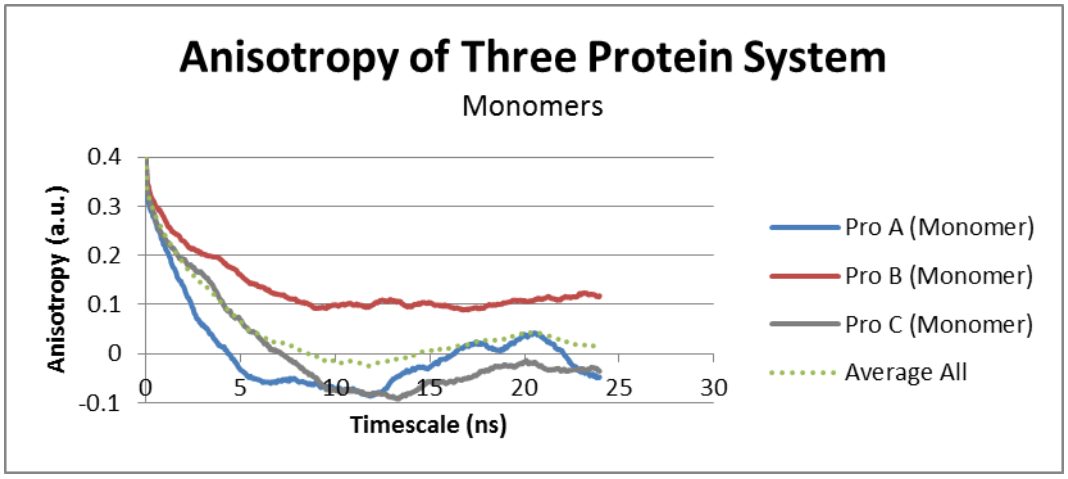

Figure 91 - Simulated Anisotropy of Three Monomer System with no ions. This graph shows the simulated anisotropy of Proteins A (blue) and B (red) and C (grey), as well as the average (dotted green).

Without ions present and room to move freely due to the size of the waterbox, three monomers of $A\beta_{1-42}$ do not readily aggregate as is apparent from the results of Monomer A and C. Monomer A has a fast initial decay followed by a longer relaxation period that reaches approximately 0 at a correlation time of 4.5ns. Monomer C has a slightly slower initial decay than monomer A, but decays to 0 as expected at a rate similar to the $A\beta_{1-40}$ monomers. These both have significant movement related to the Tyr side-chains explaining the fast initial decays. Monomer C's slower initial decay is due to the more frequent occupation of state 2. Monomer B has a plateau value of approximately 0.1 which is unexpected for a monomer, but as previously stated, when interacting with the backbone of monomer A it prevents the protein from rotating freely, and as such does not decay to 0. It also has a short lived, slower initial decay which is due to the Tyrs lack of movement between its rotamer states, due to the interactions with monomer A.

Despite this when the average is taken the resulting graph still decays to 0 with a sharp initial decay creating the appropriate characteristics of a monomer system. This shows that despite some anomalous behaviour in a system, the overall response can still be appropriate. This explains why an experimental system can show the appropriate response despite unique behaviour from individual proteins, as statistically there are so many species in the system that the results are more likely to adhere to the expected outcome due to the effects of averaging.

6.1.1. Best fits

When the average anisotropy is fitted to a two exponential fit there is almost no contribution from the slow life time (ratio of 0.37:0.05 in favour of the fast mechanism). This slow τ_r is 23.085ns, which is exceptionally slow for a monomer however this is redundant as it has almost no contribution to the system.

This suggests that a single exponential fit should be used and so the resulting single exponential fit gave reasonable results with an acceptable τ_r value of 2.4ns (Table 11.) This is slower than the $A\beta_{1\text{-}40}$ aggregates, which rotate faster as they are smaller.

6.2. Three Protein System (Amorphous Dimer + Monomer)

The next trajectory shown in Figure 92 is a three monomer system with a small waterbox (dimensions ~63Åx82Åx47Å) to promote aggregation.

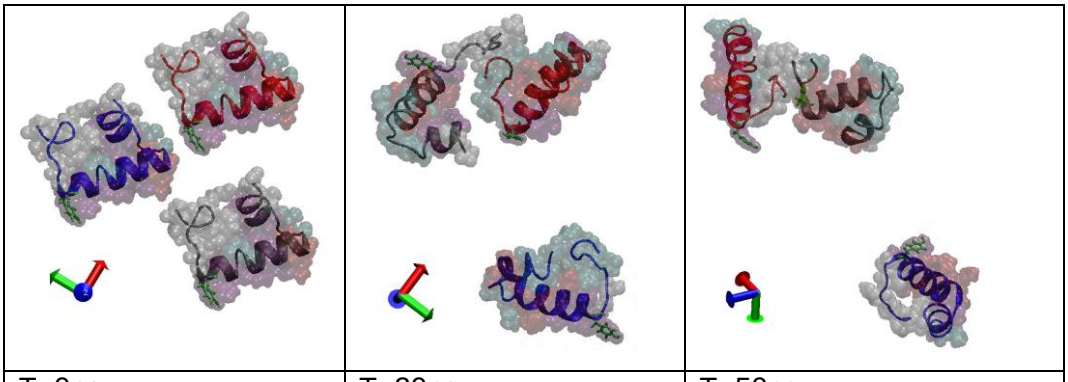

Figure 92 – Three Protein Amorphous Stabilization with Smaller Waterbox at time = 0ns, 20ns, 50ns. with protein A shown in blue, protein B shown in red and protein C shown in grey. The VDW interactions indicated by the transparent spheres: Purple denotes alpha helix structure, red denotes pi-helix, white denotes a coil and cyan denotes a beta turn. The panels show the proteins positions at the beginning of the trajecotry, 20ns and 50ns

During the progression of this trajectory proteins B and C aggregate rapidly within the first 20 nanoseconds. However, despite the extremely high concentration, protein A remains as a monomer. This is unexpected as $A\beta_{1-42}$ readily aggregates during experiments, implying that there is another contributing factor that promotes aggregation and fibrillation. This factor could be the misfolding, as protein C takes on a different conformation before aggregating with protein B, similar to what was seen in chapter 5 when aggregation occurred [172]. Another possibility is the lack of metal ions bridging [41]. The proteins have a helical configuration in the centre of themselves, that has almost fully unravel at the head and tail similar to what has been discussed before [171] [174].

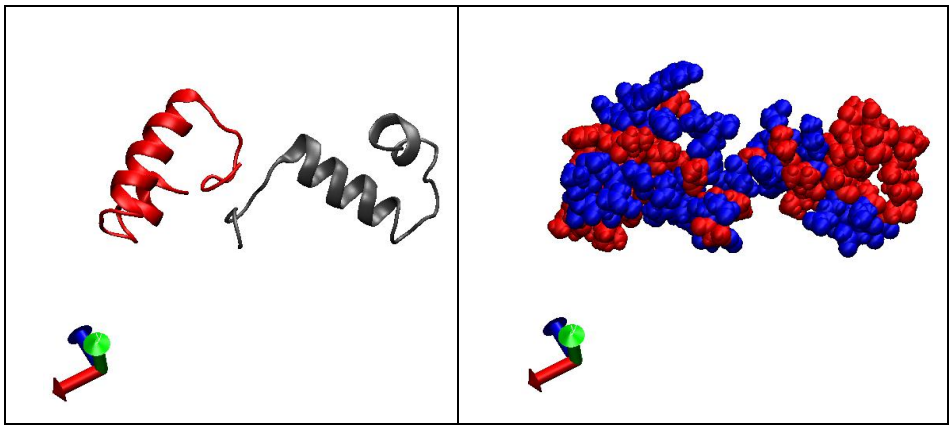

Figure 93 - Hydrophobic Sections of two $A\beta_{1-40}$ Monomers. Both pictures are taken at 50ns with the left panel showing the shape of the proteins (B and C; red and grey respective) and the right panel showing the VDW spheres with the hydrophobic sections (red) against the hydrophilic sections (blue) on the right.

The heads have aggregated together by burying their mutual hydrophobic sections into the centre of the aggregate [122], though this bond would be fairly weak compared to some other aggregates seen in these chapters. This is due to the tails having larger hydrophobic section that tend to aggregate more readily. Nonetheless this is still two monomers that have formed a dimer through aggregation.

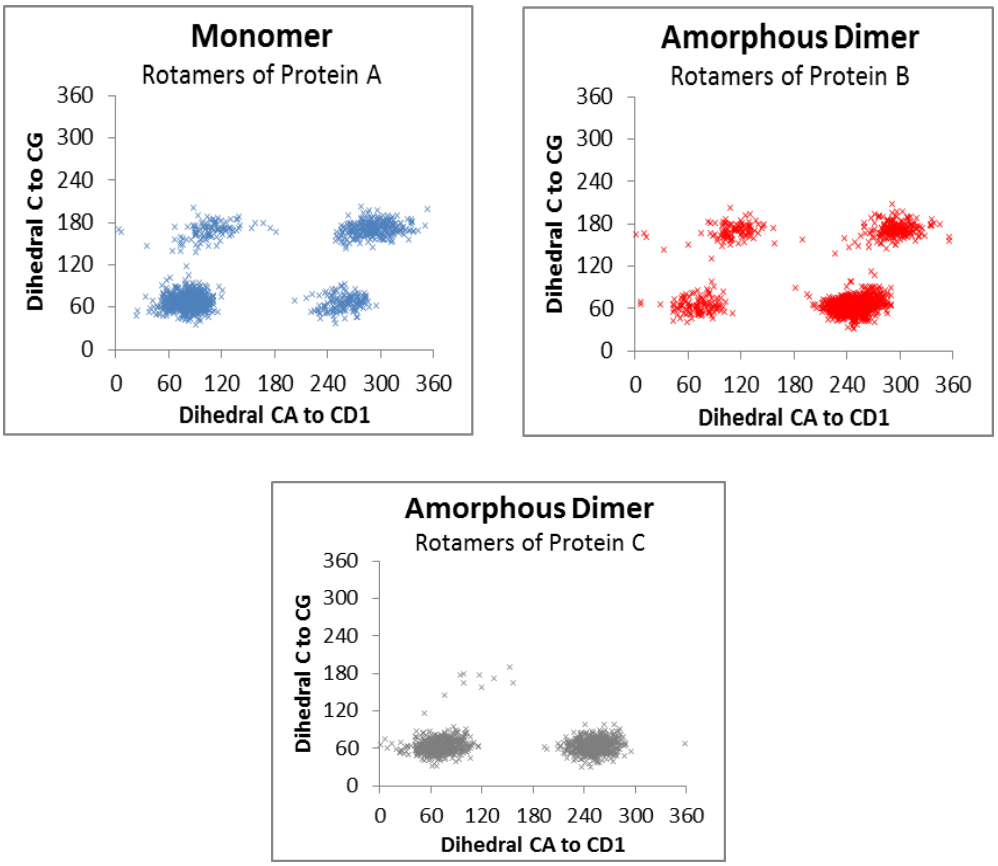

Figure 94 – Amorphous Three Protein System (with Small Waterbox) Rotamer Response. The centre for each is approximately (70,65), (255,60),(100,170) and (300,170) for Tyr A and for Tyr B. Tyr C has only two at (65,60) and (255,60).

In Figure 94 the graphs for Tyr's A and B both have all four rotamer states with a slight preferential occupation of states 1 and 2. Tyr C primarily occupies the first and second rotamer states.

Tyr A has a lot of freedom to move throughout the trajectory (Figure 92,) which is why it occupies states 1 and 2 regularly, and as expected of a monomer can be influenced by its surroundings into occupying states 3 and 4. Tyr B, as part of an aggregate would be more likely to occupy states 3 and 4 but is still expected to occupy states 1 and 2.

In contrast, Tyr C is part of an aggregate and as such would be expected to have a preference to states 3 and 4 but shows a preference to the first two. This is likely due to the fact that the aggregate is affecting the Tyrs backbone and is preventing it from readily occupying states 3 and 4, in a similar manner to what was shown in Figure 69.

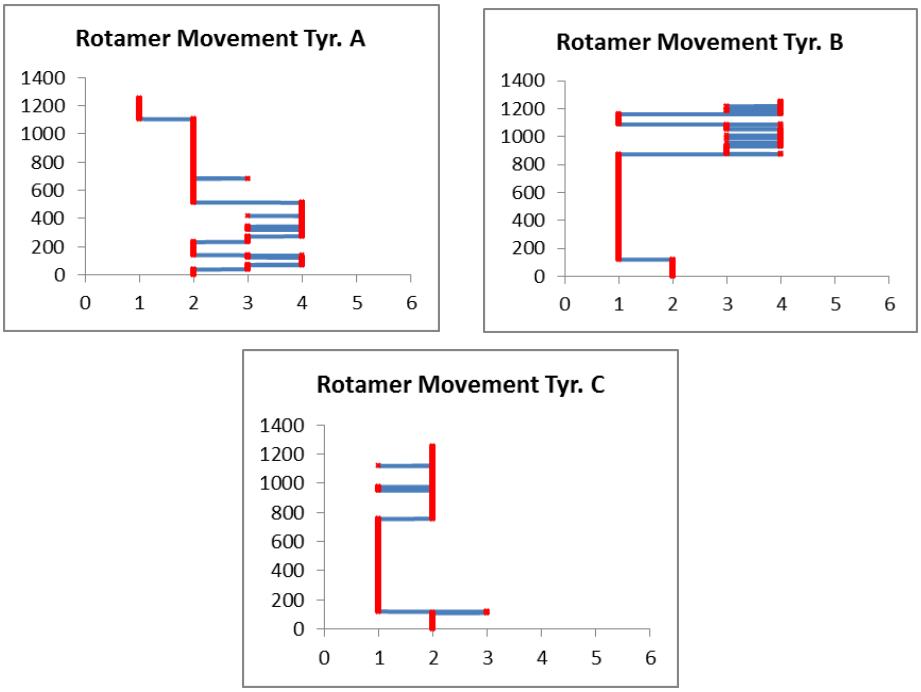

Figure 95 - Time Lapse Rotamer Responses of Amorphous Dimer and Monomer.

The evolution of the rotamer states over the course of the trajectory is shown in Figure 95; Tyr A has significant fluctuations for approximately the first 20ns of the trajectory, but has an overall preference to states 1 and 2, which is expected for a monomer. Tyr B begins the simulation with a preference towards states 1 and 2 as before aggregation occurs the Tyr is being affected by the other monomers, post aggregation it shows a clear preference to states 3 and4 due to the aggregate interactions. Tyr C shows preference to states 1 and 2; as suggested above, this might be another example of a protein finding a metastable state for the duration of the simulation.

Tyr A and B adhere to the rules specified previously for the rotamer state movements but Tyr C is able to jump from state 3 to state 1, this could be due to truncation of the frames, as it only happens for a single frame. It is possible that the Tyr can move from either state 1 or 2 up to states 3 or 4. This is because the movement between the lower and higher states comes from twisting the C to C_G angle, which could happen in this manner, though it seems it is an unfavourable movement.

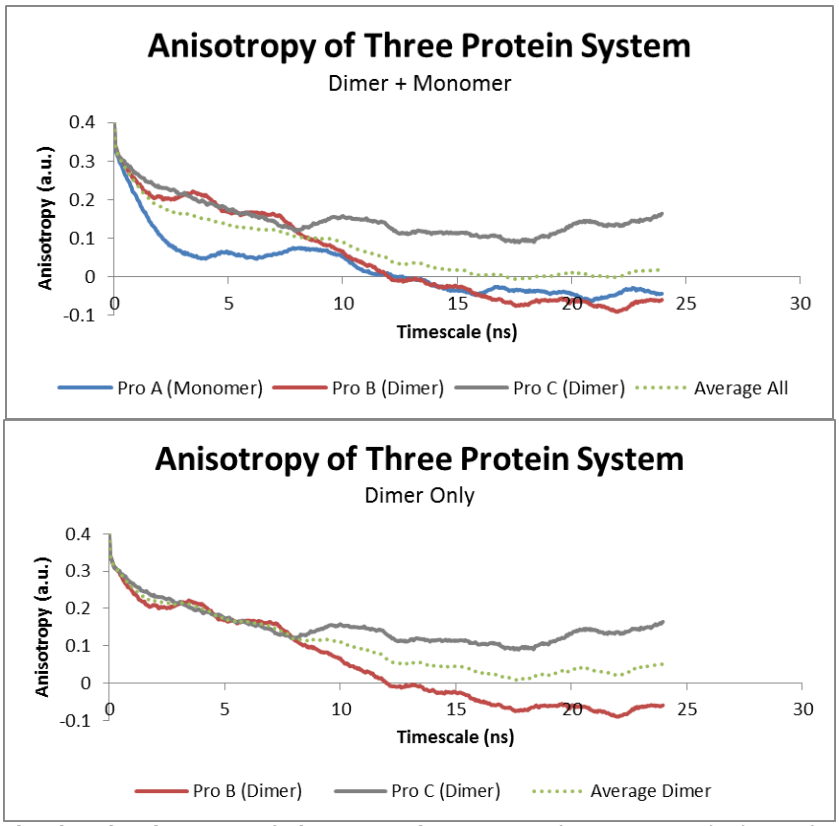

Figure 96 - Simulated Anisotropy of Three Protein System. The upper graph shows the simulated anisotropy of proteins A (blue), B (red) and C (grey), as well as the average (dotted green). The lower plot depicts the simulated anisotropy of proteins B (red) and C (grey) with the average as a dotted green line.

Protein A has a complex decay with an initial decay to roughly 0.06 at a correlation time of 3.5ns and then has a slower relaxation to 0. As discussed previously and in the MC simulations, the rapid decay is due to the rapid movements of the Tyr. The higher plateau value is a strange result for a monomer but is likely related to the small waterbox used, which creates interactions with the monomer from the surrounding proteins, complicating its decay. Regardless, this is still a reasonable result for a monomer that is being influenced by its surroundings.

Protein B has a sharp, but short lived initial decay; this is due to less frequent movements from the Tyr side-chain relative to protein A. It has a secondary decay that could be due to late movements of the Tyr or due to the aggregation process. As it is part of the dimer, protein B has a much slower relaxation period related to the slower rotation of the aggregate. This eventually decays to (and past) 0, and takes significantly longer than a monomer to do this.

Protein C displays results that can be attributed to a dimer, as it has a short lived initial decay followed by a slow secondary decay that decays to approximately 0.15. This is high for a dimer but is likely due to the fact that the Tyr remains in one state for large portions of the simulation. This decay is made slower because of the fact it is part of an aggregate.

The top graph shows the average decay between all three proteins, it has a short initial decay, due to the restricted Tyr movements, and decays to zero after a slow relaxation period and the lower graph shows the average response of the dimer. These graphs are very similar, but the effect of having a monomer in the system is clearly depicted, as the dimer anisotropy decay has a plateau value of above 0.02 and the total system anisotropy response decays to 0.

The bottom graph also has a shorter lived initial decay, related to the lack of the monomers presence which gives the system a longer and sharper initial decay as expected. The total system decay (top graph) also has a second decay which is a characteristic of a system with multiple species in it, as seen in the experimental anisotropy results.

6.2.1. Best Fits

When the entire system is studied for the best fit graphs (Figure 111 and Table 11) they do not account for the second sharp decrease near the start of the analysis. This is due to the system being more complex, with both a dimer and monomer in it. This implies that there could be three mechanisms involved; a faster rotation from the monomer, a slower rotation from the dimer and the Tyr movements themselves. The complexity in the decay could also be created by the monomer and dimer interacting. This suggests that a three exponential fit would be required to create an appropriate best fit for this type of system. However, the correlation is still within the accepted range as it has a correlation value of 0.977 and so the two exponential fit is adequate and implies the third mechanism is barely contributing.

For the best fit graph and variables that depict the response from both the monomer and dimer in Figure 111 and Table 11, the contribution of the slow and fast mechanism has a ratio of 0.26: 0.13 (respectively). There is a slow τ_r value of 6.367 which is reasonable as it is slower than the results seen for the monomer systems. The faster τ_r value related to the Tyr side-chains' movements is slower than the

values given for the dimer only analysis, but is still a reasonable result. This variation is likely from the complex decay from having multiple species analysed simultaneously.

The dimer only analysis reveals a slightly higher τ_r value for the bulk aggregate rotation, this is valid as the faster moving monomer would skew the results making the average rotation found lower. The contribution from the Tyr is lower than when both species were analysed together with a ratio of 0.29 (bulk aggregate) to 0.09 (Tyr.) This is due to the Tyr side-chains not moving as readily from state to state in proteins B and C leaving a higher contribution from the bulk aggregate rotation. The reason for the higher contributions in the first analysis is because of the more erratic movements of Tyr A.

6.3. Three Protein System with Ions (No aggregation)

Figure 97 depicts the movements of a three protein system with an ionic concentration 0.250mMol/L [162]. This system never aggregates despite the system being in a small waterbox as can be seen from panel 1 below. This again implies that there may be other mechanisms causing aggregation, such as the requirement of metal ions to bridge residues [41] [42] or perhaps the ions are having a larger screening effect than expected [175].

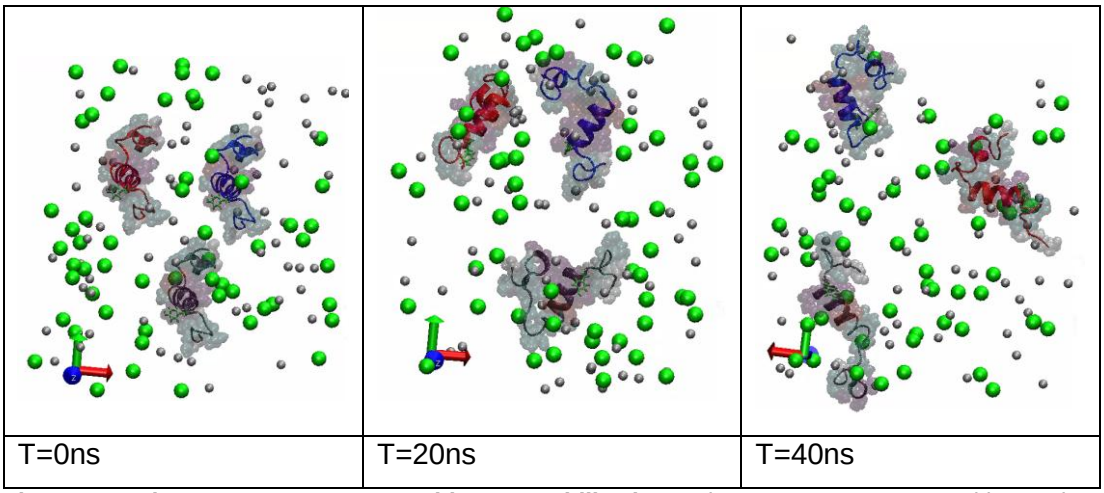

Figure 97 – Three Monomer System with Ions Stabilization at time = 0ns, 20ns, 40ns. with protein A shown in blue, protein B shown in red and protein C shown in grey. The VDW interactions indicated by the transparent spheres: Purple denotes alpha helix structure, red denotes pi-helix, white denotes a coil and cyan denotes a beta turn. The panels show the proteins positions at the beginning of the trajecotry, 20ns and 40ns and the individual spheres show the ion positions.

As can be seen above, the three monomers initially start close together but very quickly start to move away from each other creating three separate monomers in an ionic system. The changes in conformation are minimal from those seen in chapter 5. The unravelling seen at the heads and tails of the proteins is similar to what has been found in literature [172] and the alpha/pi helix sections [171] [174] are around residues 11-22 and 32-36 in all three proteins. It can also be noted that there are no distinct differences between this trajectory and those $A\beta_{1-42}$ models without ions. The lack of the horseshoe motive discussed in chapter 5 is possibly connected to why they do not readily aggregate [63] [172].

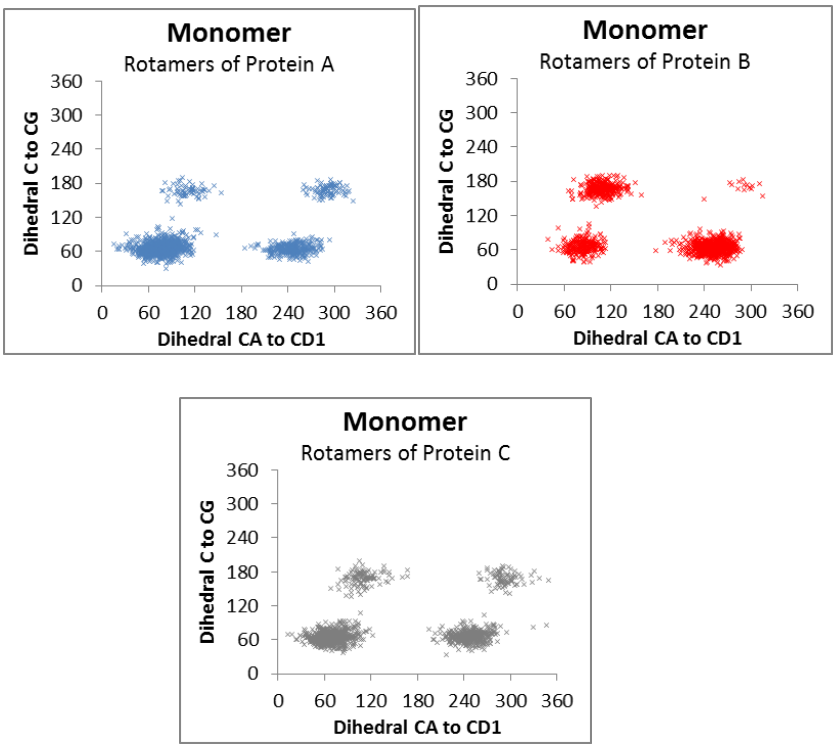

Figure 98 –Three Monomer Ionic System Rotamer Response. The centre for each is approximately (80,60), (250,60),(100,170) and (280,170) for Tyr A. Tyr B has approximately (80,60), (250,60),(100,170) and (290,170). Tyr C has (70,60), (65, 245) (110,180) and (290,170).

All three Tyr side-chains take on traditional rotamer positions with some anticipated variation as is depicted in Figure 98 with a preference towards states 1 and 2 as expected. As the proteins are all monomers, their Tyr interactions are minimal and so do not get twisted into the higher states as often. Ions and other residues from their own backbones are likely interacting with the Tyr side-chains which may be promoting the occupation of states 3 and 4.

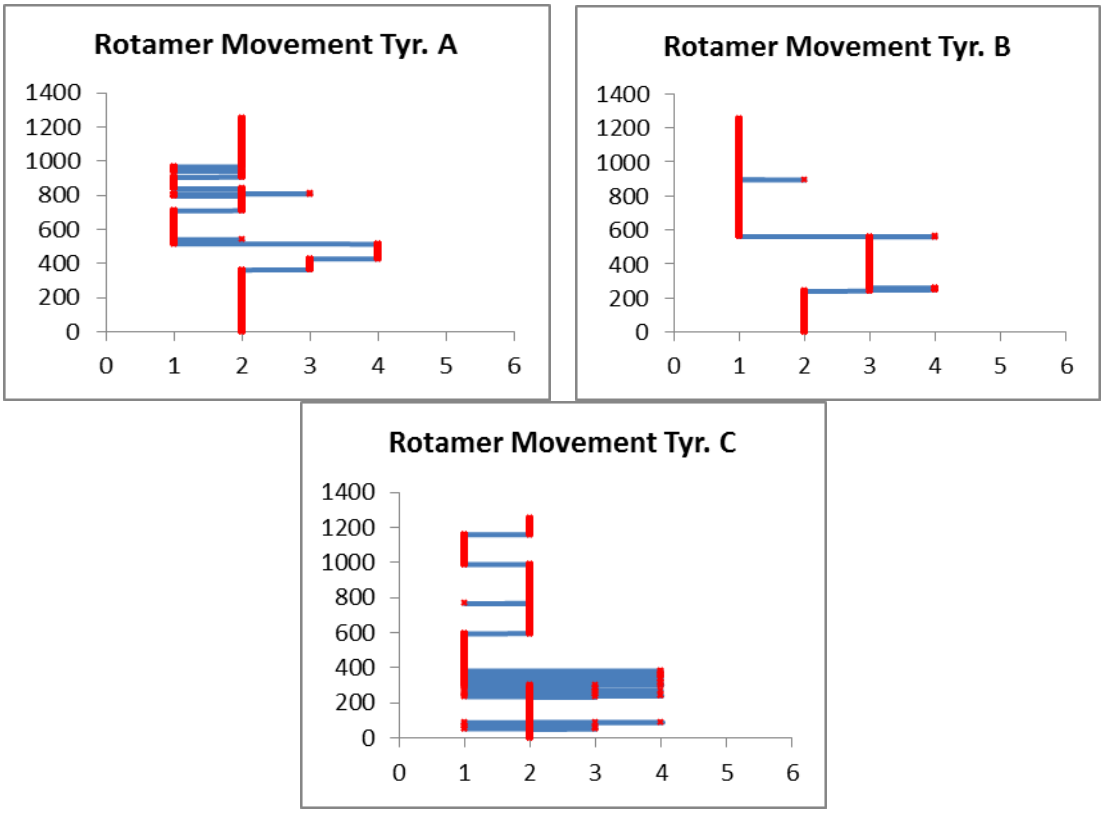

Figure 99 - Time Lapse Rotamer Response of Monomers with Ions

Figure 99 shows the evolution of the rotamer states over time. As stated above, they are all parts of a monomer and as such all have an affinity for states 1 and 2. They also show a fair degree of movement (A and C more so than B).

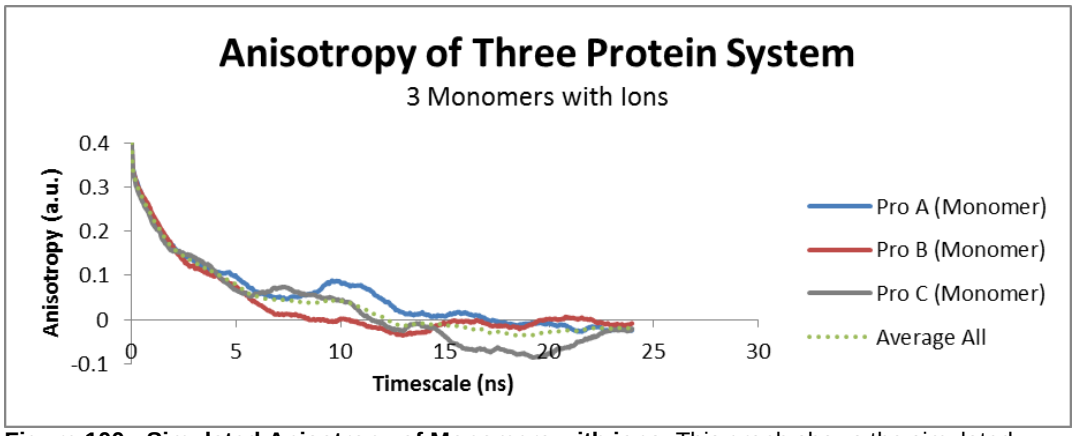

Figure 100 - Simulated Anisotropy of Monomers with ions. This graph shows the simulated anisotropy of both Proteins A (blue), B (red) and C (grey), as well as the average (dotted green).

The monomers never aggregate and as such have three sharp initial decays due to the movement of the Tyr side chains, followed by a rapid decent to 0 at a correlation time of 10-14ns.

Monomer B has characteristics most similar to what is expected for a monomer with no outside influences or interactions. This was seen in chapter 3.5 although has a slightly slower initial decay. This effect could be due to the Tyr not moving between rotamer states as often or because the proteins are slightly slower to rotate as it is a slightly longer protein. Monomer C has similar response to monomer A, both of which have more free moving Tyr residues.

As such it can be concluded that all three species show a monomer response with varying levels of effects caused by the ions. The average of these three monomers creates a more expected response that shows a smoother decay similar to a monomer response in experimental data.

6.3.1. Best Fits

For these monomers the first best fit was fitted allowing it to decay past 0 and shows almost equal contribution from both the fast and slow mechanism (Figure 110 and Table 11). It shows an incredibly slow τ_r for the bulk rotations of the system (7.468ns), comparable to what was seen for the dimer which is only reasonable if the ions are significantly slowing down the rotation of the proteins.

As such a fit was made to decay to 0 (as anisotropy decays normally do not decay past 0) which gave a more reasonable τ_r of 3.906ns. In doing this, the slower mechanism plays such a small part (a low R_0) that this mechanism can be ignored and a single exponential fit was made. The resulting τ_r value is faster than the other two best fits for this system and is a more appropriate response for a monomer with a rotational time of 4.226ns, which is slightly faster than the rotational times seen for single exponential monomers without ions. . This result is also comparable to that seen for the MC anisotropy.

It is difficult to establish which fit is most appropriate, as a one exponential fit may not be an adequate fit for a system with ions and multiple monomers in it. However, the two exponential fit gives too high a rotational time to be sensible and the forced fit to the 0 asymptote has similar resulting parameters to that of the single exponential fit. Therefore, the most reasonable conclusion is that the single

exponential has the best fit and implies that there is only one significant timescale for the monomer anisotropy.

6.4. Four Protein System (2 dimers, small waterbox)

A simulation was created for four proteins with a water box that was too small resulting in the aggregate interacting with itself through the waterbox boundary, creating an infinite loop (see Appendix 5.6). The trajectory seen in Figure 101 has a larger waterbox (dimensions ~73Åx99Åx90Å) than seen in that previous simulation (dimensions ~65Åx48Åx91Å), preventing the proteins from aggregating with themselves through the waterbox boundary which allows for less bias results and a full 50ns trajectory.

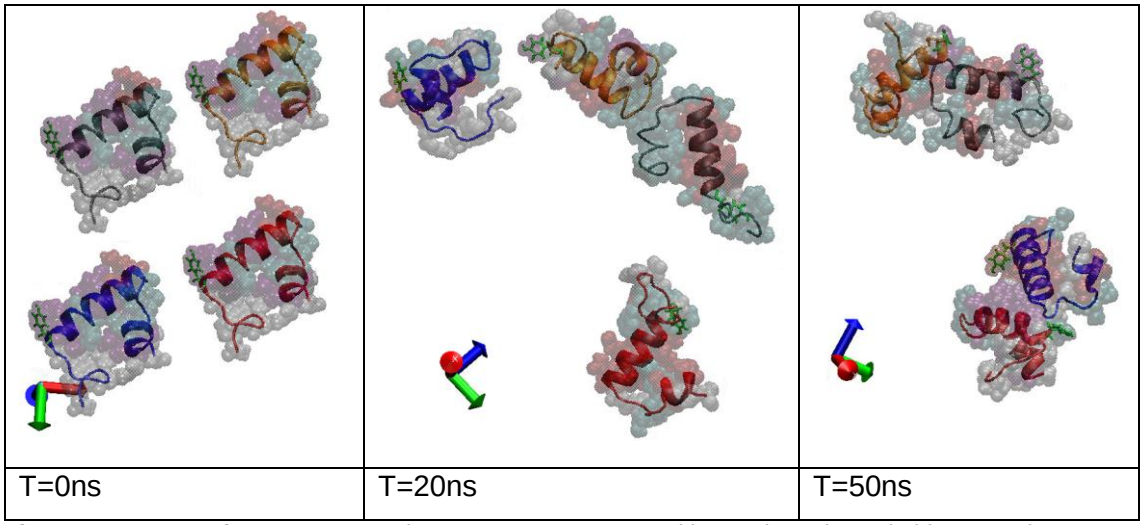

Figure 101 – Two Dimer System at time = 0ns, 20ns, 50ns. With protein A shown in blue, protein B shown in red, protein C shown in grey and protein D shown in orange. The VDW interactions indicated by the transparent spheres: Purple denotes alpha helix structure, red denotes pi-helix, white denotes a coil and cyan denotes a beta turn.

The trajectory begins with all four monomers in close proximity. The proteins have more distinct horseshoe motif which appears to cause aggregates to form [63] [172]. After 20ns monomers C and D begin to aggregate forming a dimer whereas monomers A and B move away from each other. Monomer A continues to move down through the waterbox, wrapping to the top where it begins to aggregate with monomer B at approximately 37.5ns. The trajectory then contains two dimers for the rest of the trajectory. As with all previous $A\beta_{1\text{-}42}$ simulations, the structures are predominantly alpha helical in shape and do not change much throughout the trajectory [171] [174]. One notable change is that, once aggregated, protein B has a

significantly shorter coil than the other proteins for brief periods throughout the trajectory which resembles other configurations seen in literature [172].

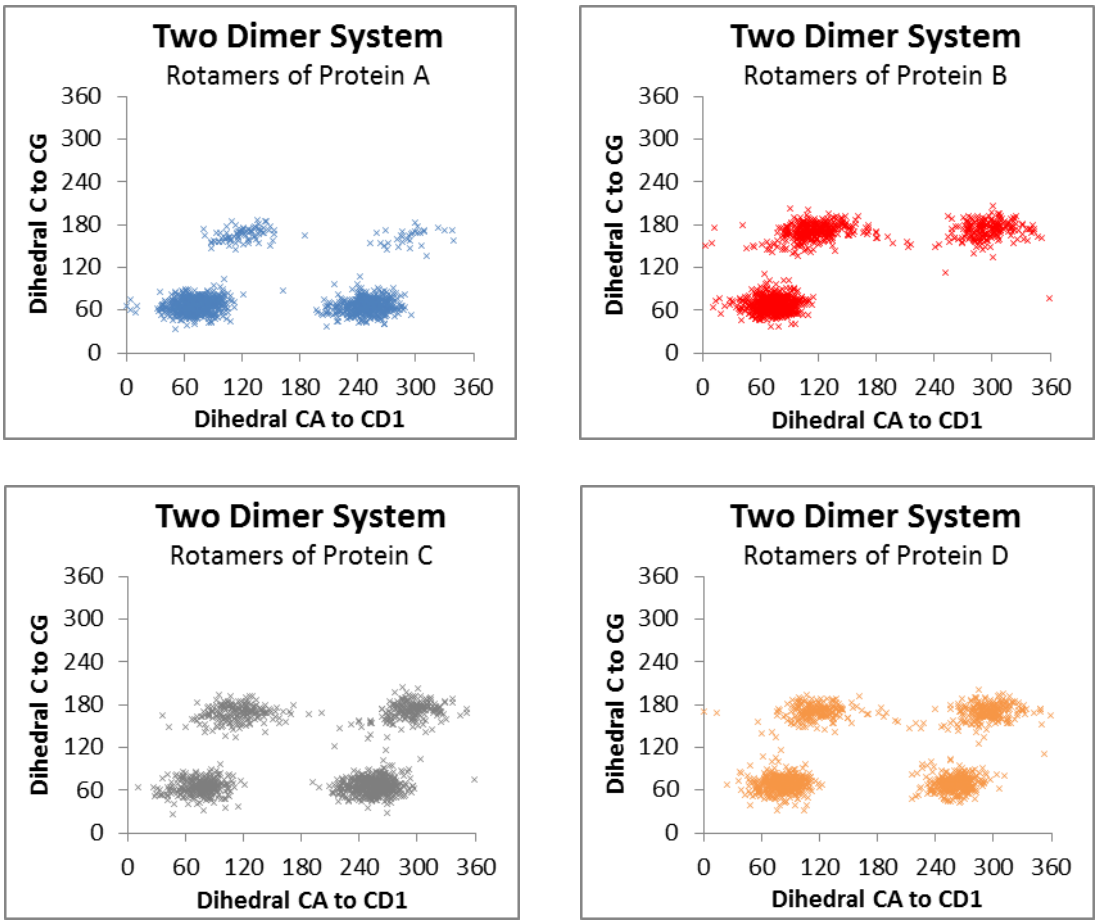

Figure 102 – Four Protein Two Dimer System Rotamer Response. The centre for each is approximately (70,65), (250,65),(110,175) and (290,170) for Tyr A. Tyr B has approximately (70,65),(100,170) and (290,175). Tyr C has (70,65), (255,65),(110,170) and (290,170). Tyr D has (75,65), (260,65),(110,175) and (290,170).

Figure 102 shows the expected results for all four proteins. Tyr C and D have equal distribution for the four rotamer states as they spend over half the trajectory as a dimer and so their preference will start shifting to states 3 and 4 due to the interactions (Figure 150).

Tyr A shows a preference for occupying states 1 and 2 which is logical as it spends more than half the trajectory as a monomer. This means that the interactions affecting the Tyr will be minimal and so they will not as readily occupy states 3 and 4.

Tyr B, in contrast, shows only three rotamer states and seems to prefer occupying state 2, and then spends equal time in states 3 and 4. This is a reasonable result as the first half of the trajectory is spent as a monomer where it would prefer the lower state(s) and then moves into an aggregate which affects the surrounding residues due to the backbone interactions, causing the Tyr to be influenced into occupying the more twisted states 3 and 4.

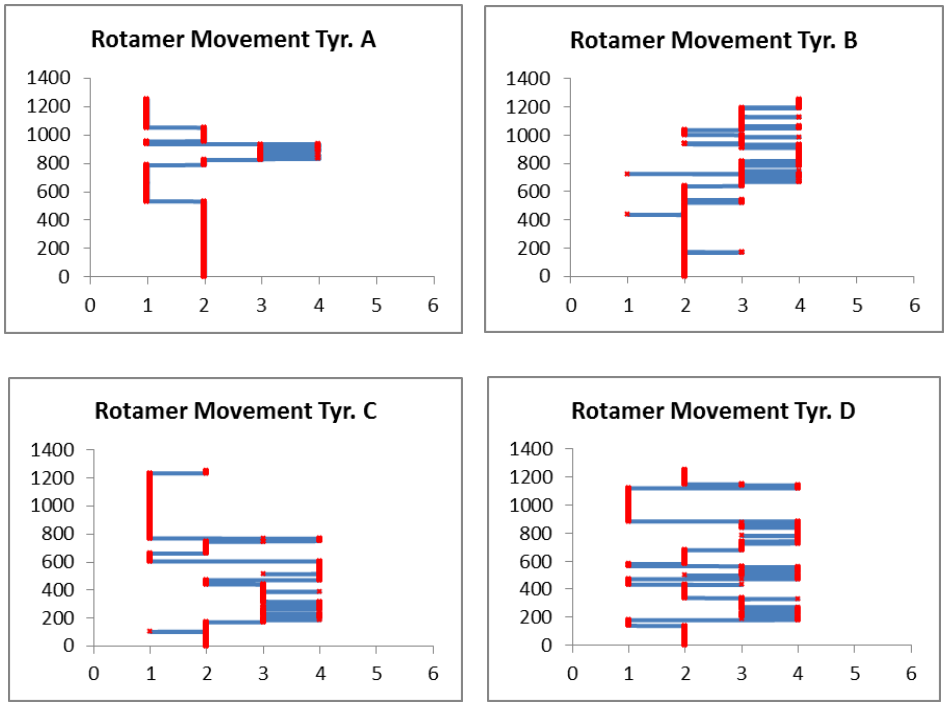

Figure 103 - Time Lapse Rotamer Response of Two Dimer system

Proteins A and B do not aggregate until approximately 37ns (900th frame) which is reflected in the results seen in Figure 103, as there is a shift towards states 3 and 4 in the Tyr movements in the second half of the trajectory. Tyr A has more freedom to move as seen in Figure 101 as its Tyr is located at the bottom of the dimer whereas Tyr B is much closer to Protein A. Tyr A has a preference to states 1 and 2 even after aggregation, likely due to external forces affecting its ability to move (but does not allow for the twisting to occur into states 3 and 4.) Tyr B in contrast, prefers states 3 and 4 once aggregation begins, further proving the effect that external forces have on influencing how twisted the Tyr becomes along the C to C_G dihedral angle.

Proteins C and D have formed a dimer by 20ns (or the 500th frame) and as such, both Tyr's preference shift towards states 3 and 4 much earlier as they get

influenced by aggregation fairly early on in the trajectory. Protein C shows a preference towards state 1 near the end and is likely due to the external forces not influencing the Tyr's dihedral angle into occupying states 3 and 4. Furthermore, the local interactions of its own residues could be preventing it from moving freely between states 1 and 2.

All Tyr's adhere to the movement rules for occupying their rotamer states, except one instance in protein C where a jump from the state 1 to 3 is made, however this is either an unfavourable movement or due to truncation of the trajectory.

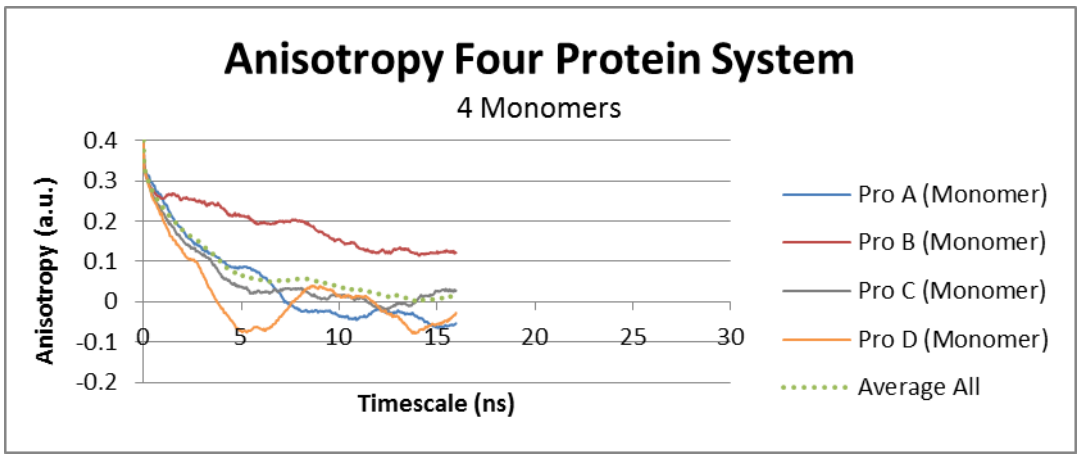

Figure 104 - Simulated Anisotropy of Four monomer System beginning to aggregate. This graph shows the simulated anisotropy of both Proteins A (blue), B (red) C (grey) and D (orange) as well as the average (dotted green).

The anisotropy for this system has been split into two graphs of anisotropy, the graph in Figure 104 analyses the trajectory before aggregation fully completes and still has a timescale axis of 30ns to aid comparison with other graphs. This creates monomer results with some minor complications in the anisotropy decay as there is some aggregation taking place during the analysis.

For the monomer graph, protein A decays readily to 0 at a correlation time of around 7ns with a moderately fast initial decay. As a monomer, it moves around the system a lot and only stops moving as freely after aggregation occurs which is after the analysis ends. Its initial decay is slightly shorter lived than C and D due to its lack of Tyr movement relative to them (Figure 103.)

Protein B shows distinct signs of aggregation as it does start to form a dimer within the analysis window. Its initial decay is short lived, due to the early lack of

movement from Tyr B (Figure 103) and it never reaches zero, this is most likely because it spends the entire trajectory at the top right hand corner of the waterbox without moving significantly and then forms an aggregate. This implies that some interactions with other proteins are likely occurring to keep it in this position.

Protein C does not move much during the trajectory but has fair movement in the Tyr residue. This is reflected in its anisotropy decay as it shows a fast initial decay that levels out at a value of 0.11 at a correlation time of 4ns, which is due to the early rapid movements of the Tyr side-chain. This is followed by a second slower decay to 0 at a correlation time of 12ns. Finally, protein D has a fast initial decay typical of a free moving Tyr residue response but has an increasing anisotropy curve. The complex behaviours seen in proteins C and D are likely due to the aggregate forming in the early stages of the trajectory.

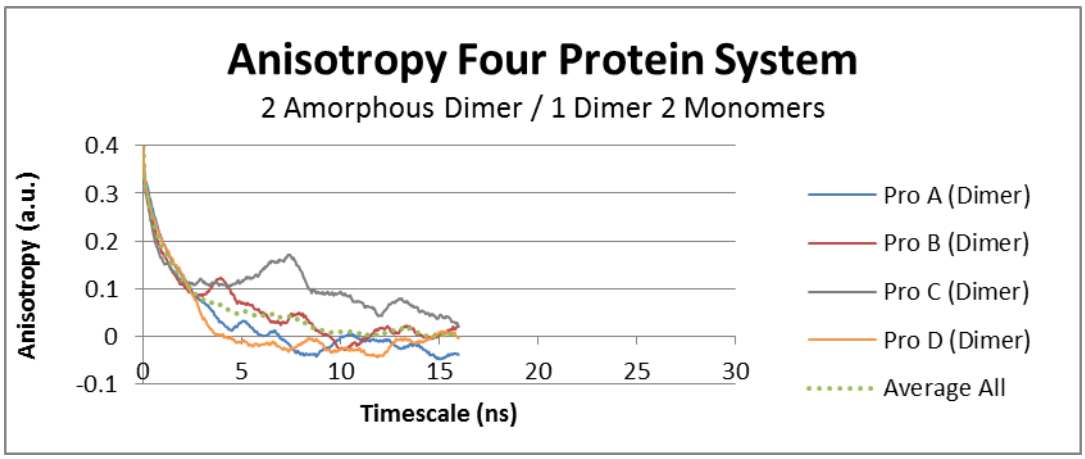

Figure 105 - Simulated Anisotropy of Two Dimer System. This graph shows the simulated anisotropy of both Proteins A (blue), B (red) C (grey) and D (orange) as well as the average (dotted green).

Unfortunately there is not enough data available post aggregation for this system and as such the graph, depicted in Figure 105, begins its analysis at a trajectory time of 18ns, where proteins C and D are beginning to form a dimer and proteins A and B are monomers and begin aggregating over 10ns later. This creates complexities for the decay as there is also aggregation occurring during this anisotropy analysis.

In Figure 105 the timescale axis, again, ends at 30ns to aid comparison with other graphs. Proteins A, B and D have very fast initial decays as their Tyr side-chains have a lot of movement in the second half of the trajectory (Figure 103). Protein A

plateaus at a value of 0, at a correlation time of around 7ns had has some variation in its decay. This is caused by the aggregation process. Protein B has an increase in anisotropy after the initial decay and a slow relaxation time. This relaxation may be due to the forming aggregate, but is more likely an artefact of having such a small window to analyse.

Protein C has a very slow initial decay levelling out at a correlation time of 4ns which then increases and decays again. This increase is likely due to the aggregation process occurring right as this analysis starts. The high initial plateau is due to the lack of late movement from this Tyr (Figure 103) and the fact that it is part of an aggregate for almost the whole trajectory.

Protein D has a similar decay to that of a monomer, with some variation in the initial decay. This is likely due to the fact that despite being part of an aggregate, it spends a significant portion of the trajectory (between 20ns and 50ns) rotating as can be seen in Figure 101.

6.4.1. Best fits

The two resulting anisotropy graphs both have separate fits in Figure 111 and Table 11, one shows the monomer response and the other depicts the dimer response. The monomer response shows a higher contribution from the bulk aggregate rotation (0.256 vs. 0.144 for the monomer) and τ_r values of 0.437ns and 4.603ns for the Tyr rotation and bulk aggregate rotation respectively. These rotational times are reasonable for this trajectory as they are slightly higher than a simple monomer system because aggregation begins during this analysis and so the resulting rotation would be affected.

For the dimer response there are two best fit graphs that seem appropriate. The two fits show similar contributions as they both have a preference for the fast Tyr mechanism, but exhibit different r_∞ values, (0 and 0.15) and also different rotational times. The first fit with the r_∞ value of 0 has rotational times of 1.01ns for the Tyr which is significantly slower than what has been seen for the monomers, likely due to the Tyr side-chains not moving around as much when aggregation occurs and 7.97ns for the bulk rotation which is slower than that of the monomer response.

The second dimer fit that has an r_∞ value of 0.15 shows rotational times of 0.261ns and 4.000ns, which does not exhibit a longer rotational time than the monomer results. This is likely to be a inappropriate fit in terms of physical relevance. These results could be explained by amorphous aggregates allowing a larger degree of freedom to move as the backbones have not been rigidly held in place, meaning that there would be an insignificant difference between the rotational times of two monomers beginning to aggregate and two monomers that have aggregated. However, based on the movement patterns seen in the trajectory the first option seems more likely to be correct.

6.5. Six Protein System (Tetramer/dimer chain breaking)

Figure 106 depicts an amorphous six protein system that runs for 750 frames (30ns.) This limitation is due the amount of trajectories produced and also the size of this individual simulation. Running this simulation for a longer trajectory would be beneficial as there is limited information that can be gathered from this trajectory. In order to run this simulation, the waterbox was relatively small (dimensions ~72Åx99Åx87Å) to save processing hours, which creates a high concentration and promotes aggregation.

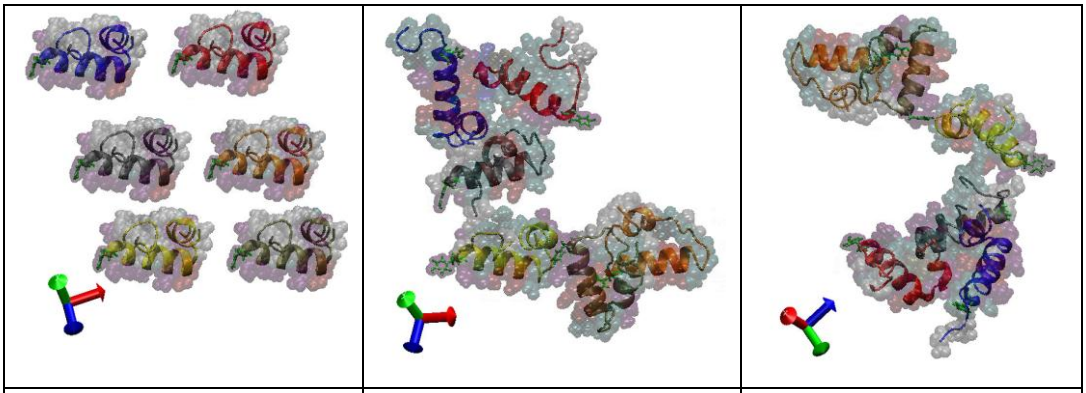

T=0ns	T=20ns	T=30ns

Figure 106 –Six Monomer System Aggregating to Amorphous Tetramer / Dimer at time = 0ns, 20ns, 30ns. With protein A shown in blue, protein B shown in red, protein C shown in grey, protein D shown in orange, protein E shown in yellow and protein F shown in tan. The VDW interactions indicated by the transparent spheres: Purple denotes alpha helix structure, red denotes pi-helix, white denotes a coil and cyan denotes a beta turn.

All six monomers immediately start aggregating together due to the concentration within the waterbox and do appear to have folds that form the horseshoe motif [63] [172]. This is unexpected as all previous A$\beta_{1\text{-}42}$ amorphous aggregate systems do

not aggregate so readily, suggesting that $A\beta_{1-42}$ may only begin to form an amorphous aggregate when the systems concentration of monomers is high enough [39]. Another reason could be that higher concentrations allow the proteins to interact more readily, causing them to misfold into their beta-sheet structures. It should also be noted that anti-parallel beta-sheets form between the head and tail of proteins D (folding over on itself to do this) and the head of protein B (the head creates a small hairpin motif) [171]. Other than this all proteins share the common feature of still maintaining their helical structures [174].

Within the first 4.8ns monomers A and B begin to aggregate together forming a dimer, and monomers C through F begin to form a tetramer. By 7.2ns all six proteins have begun to interact, showing signs of aggregating into a hexamer. At 26.4ns proteins D (orange) and F (tan) break off and form a dimer, which leaves A, B, C and E to remain as a tetramer for the remainder of the trajectory. It should also be noted that proteins A, B, C, E and F have Tyr side-chains with minimal interactions from the surrounding proteins, and protein D has Tyr side-chain that is interacting with its environment more closely.

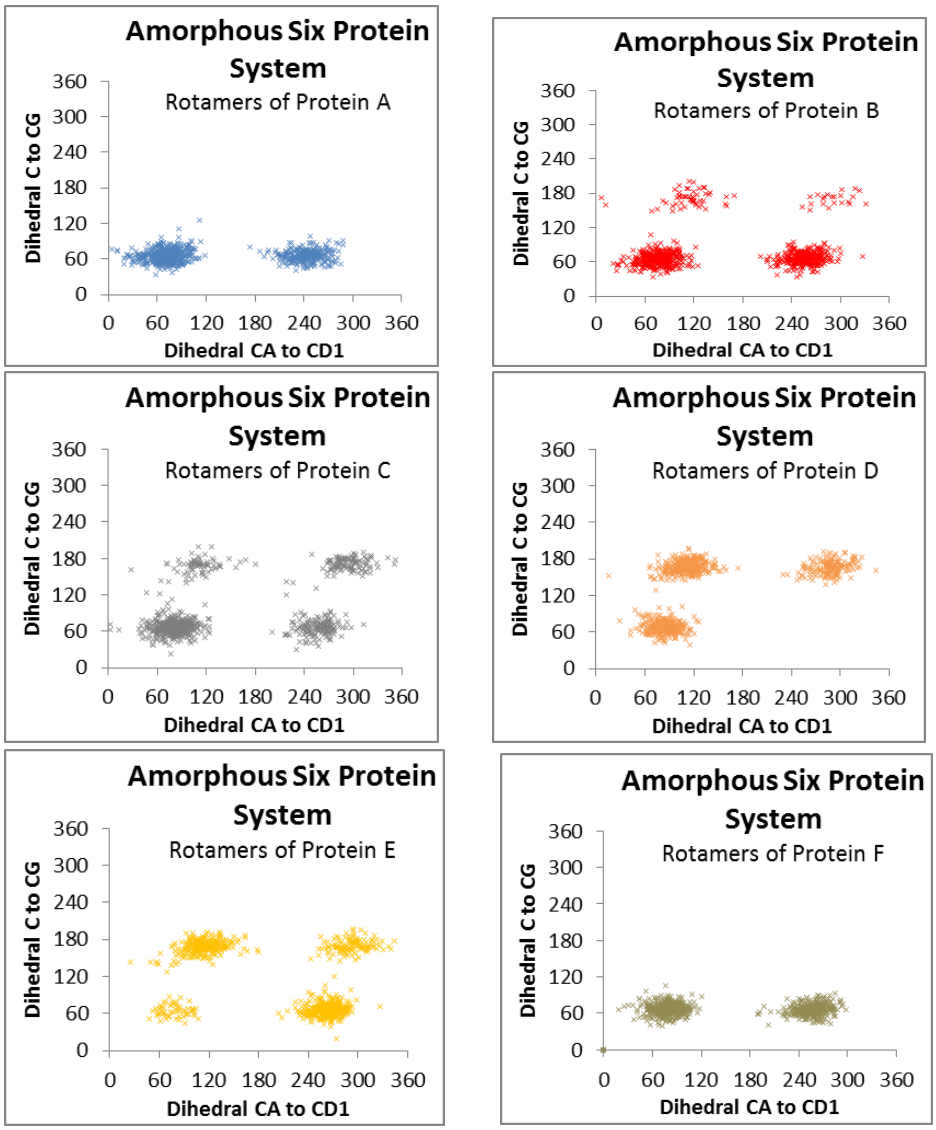

Figure 107 – Amorphous Six Protein System Rotamer Response. The centre for each is approximately (70,65) and (245,65) for Tyr A. Tyr B has approximately (70,65),(260,65), (110, 180) and (290,175). Tyr C has (70,65), (250,65),(110,175) and (290,170). Tyr D has (80,65),(110,175) and (290,170).). Tyr E has (70,65), (250,65),(110,175) and (280,170). Tyr F has (70,65) and (250,65).

The Tyr positions shown in Figure 107 demonstrate that proteins C and E have a preference towards all four rotamer states which would be expected from a monomer/ amorphous aggregate system. Tyr B has a distinct preference towards states 1 and 2, but occupies 3 and 4 occasionally as expected from a Tyr side-chain that has minimal external interactions. The graphs depict that Tyrs A and F have a preference for occupying states 1 and 2.

Tyr A is being influenced by its surroundings causing it to stay in states 1 and 2. Tyr F also has a sensible result as at 30ns it can be seen interacting directly with the

aggregate, holding it in position. Protein D shows a preference for occupying states 3 and 4 as expected for a Tyr being influenced by its surroundings as seen in Figure 106 where Tyr D is seen constantly in close proximity to other proteins.

This system would benefit from longer trajectories to verify these rotamer preferences are accurate, as it would be expected that a longer trajectory would allow more of the proteins to show Tyr movements into all 4 rotamer states as 30 seconds is probably not long enough to fully explore the movement patterns. Despite this, the rotamer characteristics and protein positioning in Figure 106 do adhere to the expectations created by previous trajectories.

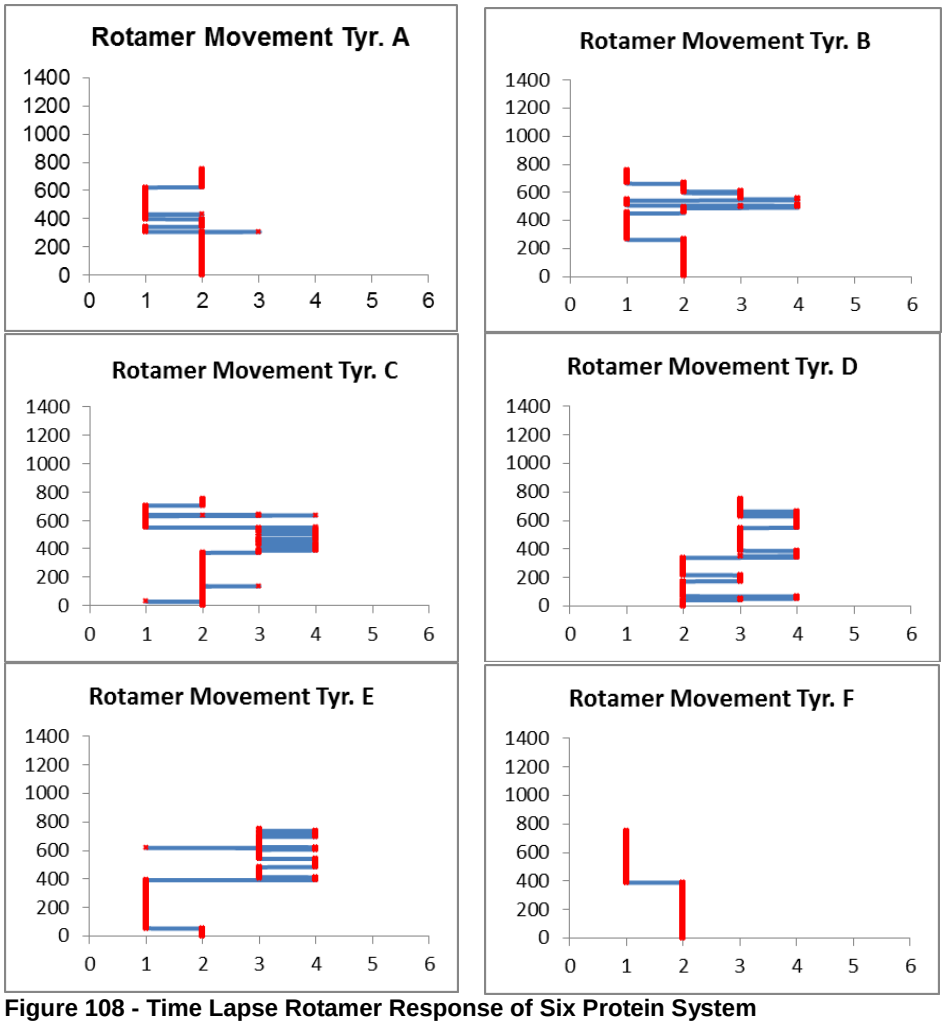

Figure 108 - Time Lapse Rotamer Response of Six Protein System

As there are only 750 frames (30ns) for this trajectory, it is not as easy to establish behavioural patterns within the system (Figure 108). Tyrs A and F appear to have the results expected, as they are not able to move freely.

Tyr B has some freedom to move and as such shows a preference towards occupying states 1 and 2 due to the restrictions, but does occasionally occupy states 3 and 4 as expected for a monomer / amorphous aggregate. Tyrs C and E initially prefer to be in states 1 and 2 but as the interactions between the proteins become more intense through aggregation, there is a shift in preference as they start occupying states 3 and 4 more readily. Protein D has one of the most interactive Tyr side-chains as it is always in contact with another protein in the aggregate and as such has a clear preference towards states 3 and 4 but is not being restricted.

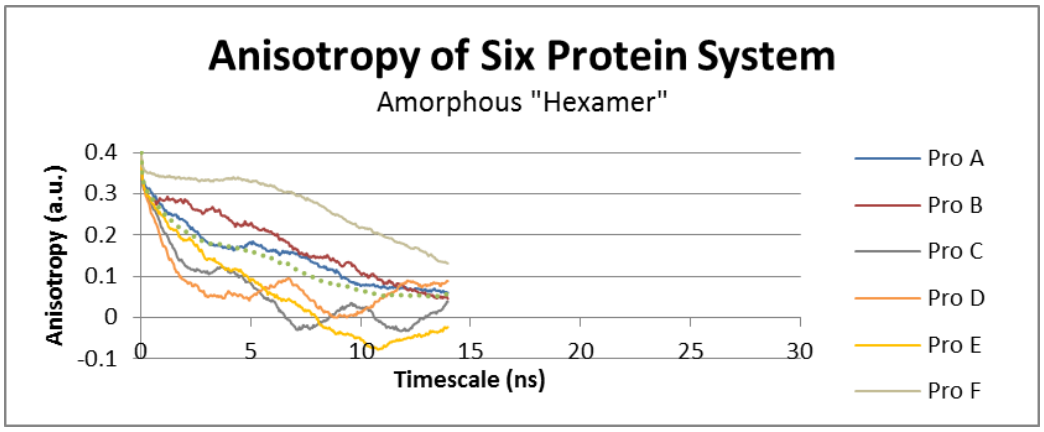

Figure 109 - Simulated Anisotropy of Six Protein System. This graph shows the simulated anisotropy of both Proteins A (blue), B (red), C (grey), D (orange), E (yellow) and F (tan) as well as the average (dotted green).

Figure 109 shows the calculated anisotropies from this simulation, using a maximum correlation time of 14ns (the total trajectory duration is only 30ns). Proteins A, B and F have short lived initial decays due to their Tyr movements and have a slow relaxation period. This is reasonable as proteins A and B spend most of the trajectory as part of the tetramer and therefore have a slow rotation. Similarly, Protein F spends the first part of the trajectory being part of a tetramer and then being part of dimer and is stuck in the middle of the hexamer aggregate when it starts to form before splitting. As such, Protein F has limited movement which is shown in the slow relaxation to a nonzero plateau value.

Proteins C and D have relatively quick initial decays which level out at around 0.1 initially at a correlation time of around 4ns, which is likely due to the rotamer state movements discussed above. Despite this the system still shows characteristics of an aggregate forming as the secondary decay shows some complex behaviour on

its decay to 0 at a correlation time of 6ns for C and 9ns for D. This monomer like response could be due to the shorter time window for analysis and due to the rotation of both proteins seen in Figure 106.

Protein E remains a part of the tetramer throughout the whole trajectory post aggregation and this is reflected in the anisotropy decay curve as it has a relatively long lived initial decay (due to the Tyr side-chains ability to move) followed by a slower relaxation time (that is due to the slow movements within the aggregate) that decays to 0 at a correlation time of 8ns.

6.5.1. Best Fits

There are two best fit anisotropy graphs for the amorphous hexamer aggregate seen in Figure 111 and Table 11, the first has a significantly better correlation fit of 0.992 and has a larger contribution of 0.272 for the bulk aggregate rotation compared to the smaller 0.098 for the Tyr movement. It has an r_∞ value of 0.03 and τ_r values of 0.112ns for the Tyr side-chain and 5.674ns for the bulk aggregate.

The second shows a weaker but still acceptable correlation of 0.959 and has a significantly higher contribution of 0.325 for the Tyr movements, and a more insignificant 0.025 contribution from the bulk aggregate. This is logical as the proteins will be unable to move as freely as they are part of a large aggregate in a small waterbox. Furthermore, the τ_r values appear more reasonable at 25.183ns and 2.897ns for the bulk aggregate and Tyr respectively. These are preferable results as a large aggregate in a small waterbox would be expected to have a slower rotation than the smaller aggregates discussed previously. The Tyr rotation is slow as it spends long periods spent stationary in a single rotamer state (Figure 108.)

These rotational times for the second fit are reasonable as they are part of a large aggregate in a small waterbox. The aggregate is long and thin, unlike the beta-sheet hexamer below which is tightly compact. This implies that the amorphous aggregate would have a significantly slower and more complex rotational time when compared to the beta-sheet hexamer.

Never the less, these results seem reasonable as the rotational speeds are slow and the anisotropy decay has a relaxation period approximately double that of a

monomer. Furthermore, the reason for the decay to 0 for the r_∞ value is likely due to the presence of dimers in the system and the proteins inability to fully aggregate.

6.6. $A\beta_{1\text{-}42}$ Amorphous Aggregates Comparative Results

Simulation Name	Species and Decay Type	$r_{\infty T}+r_{\infty B}$	$r_{oT}-r_{\infty T}$	T_T (ns)	$r_{oB}-r_{\infty B}$	T_B (ns)
Three Protein System	3 Monomers, 2 Exp.	-0.02	0.37	2.27	0.05	23.08
(No Agg. No Ions)	3 Monomers, 1 Exp.	0.01	-	-	0.39	2.44
Three Protein System	3 Monomers, 2 Exp.	-0.04	0.20	0.81	0.24	7.47
(No Agg. Ions)	3 Monomers, 2 exp (r_∞=0)	0.00	0.13	0.36	0.27	3.89
	3 Monomers, 1 Exp.	-0.01	-	-	0.41	2.96
Four Protein System						
(smallest w.b.,	Inf. tetramer, 2 Exp. 1	0.00	0.08	0.04	0.32	5.21
No Ions)*	Inf. tetramer, 2 Exp. 2	0.01	0.11	1.23	0.28	4.951
Three Protein System						
(Amorph. Dimer	Di. & Mon. 2 Exp.	0.01	0.13	0.24	0.26	6.37
& Monomer, No Ions)	Dimer 2 Exp.	0.02	0.09	0.08	0.29	7.48
Four Protein System	4 Monomers, 2 Exp.	0.00	0.14	0.44	0.26	4.60
(2 dimers, small w.b.,	2 Dimers, 2 Exp. Fit 1	0.00	0.32	1.01	0.08	7.97
No Ions)	2 Dimers, 2 Exp. Fit 2	0.02	0.26	0.72	0.12	4.00
Six Protein System	Tet. & Dimer. 2 Exp. Fit 1	0.03	0.10	0.11	0.27	5.67
(Tetramer/dimer)	Tet. & Dimer. 2 Exp. Fit 2	0.05	0.33	2.90	0.02	25.18

* see Appendix 5.6 for results of Inf. Tetramer due to a small waterbox.

Table 11 – $A\beta_{1\text{-}42}$ Amorphous Aggregates Anisotropy Best Fit Variables. W.B is an abbreviation of waterbox.

The amorphous systems are difficult to analyse due to the complexities created by including the aggregation and stabilisation processes in the analysis (much like the current experimental method used for anisotropy seen in chapter 3). As such, the variables used to create the fits are less reliable than that of the beta-sheet aggregates. Nevertheless, a pattern can be seen forming when poor fits are ignored for example, the first and last results are ignored as they have insignificant contributions.

Simulation Name	Correlation
3 Monomers, 2 Exp.	0.937
3 Monomers, 1 Exp.	0.947
3 Monomers, 2 Exp.	0.992
3 Monomers, 2 exp (r_∞=0)	0.981
3 Monomers, 1 Exp.	0.97
Inf. tetramer, 2 Exp. 1	0.989
Inf. tetramer, 2 Exp. 2	0.973
Di. & Mon. 2 Exp.	0.977
Dimer 2 Exp.	0.983
4 Monomers, 2 Exp.	0.989
2 Dimers, 2 Exp. Fit 1	0.985
2 Dimers, 2 Exp. Fit 2	0.987
Tet. & Dimer. 2 Exp. Fit 1	0.992
Tet. & Dimer. 2 Exp. Fit 2	0.959

Table 12 – $A\beta_{1-42}$ Amorphous Aggregates Anisotropy Correlations of fits [168].

The monomer systems with an acceptably sized waterbox tend to have a bulk aggregate τ_r value of 2.4ns-3.89ns, which is faster than the best fit associated with the flat-sheet dimer (see next chapter), which has a τ_r value of 4.9ns as. They also rotate more slowly than the $A\beta_{1-40}$ monomers likely due to the higher concentration [39] and longer proteins analysed in this chapter.

The dimer systems tend to have a τ_r value of 6.4ns-7.9ns, which is slower than that of the beta-sheet dimer aggregates. These results are reasonable as the aggregates are not fully formed and are not as tightly compact. As such, the amorphous dimers will be larger aggregates than their beta-sheet counterparts and therefore will rotate more slowly [112]. The $A\beta_{1-40}$ amorphous dimers rotate faster than these as expected as they are slightly smaller and aggregate more readily.

When the dimer-monomer system is compared to the two dimer system, the dimer-monomer system has a slightly faster rotation associated with it, as the monomer in the system will rotate faster than the dimer, affecting the anisotropy curve (simulating a multi-species anisotropy system). When the monomer is removed from

the averaging for the decay, the resulting τ_r value for the anisotropy fit (7.5ns) is similar to the first τ_r value of the two dimer system (7.9ns). This seems reasonable for this system and also shows the impact of multiple species being in one system, as the presence of the monomer appears to speed up the average Tyr response within the system.

Finally, the six protein system has two very different results associated with it, and as stated above, the second result is more physically reasonable. This is because of the small waterbox not allowing the large aggregate to move around freely.

The Tyr residue rotational times adhere to what is seen previously. The first system has no movement from Tyrs B and C and some movement from Tyr A, which creates a slow moving rotational time of 2.27ns (potentially a little too slow but still follows the general pattern.) The second system has a fair bit of rotamer movement for A and B with limited movement in C giving a rotational time of 0.24ns. The third system has a lot of movement from Tyrs A and C with less for Tyr B, which is also reflected in the rotational times of 0.81ns or 0.36ns. The original τ_T value for the fourth system was far too short to be considered correct, so a second fit was created and though it has a larger error associated with it, it is still within the accepted range (0.973) and gives more reasonable results. It shows a similar backbone rotational time and a 1.2ns τ_T value which is reasonable as the Tyrs do not move between rotamer states as readily in this trajectory. The fifth system has an analysis before and (as much as possible) after aggregation. On average there is more movement pre-aggregation than there is post aggregation, which is reflected in the rotational times in the table above which are 0.44ns and 1.01ns/72ns respectively. Finally, the last trajectory has fast moving Tyr residues, which is reflected in the τ_T value 0.11ns. This result follows the pattern but is likely too short to be the true value; this is probably related to the short length of the trajectory. The second fit had already been ignore due to put backbone rotational time, but can also be ignored due to its incredible fast Tyr rotational time too.

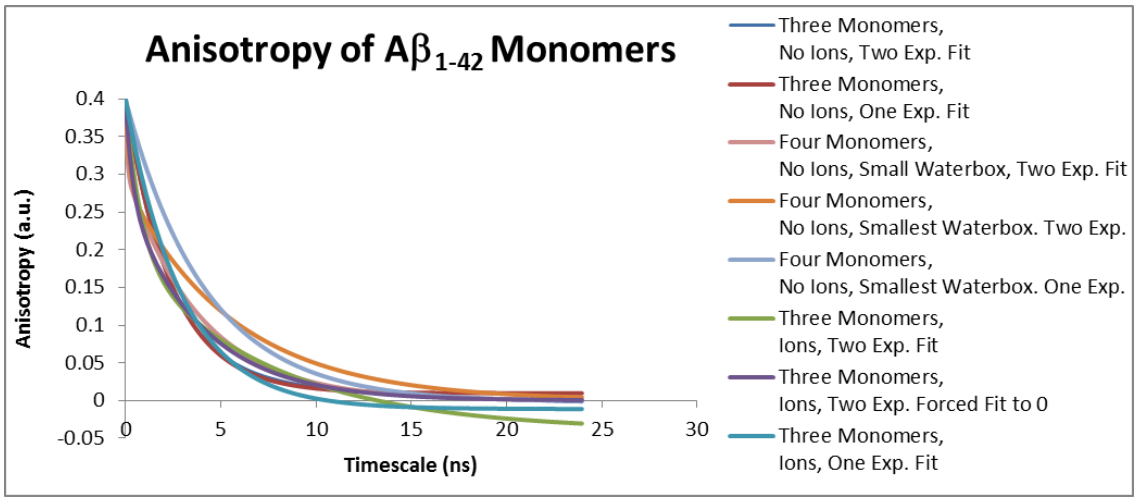

Figure 110 – $A\beta_{1-42}$ Amorphous Monomer Best Fit Graphs

As expected, Figure 110 shows that all monomer proteins behave in a similar manner as they decay rapidly in the beginning within the first 5ns of the correlation and the variation seen is due to varying levels of rigidness in the Tyr movements as depicted by the rotamer graphs [112]. The two curves with the slowest initial decay (orange and light blue) both have extremely small waterboxes, which hinders the proteins rotation due to the lack of space and as such are expected to take longer to plateau [112] [163].

The other monomer trajectories all show similar results with only small variations created from the unique environments of each of the monomers, which is caused by the random nature of the NAMD calculations [173]. They also show slightly slower decay times than a single monomer system (see Chapter 5.9), this is because there are multiple proteins in each system which will interact and affect the overall rotational time of the monomers. This is further supported as the curves take longer to plateau at a value of 0 for the four monomer systems, when compared to the three monomer systems [112].

Although a lot of these monomers do not change conformation (which is possibly a sign of misfolding [172]). There are still some that change conformation and do not aggregate. Regardless, the results we see for the anisotropy are still sensible [112] [163]. There is also no guarantee that this change in conformation was needed for the aggregates seen below in Figure 111.

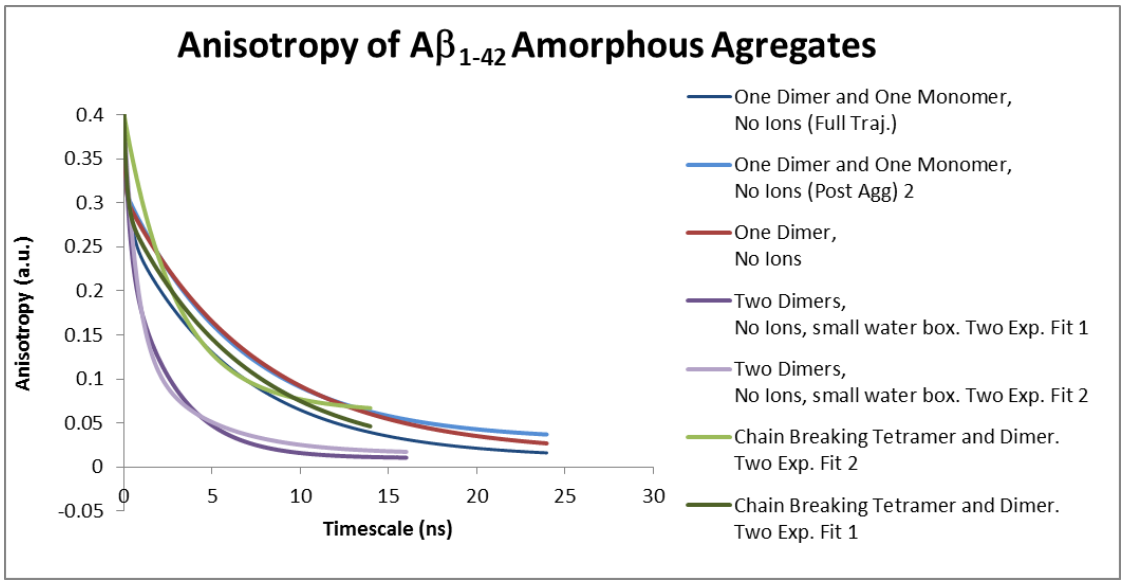

Figure 111 – $A\beta_{1\text{-}42}$ Amorphous Aggregates Best Fit Graphs

The trajectories that involve amorphous aggregation are in Figure 111 and also show promising anisotropy decays. The results are colour coded to help distinguish when more than one fit is associated with one system. The blue curves show the results for the system that contained a dimer and a monomer. The darker blue curve depicts the results for the full trajectory (which includes before aggregation occurs) and it has a significantly faster decay and a lower r_∞ value.

The light blue decay shows the results for after the dimer has formed and shows a slower decay towards 0 as expected from literature [112]. When the monomer is ignored and the average of the dimer is taken, the resulting graph (in red) shows an almost identical decay curve, but has different fitted variables associated with it, due to the effects of the monomer.

As the single monomer does not affect the average decay curve significantly, it suggests that the aggregation process has a greater effect on the curve. This has been seen in the experiments as the aggregation clearly affected the anisotropy as the aggregates increased in size, the second lifetime become more dominant (Chapter 3.3) [112] [167]. This is confirmed when the full trajectory and the post-aggregation trajectory are compared, which are different due to the proteins moving in different ways.

The dark and light purple graphs depict a two dimer system, which have very similar results. The subtle difference in these two best fit curves is impacted by significantly

different variables used for fitting (see Table 11.) The variables associated with the dark purple fit follow the pattern that is forming form the results, as they show an aggregate of a more appropriate size relative to the monomer results. Regardless, both graphs have a significantly faster decay than expected when compared to the dimer-monomer system discussed above.

Firstly, this is due to the smaller range of results available for analysis, as can be seen in the shorter correlation time available, but is also due to the two dimer system being analysed before the aggregates starts to form. This is unavoidable due to the length of the trajectory causing the early stages of the analysis window to include the erratic movements of the proteins forming the dimers. As explained previously, this will affect the anisotropy decay, making the curve decay to 0 much more readily. These results further show the complications within the experimental anisotropy method being used currently as aggregation occurs during the anisotropy analysis.

The results in green depict the six protein system which almost instantaneously forms a dimer-tetramer system, which begins to form a hexamer before splitting off again into a different dimer-tetramer system. As such these best fit graphs show significantly slower decays than the smaller aggregates [112] [167].

6.7. $A\beta_{1-42}$ Monomers and Aggregation Conclusions

In conclusion, the overall shape of these proteins is very similar to that of the $A\beta_{1-40}$ simulations showing very few differences with regards to the alpha helical structure found in the central region of the proteins and near the tails [171] [174]. These helical structures do appear to unravel sometimes (and more commonly in aggregated proteins [172]). Furthermore, when part of an aggregate, there appears to also be a small probability for beta-sheets to start forming, though within the scope of these simulations it is still far from the shape suspected to be required for fibril formation and growth [63] [172]. Furthermore, as with $A\beta_{1-40}$, there is no presence of the 5^{th} or 6^{th} rotamer state, with rotamer states 3 and 4 being more dominant in aggregated proteins, further suggesting that the interactions are what cause this stability for holding the 3^{rd} and 4^{th} states.

There is a general increase in the τ_r values associated with bulk aggregates as they increase in size as seen previously [112] [163]. As discussed in the previous

chapter, this can be directly related to the changes in the decay curves. These changes are caused by the Tyr side-chain movements (as shown by their rotamer movements,) which causes changes in the initial decay. The slowing rotation of the entire aggregate (due to its increase in size seen in the trajectory images) also causes changes to the relaxation period leading to a rising plateau level. This can be seen throughout all three MD chapters and is supported by the results in the MC simulation results [112].

These connections help strengthen the understanding of what affects experimental anisotropy decays and how these simulated anisotropy decays relate to those experiments. These results are also comparable to that of the beta-sheet structures in chapter 7, with some variances that can be easily explained. This further strengthens the reliability of the results and further shows that rotamer states 5 and 6 only appear in the more rigidly aggregated beta-sheet models (see chapter 7). The results also potentially indicate that the protein misfolding plays a part in the aggregation [172], as the proteins did not readily aggregate when the horseshoe motif did not appear to be readily forming [63] [172].

Though it is not clear from the results shown here whether protein misfolding occurs prior to or during aggregation, it is clear that it must occur for the protofibril structures (see below) to form [63]. Some trajectories show an increased ability for the proteins to aggregate when their conformation has folded into other shapes [172]. However, many of the simulations demonstrated the fact that an amorphous aggregate would form with and without the “misfolded” shape. These results suggest that misfolding and amorphous aggregation occurs simultaneously in the early stages of the aggregation process, though significantly longer simulations would be required to justify this, as it is possible that one must occur before the other. For example, amorphous aggregates form first, then misfolding leads to the protofibril stacking or the misfolding occurs first then the aggregation occurs. Misfolding occurring after amorphous aggregation is supported by work by Strodel et al where they also saw aggregation preceding conformational changes [176].

7. Results and Discussion: MD Beta-sheet Aggregation for Aβ1-42

This final chapter shows the MD results of the trajectories of $A\beta_{1-42}$ proteins which have either begun to formed or have formed a protofibril [63]. These simulations follow the same pattern as the previous two chapters, using MD and VMD to extract the structural changes, Tyr residue position and overall aggregate shape. Each simulation in this section was allowed to run for a minimum of 40ns and the full protofibril structure was run for 200ns without ions and 110ns with ions.

The original structure used for these simulations was taken from work by Waelti et al (2NAO.pdb) [63]. This system is originally made up of six $A\beta_{1-42}$ proteins configured into the shape of a basic proto fibril and is considered to be one of the stable conformations. Charmm22 and Charm27 hybrid forcefield and TIP3P water model were used [124] [125] and the visualisation of each of the simulations was created through VMD [146].

The systems discussed in this chapter have been created by removing different proteins from the hexamer protofibril structure ranging from dimers to tetramers, in an attempt to discover possible aggregation pathways associated with these proteins. As the proteins must aggregate together and have a specific conformation to repeatedly stack to form the fibrils [50] [63], one (or more) of these dimer-tetramer structures could be part of the aggregation process. These systems will be studied in a similar manner as the previous chapters; studying how the proteins move, noting conformational changes, or any other features, such as Tyr residue position, dihedral angles (rotamer states) and freedom as was done in other work [44]. As has been seen in the previous chapters, the combination these can reveal important information that could be potentially linked to experimental work [44] [112]. Simulated anisotropy models are then created and compare to both the experimental work and the other Aβ simulated anisotropy results. This chapter is a detailed study of how the early stages of $A\beta_{1-42}$ fibril formation may begin to occur, as well as reveal information about the basic protofibril structure.

7.1. Flat-sheet Dimer

A simulation of a potential dimer structure for $A\beta_{1-42}$ is illustrated in Figure 112. The simulation begins with two proteins that have aggregated together to form a “plate-like” structure used as the foundation for fibril stacking [50] [63]. This structure could potentially aggregate with another dimer of the same shape; stacking one atop the other to create a tetramer as seen in Figure 130. This process could repeat to form a hexamer (Figure 139) and continue to repeat forming larger aggregates until there are no monomers left in the system [50]. This shape is supported in the literature: beta-sheets begin to form when enough of these structures stack and forms the prefibrilar assemblies (protofibrils) discussed in Figure 6 and would be the basic building block for the creation of protofilaments [50]. This dimer may not necessarily occur during the aggregation process, another example pathway that could create the prefibrilar assemblies, would be amorphous aggregates that misfold to form a hexamer prefibrilar assembly. The time scales of MD do not allow for us to obtain this information and there are many different potential pathways that could be responsible for the beta-sheet formation.

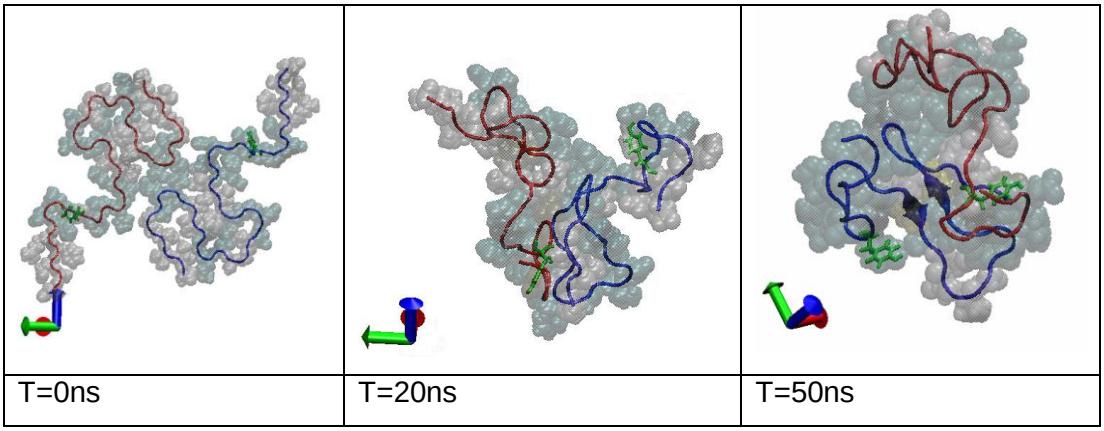

Figure 112 – Flat-sheet Dimer Stabilization. The panels shows the position of protiens A (blue), B (red), with Tyr side-chains highlighted (green) with the The VDW interactions indicated by the transparent spheres: Purple denotes alpha-helix structure, red denotes pi-helix, white denotes a coil, cyan denotes a beta turn and yellow or tan denotes beta-sheet structures. The beta-sheets are further denoted by the arrow-like shape with the proteins.The first panel shows the starting postion of the proteins. The middle panel shows the trajectory at 20ns and the right panel shows the system at the end fo the trajectory at a time of 50ns.

In theory, if this dimer is the foundation of the aggregation process, it must be in a state of equilibrium and therefore the conformation of the aggregate should remain stable. However, as the trajectory progresses the dimer begins to fold in on itself,

burying its hydrophobic regions showing structural similarities to that of the amorphous aggregates seen above [122], implying that this is an unstable structure and is unlikely that the aggregate would readily form like this.

This change in conformation begins to happen instantaneously and as seen in Figure 112 by T=20ns monomer B has already folded into monomer A. Beta-sheets begin to form instantly within the individual proteins themselves [171], though the first beta-sheet does not become stable until the later stages (characterised by the arrows in the blue protein at 50ns). These beta-sheets form due to the close proximity of the backbone allowing the anti-parallel beta-sheets to form in both protein A and B (but there are no beta-sheet interactions between the two proteins) [49], by the end the only stable beta-sheet present is in protein A between residues Val_{18} and Phe_{19} and Ile_{31} and Ile_{32}.

The hydrophobic residues continue to bury themselves away from the water molecules throughout the rest of the trajectory and reach the final position shown in Figure 113 [122].

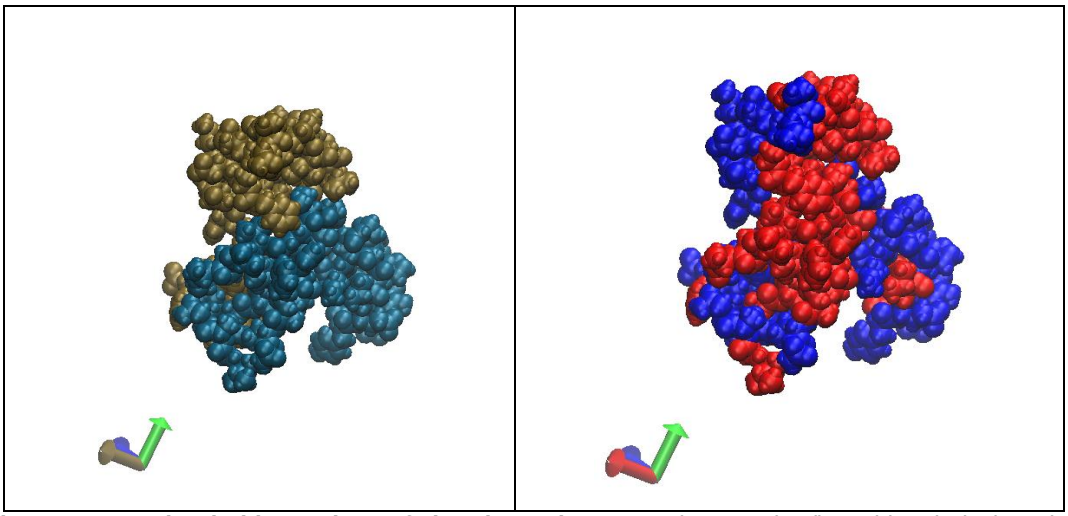

Figure 113 - Hydrophobic Sections of Flat-Sheet Dimer. Proteins A and B (in Gold and Blue) on the left and the hydrophobic sections (in red) are shown against the hydrophilic (blue) sections on the right at T=40ns.

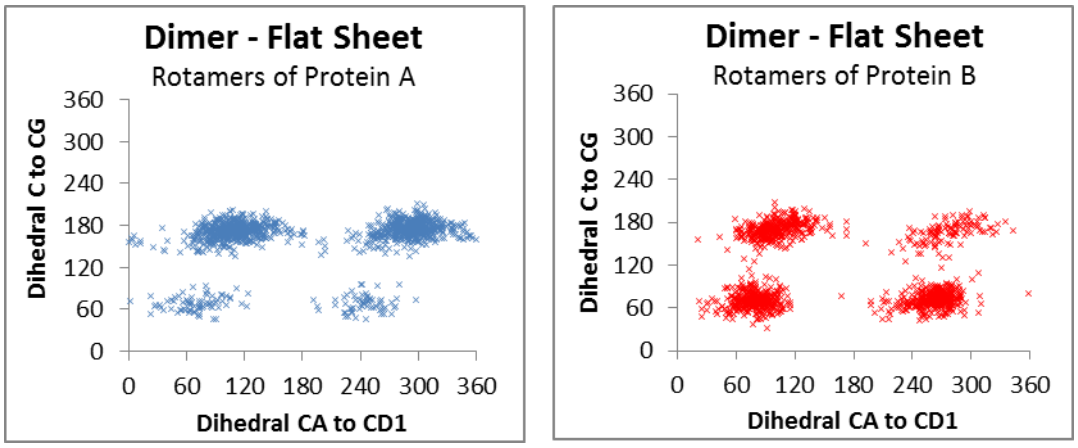

Figure 114 - Flat Sheet Dimer Rotameric Response. The two graphs depict the orientations that the Tyr side-chains of monomer A (blue) and B (red) favour during the 50ns trajectory. The centre for each is approximately (60,60), (240,60), (120,180), (300,180) for Tyr A and (80,70),(260,70) (100,170), (395,175) for Tyr B.

The Tyr residue's rotamer conformations are shown in Figure 114. These results indicate that both Tyr side-chains in protein A and B have the same four rotamer forms seen in the amorphous aggregates. However, Tyr A appears to have a larger affinity towards states 3 and 4 and Tyr B shows a preference to states 1,2 and 3.

As discussed in Figure 149 and Figure 150, these affinities to certain rotamer states occur due to the subtle differences in the environment surrounding the Tyr side-chains, through the interactions with the aggregate backbone and the local surrounding residues. Figure 112 illustrates that protein B has more restrictions than A, though the state movements suggest it is a minimal difference.

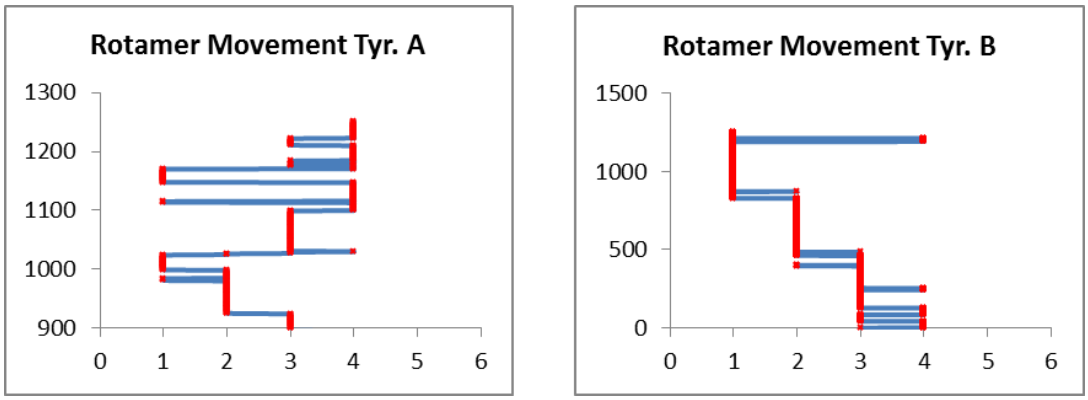

Figure 115 - Tyr movement between States of Flat Sheet Dimer. These graphs show the Tyr side-chain movements between the different states over the course of the trajectory with the x axis showing the different states and the y axis showing the frame within the trajectory.

The graphs in Figure 115 show that Tyr A moves between the four states in a more erratic manner than Tyr B. Once the proteins have aggregated more closely together Tyr A shows a preference to states 3 and 4. This is because the local environment is close to the Tyr side chain, influencing it to twist. It should be noted that the Tyr side-chains move from state 1 to 2, 2 to 3, 3 to 4 and 4 to 1, as expected for the Tyr side-chains.

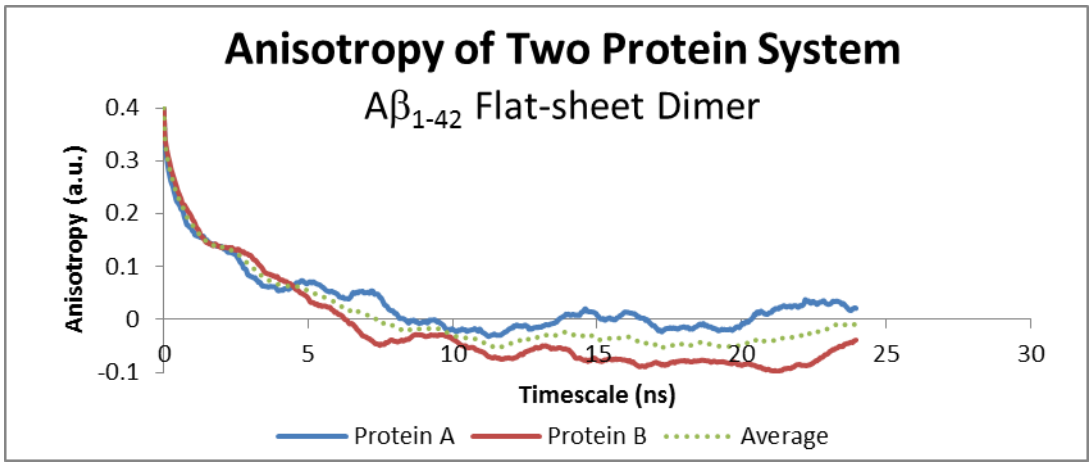

Figure 116 - Simulated Anisotropy of Flat Sheet Dimer. This graph shows the simulated anisotropy of both Proteins A (blue) and B (red), as well as the average that both create (dotted green).

The anisotropy decay of this dimer trajectory is shown in Figure 116. This system starts with the proteins already aggregated, unlike the amorphous aggregates. The system has a short lived initial sharp decay, followed by a slower relaxation period that decays to ~0 as expected from an aggregate. This sharp decay is initially quite

steep but is more shallow at a correlation time of around 1ns which indicates that the Tyrs have less movement available to them than a free moving Tyr, as is seen in Figure 115. This relaxation period is also logical as the aggregate moves more slowly than a monomer.

An early plateau value of 0 usually suggests that there is no aggregation in the system. However, this characteristic is potentially related to the large movements created by the folding of the protein. The flat-sheet configuration is not stable, and as such the proteins try to find a conformation that is more favourable. This causes large movements at the start of the trajectory allowing the aggregate backbone to move more freely.

7.1.1. Best Fits

When fitting the best fit graph to the flat-sheet dimer's average anisotropy of both Tyr side-chains, there are two potential results (see Table 13). The first fit is forced to decay to 0 to allow for ideal results as there should not be a negative r_∞ value. This results in a rotational time (τ_r) of 0.33ns for the Tyr's fast response and 2.56ns for the entire aggregates slower rotation, where both mechanisms have significant contributions (0.167 and 0.233 respectively).

The second graph fit allows the best fit program to take on any values, including r_∞ values of lower than 0. This creates resulting τ_r values of 0.32ns (for the Tyr) and 4.8ns (for the backbone) with contributions of comparable size (0.188 and 0.262 respectively). Despite some minor differences, the two graphs for fitting are similar and both appear feasible as they have correlations of 0.970 and 0.985 for the first and second fits respectively, so the error in the fits is minimal.

The lack of stability here suggests that it may require interaction from other ions or proteins to be stable and be part of the aggregation pathway. There must be external forces maintaining the structure to allow aggregation to occur. This could be due to ions present in the system, or perhaps bonded metal ions as discussed in previously.

7.2. Stacked Dimer

In Figure 117 another potential dimer shape is shown, using a parallel “stacked” formation rather than a flat-sheet like formation. It does not interact with itself through the periodic boundary.

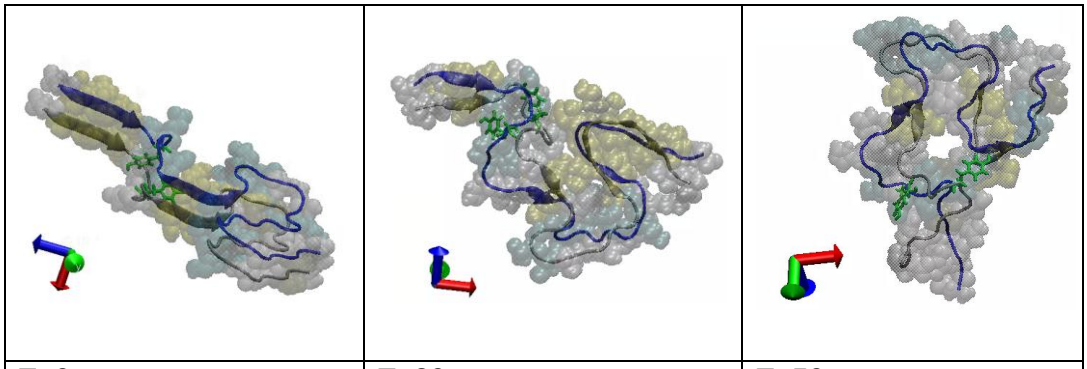

T=0ns	T=20ns	T=50ns

Figure 117 –Stacked Dimer Stabilization. The panels shows the position of protiens A (blue), B (grey), with Tyr side-chains highlighted (green) with the The VDW interactions indicated by the transparent spheres: Purple denotes alpha-helix structure, red denotes pi-helix, white denotes a coil, cyan denotes a beta turn and yellow or tan denotes beta-sheet structures. The beta-sheets are further denoted by the arrow-like shape with the proteins.The first panel shows the starting postion of the proteins. The middle panel shows the trajectory at 20ns and the right panel shows the system at the end fo the trajectory at a time of 50ns.

This structure in Figure 117 appears more stable and is a much more likely candidate for the aggregation from the amorphous structures to the protofibril structures as is seen for Aβ fragments in literature [48] [176] [244]. The stability appears to be due to the beta-sheets present above and below the Tyr residue (in green) [49] [171]. The beta-sheets are indicated by the yellow transparent VDW spheres and the long arrow-shapes in the MD “cartoon” representation. This aggregate holds its shape and does not fold in on itself, unlike the flat-sheet dimer. However, the trajectory shows signs that the structural stability is still lacking (relative to the hexamer protofibril), as the backbone at the head of the protein (above the Tyr’s) start to lose form and is incapable of forming stable beta-sheets.

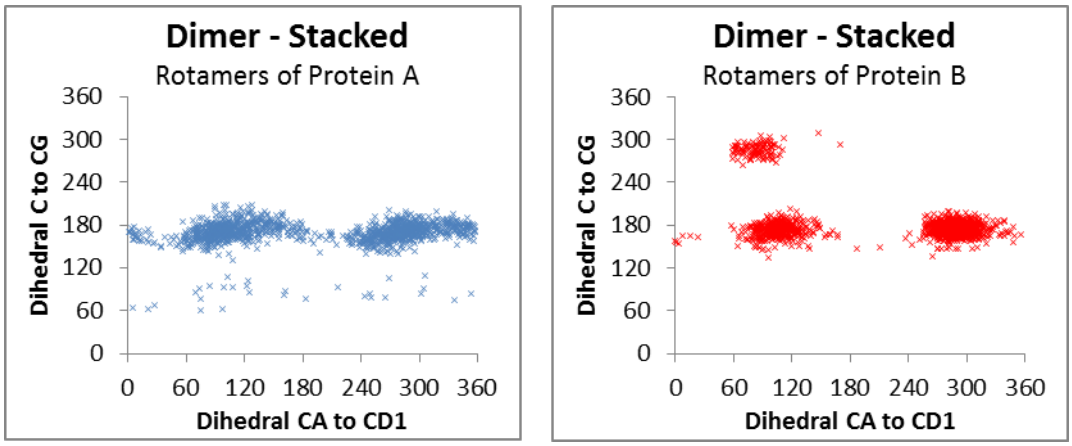

Figure 118 – A Stacked Dimer Rotameric Responses. The centre for each is approximately (110,170) and (290,170) for Tyr A and for Tyr B (100,170),(290,170) and (80,290).

Figure 118 shows the rotamers for Tyr side-chains in the stacked dimer. Both Tyr side-chains have a preference for occupying the third and fourth rotamer states with Tyr A having two main rotamer states with a wide spread occupation across the C to C_G dihedral angle. This could be attributed to the restrictions that can be seen in Figure 117, as Tyr A is interacting with the first few residues in its own backbone. These interactions affect the Tyr by restricting its movement and forcing it to twist into the higher states. This is further supported by the anisotropy data seen in Figure 120 as it shows clear signs of aggregation and a shallow initial decay.

In contrast, Tyr B occupies states 3 and 4 readily and also a new rotamer state (state 5). Based on the Tyrs position seen in Figure 117 it is influenced by the head and tail of the backbone affecting its ability to move allowing it to occupy a new rotamer state, only seen in the stacked structures (see Figure 151.) Furthermore, these rotamers in Figure 118 are more concentrated on the graph with a narrow distribution. The difference seen between the two Tyr side-chains is due to the local environments surrounding them.

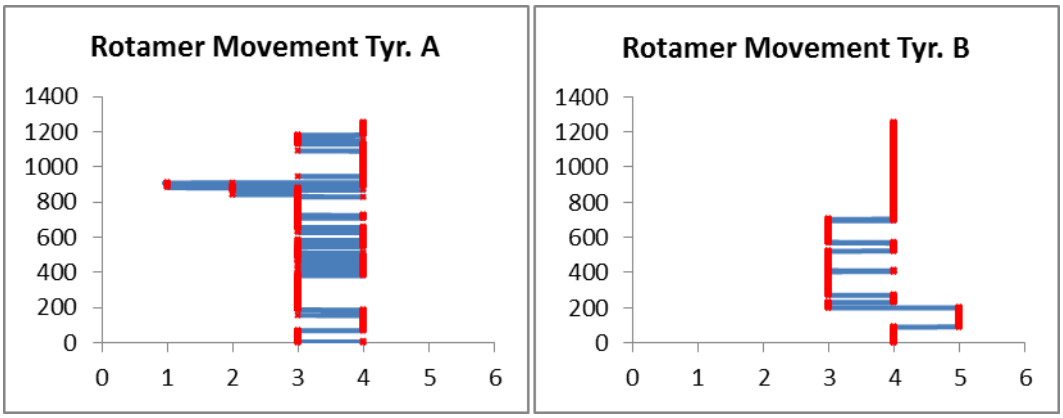

Figure 119 - Time Lapse Rotamer Response of Stacked Dimer.

The evolution of the Tyrs rotamer states can be seen in Figure 119. Tyr A has more variable motion in its C_{α}-C_{D1} angle and almost no movement in its C to C_G angle which is why it remains in states 3 and 4 throughout the trajectory. This shows that the stacked aggregate conformation must be influencing the Tyr side-chain, forcing it to twist along the C to C_G dihedral angle and allowing it to occupy states 3 and 4 readily (Figure 150). Tyr B has less frequent movements between states, as it remains in one state for long periods, although it does have some more motion associated with it as it moves into state 5. This will be due to the surrounding environment influencing its movements.

The movement between rotamer states for both Tyr side-chains adhere to the pattern discussed previously. However, Tyr B also briefly accesses the fifth rotamer state by traversing from rotamer 4 to 5 and back to 3, which is caused by strong local interactions (Figure 151).

Rotamer states 5 and 6 do not appear in any results except the beta-sheet aggregates that have a stacking mechanism in them. This implies that once influenced into favouring states 3 and 4, the Tyr can then further twist along the C to C_G dihedral angle, and begin occupying these previously unseen states 5 and 6 (see Figure 148 and Figure 151.)

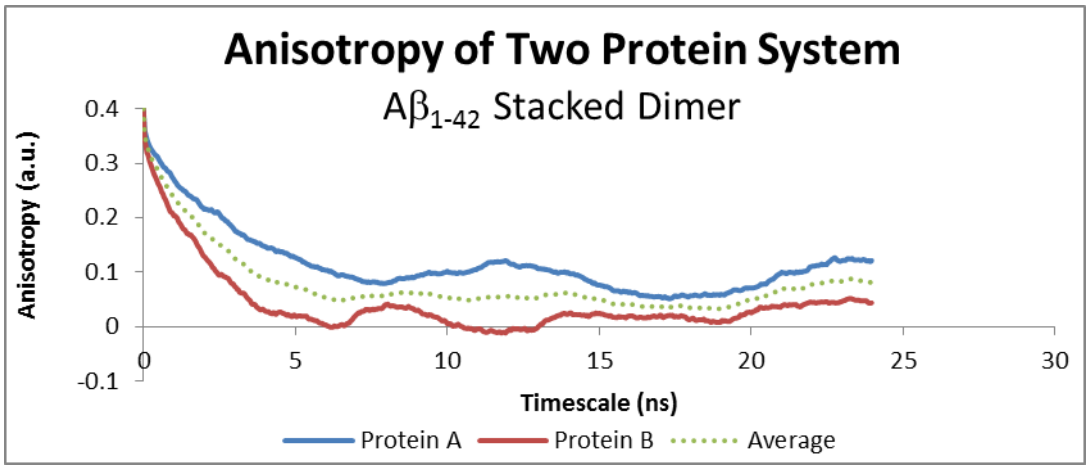

Figure 120 - Simulated Anisotropy of Stacked Dimer. This graph shows the simulated anisotropy of both Proteins A (blue) and B (red), as well as the average that both create (dotted green).

The anisotropy response of protein A has a short lived initial decay followed by a relaxation that plateaus at roughly 0.1, implying it is part of an aggregate. This adheres to what has been stated previously suggesting that Tyr A has limited movement due to its surroundings.

Protein B has a sharper initial decay similar to that of a monomer. This is due to the backbone twisting within the aggregate, creating a larger degree of movement for Tyr B and could also be related to the movement seen in both dihedral angles. The graph then relaxes to approximately 0.01.

The average response shows signs of aggregation as it has a slower initial decay than a monomer, this is then followed by a relaxation time that gives a plateau value of 0.06. The increased rigidity in the backbone creates a smoother average curve as there is less movement from the Tyr movements when compared to the flat-sheet dimer as the folding mechanism allows greater movement from the Tyr side-chains.

7.2.1. Best Fits

The resulting variables for the best fit graph in Table 13 a stronger involvement of the mechanism with the τ_r value that is likely associated with the bulk aggregate rotation. This slow τ_r value of 2.08ns has a contribution of 0.254 and the Tyr's fast response has a contribution of 0.046 and a value of 0.019ns. This difference in τ_r values between the two dimer systems can be explained as the stacked dimer is more compact and therefore will have a faster τ_r associated with the bulk aggregate.

7.3. L-Shaped Trimer

The aggregate shown in Figure 121 has an L-shape structure, which is assumed to form from a monomer aggregating into a dimer rather than multiple flat-sheet dimers stacking to form the protofibril, as was suggested above [63]. The initial structure combines the two beta-sheet simulations seen previously as this system has features from both the “stacked” structure and the flat-sheet structure.

As such, this structure would form by either a monomer aggregating with a stacked dimer or a monomer aggregating with a flat-sheet dimer. This is an unlikely pathway for the aggregation process to take based on the literature [50] [63] and is seen by the unstable nature of the protein in Figure 121. It would be impossible for another protein to aggregate on top to create a fibril-like tetramer. Nevertheless, the resulting anisotropy decays gives a deeper understanding of what they depict and can be compared to the dimer structures [112], as it shares characteristics from both the flat-sheet dimer and the stacked dimer.

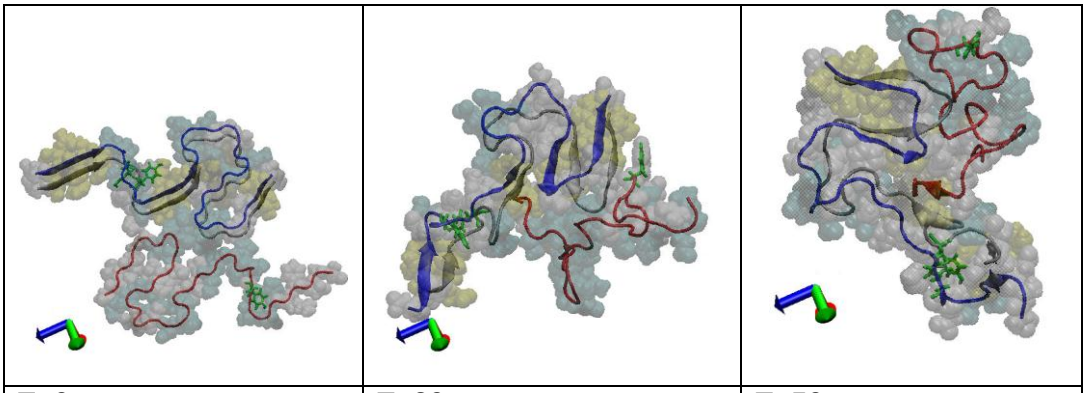

Figure 121 – L-Shaped Trimer Stabilization. The panels shows the position of protiens A (blue), B (red) and C (grey) with Tyr side-chains highlighted (green) with the The VDW interactions indicated by the transparent spheres: Purple denotes alpha-helix structure, red denotes pi-helix, white denotes a coil, cyan denotes a beta turn and yellow or tan denotes beta-sheet structures. The beta-sheets are further denoted by the arrow-like shape with the proteins.The first panel shows the starting postion of the proteins. The middle panel shows the trajectory at 20ns and the right panel shows the system at the end fo the trajectory at a time of 50ns.

As stated previously, this structure requires stability to be a candidate for the aggregation process. At T=0ns the expected stable structure is shown as another protein would aggregate onto this to create a flat-sheet tetramer (see Figure 130). However, once the trajectory begins it is apparent that the structure is not stable.

The beta-sheets are initially between the proteins A and C from Asp_1-Hsd_6, Gln_{15}-Phe_{19} and Val_{40}-Ile_{41}, and end as Phe_4-Arg_5, Ala_{30}-Gly_{33} and Gly_{38}-Ile_{41}. A beta-sheet also forms between protein B and C (Gln_{15}-Lys_{16} in protein C and Gly_{37}-Gly_{38} in protein B). The stacked part loses conformational stability in a manner similar to the stacked dimer; with the tips of the protein backbones losing structural stability at the points where the beta-sheet bonds were not as strong.

The grey protein (C) folds in on itself quickly just like the flat-sheet dimer, due to hydrophobic sections burying themselves away from the water and the hydrophilic sections protecting them as seen in Figure 122 [112].

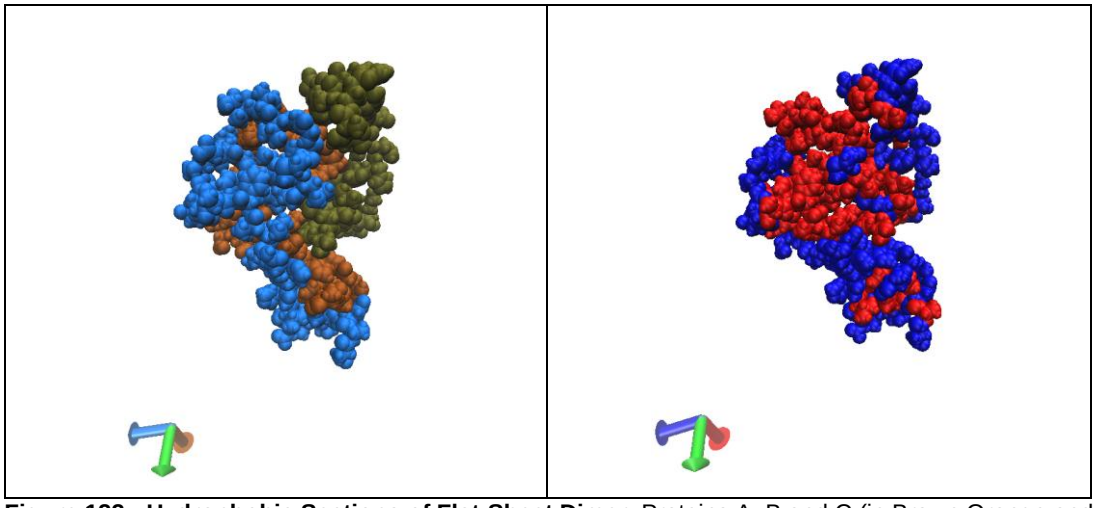

Figure 122 - Hydrophobic Sections of Flat-Sheet Dimer. Proteins A, B and C (in Brown Orange and Blue) on the left and the hydrophobic sections (in red) are shown against the hydrophilic (blue) sections on the right.

The structure loses most of its shape as the trajectory progresses and begins to share characteristics with an amorphous aggregate, though it is more structured than both the flat-sheet and the stacked dimer. This could suggest that as the aggregate gets bigger, it becomes more stable and could promote growth once the aggregate reaches a particular size, which could explain the lag phase observed experimentally in protein fibrillation [44] [50].

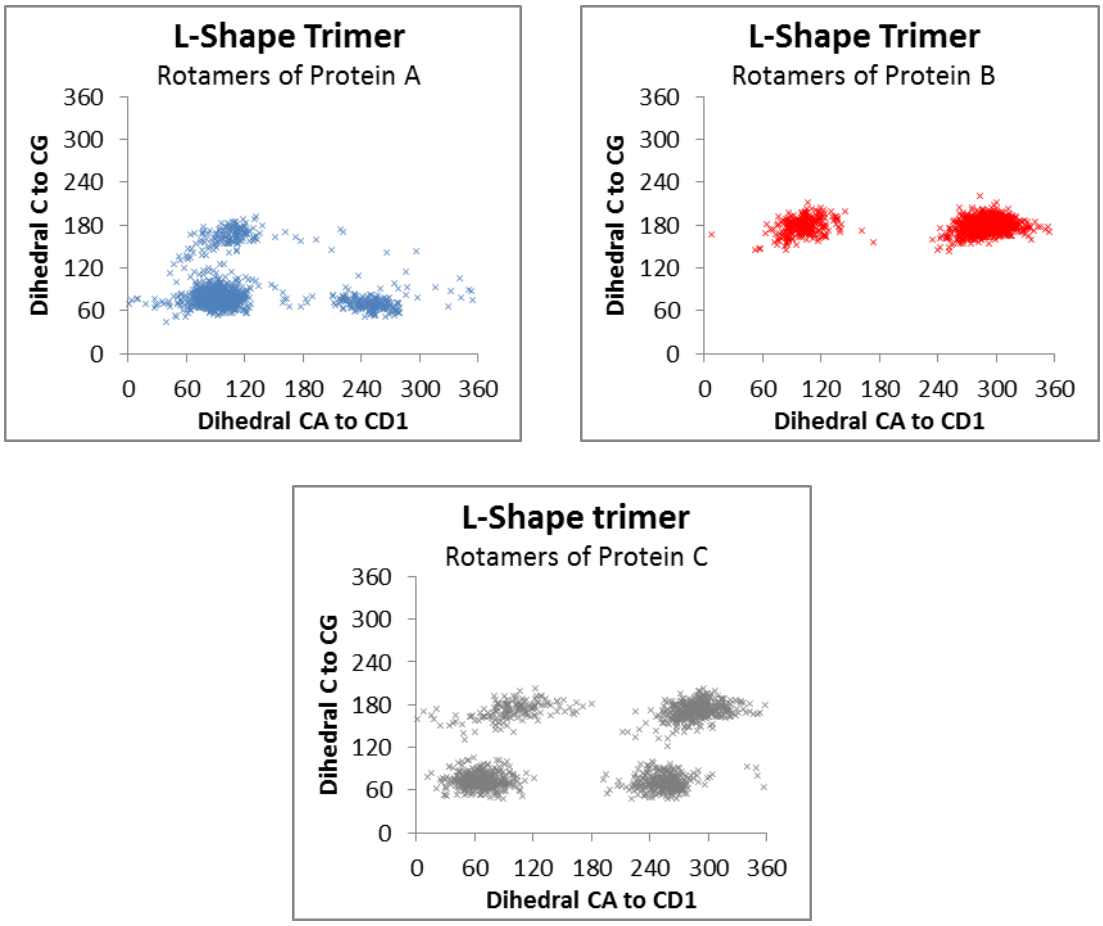

Figure 123 – L Shaped Trimer System Rotamer Response. The central coordinates for Tyr A's rotamer's are approximately (110,65), (250,60) and (110,170). Tyr B has two rotomer state (100,170) and (290,175). Tyr C has more traditional positons (65,65), (250,65),(110,175) and (290,175).

With protein A and B being part of the stacked aggregate they both shows signs that the Tyr side-chains are trapped. Protein A has a preference to occupying the least twisted states (states 1 and 2) and protein B has a preference towards states 3 and 4. This is due to the way the Tyr residues are interacting with each other, as Tyr A is being restricted to states 1 and 2 and Tyr B is being forced into the more twisted states (3 and 4). This is comparable to the Tyr positions in Figure 69. These responses are very similar to that of the stacked dimer. The reason that the responses are different is, firstly, due to random interactions, but can also be due to the interactions with the other nearby proteins causing the Tyr residue to favour different positions due to its local environment, as discussed previously.

In contrast, Protein C has the four rotamer positions, identified previously for monomers. Although it is part of the aggregate, protein C is still freely moving and

spends a significant portion of the trajectory seeking a stable conformation. There are no external interactions affecting Tyr C except the backbone being slowed as part of the aggregate.

Both these effects are seen in previous simulations as protein A and B show similar responses to that of the stacked dimer with some variation that could be attributed to the influences of protein C. Protein C shows results similar to that of the flat-sheet dimer, with some variation attributed to being part of a bigger aggregate and not folding in on itself in the same manner as seen in the flat-sheet dimer.

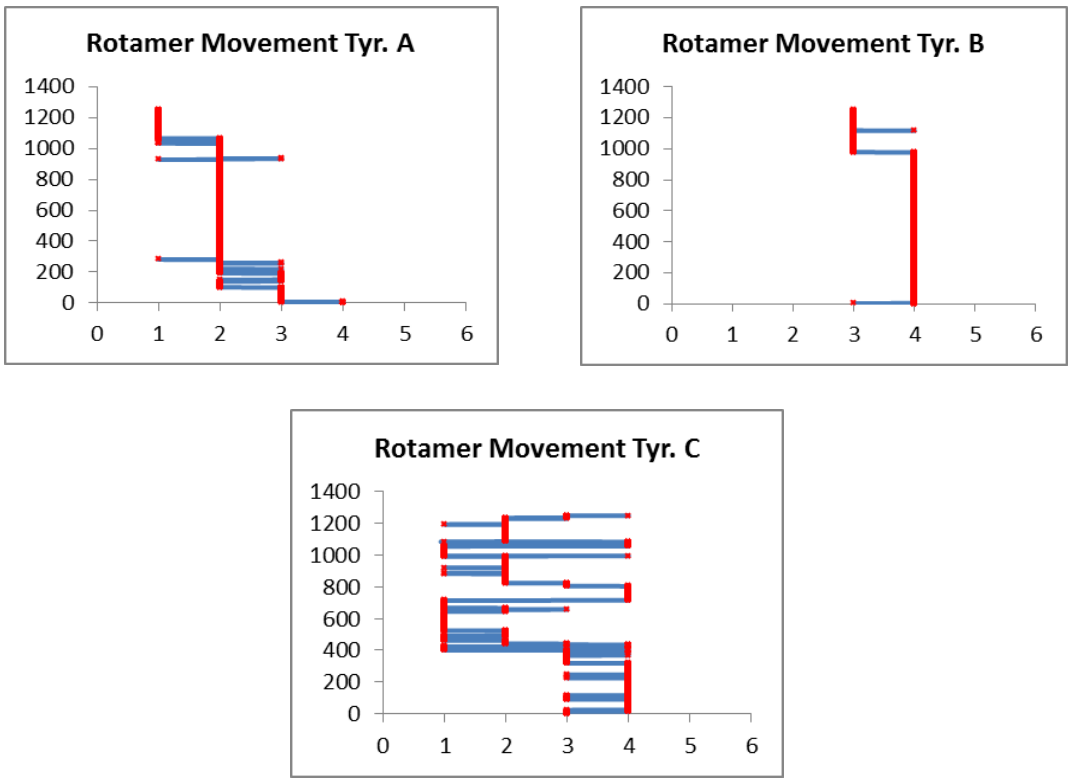

Figure 124 - Time Lapse Rotamer Responses of L-Shaped Trimer.

The early occupation of states 3 and 4 in Figure 124 for Tyr A will be due to its surroundings. Just before 10ns Tyr A's backbone twists in the trajectory, which allows it enough freedom to move into states 1 and 2 and is forced to remain there due to the interactions with Tyr B. Tyr B remains in the states 3 and 4 throughout the entire trajectory due to these interactions as discussed above causing restricted movement. These results are similar to the responses seen in the stacked dimer.

Tyr C has erratic movement due to its freedom, which is similar to what is seen in the flat-sheet dimer as the Tyr's are moving freely with minimal restriction. The response is much more erratic here, which is likely due to having a larger aggregate attached to it.

The L shape requires stabilisation for this system and prevents the fifth and sixth rotamer states from forming. This is due to the influence of the folding mechanism making it unfavourable as the aggregate does not remain as tightly packed.

The external influences of the backbones and aggregate skew the average position of the rotamers when compared to other systems, implying that the external forces are having an impact on the Tyr's movements. Regardless of this, they also adhere to the rules 1 to 2, 2 to 3, 3 to 4, 4 to 1. This includes Tyr C, although it has a single instance of moving from state 1 to 3 which is a frame-rate truncation effect, or an unusual twisting motion.

These results further suggest that the Tyr side-chains likely prefer to move through the states in a certain order, with states 5 and 6 being difficult to occupy as they must be part of a tightly packed aggregate (such as the stacked dimer) to force the Tyr to twist in the manner required (Figure 151.)

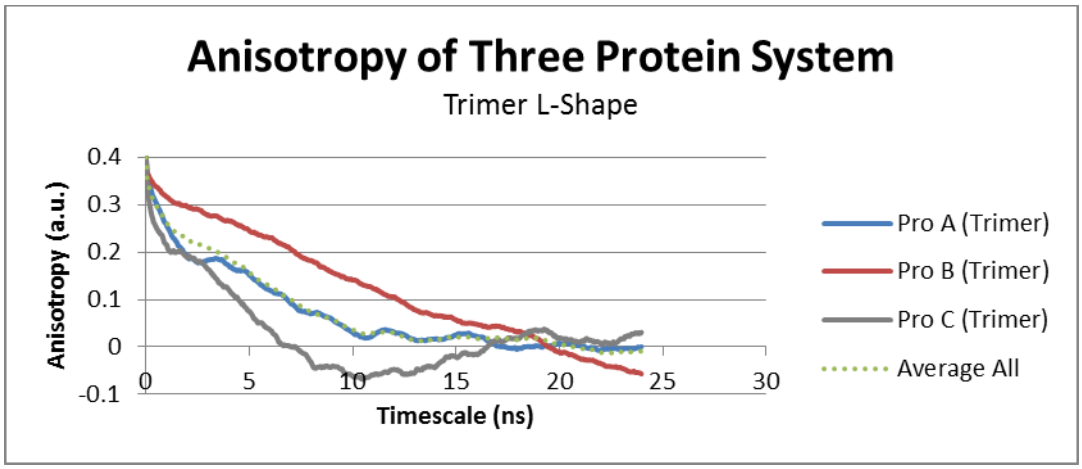

Figure 125 - Simulated Anisotropy of L-Shaped Trimer. This graph shows the simulated anisotropy of Proteins A (blue) and B (red) and C (grey), as well as the average (dotted green).

Proteins A and B simultaneously reach 0 at a correlation time of roughly 18-20ns which is much later than the dimer response that is seen above. Proteins C has a sharp initial decay followed by a slower secondary decay as seen with the flat-sheet

dimer which is likely due to the Tyr's erratic movements. The slower decays from proteins A and B, is due to the lack of movement from their Tyr residues.

When compared to the dimers, protein A has a significantly slower initial decay due to the fact that the Tyr is interacting closely with protein B, which traps it. The response is still comparable to the stacked dimers as it is a slow decay, despite the folding movement, creating an apparent faster rotation.

Protein B shares similar characteristics to that of protein A as it has a significantly slower initial decay due to the Tyr's position between the backbones of protein A and B that traps it, and limits its movement.

As it is in a similar position as the proteins in the flat-sheet dimer simulation, Protein C has significantly more freedom and is the cause of the faster decay to a plateau value of approximately 0. This is a similar response to a monomer, though slower as it is part of a slower moving aggregate. The initial drop followed by a secondary slower drop is either a complexity caused by the involvement of three mechanisms influencing the Tyr or more likely an artefact from the analysis window being relatively narrow. These mechanisms are Tyr side-chain movements, the bulk aggregate rotation and folding mechanism. Despite these complexities the average graph is relatively unaffected and a two exponential fit is adequate.

7.3.1. Best Fits

The best fit graph shows a contribution value 0.34 for slow mechanisms with a τ_r value of 5.454ns and a 0.061 contribution for the fast mechanism with a value of 0.05ns for the Tyr. The rotation of the bulk aggregate has slowed significantly due to the increase in size, when compared to the dimers.

7.4. Stacked Trimer

The following structure is also a potential structure for how $A\beta_{1\text{-}42}$ monomers aggregate to form a trimer, though there are other works that describe similar stacking processes, though there are some conformational differences [48][176] [244]. It is impossible at this point to know conclusively if this stacked trimer is incorrect as it appears stable. Despite which is correct, the structure still creates useful information about how $A\beta_{1\text{–}42}$ anisotropy curves begin to form compared to the literature [112]. The trajectory seen in Figure 126 begins with three proteins stacked

on top of each other, similar to the stacked dimer and protofibril literature [176] [244].

For the first 20ns there is limited movement with some minor loss of shape beginning to occur at the beta-sheet sites near where the Tyr side-chains are located (parallel beta-sheets between the three proteins at Ala_2-Hsd_6, Gln_{15}-Val_{18}, Asn_{27}-Val_{36} and Val_{39}-Ile_{41}). The beta-sheets do not lose their structure completely, but do move slightly throughout the trajectory as it becomes more stable, ending at Asp_1-Phe_4, Leu_{17}-Phe_{20} Ala_{30}-Ile_{32} and Val_{39}-Ile_{41} [49] [171]. The Tyr's appear to spread out as far as they can from each other, within the limits of what the protein backbone aggregates allow at 30ns. Furthermore, the conformational changes become more distinct at 30ns which is similar to what is observed for the stacked dimer.

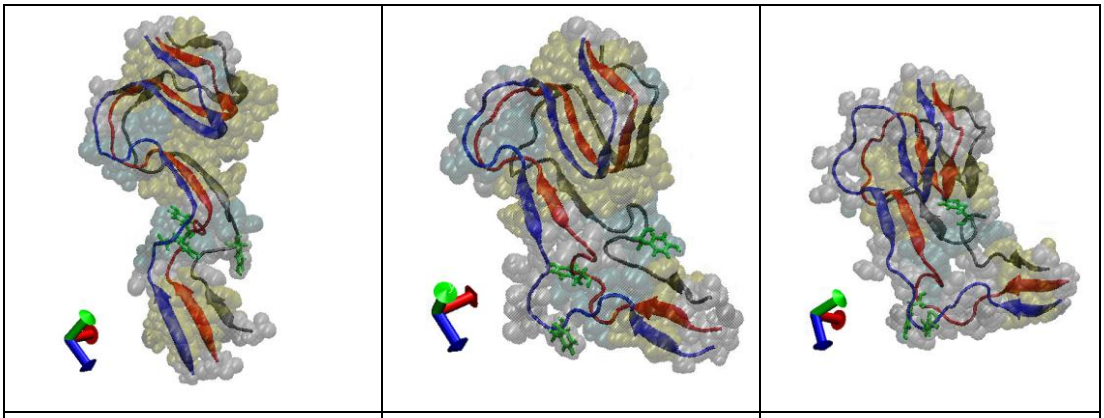

T=0ns	T=30ns	T=50ns

Figure 126 – Stacked Trimer Stabilization. The panels the position of protiens A (blue), B (red) and C (grey) with Tyr side-chains highlighted (green) with the The VDW interactions indicated by the transparent spheres: Purple denotes alpha-helix structure, red denotes pi-helix, white denotes a coil, cyan denotes a beta turn and yellow or tan denotes beta-sheet structures. The beta-sheets are further denoted by the arrow-like shape with the proteins.The first panel shows the starting postion of the proteins. The middle panel shows the trajectory at 20ns and the right panel shows the system at the end fo the trajectory at a time of 50ns.

This bend in conformation becomes progressively more apparent throughout the rest of the simulation (50ns) and the three Tyr residues stay as far from each other as they can. The Tyr side-chains have freedom to move but are affected by interactions caused by the proximity of the protein backbones within the aggregate. The overall structure of this stacked trimer stays consistent without becoming unstable, except at the heads of the proteins, implying that this structure is more

stable than the dimer. This suggests that a larger stack will create a more stable system; see Figure 139 below for the largest (and most stable) aggregate we have explored [63].

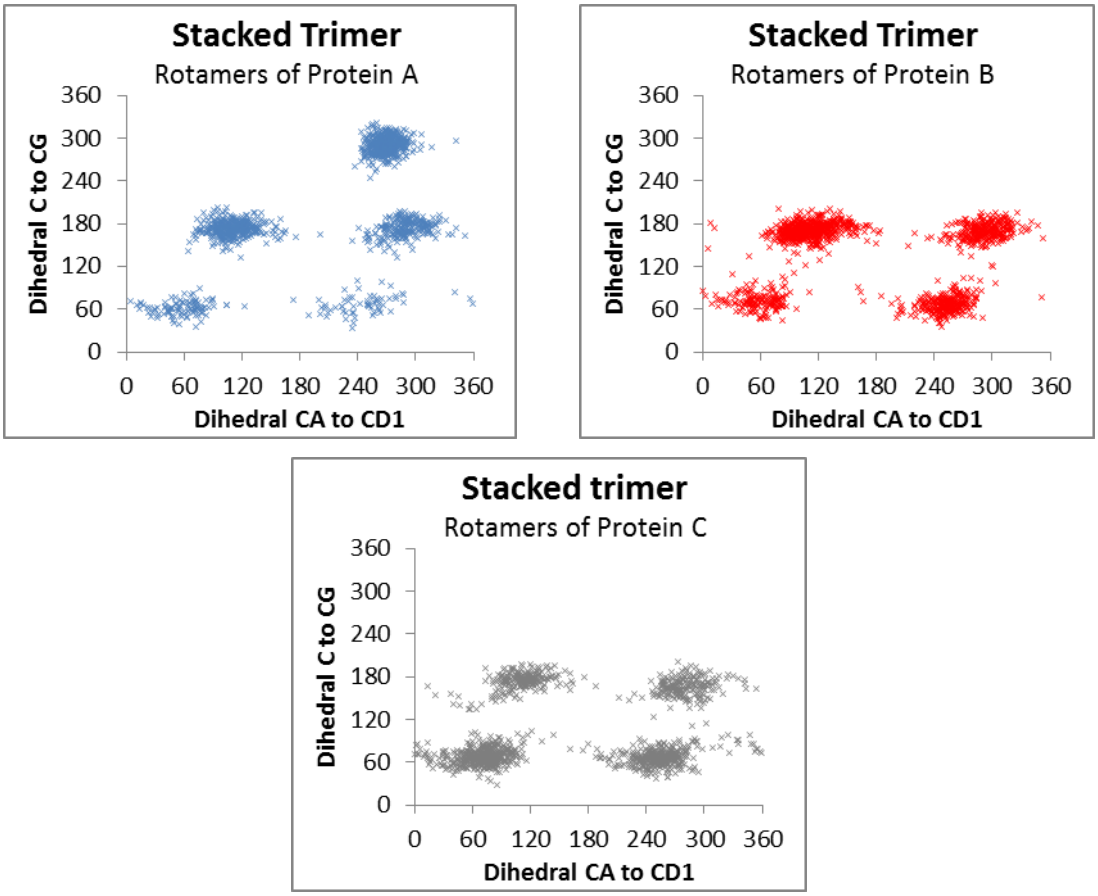

Figure 127 – Stacked Trimer's Rotamer Response. The central coordinates for Tyr A's rotamer's are approximately (60,60), (240,60), (110,170), (290,170) and the rarer (280,290). Tyr B has the regular (but slightly skewed) rotomer state 55,65), (250,60), (110,175) and (290,170). Tyr C also has the more traditional positons (65,65), (260,60), (115,175) and (290,170).

For the stacked trimer, the Tyr side-chain in Protein A (Figure 127) has similar results to those seen for Tyr B in Figure 118 in the stacked dimer trajectory. It has a preference towards states 3 and 4 but also occupies the sixth rotamer state. This suggests that the stacking mechanism must influence the Tyr. The stacking mechanism creates tightly packed aggregates that appear to influence the Tyr side-chains, which allows them to occupy these more extreme rotamer states. This in contrast with that seen in the stacked dimer as the new 6th states are completely uninhabited.

Tyr B and C have typical rotamer states with Tyr B having a higher density of states 3 and 4, a characteristic seen in these tightly aggregated systems. Tyr C being on the bottom of the stack has more manoeuvrability and does not get trapped between the stacks allowing it to favour the first and second rotamer states as expected.

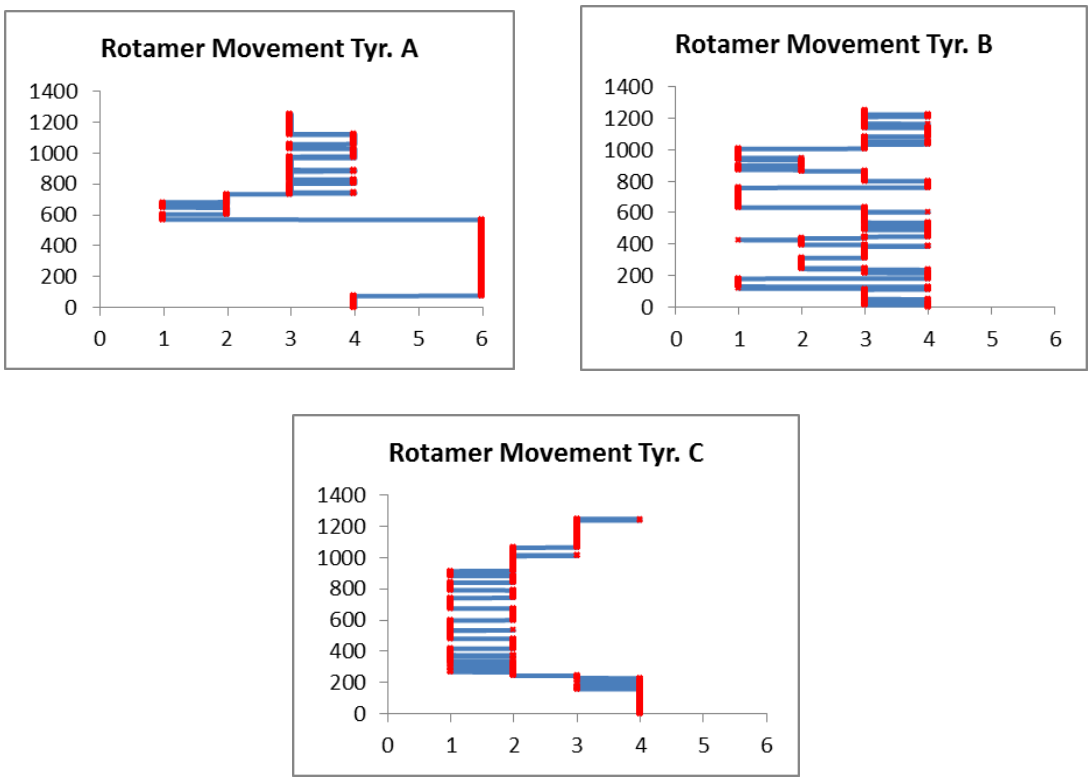

Figure 128 - Time Lapse Rotamer Responses of Stacked Trimer.

As can be seen in Figure 128, all three Tyr residues have significant movement around their rotamer states due to the local interactions. Tyr A and C appear to be the more restricted Tyrs in this system. Tyr B has the most erratic movements possibly due to being between the other two proteins, but has freedom to move due to the twist in the backbone giving it relative freedom. Tyr A's C to C_G dihedral angle movement is significantly more rigid and favours staying twisted away from states 1 and 2 due to its proximity to the other protein backbones.

The Tyr side-chains adhere to the traditional movements between rotamer states, except one instance of a jump from state 3 to 1 for Tyr B. Tyr C also occupies rotamer states for brief periods; however it spends most of its time manoeuvring between the first and second states. This is due to the Tyr position at the bottom of the stack within the aggregate. Tyr A spends a large portion of its time in the sixth

rotamer state after moving there from the fourth rotamer state, before jumping back to the first state where it continues to occupy the traditional states.

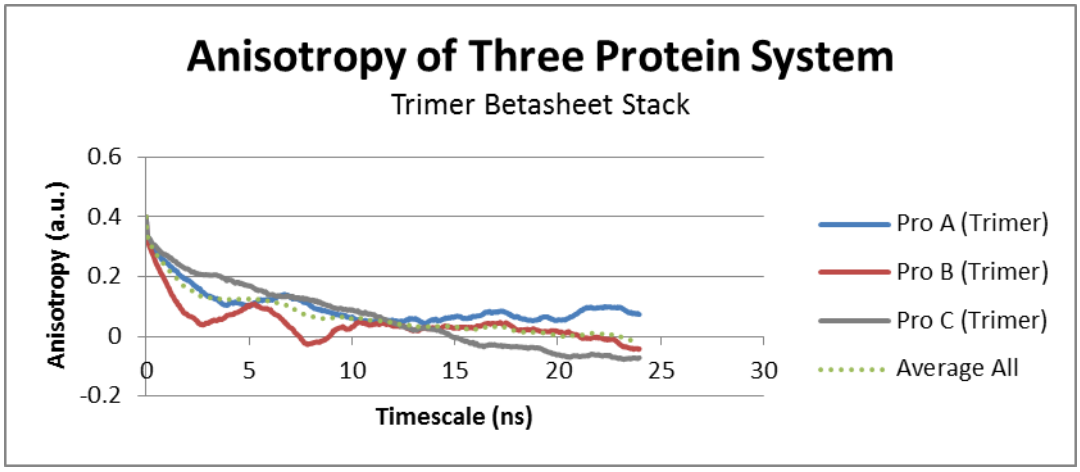

Figure 129 - Simulated Anisotropy of Stacked Trimer. This graph shows the simulated anisotropy of Proteins A (blue) and B (red) and C (grey), as well as the average (dotted green).

Anisotropy results for this simulation are shown in Figure 129. Protein A has a shallow initial decay followed by a slow relaxation that decays to just about 0.1 by the end of the 23ns correlation time window. This is reasonable as it is interacting closely with protein B throughout the whole trajectory, which caused rigidity in the protein and Tyr movements.

Protein B in contrast, has a much sharper initial decay and has plateau value of 0. This initial decay resembles a monomer response, as the Tyr has erratic movements due to the freedom it has to move, despite being the middle protein in the aggregate. However, it does have some complex behaviour and it takes a long time to level out to 0. These complications are indicative of an aggregate response and are due to the interactions with the other proteins and the slow bulk aggregate rotation.

Protein C has a slower initial decay due to the Tyrs interactions with the aggregate backbone, giving it slow movements relative to the other two proteins as shown in Figure 128. It then has a relatively fast relaxation to a negative plateau value. This relaxation is slower than a monomer response due to the larger size of the aggregate, but is relatively quick for the aggregate as it is on the bottom of the aggregate giving it more room to move.

These results are feasible as the Tyr side-chains for proteins have freedom to move around but are limited by their backbones being more rigidly aggregated together.

7.4.1. Best Fits

The best fit graph for the average of this anisotropy decay is shown in Figure 147 and Table 13. It shows contributions of 0.34 and 0.06 for the aggregate and Tyr responses respectively with rotational times of 7.58ns and 0.51ns. These results conform to what is expected of this system, as the larger τ_r value for the bulk aggregate is indicative of a slower rotation and therefore a larger aggregate, which is expected as there is one extra protein in the aggregate when compared to the dimer. The system shows the response of a larger aggregate than the L-shape trimer as it is in a more stable and compact conformation and does not move as erratically and therefore, rotates more slowly. The Tyr's slow τ_r will be due to the interactions from their surrounding environments.

7.5. Flat-sheet Tetramer

The following structure (Figure 130) is a crucial candidate pathway for how $A\beta_{1-42}$ aggregates into fibril structures, as seen in the Figure 6 [50] [63]. This aggregate forms when two flat-sheet dimer's come into contact and aggregate together, creating this flat-sheet tetramer. The two sheets will stack on top of each other, with a slight rotation about the normal axis between the sheets, in order to create the "spiralling" characteristic of a fibril. This process could continue until an $A\beta_{1-42}$ amyloid fibril is formed [50]. Again, this is only hypothetical as there are other aggregation pathways that could occur.

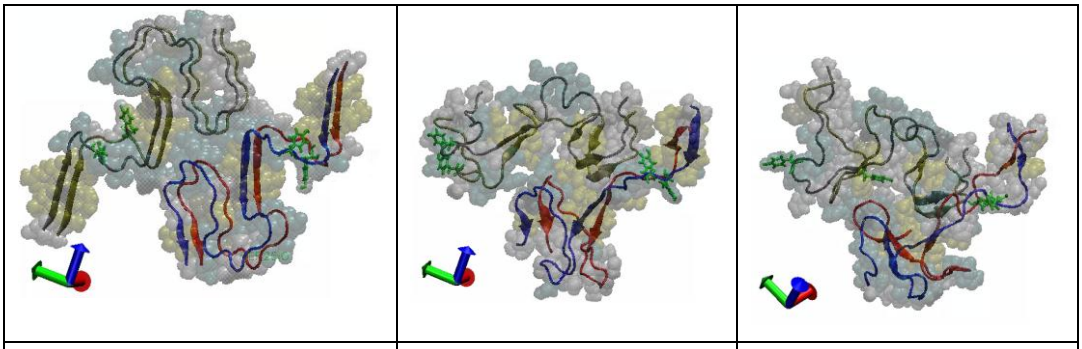

T=0ns	T=10ns	T=50ns

Figure 130 – Flat-Sheet Tetramer Stabilization. The panels the position of protiens A (blue), B (red), C (grey) and D (orange) with Tyr side-chains highlighted (green) with the The VDW interactions indicated by the transparent spheres: Purple denotes alpha-helix structure, red denotes pi-helix, white denotes a coil, cyan denotes a beta turn and yellow or tan denotes beta-sheet structures. The beta-sheets are further denoted by the arrow-like shape with the proteins.The first panel shows the starting postion of the proteins. The middle panel shows the trajectory at 20ns and the right panel shows the system at the end fo the trajectory at a time of 50ns.

Figure 130 depicts the trajectory of the flat-sheet tetramer and begins in what is assumed to be a stable formation for this aggregate [63]. However, after the first 10ns there is significant bending in the structure as it tries to find its preferred configuration. This bending is visible at all the beta-sheet sites, which is seen to a similar degree in the previous stacking/flat-sheet simulations [49] [171]. The initial beta-sheets are situated at Asp_1-Hsd_6, Gln_{15}-Phe_{19} and Val_{40}-Ile_{41} between proteins A and B and C and D. After the first 10ns proteins A and B still show good beta-sheet structuring but proteins C and D lose the beta-sheet at the heads of the proteins leaving beta-sheets between His_{16}-Val_{18}, Ala_{30}-Ile_{31} and Leu_{34}-$Val_{40.}$ These beta-sheets remain relatively stable throughout the rest of the trajectory, with only

minor changes occurring but at the end of the trajectory, end in these approximate positions.

The Tyr side-chains are very close together with little movement away from the backbone for the first 10ns. However, by 20ns the Tyr side-chains of proteins C and D move away from each other allowing a greater degree of freedom, whereas the Tyr's in A and B stay rigidly together for the entirety of the simulation.

By 30ns the changes to the alignment of the backbone become more extreme and the Tyr side-chains in proteins C and D are as far apart as the backbone allows them to be, with Tyr C being affected by local interactions to a lesser degree than Tyr D. This is a characteristic seen in the stacked dimer and stacked trimer [176] [244], but the system also shares the backbone structural bending seen in the flat-sheet and L-shape aggregates.

For the rest of the trajectory (up to 50ns) these characteristics described become increasingly more apparent. The Tyr side-chain for protein C has significantly more freedom than the other three Tyr side-chains but the rigid backbone still affects that freedom. This structure shows a lack of stability in its configuration similar to that observed in previous examples; however it shows less stability than the stacked trimer. This further implies that as a beta-sheet aggregate stack gets larger, it becomes more stable (see Figure 139). Despite this, the lack of stability seen in these structures could be helped with salt ions [162] or metal ions [41] [42] could be causing the initial structure to be unstable.

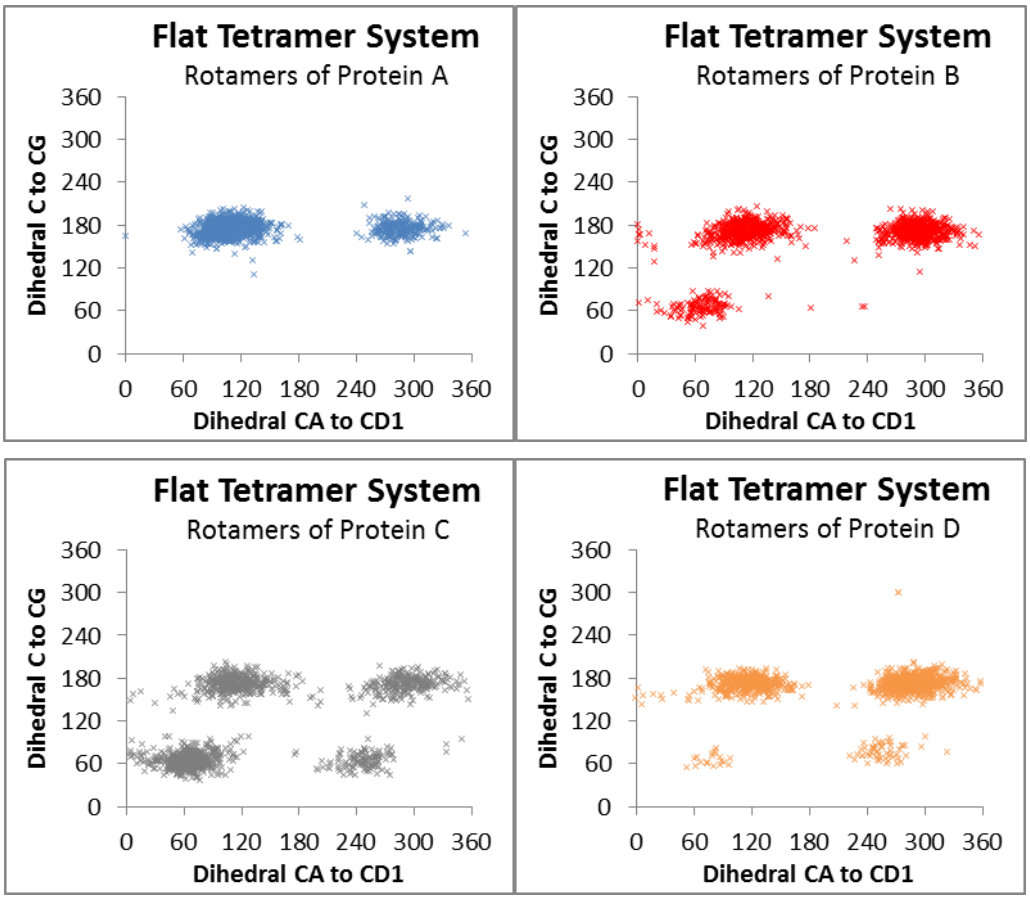

Figure 131 – Flat-Sheet Tetramer Rotamer Response. The central coordinates for Tyr A's rotamer's are approximately (110,170), (280,175). Tyr B has the rotomer states (55,65), (110,175) and (290,175). Tyr C has more traditional positons (65,65), (250,60), (110,175) and (290,170). Tyr D also has traditional positons (70,65), (255,70), (115,175) and (280,175).

The Tyr side-chains in Protein's A and B (Figure 131) both have limited movements, Tyr A only having two rotamer states and B having three states that are readily favoured. This is due to their position within the aggregate and how closely they are interacting; influencing each other and allowing them to favour states 3 and 4. The presence of state 2 for Tyr B implies that it has more movement available to it than Tyr A, which is reflected in their positions.

Tyrosine C and D occupy the four usual rotamer states with an affinity for the third and fourth rotamer states. Tyr C shows less of a preference due to its freedom within the aggregate. Tyr D is buried and therefore, is still being influenced and so has fewer instances of occupying states 1 and 2 and also has a single instance of entering state 6.

This further suggests that the Tyr side-chains favour states 3 and 4 when they are influenced by external forced. When they reach these states comfortably, the Tyr can twist further and move into states 5 and 6, due to further external forces influencing the Tyr's rotamer state (see Figure 151.)

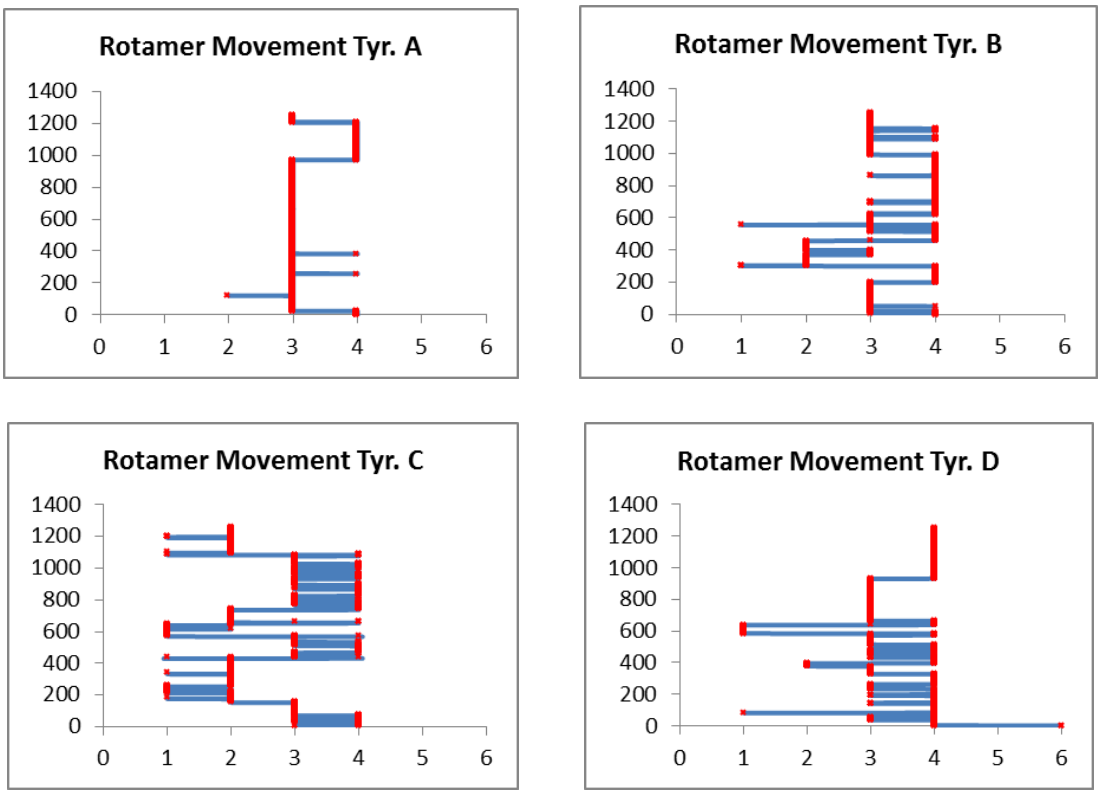

Figure 132 - Time Lapse Rotamer Responses of Flat-Sheet Tetramer.

As discussed previously, all Tyr side-chains shown in Figure 132 have a preference for rotamer states 3 and 4, which is expected for a tightly aggregated system. Despite this aggregated environment affecting all the Tyr side-chains they still adhere to the traditional movements between rotamer states.

Tyr A almost exclusively occupies states 3 and 4 due to the proximity of the Tyr side-chain to the aggregated backbone and Tyr B causing rigidity in the C to C_G angle.

Tyr B shares a similar surrounding environment as Tyr A and as expected, has near-identical rotamer state occupation preferences. Tyr B also has significantly more erratic movements between the states than A, which means Tyr B has more freedom than Tyr A. This is likely due to the tail of the proteins C and D interacting

frequently with Tyr B, affecting its preference, but does not aggregate close enough to affect its freedom. This suggests that a tightly aggregated Tyr residue will have little movement in the C to C_G dihedral angle.

Tyr C has significantly more movement between all its states due to its freedom within the aggregate, though it still prefers to occupy states 3 and 4. It does not reside in a single rotamer state for an extended period and instead prefers to rapidly move between two states for extended periods, before swapping to the other state-pair. This is likely due to the external interactions from the backbone.

Tyr D infrequently occupies states 1 and 2. This is due to the backbone residues affecting the Tyr, as its buried position within the aggregate would contribute to this preferential movement. Furthermore, it also briefly occupies state 6, a feature present in the beta-sheet aggregates that have the stacking mechanism.

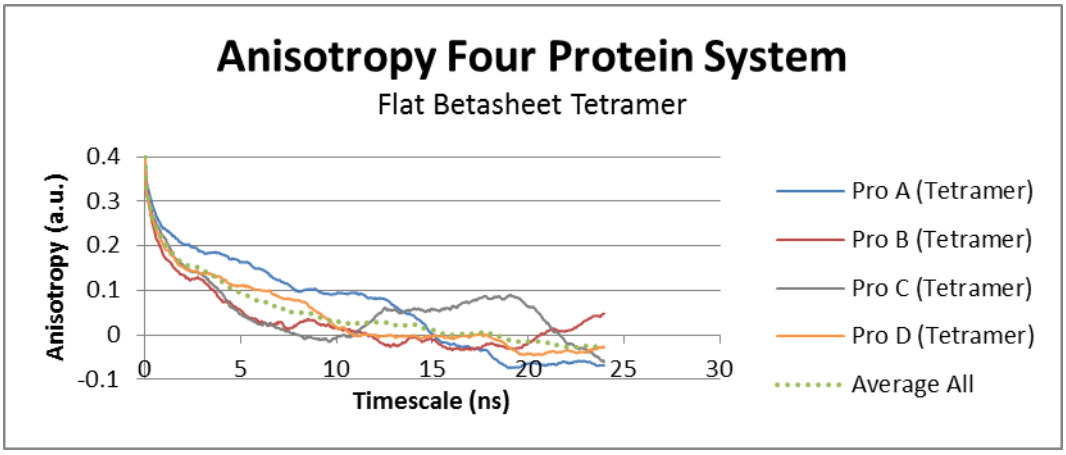

Figure 133 - Simulated Anisotropy of Flat-Sheet Tetramer. This graph shows the simulated anisotropy of Proteins A (blue), B (red), C (grey), and D (orange) as well as the average (dotted green).

Protein A has a short lived initial decay to about 0.18 at a correlation time of 3ns, followed by a more complicated relaxation period which involves a second slower decay that levels out at 0.1 and third faster decay that decays to 0. This is a complex decay, which shows characteristics of a larger aggregate than seen previously, due to the slow overall decay time. The slow decay is due to the slow bulk aggregate rotation and the Tyr side-chain is held in place and lacks freedom to move, creating the slow initial decay. The resulting anisotropy is sensible as it shows that there is rigidity in Tyr A's movement.

Protein B has a sharp initially decay that temporarily plateaus to 0.02 at 6ns. However, protein B still shows evidence of being part of an aggregate. Tyr B causes the short lived initial sharp decay that levels out at about 3ns. This is relatively fast when compared to protein A and is related to the Tyr's larger degree of freedom. There is then a second decay, which levels out at 0.02 before finally dropping to 0 at 12ns. This complexity is a clear indicator that protein B is part an aggregate, as the multiple temporary plateaus create a slow relaxation period, indicative of an aggregate.

Protein C has a similar response to a monomer as it has a sharp initial decay, followed by a slower relaxation period which decays steadily to 0 at 7ns. The complexities in the curve suggest it is an aggregate despite the fast moving Tyr, which gives the sharp initial decay.

Protein D initially levels out at 0.14 within the first 3ns of the correlation time window due to the lack of Tyr movement; it then continues to slowly relax till 0.9 at 9ns, and then decays to 0 at 10ns, which is slower than a monomer response. These four combined create an average decay that has a slow relaxation to 0 at 15ns, which is indicative of an oligomer.

7.5.1. Best Fits

The best fit shown in Figure 147 has a low error associated with it, as its correlation is 0.9953 seen in Table 13. The resulting variables show that there are two mechanisms at work, with decent contributions from both variables. The fast moving Tyr side-chains show a contribution of 0.18 and a τ_r value of 0.35ns and the slower bulk aggregate has a τ_r value of 7.53ns with a contribution of 0.25.

This bulk rotational time is slower than seen previously for the flat-sheet dimer as it is a bigger aggregate. It shows similar rotational times to that of the stacked trimer, which is reasonable as they are different shapes which could explain the similarity in rotational time, as this could affect the rotational times.

The r_∞ value decays past 0 but takes a significantly longer time than a monomer to reach this point and as such is typical of an aggregate.

7.6. L-Shaped Tetramer

As stated previously the L-shape structure (seen in Figure 134) is an unlikely aggregation pathway for this system but is still useful as a tool to better understand individual responses within an aggregate compared to literature [112]. The principle of this system forming would be either an L-shape or stacked trimer aggregating with a monomer or even a stacked and flat-sheet dimer aggregating together. This would create the structure seen below with three proteins stacked on top of each other and protein D aggregated onto the side, creating a flat-sheet with protein A.

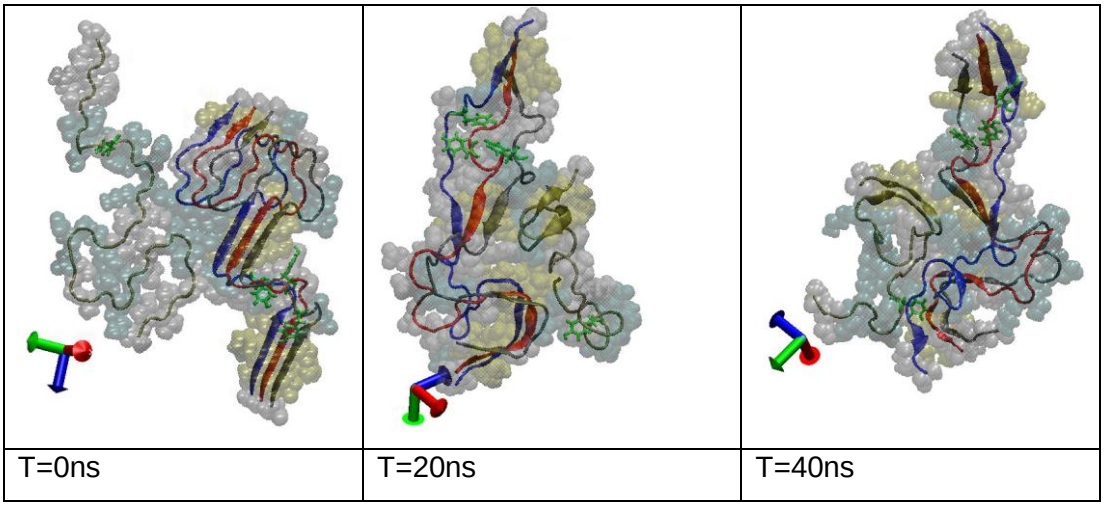

Figure 134 – L-Shaped Tetramer Stabilization. The panels the position of protiens A (blue), B (red), C (grey) and D (orange) with Tyr side-chains highlighted (green) with the The VDW interactions indicated by the transparent spheres: Purple denotes alpha-helix structure, red denotes pi-helix, white denotes a coil, cyan denotes a beta turn and yellow or tan denotes beta-sheet structures. The beta-sheets are further denoted by the arrow-like shape with the proteins.The first panel shows the starting postion of the proteins. The middle panel shows the trajectory at 20ns and the right panel shows the system at the end fo the trajectory at a time of 50ns.

The L-shape tetramer begins in the assumed stable position. However, because this structure is unfavourable, it begins to fold and lose its shape as soon as the trajectory starts as seen with the flat-sheet dimer and L-shape trimer and no longer resembles the protofibril structure [63]. Protein D folds into the stacked section of the aggregate because the hydrophobic sections prefer to bury themselves away from the water as discussed previously. The stack in contrast only has minor bending to the overall structure, similar to the stacked trimer (Figure 126), and further suggests that this stacking mechanism is the preferred aggregation pathway due to its stability [48].

This is further shown by the beta-sheet structuring [49] [171], as Proteins A-C maintain contains beta-sheets between Asp_1-Hsd_6, Gln_{15}-Phe_{19} and Val_{40}-Ile_{41}, that only change slightly throughout the trajectory, in a similar fashion to what was seen in the stacked trimer. Interestingly protein D forms an anti-parallel with itself between Ala_{30}-Leu_{24} and Gly_{37}-Val_{40}. Though this has been an uncommon feature, it has been seen in amorphous aggregates, especially when a protein is interacting closely with another, this suggests that once unravelled the proteins form beta-sheets with themselves when they are part of an aggregate or are interacting closely with another backbone [49] [172].

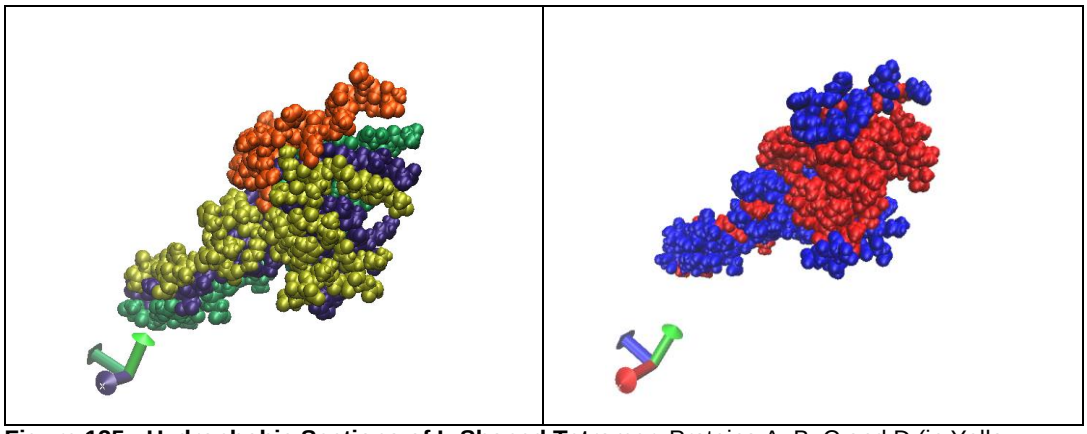

Figure 135 - Hydrophobic Sections of L-Shaped Tetramer. Proteins A, B, C and D (in Yellow, Orange, Blue and green) on the left and the hydrophobic sections (in red) are shown against the hydrophilic (blue) sections on the right.

As the trajectory continues the stack does lose some stability in its shape as the tail does bend more significantly and the middle section of the stack has mirror changes to the conformation. Despite this, the stacked portion of the aggregate does retain its overall shape and the head of the stack does maintain its rigidity throughout the simulation [63]. The loose protein folds in on itself as seen previously and buries its hydrophobic sections into the stacked part as shown in Figure 135 [122].

The stacked part of the aggregate has the same characteristics as the previous stacked trimer, and Protein D shares characteristics with the L shaped trimer and the flat-sheet dimer. This further provides evidence that as the stack becomes larger it become more stable and also that the L shape is an unfavourable conformation. This further implies that the L-shaped aggregation process again, appears unstable and either of the stacking processes (flat sheet stacking, or monomer stacking) are more likely candidates [48]. Although, the stacking mechanism seems more stable

some external forces would be required to stabilise the flat-sheet dimer to prevent it folding in on itself as discussed above (metal ions [41] [42] or salt ions [162]).

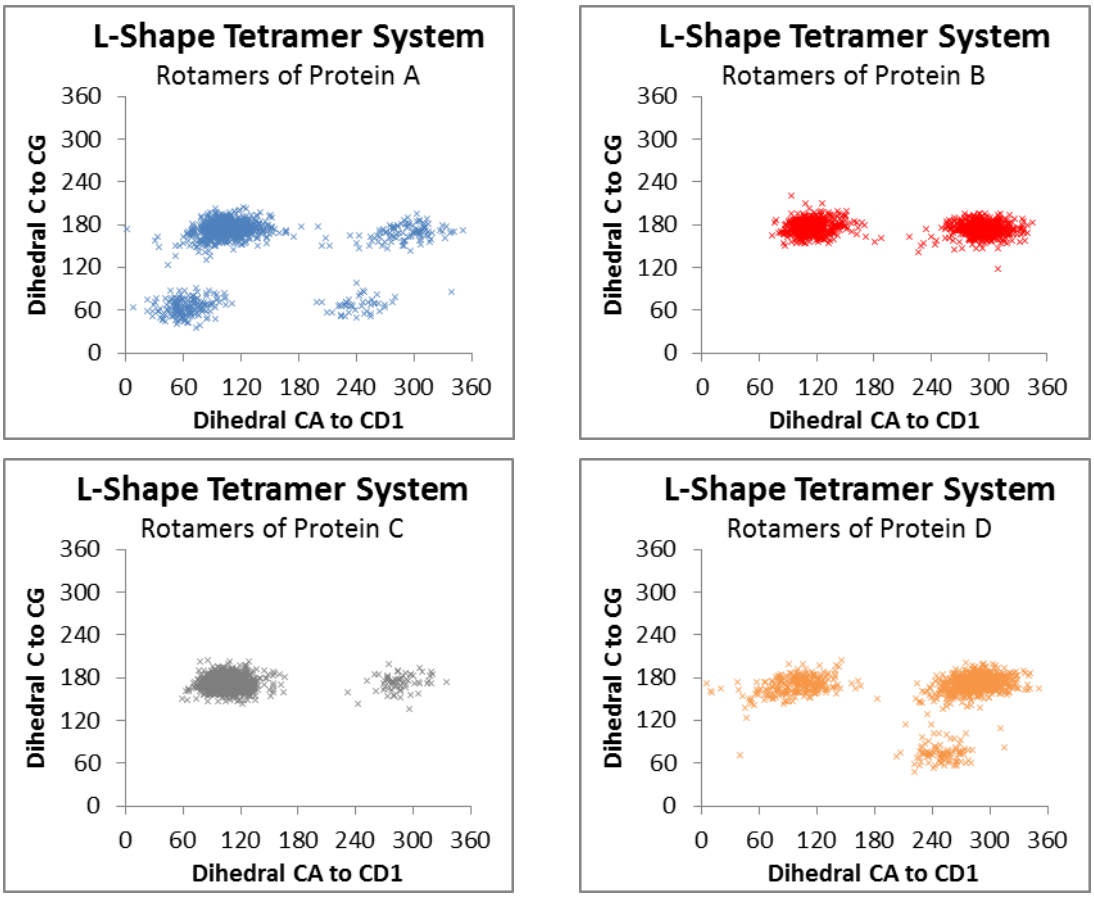

Figure 136 – L-shape Tetramer Rotamer Response. The central coordinates for Tyr A's rotamer's are approximately (60,60), (245,60), (110,175) and (290,170). Tyr B has the rotomer states (110,180) and (290,175). Tyr C has more traditional positons (100,170) and (280,175). Tyr D also has traditional positons (250,70), (100,170) and (285,170).

All proteins favour the third and fourth rotamer states but no signs of the fifth or sixth states likely due to the L-shapes interactions. Despite this preference, protein A still has access to states 1 and 2, this is due to the fact that it is has slightly more freedom than Tyr's B and C.

Proteins B and C have the least amount of movement as they exclusively occupy states 3 and 4. This is because they are aggregated closely together and as such they are being influenced by the surrounding residues from their own backbone and the other proteins backbone which twists them into favouring states 3 and 4. If the L-shape was not influencing these backbones, it is likely that the fifth or sixth rotamer state may have appeared here.

Protein D has three main rotamer states it prefers to be in, with only one instance of it taking on the second rotamer state. This is likely related to how the protein backbone has folded in on itself making states 1 and 2 unfavourable.

These results continue to suggest that the Tyr side-chains that are aggregated closely together are forced to prefer the occupation of states 3 and 4. States 5 and 6 could appear in this system due to the tightly aggregated stack, but the influence from protein D is likely pulling on the aggregate backbone. This gives the Tyr side-chains more room to move within the stacked part which is why state 5 or 6 are never occupied during this trajectory, much like the L-shaped trimer.

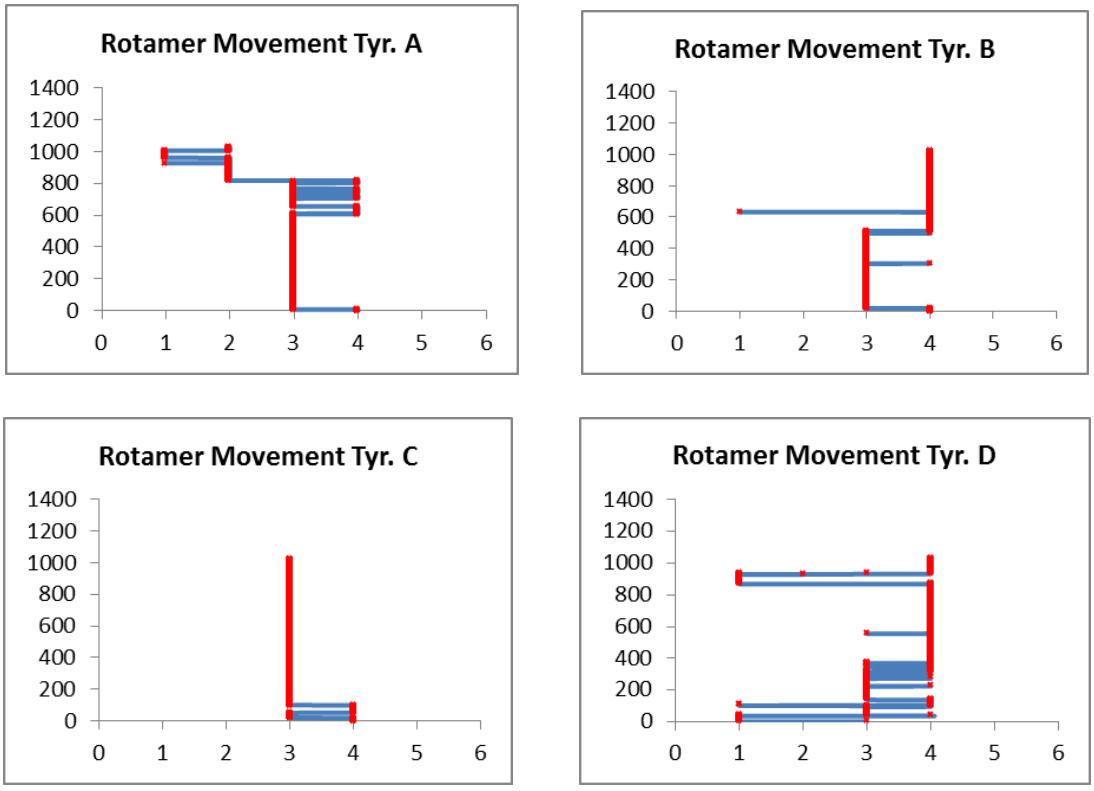

Figure 137 - Time Lapse Rotamer Responses of L-shape Tetramer.

All four Tyr side-chains favour states 3 and 4 due to the rigidity in the C to C_G angle caused by the influence from the aggregate's backbones. Tyr A initially is trapped due to its position within the aggregate, however after some time it finds more freedom. This is reflected in Figure 137 as it spends the first 30ns in state 3 but then moves into states 1-3 near the end of the trajectory.

Tyr B and C show signs of being heavily aggregated as they prefer to be in states 3 and 4 almost exclusively, a feature seen in all stacked aggregates, with little freedom to move. This is due to the stacking mechanism which limits the movement available to any Tyr side-chain position through the rigidity of the stack and position of the Tyr side-chains.

Tyr D also shows an affinity for states 3 and 4, though does occupy the other states repeatedly as this side-chain has the most freedom. This is likely due to its position as part of the L-shape; it has a larger degree of movement that is reflected in the early occupation of state 1 and the higher degree of movement between states. As the protein folds within the first 10ns it buries the Tyr side-chain within the aggregate. This limits the Tyr movement and is the cause of the long period where it occupies state 4. All Tyr resides adhere to the rules of movement set out previously.

These results are unique but do share many characteristics with the L-shaped trimer, implying that the shape of the aggregate affects the overall movement patterns of the Tyr's within the system. This may be due to the way the aggregate is being manipulated by the external forces put on the individual backbones, as well as the Tyr residues themselves.

When Figure 124 and Figure 137 are compared the proteins that are part of the stack do share similar characteristics. They have some differences caused by their local environments, but the stacked sections show a preference towards states 3 and 4. The L-shaped sections show a preference towards all states, except when the folding mechanism effects the Tyr side-chain position.

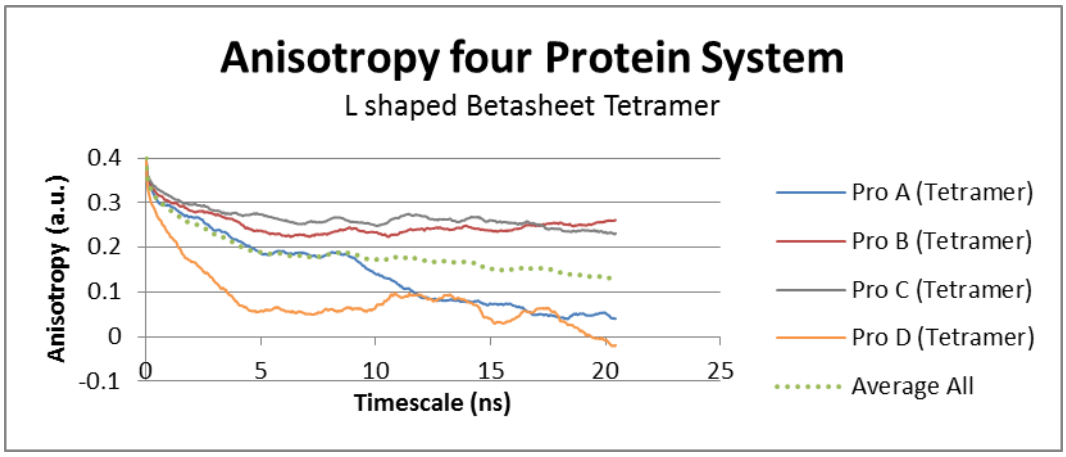

Figure 138 - Simulated Anisotropy of L-shape Tetramer. This graph shows the simulated anisotropy of Proteins A (blue), B (red), C (grey), and D (orange) as well as the average (dotted green).

Protein A in Figure 138 has an initial decay that plateaus to a value of 0.18 at a correlation time of approximately 9ns, which is due to the fair amount of movement seen from the Tyr in the second half of the trajectory. It then has a slow relaxation time to a value of 0.04. This decay is slower than what is seen previously, this is because it is part of a larger aggregate which will rotate more slowly.

Protein B and C have near enough identical responses that are significantly more aggregated than what has been seen previously. This is likely due to the aggregate holding both the Tyr side-chains rigidly in position, creating short lived initial decays, and the aggregate rotating very slow. They have long relaxation periods that level out at 0.26 and 0.23 for B and C respectively. These characteristics continue to show the importance of the MC simulation results.

Protein D also has a convincing response as it has a sharp initial decay that plateaus at a correlation time of 4ns to a value of 0.06, which is due to the Tyr's ability to move freely. The longer relaxation time associated with the aggregate rotation is faster than what is seen for the other proteins in the system, which is because the folding mechanism creates more movement for this protein.

7.6.1. Best Fits

The average anisotropy for these proteins is also sensible for a tightly packed aggregate, as it has a slow initial decay followed by a long relaxation period ending at 0.127. This average has two fits associated with it (Table 13) as this system has a complicated decay due to the inclusion of the folding mechanism, the bulk aggregate rotation and the Tyr side-chain movements. This complexity creates a

subtle secondary decay at the end of the graph, which means a two exponential fit will be limited to either fitting for the first or second decay. This is because a two exponential fit cannot account for three mechanisms, which was also true of the L-shape trimer to a lesser degree.

The first best fit graph (see Figure 147) is produced by allowing it to follow the curve in the initial decay, which ignores the subtle secondary decay. The second graph was allowed to fit for the end of the graph. This ignores the initial decay and makes best fit decay significantly sharper than it should be, creating a potentially poor fit. This suggests that there are three mechanisms associated with this decay. Both fits have a similar set of contributions from both the slow and fast mechanisms; they are of approximately equal weight, implying both mechanisms contribute to the decay curve.

The first graph has a τ_r value of 1.001ns for the fast mechanism, which is significantly slower than previous Tyr responses for the beta-sheet aggregates. This is likely due to the fact most of the Tyr side-chains are not able to move freely. There is also a large τ_r value of 17.483ns that will be due to the size and shape of the aggregate making the system rotate more slowly. It has a correlation value of 0.981.

The second graph has a τ_r value of 0.31ns which is closer to what is expected for the Tyr that is free to move and has a significantly slower τ_r value of 25.0ns for the aggregate. This result is feasible, but implies a significantly faster progression of the rotational times with increasing aggregate size; however it does have a lower correlation value of 0.94.

An annealing optimiser that includes a third set of variables for the third mechanism would be best to find a more appropriate fit for this system, as the second decay in the anisotropy curve cannot be captured using only two sets of variables. Despite this, the first fit has a better correlation and therefore has less of an error associated with the fit and also has more reasonable results. This implies that the first fit is both acceptable and the best fit available.

7.7. Beta-sheet Hexamer without Ions

This beta-sheet hexamer shown in Figure 143 is another potential candidate for the formation of $A\beta_{1-42}$ fibrils, and as such this should be the most stable form of all the aggregates we study, it is a small protofibril that would stack to form protofilaments [50] [63] [176] [244]. However, due to the size of the protein (~83.78Å x 51.91Å x 13.82Å), there are limitations on the waterbox size (~90Å x 94Å x 87Å) and as such there are likely to be some self-interactions through the periodic boundary conditions which slow down the rotation (specifically along the x-axis). This could create results that depict a system with a high concentration of aggregating hexamers in it. A second hexamer could be stacked on top of this one [50]; unfortunately this would require a significantly large amount of processing power.

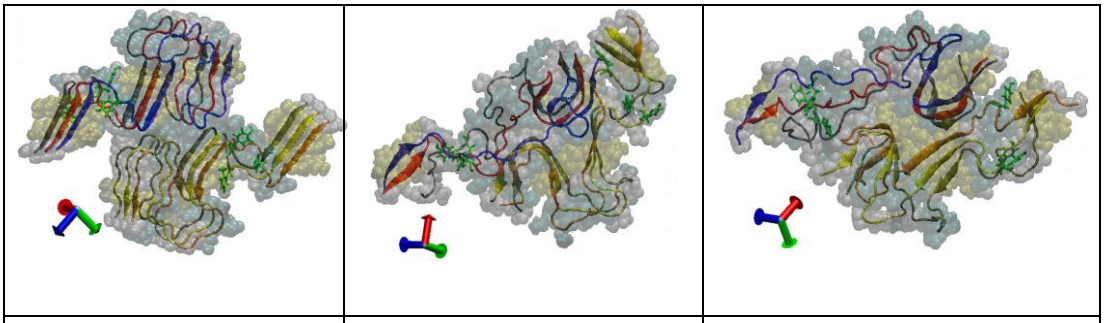

T=0ns	T=100ns	T=200ns

Figure 139 – Beta-sheet Hexamer without Ions. The panels the position of protiens A (blue), B (red), C (grey), D (orange), E (yellow), and F (tan) with Tyr side-chains highlighted (green) with the The VDW interactions indicated by the transparent spheres: Purple denotes alpha-helix structure, red denotes pi-helix, white denotes a coil, cyan denotes a beta turn and yellow or tan denotes beta-sheet structures. The beta-sheets are further denoted by the arrow-like shape with the proteins.The first panel shows the starting postion of the proteins. The middle panel shows the trajectory at 100ns and the right panel shows the system at the end fo the trajectory at a time of 200ns.

This structure begins in the expected orientation that would be stable for a beta-sheet hexamer [63]. As the trajectory begins the backbones around Tyr's D E and F spread apart, whereas the rest of the aggregate remains rigid and relatively unmoving. At 20ns there are significant conformational changes visible near the head of the proteins in the stacked section containing proteins A-C. There is less of a change to the backbone conformation of proteins D-F as Tyr D is completely separate from the other two and has the most freedom. The backbones of all the proteins are separated at the middle also and are not nearly as rigidly aggregated. At 40ns the structure has lost significant shape despite still being a hexamer

aggregate, with many of the beta-sheet sections starting to shift [49] [171]. The closeness of the Tyr residues here could explain why experimental anisotropy measurements become increasingly more difficult. A large fibril with this shape has very close proximity Tyr residues, which in a large aggregate, would make it more likely for a Tyr to release its photon, only to have it absorbed by another Tyr and therefore detector photon count would diminish over time, causing more scattering [112].

By 60ns the stacked portion containing A-C is more misshapen but still contains most of its beta-sheet structuring (the structure does begin to break apart as the trajectory continues and the mid sections are completely unravelled by the end) but the stack containing D-F is still relatively structured. At 100ns the aggregate holds its structure for roughly 30ns, though the structure is still misshapen when compared to the expected structure [63]. By 130ns the middle sections of the protein backbones have all spread out again. For the rest of the simulation, the midsections of the proteins get closer and then spread out repeatedly. The final beta-sheet structures within the system are as follows: A, B and C have parallel beta-sheets between them around Ile_{31}-Val_{36} and Val_{39}-Val_{40}. A and B also have a beta-sheet between Glu_3-Arg_5, which was lost in C, Furthermore the beta-sheet sections in the mid-section of these proteins (present at the start) have disappeared, explaining why the proteins backbone spread apart as discussed above. Proteins D, E and F hold a much more stable structure throughout with all three of the proteins containing beta-sheets around residues Phe_4-Hsd_6, Gln_{15}-Phe_{20} and Ile_{31}-Val_{36}, similar to what has been seen in the stacked trimer for example. E and F also contain a beta sheet at the tail around Val_{39}-Val_{40}.

This lack of stability is likely caused by the fact that this aggregate is struggling to find a favourable orientation and could be due to a lack of external influences on it. These influences could be salt concentration (similar to that of blood) [162] (hexamer structure with ions below has improved stability), metal ion bridging [41] [42] or perhaps it does not form this is not the true pathway for the prefibrilar assemblies [50] which is unlikely. This is apparent when the results from this trajectory are compared to those of the beta-sheet hexamer system below with ions. This system appears less stable and is constantly moving, which implies there is a need for ions in the system to make a stable beta-sheet structure [162]. At the end

of the trajectory Tyr A-C are very close together whereas Tyr D is still free in comparison to the rest.

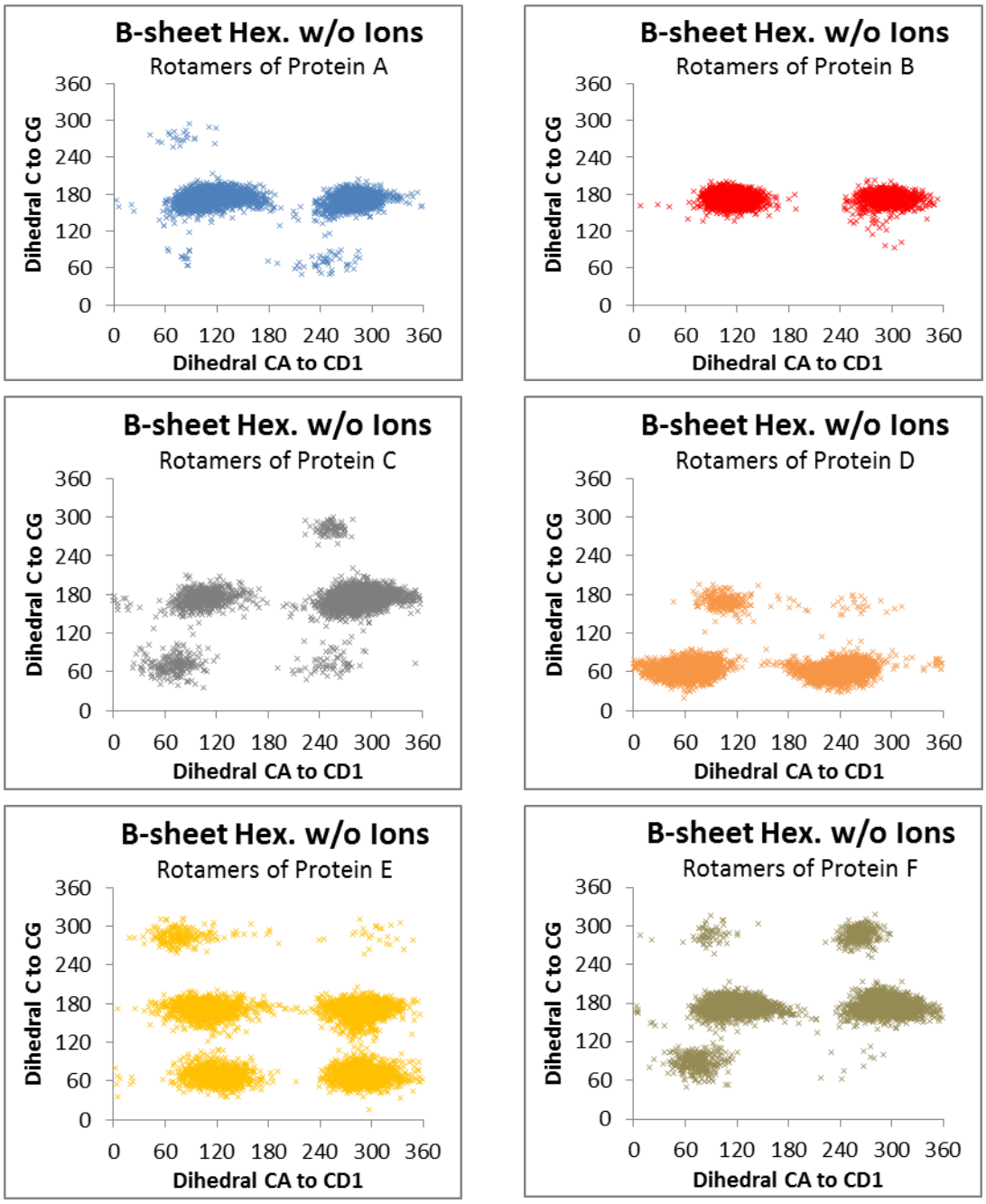

Figure 140 – Beta-sheet Hexamer w/ions Rotamer Response. The centre for each is approximately (80,80), (245,65), (110, 170), (280,170) and the uncommon (65,265) for Tyr A. Tyr B has approximately (110, 175) and (295,170). Tyr C has (65,65), (245,70), (115, 175), (280,170) and the uncommon (250,285). Tyr D has (60,60), (240,60), (110, 170), (260,140). Tyr E has (115,65), (290,65), (110, 170), (290,170) and the uncommon (80,285) and (310,280). Tyr F has approximately (75,75), a small amount at (240,75), (120, 175), (295,170) and the uncommon (85,290) and (255,290)

In Figure 140, all favour occupying states 3 and 4 with multiple instances of states 5 and 6 being occupied in Tyr's A,C,E,F. Due to the extended length of the trajectory there is a lot more data available and as such the Tyr rotamer states are occupied more often.

Tyr A predominantly occupies the third and fourth states, but also occupies the states 1, 2 and 5, this is likely connected to the beta-sheet aggregate affecting the Tyr's position. Tyr B only occupies the middle states, this is because it is part of the stack and is trapped between protein A and protein C, but is not being influenced into states 5 or 6. Tyr B remains limited in its movements for 200ns, which implies it will unlikely have any other rotamer occupations.

Tyr C shows the four common rotamers seen previously with the same preference for occupying states 3 and 4, but also spends some time in the sixth state. Tyr D shows the common rotamer states with a preference for states 1 and 2, most commonly seen in monomers. This is due to the fact it is the least influenced as the backbone it is part of is not aggregated closely with the rest of the aggregate backbones and so the Tyr side-chain will not be influenced into taking on states 3-6.

Tyr E occupies all the rotamer states, with a fairly equal distribution, except from the sixth rotamer state, which is short-lived; this is likely due to its position within the aggregate influencing its movements but not its freedom to move. Tyr F also occupies all rotamer states with an aversion to occupying state 1. These results further prove that the three rotamer state pairs are only found in certain aggregate environments (see Figure 148 to Figure 151.)

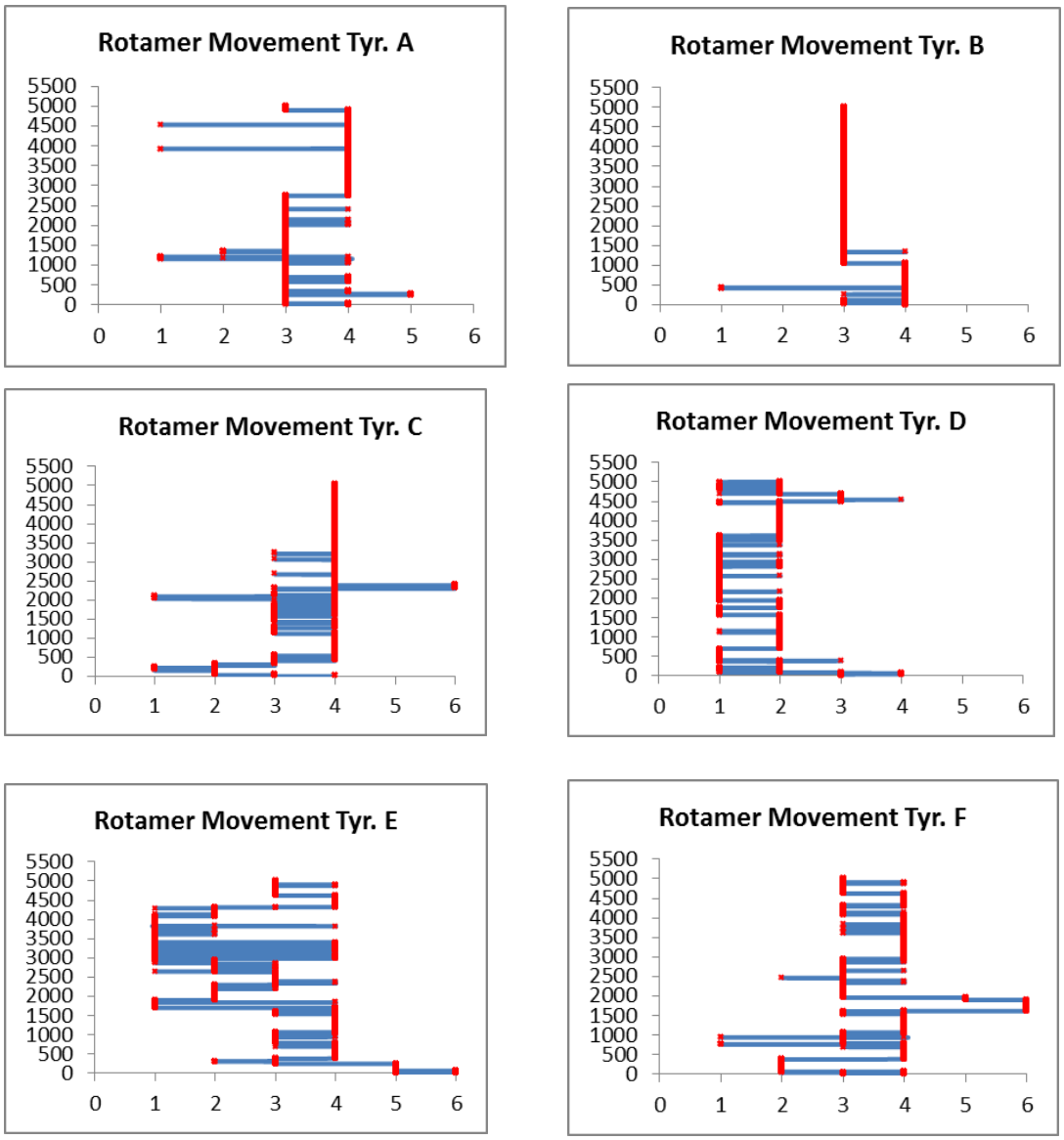

Figure 141 - Time Lapse Rotamer Responses of Beta-sheet Hexamer without Ions.

As expected from what is visible in the trajectory, Tyr A-C have the most limited movement of the proteins, as they are aggregated closely together and rarely break away from each other, which is reflected in the results seen in Figure 141.

Tyr's D and F also show restrictions on their movements, to a lesser degree. Tyr D only briefly occupies states 3 and 4 due to its restricted movements. Tyr's A-D all adhere to the rules stipulated for rotamer movement as seen previously. Tyr F occupies all six states but still shows some restrictions as it does not move freely or erratically. Tyr E has a higher degree of movement which is due to its freedom as discussed above.

There are two instances of transitions from state 5 to 3 in Tyrs E and F. This uncommon transition has been noted above though still rarely and could still be due to truncation in the frame rate. However, as it has appeared multiple times it could be a specific but unfavourable twisting motion within the C to C_G angle, much like the jump from state 1 to 3.

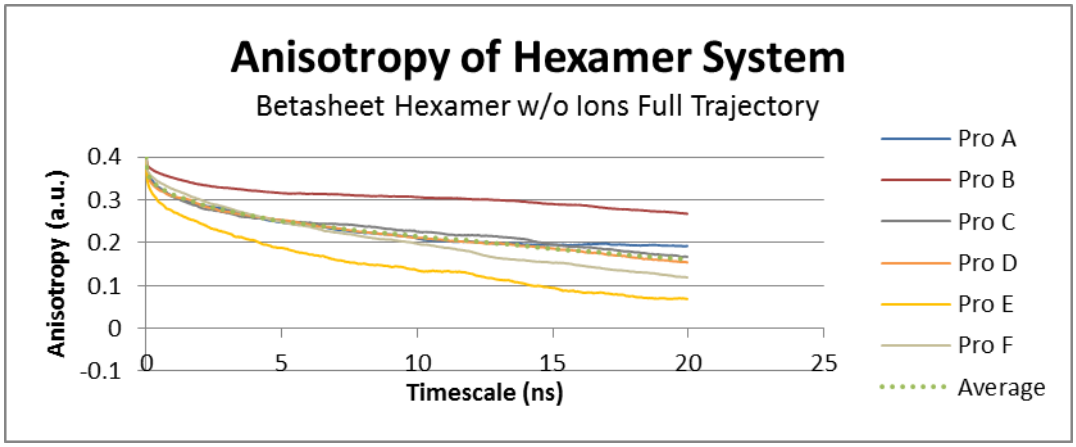

Figure 142 - Simulated Anisotropy of Beta-sheet Hexamer without Ions. This graph shows the simulated anisotropy of Proteins A (blue), B (red), C (grey), D (orange), E (yellow) and F (tan) as well as the average (dotted green).

Figure 142 depicts the anisotropy of the full trajectory of the beta-sheet hexamer system without ions. Protein's A, C and D, all follow the average anisotropy decay curve with only some minor difference; they all have a slow relaxation, with a very short sharp decay at the beginning of the decay and plateau to 0.16 (protein A is closer to 0.19). These three proteins and protein F all have Tyr side-chains that share very similar movement transitions, explaining the near identical initial decay. The slightly lower value associated with protein F is due to the slightly greater degree of freedom on the Tyr. The aggregate will be moving very slowly as discussed above and this is why there is such a high plateau value for the relaxation time.

Proteins B and E are interesting, as they are equivalent positions within the aggregate, however their local Tyr environments are vastly different. Tyr B has very little movement associated with it due to the tight aggregate and Tyr E has a high degree of freedom due to the spread in backbones here (Figure 139.)

As such, protein B is the most aggregated as it has plateau value of 0.28. This is reasonable as it is wedged between A and C which remains closely aggregated

throughout the trajectory and only has access to two rotamer states, spending most of the trajectory occupying state 3.

Tyr E's spend most of the trajectory moving, spending large portions of the trajectory free and sometimes spending it closer to other residues, which explains the fast initial decay.

7.7.1. Best Fits

The beta-sheet hexamer without ions best fit graph is also shown Figure 147 and Table 13 and as a τ_R value of 0.18ns for the fast mechanism and τ_R of 9.34ns for the slow mechanism. With an emphasis of contribution from the bulk aggregate rotation as it has an r_∞ value of 0.15 whereas the contribution from the Tyr side-chain is 0.07 and a 0.18 contribution from the whole aggregate. These results are probable as they show slower τ_r than the smaller aggregates, but a faster τ_r than seen below for the beta-sheet hexamer with ions present.

The lack of stability in the system also contributes to the extra movement seen in the decay, resulting in an anisotropy decay that depicts a smaller aggregate than a hexamer aggregate with ions (see Figure 146.) It does not seem to be affected too significantly by the relatively small waterbox.

7.8. Beta-sheet Hexamer with Ions

The hexamer structure shown in Figure 143 is similar to the previous trajectory, however it also includes an ionic concentration close to that of the body (0.250mMol/L [162]), and as such this should be the most stable form of all the aggregates. Unfortunately, the system is still limited by the size of the waterbox (~92Å x 95Å x 90Å compared to the protein size of ~83.78Å x 51.91Å x 13.82Å). Though big enough to run, it may still have some interactions across the periodic boundaries if the proteins spread out. The system will be comparable to a high concentration of hexamers in a system that are interacting but not aggregating, due to the screen effect caused by the surrounding ions [175].

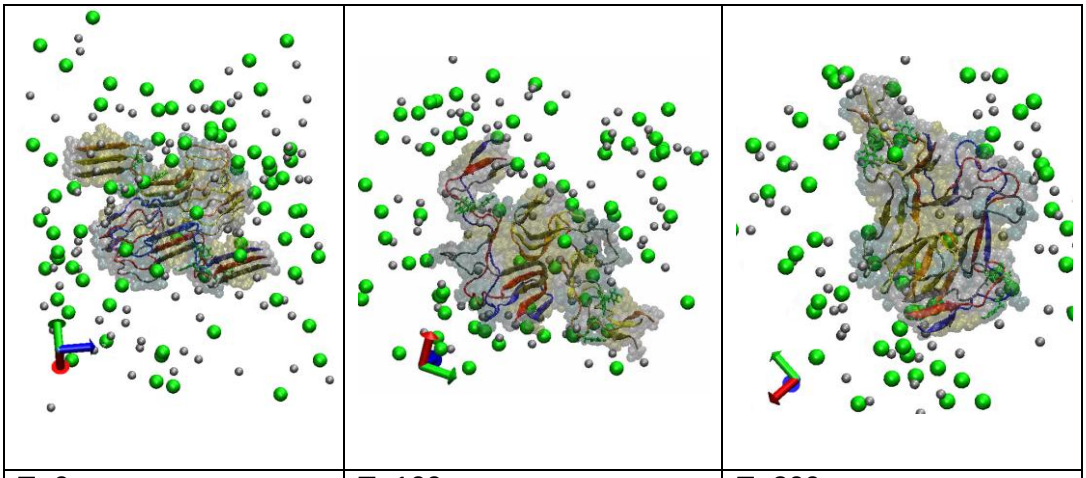

T=0ns	T=100ns	T=200ns

Figure 143 – Beta-sheet Hexamer with Ions Stabilization. The panels the position of protiens A (blue), B (red), C (grey), D (orange), E (yellow), and F (tan) with Tyr side-chains highlighted (green) with the The VDW interactions indicated by the transparent spheres: Purple denotes alpha-helix structure, red denotes pi-helix, white denotes a coil, cyan denotes a beta turn and yellow or tan denotes beta-sheet structures. The beta-sheets are further denoted by the arrow-like shape with the proteins.The first panel shows the starting postion of the proteins. The middle panel shows the trajectory at 100ns and the right panel shows the system at the end fo the trajectory at a time of 200ns**.**

The trajectory begins in the expected stable form for a beta-sheet hexamer and is allowed to move [63]. After 10ns the structure is mostly unaffected and the stack containing proteins A B and C have started to bend conformation at the head of the proteins whereas the other stack is more rigid. Tyr A and D are likely the most trapped but all Tyr are fairly spread out.

At 40ns the overall structure of the hexamer has remained relatively unchanged, except some noticeable bends in the mid-section of both stack's backbones. No interesting characteristics occur until 70ns where Tyr A and D do seem to be more free to move, though the aggregate itself remains significantly more stable throughout the 200ns trajectory than all previous aggregates, as with most of the systems with ions, likely due to the screen effects [175].

By the end of the trajectory, the beta-sheet sections within all proteins do shift and move, but relative to the protofibril without ions, this one appears stable [63]. Proteins A and B have beta-sheet sections within the regions of Glu_3-Arg_5, Gln_{15}-Phe_{20}, Ile_{31}-Gly_{33} and Gly_{38}-Ile_{41}. Protein C has beta-sheet sections in similar positions, however as it is not as tightly aggregated it has some variation (Gln_{15}-Leu_{17} rather than Gln_{15}-Phe_{20}). Proteins D and E have beta-sheet regions at Glu_3-Arg_5, Lys_{16}-Val_{18}, Ala_{30}-Val_{36} and Val_{39}-Ile_{41}. Protein F also has them in these

locations, except at the head (Glu_3-Arg_5) which has separated itself from the other two proteins.

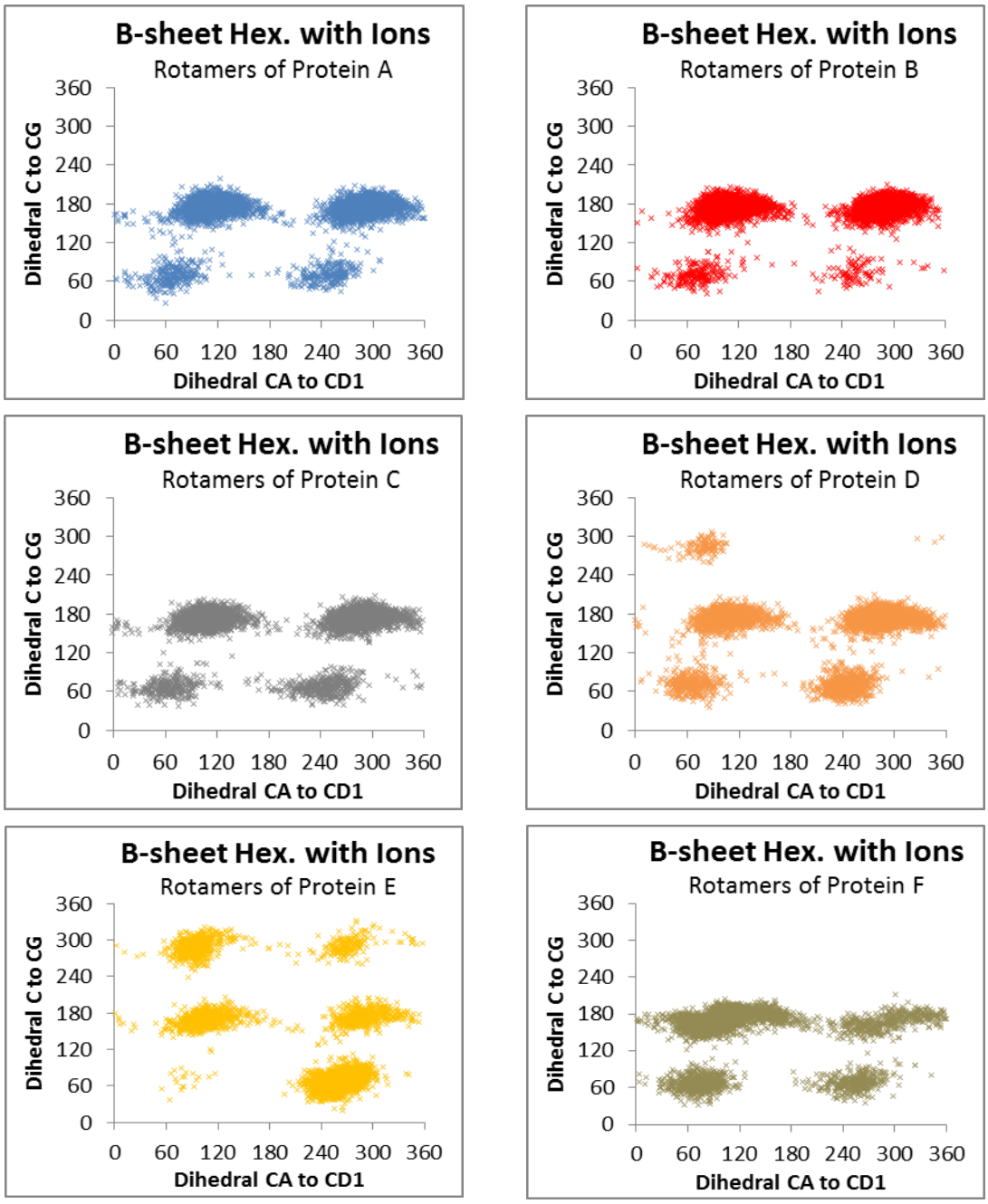

Figure 144 – Beta-sheet Hexamer w/ions Rotamer Response. The centre for each is approximately (70,65), (250,70), (110, 180) and (290,175) for Tyr A. Tyr B has approximately (70,65), (250,70), (110, 180) and (290,175). Tyr C has (70,65), (250,70), (110, 180) and (290,175). Tyr D has (70,65), (245,65), (110, 175), (300,175) and the uncommon (70,280). Tyr E has (75,65), (255,65), (110, 170), (290,170) and the uncommon (85,290) and (255,285). Tyr F has approximately (70,65), (250,65), (110, 175) and (295,170).

In Figure 144 the extended length of the trajectory again allows for greater data collection and as such the Tyr rotamer states are more pronounced. Protein A, B and C all have a Tyr side-chain that occupies the four common rotamer states. Tyr's D and E both have the less common rotamer states, with Tyr D occupying the fifth rotamer state; with some breif moments spent in the sixth, and with Tyr E favouring to occupy all rotamer states except state two. These uncommon rotamer states still only appear as part of stacked / beta-sheet aggregate due to the interactions with the sheet as discussed prevously.

Tyr F has the four common rotamer states, however they have been affected by the aggregate and the surrounding external forces due to the small waterbox and as such states 3 and 4 show a wide population of these states, due to a slow twisting motion that is probably be occuring due to substantial external interactions. These characteristics further explain how a growing aggregate is affecting the Tyr side-chains in the system.

As with the other beta-sheet related systems most of Tyr side-chains favour states 3 and 4, suggesting the Tyrs are being influenced along their C to C_G dihedral angle making movements into states 1 and 2 unfavourable as can be seen in Figure 145 (below). This is shown most clearly by Tyr's A B and C, with only brief periods spent in the lower dihedral angle states for A and B and not until the end of the trajectory for C.

Furthermore, as well as having access to the all rotamer states, including states 5 and 6, Tyr's D and F also show a bias towards states 3 and 4, as expected from these stacked aggregate interactions.

Tyrs D- F all show initially a lot of movement, then become significantly more restricted in the later portions of the trajectory, which is the opposite of what happens for Tyrs A through C. These results follow the patterns seen previously and further show the movement of the Tyr under pressure from external forces such as aggregates.

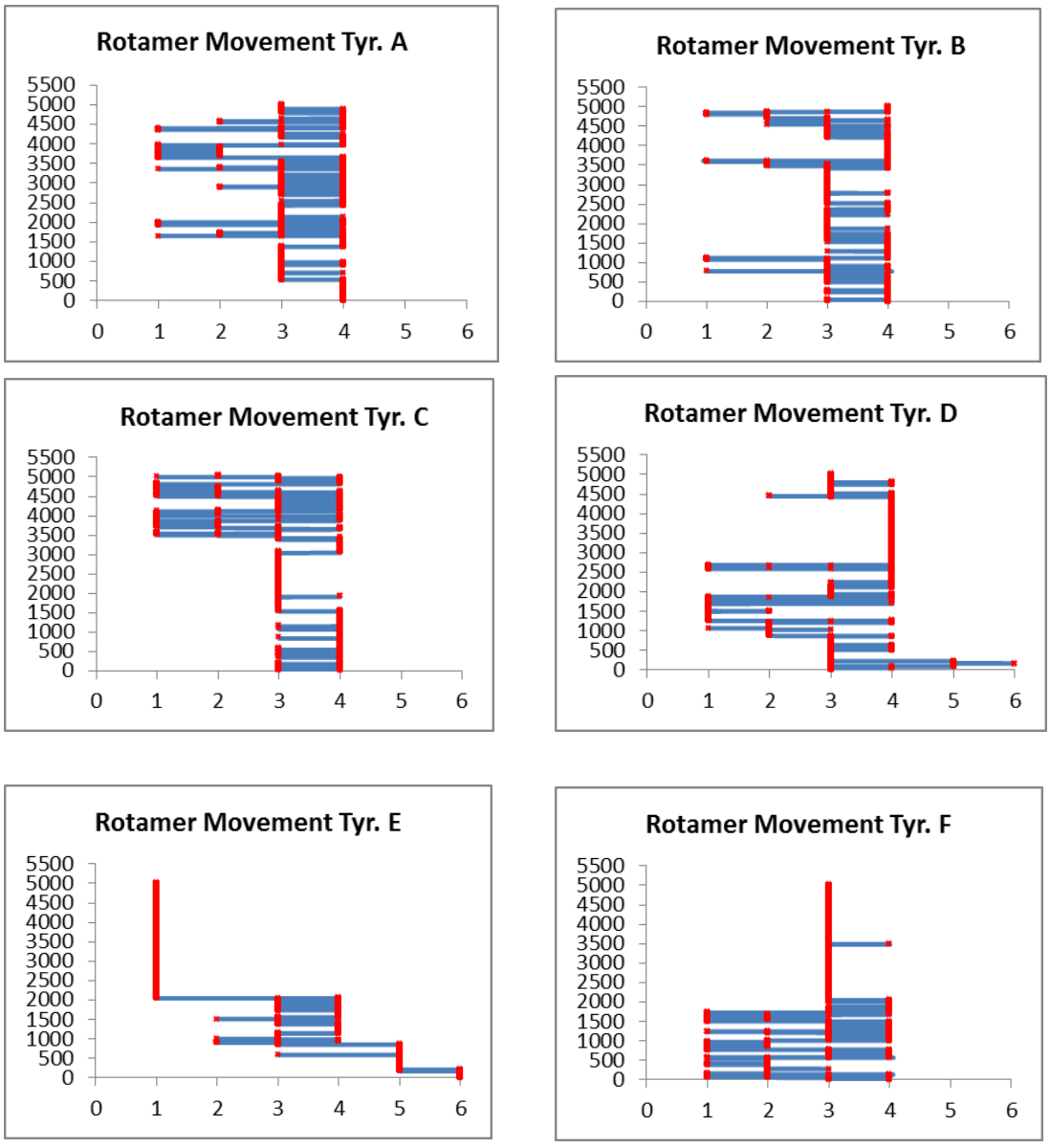

Figure 145 - Time Lapse Rotamer Responses of Beta-sheet Hexamer with Ions.

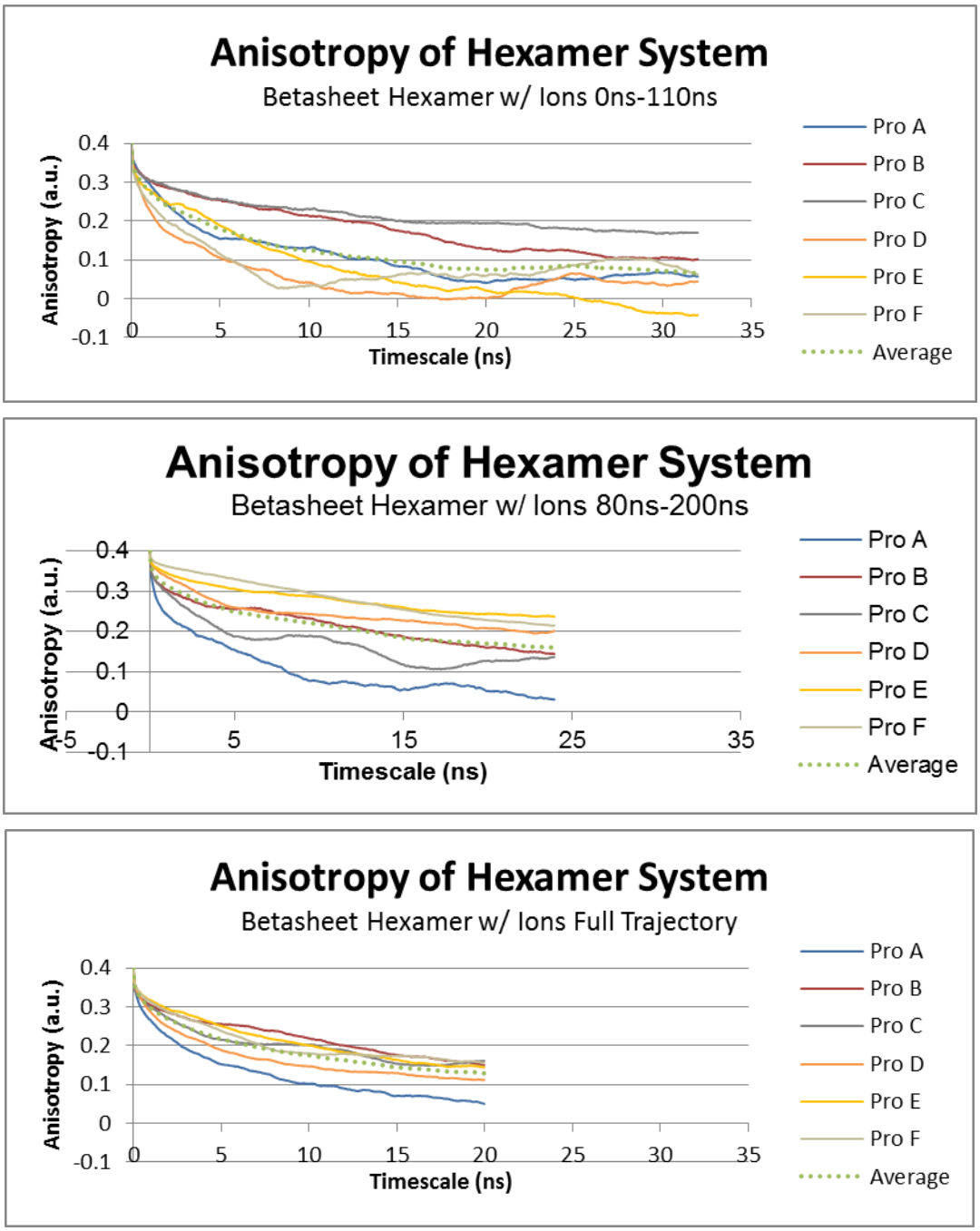

Figure 146 - Simulated Anisotropy of Beta-sheet Hexamer with Ions. These graphs shows the simulated anisotropy of Proteins A (blue), B (red), C (grey), D (orange), E (yellow) and F (tan) as well as the average (dotted green) within various analysis windows.

As the trajectory is 200ns in length, the analysis window can be altered, and as such three different analyses windows were chosen to create the above graphs seen in Figure 146. This is useful as the Tyr movements change drastically depending on which section of the trajectory is analysed. As they are part of such a large

aggregate it can be assumed that their rotational times will be very similar, and as such they will all have similar relaxation times (seen by the similar slopes in the decays for the relaxation period). This allows for an in depth analysis of the effects the Tyr has on the system.

The first has an analysis window of 0ns-110ns with a correlation time of 30ns (these are not comparable timescales.) As this is the first half of the trajectory, Proteins A through C have limited movement when compared to D to F due to their environments. This is reflected in the anisotropy decays as proteins B and C have short lived initial decays and protein A has a more pronounced initial decay relative to B and C. This is because it moves more often than the other two.

In contrast, Proteins D and F have the sharpest initial decay and lowest plateau levels as they have the highest degree of movements for their Tyrs within this analysis window. Tyr E has significantly less movement, and in fact its movements are comparable to Tyr A's and as such, have fairly similar decays. These results clearly shows the effect that Tyr side-chain movements have on the plateau level for systems, as their will be minimal effect from differing relaxation times. These results also directly agree with what is seen in the MC simulations, further strengthening this concept. This is because the Tyr residues appear fast moving and the bulk aggregate is slow moving as seen in Figure 143 and Figure 145, which are the simplified characteristics of the oligomer created in the MC simulations. The resulting anisotropies for both the MC and MD simulations have given similar results throughout this chapter.

The second analysis occurs during the 80ns-200ns time period within the trajectory and has a correlation time of 25ns. As expected the decay lines have swapped positions, as the Tyr's that are moving rapidly in the early stages, are now moving slowly, and vice versa. As such, Tyrs D to F all have high plateau levels, with short lived initial decays, with Tyr D being slightly quicker due to its larger degree of movement. Tyrs A through C all have sharp initial decays but retain an aggregate response due to their slow relaxation times. Tyr A is the most free to move and as such decays the quickest.

The final graph encompasses the total trajectory, and as such the initial decays are related to the average overall movement of each of the Tyr residues, which is why

the results are different from what is seen in the previous two graphs. A D and C have the most movement overall and as such have the sharpest decays. The relaxation periods are identical to the other graphs as expected. These results strengthen our understanding of what the Tyr side-chain environments are like and how they affect anisotropy, as well as how aggregate sizes affect the relaxation timescale of the system (Figure 46.)

7.8.1. Best Fits

Figure 147 and Table 13 show the best fit graphs for the beta-sheet hexamer with ions and the top two graphs give fairly similar results. The first graph has a τ_R value of 0.37ns for the fast mechanism and for the slow mechanism a τ_R value of 8.22ns, with a 0.12 and 0.23 contribution split.

The second fit has rotational times of 0.42ns and 14.57ns, which are also acceptable results. This graph is analysed after stabilisation has occurred and as such both the bulk aggregate and the Tyrs will be more stable and moving less, which could explain the slower rotational time. Unlike the previous two graphs the best fit for this system shows a much higher contribution from the Tyr side-chains than the backbone, this suggest that the backbone could be moving slowly and as such is not the driving force for the anisotropy decay. This seems sensible as the aggregate has become very large, and due to the limitations of the size of waterbox, it is interacting with itself which will hold the structure in place.

The third graph has similar variable results as the first graph with rotational times of 0.22ns and 7.94ns; this implies that the stabilisation greatly affects the results in an aggregate. As such, the second graph, taken after stabilisation, is the best indication of the nature of the movements within a beta-sheet hexamer system. This further shows the issues that the current experimental anisotropy method faces. Therefore, the most appropriate fit for this system is the second result, as the analysis window is post stabilisation.

7.9. $A\beta_{1-42}$ Beta-sheet Aggregates Comparative Results

(A)

Decay Curve	$r_{\infty T}+r_{\infty B}$	$r_{oT}-r_{\infty T}$	τ_T (ns)	$r_{oB}-r_{\infty B}$	τ_B (ns)	Correlation
Flat sheet Dimer (decay to 0)	0.00	0.17	0.33	0.23	2.56	0.970
Flat sheet Dimer (Best Fit)	-0.05	0.19	0.32	0.26	4.86	0.985
Stacked Dimer	0.10	0.05	0.02	0.25	2.08	0.976
L-Shape Trimer	0.00	0.06	0.05	0.34	5.45	0.991
Stacked Trimer	0.00	0.18	0.51	0.22	7.58	0.989
Flat Sheet Tetramer	-0.03	0.18	0.35	0.25	7.52	0.995
L-Shape Tetramer 1	0.10	0.17	1.00	0.13	17.48	0.981
L-Shape Tetramer 2	0.34	0.18	0.31	-0.12	25.00	0.943
B-Sheet Hexamer (no Ions)	0.15	0.07	0.18	0.18	9.34	0.996
B-Sheet Hexamer (0-110ns)	0.06	0.12	0.37	0.22	8.22	0.997
B-Sheet Hexamer (60-110ns)	0.13	0.12	0.36	0.15	8.92	0.994
B-Sheet Hexamer (80-200ns)	0.14	0.08	0.29	0.18	11.12	0.997
B-Sheet Hexamer (Full Traj.)	0.12	0.09	0.22	0.20	7.94	0.998

(B)

Decay Curve	Dimensions	τ_B
Flat sheet Dimer	33.5Å, 28.8Å, 39.5Å	2.56ns/ 4.86ns
Stacked Dimer	4.9Å, 26.31Å, 59.0Å	2.08ns
L-Shape Trimer	30.6Å, 40.5Å, 51.9Å	5.45ns
Stacked Trimer	9.7Å, 30.9Å, 57.6Å	7.58ns
Flat Sheet Tetramer	30.7Å, 60.6Å, 60.7Å	7.52ns
L-Shape Tetramer	30.1Å, 40.1Å, 71.4Å	17.48ns/ 25.00ns
B-Sheet Hexamer (no Ions)	27.7Å, 54.4Å, 86.6Å	9.34ns
B-Sheet Hexamer (Ions)	29.9Å, 57.6Å, 73.4Å	7.94ns/ 11.12ns

Table 13 – (A) Beta-sheet Anisotropy Best Fits Variables (B) Approximate Dimensions for Size Comparison.

In general, there is an increasing r_∞ value as the aggregate gets bigger as expected from literature [112] however, due to limitations in the length of trajectories, not all trajectories could be analysed post stabilisation. The early movement of the proteins as they try to find favourable positions, are included in the decays; skewing the results closer to an r_∞ 0 value.

The monomers from the previous sections rotate slower than the stacked dimer (which has a τ_B value of 2.08ns), which could be due to the size increase from a monomer to a tightly aggregated stacked dimer is insignificant, as the length of the protein is significantly longer than the difference created from stacking two proteins on top of each other. The monomers also rotate slower due to interactions with each other (and in some cases ions [175]). Whereas the stacked dimer has no other proteins to interact with, allowing it to move freely [112].

The contributions from both the fast and slow mechanisms are generally close to equal, with a preference towards the bulk rotation, with some instances of the Tyr contributions being significantly smaller, usually related to negative r_∞ values. The Tyr τ_T values stay fairly consistent as they all have very similar movement patterns. The notable outliers are the stacked dimer and L-shaped trimer, which have incredibly fast Tyr τ_T values due to the erratic rotamer movements, fitting the general pattern see in the previous chapters and other work [44]. The next notable trajectory is the L-shaped tetramer which has a τ_T value that is three times longer than most of the other Tyr's. This is due to the fact that the Tyr residues do not move as much during this trajectory as they are relatively more trapped as discussed above. The hexamer systems, on average, move between rotamer states frequently, and as such the lack of variance from the different analysis windows is reasonable as they all average out to be the same rough movements. This further shows that these Tyr rotational times seem reasonable for the simulations.

The bulk aggregate rotational times reveal the most information about these systems, with a steady increase in the τ_B values, which is expected as the aggregate gets bigger [112] [163]. Finally, all fits are very well correlated to the data; ensuring errors are at a minimum [168]. The exception to this is "L-shape tetramer 2" that has a correlation of 0.9431 which, although still perhaps acceptable, is relatively low compared to the rest. As explained above, this is due to fitting to the initial or secondary decay of the curve rather than the whole curve. This explains the unexpected result seen here, as it has a very high r_∞ value, caused by fitting to the initial drop in the decay rather than the drop to the lowest value. When this is considered, it also explains why the aggregate rotation is so long (25ns) as the fit is assumed to be significantly more aggregated than it actually is, perhaps a three exponential fit would be required.

By the end of the trajectory, the dimers shown in Table 13B have dimensions ~(33.5Å, 28.8Å, 39.5Å) for the flat-sheet dimer, and ~(4.9Å, 26.31Å, 59.0Å) for the stacked dimer. This explains why there is a difference in rotational times, as the stacked dimer is more compacted it can rotate faster around the x and y axes, however it should be noted that it would be slightly slower if it were to rotate purely around its z axis. In addition, the flat-sheet dimer is also larger at the start of its trajectory than at the end, which would further explain the slightly slower rotational time seen here [112] [163]. The results also show a general trend for as the dimensions of the aggregate get larger, the corresponding rotational times also take longer [112] [163].

The trimer systems also show anomalous results, as the dimensions would suggest that the L-shaped trimer should rotate more slowly, however, during the stabilisation process the proteins have to fold in on themselves, creating an artificially faster rotational time. The relative dimensions of the stacked trimer and the flat sheet tetramer are very different, however they have similar rotational times, this could be an error in the fitting or due to the fact that one is a rod shape and the other can be considered spherical, they both have similar dimensions along one axis and therefore could potentially rotate at similar speeds along these axes.

The L-shaped tetramer has a significantly longer rotational time despite having similar dimensions to that of the two hexamers. This can be explained by the rod-like shape associated with this aggregate, causing a very slow rotational time along one axis. The slow rotational time can be viewed in the trajectory as the proteins do move rotate and move, but along the axis in question it moves significantly less. Finally, the differences seen between the two hexamer rotational times, is due to the stabilisation process, when this process is included the times are almost identical. However, the longer rotational time associated with the late stages of the hexamer containing ions is due to the stabilisation process being completed. Therefore, there is no longer erratic movements and so the resulting rotational time is likely more accurate.

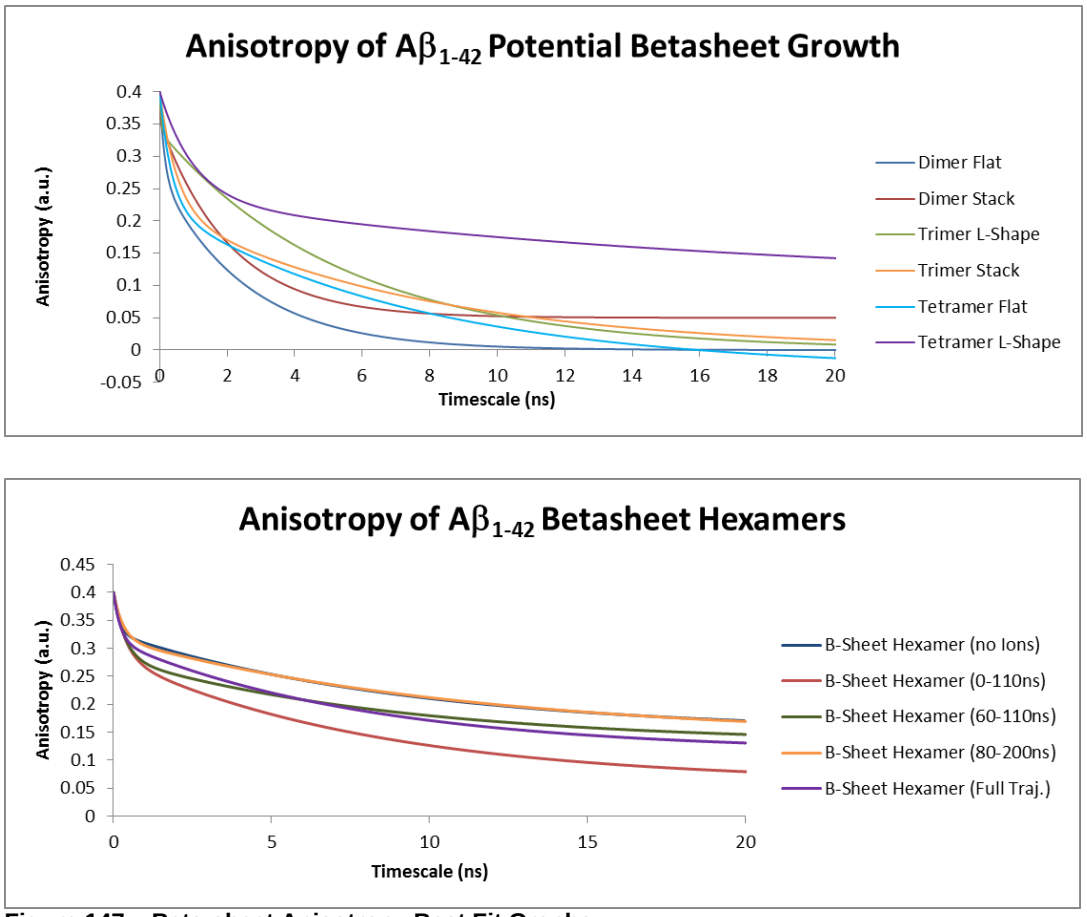

Figure 147 – Beta-sheet Anisotropy Best Fit Graphs

As the rotational times in Table 13 suggest that as the aggregate gets bigger the anisotropy decays take longer to decay to 0. The initial decays in Figure 147 reveal more about the systems in question.

Due to the fact that pre and post stabilisation are included for most of these trajectories, the systems are more complex and tend to have a secondary decay after the initial decay as explained for the L-shape tetramer [112]. As there are limitations in the two mechanism fit, the secondary decays seen in the actual anisotropy curves are not present in Figure 147.

For the actual average curves, the early stages of the trajectory will have fast moving aggregates as the proteins fold in on themselves and move more erratically. As they become stable the individual proteins in the aggregate will stop moving so erratically and a slower rotation will be seen that represents the bulk aggregate rotation. The initial decay in the anisotropy graphs is likely related to the slow moving aggregate and the slower decay to 0 is caused by the unstable initial stages.

By observing the graphs at the correlation time of 2ns, the initial decay can be analysed here as they decay to a higher point as the aggregate size increases. This further shows that the initial stages of the anisotropy decay reveal more about the Tyr movement and the secondary decays reveal more about the complexity of the system and how fast it rotates [112]. These results help give a clearer understanding of what causes the changes in anisotropy decays as aggregates get bigger.

It is also expected that the average results are different than the experimental results due to the smaller amount of Tyr side-chains available for analysis and also due to the simplification of the analysis as the excitation phase cannot be included in the MD [112] [163].

The bottom graph shows results from two different trajectories, however the hexamer with ions [162] has been analysed at different stages to see how this affects the decay. As expected, the decay has a lower plateau value when the initial stages are included, because the system is trying to find its most stable conformation, causing significant movement from the bulk aggregate, the individual protein backbones and the residues themselves. The r_∞ values take logical increases: with the lowest graph being only the initial stages, the second lowest being the full trajectory including the initial stages and the third lowest being the early midsection where some stabilisation will still be occurring. Interestingly, the system with no ions and the trajectory called “B-Sheet Hexamer (80-200ns)” are both analysed after stabilisation with the same correlation time used to create the anisotropy decay. They have almost identical decay curves, with only some minor differences near the start which only affects the rotation of the bulk aggregate rotation. The differences in the decay curves can be attributed directly to the bulk movement, and more specifically the Tyr movement for the particular widow being analysed. This is reflected in Table 13 as they have similar resulting r_∞ values, contributions and Tyr τ_T values. The τ_B value for the bulk aggregate is slightly slower with ions. Other than the structural differences seen in the trajectories, most notably the stabilisation of the initial structure, the slowing of the bulk aggregate rotation appears to be the only affect that the ions have had on the system as the graphs appear almost identical.

7.10. The New Rotamer States

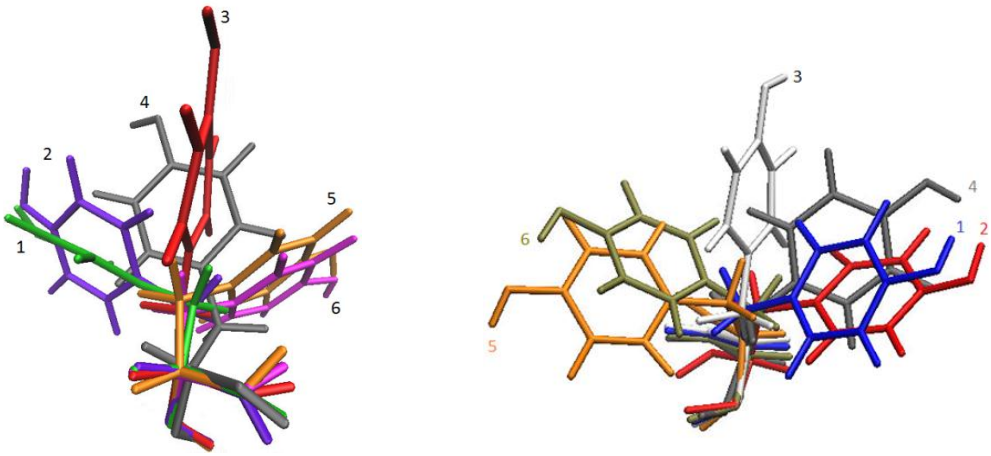

Figure 148 – Two examples of the rotamer states six rotamer states

There are traditionally only four rotamer states seen for Tyr in beta amyloid [44], which is demonstrated in the amorphous aggregates for $A\beta_{1\text{-}40}$ and $A\beta_{1\text{-}42}$ (see previous chapters). However as seen in Figure 148, there are six states that the Tyr side-chain can occupy in a trajectory for a beta-sheet aggregate. There is also minor variation between positions that each rotomer state can be in. The trajectory studied in detail in Figure 148 - Figure 151 is Tyr F in the beta-sheet hexamer with no ions simulation as it most clearly depicts all six rotamer states.

These states are somewhat paralleled in the spectroscopy experiments [44]. Each experimental lifetime represents a possible Tyr environment, three are seen for non-aggregating systems and three or four are present when aggregation occurs as seen in chapter 3. These Tyr environments could be connected to the rotamer state environments here. Though the number of rotamers is larger than that of the lifetimes, this is explained by quenching, as certain environments (rotamer states) will not fluorescence. This is further strengthened by the formation of beta-sheets and the appearance of the two new rotamer states, which can be compared directly to the extra lifetime possibly found post-aggregation in experiments. The changes in lifetimes seen during the aggregation could be due to the Tyr residue moving into the other rotamer states, where they are more buried (see below) which could cause less quenching [44] [112].

Assuming the fourth lifetime is not due to background noise, the reason for it being present from the beginning of the experiment is because aggregation occurs rapidly

and perhaps protofibrils (oligomers) are forming before the first measurement is even taken and so this fourth lifetime (possible rotamer state) is already present / no longer quenched. The rapid aggregation of oligomers to protofilaments still does not occur until the much later stages, judging by the results in this work.

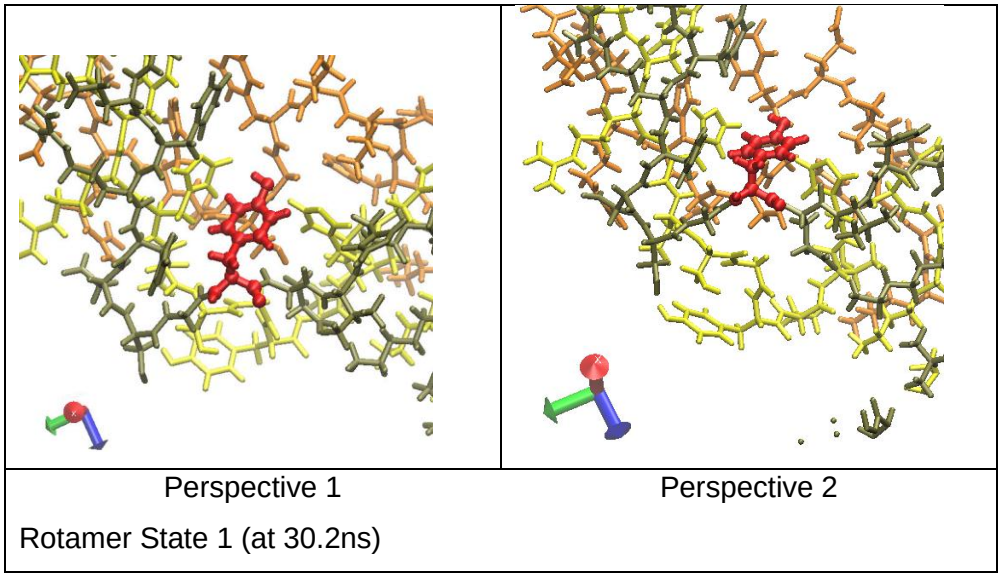

Perspective 1	Perspective 2
Rotamer State 1 (at 30.2ns)	

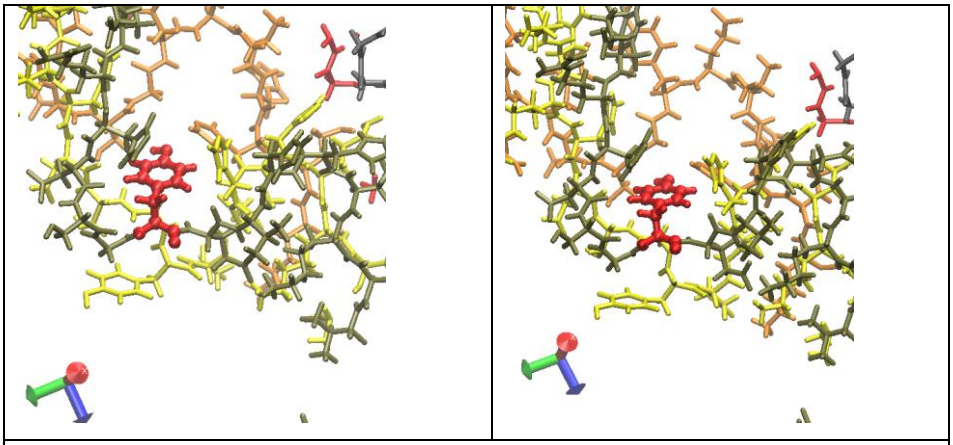

Perspective 1	Perspective 2
Rotamer State 2 (at 9.84ns)	

Figure 149 - Rotamer States 1 and 2 (in red and CPK visualisation) with surrounding protein chains viewed from two angles

As can be seen from Figure 149 rotamer states 1 and 2 have very little interaction with the surrounding backbones and residues and therefore the C to C_G dihedral angle has no limitations influencing it. As such they are not twisted and have full movement to occupy the state they prefer. These states appear to be most common

in monomers but can still be occupied during both amorphous and fibril aggregation (see previous chapters). The reason that these states are preferred by monomers appears to be because the Tyr side-chains are not interacting with other protein backbones and so, are less likely to interact with its own surrounding residues in such a way that they would be forced into the other states as readily (as shown by the absence of the fifth and sixth state, and the low populations of third and fourth states). The distinction between these two rotamers is clear as the backbones are in similar positions for both figures and the aromatic rings are tilted in different directions as shown in Figure 149.

For the trajectory in question, the Tyr begins in state 4 before entering state 1; there are interactions with the surrounding residues during this period which affects the Tyr side-chain and influences it into occupying state 4. It then moves to the position seen in Figure 149 which is state 1. The Tyr then begins to occupy state 4 again once the interactions with the surrounding residues and backbones begin to occur again.

It should be noted that systems that tend to remain in the lower states have very little movement, staying in one rotamer state for extended times, as seen with a lot of the $A\beta_{1\text{-}40}$ proteins. Though not always true it can explain the slower rotational times associated with the Tyr residues.

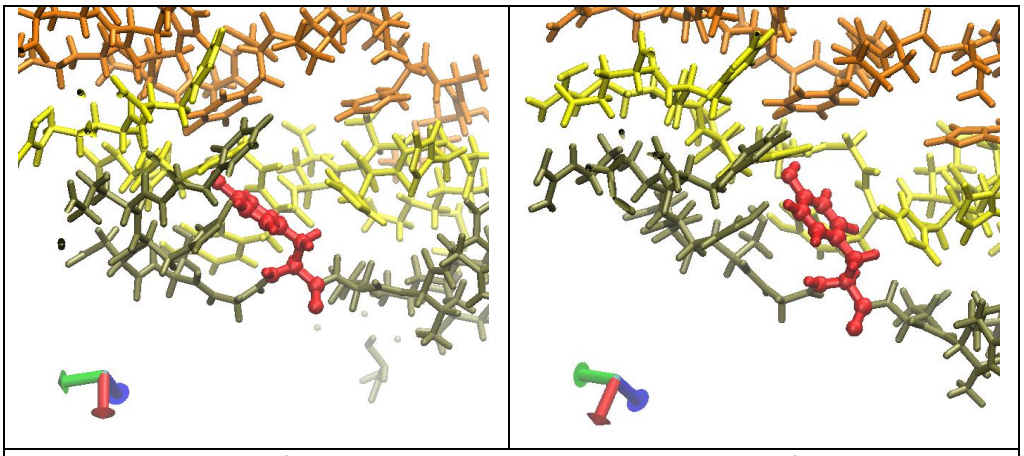

Perspective 1 Perspective 2

Rotamer State 3 (at T=0.32ns)

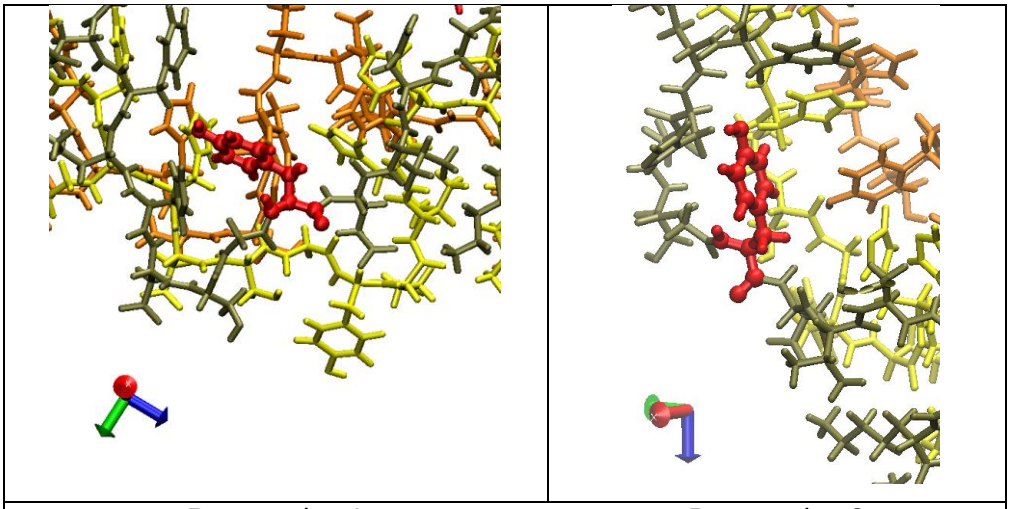

Perspective 1 Perspective 2

Rotamer State 4 (at T=2ns)

Figure 150 - Rotamer States 3 and 4 (in red and CPK visualisation) with surrounding protein chains viewed from two angles

Figure 150 demonstrates rotamer states 3 and 4 for the Tyr residue, which can be seen interacting more closely with the surrounding backbones and residues than states 1 and 2. The Tyr side-chain can still move with a relative amount of freedom, but has been influenced by the environment as the surrounding residues are closer, inducing a more defined twist in the rotamer's C to C_G angle influencing the Tyr into occupying states 3 and 4. These states appear to be common amongst the aggregated systems but are still present for monomers to a lesser degree (as seen previous chapters) as surrounding residues in monomers will still interact and cause

this twisting. Note that in Figure 150 the difference between states 3 and 4 is the twisting motion of the aromatic ring as the backbone is in a similar position in all images for perspective 1. The overall position of the Tyr residue is different from what was seen in states 1 and 2 as the aromatic ring is bending in a different (and more severe) direction perpendicular to the backbone.

The trajectory begins with the Tyr in state 4 before moving into state 3 which are both shown above at appropriate timestamps. After being in state 3 briefly the Tyr moves back into state 4. Constant movement between two rotamer states is common in many trajectories discussed and is due to the C to C_G dihedral angle being influenced by the surrounding environment not allowing it to move, but the other dihedral angle moves freely as it is not affected by the configuration.

Tyrs that prefer states 3 and 4 (and also states 5 and 6) tend to move between these states rapidly, preferring to occupy a different state as often as possible. This explains the faster rotational times associated with aggregates seen throughout the last three chapters.

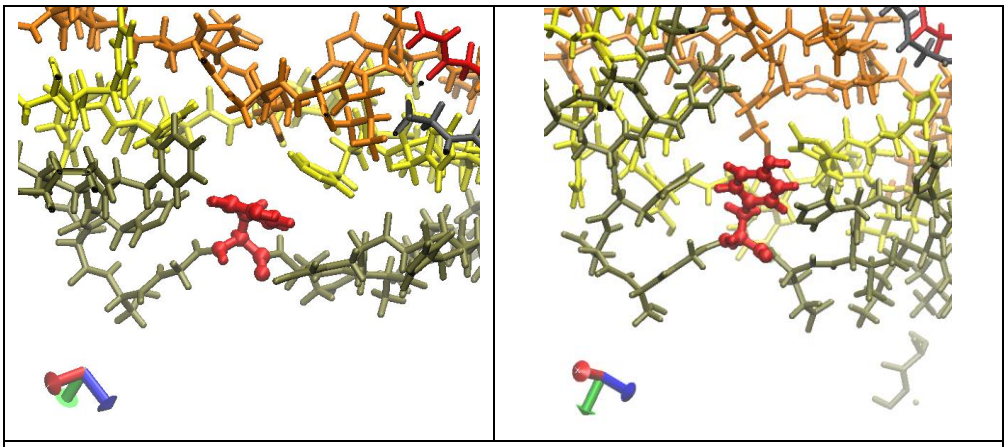

Perspective 1 Perspective 2

Rotamer State 5 (at 76.28ns)

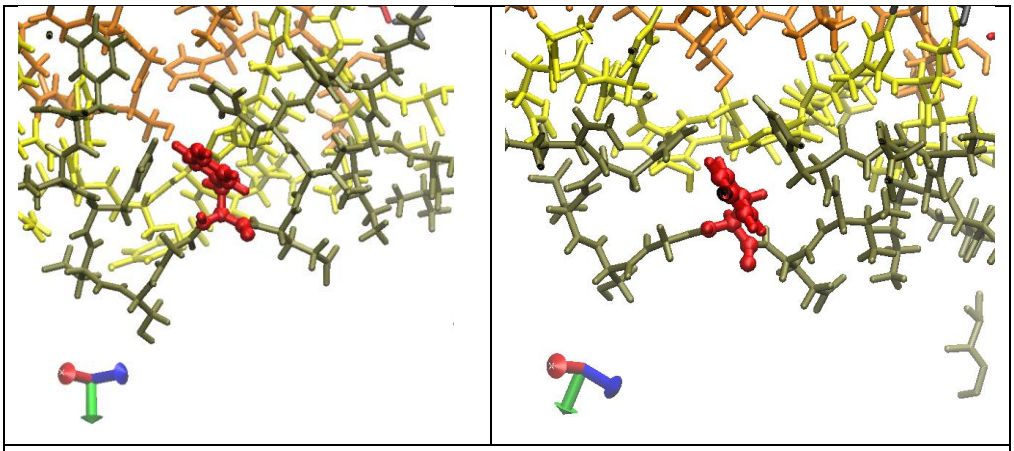

Perspective 1 Perspective 2

Rotamer State 6 (at 64.6ns)

Figure 151 - Rotamer States 5 and 6 (in red and CPK visualisation) with surrounding protein chains viewed from two angles

The Tyr side-chain occupies state 4 before moving into state 6. From state 6 it moves into state 5 (both depicted in Figure 151) before finally moving to state 3. The surrounding residues from the aggregated protein backbones are significantly closer to the Tyr side-chain than seen previously, which heavily affects its movements and forces the Try into a more twisted state. These states have only been viewed in the beta-sheet aggregates, as it appears that they need to be tightly packed in order to have the interactions required to influence the Tyr's dihedral angles. This also implies that when a Tyr side-chain is in states 3 or 4, the surrounding residues and backbone are what influence and twist the Tyr into states 5 or 6 explaining why

jumps from 3 or 4 to states 5 or 6 can be made and vice versa. It is clear that states 5 and 6 have a more pronounced bend perpendicular to the backbone than the previous states due to the surrounding interactions forcing it to take on this state, and the twisting motion of the aromatic ring indicates the difference in states 5 and 6.

It is logical that states 5 and 6 can occur one after another as described; as the C to C_G dihedral angle will have limited movement due to the surrounding interactions. This suggests that only the C_A to C_{D1} dihedral angle will be able to move, which allows the Tyr to occupy the two states. The Tyr side-chain will be free to move when the surrounding backbone residues move away from it, allowing the Tyr to move from states 5 or 6 into states 3 or 4 and vice versa when the backbone moves closer. This explains the pattern seen for the rotamer state movements; moving from state 3 or 4 to state 5 or 6 or instead moving from state 5 or 6 to state 3 or 4.

Table 14 (below) arbitrarily depicts when a rotamer state has been detected to a significant degree (judged by eye) for all the simulations. This means that if there is a relatively small percentage of a particular state occupation (<1% occupation of state 2 for example) relative to the thousands of instances of other states being occupied, then it is not considered detected. Amorphous aggregates and monomers share similar Tyr rotamer state occupation. They all show an equal distribution of the rotamer states except a minor preference towards states 2 (though not significantly). In contrast, Tyr rotamer states of proteins with a beta-sheet protofibril show a distinct shift towards states 3 and 4. These preferences cannot be definitively conclude, as the trajectories are not run long enough. However, it can be concluded that there are no signs of states 5 and 6 unless the tightly stacked beta-sheet aggregate is formed (shown to be a low proportion).

(A)

$A\beta_{1-40}$ Monomer	Significant Appearances	Proportions
State 1	3	0.231
State 2	4	0.308
State 3	3	0.231
State 4	3	0.231
Total	13	

(B)

$A\beta_{1-42}$ Monomer	Significant Appearances	Proportions
State 1	6	0.261
State 2	7	0.304
State 3	6	0.261
State 4	4	0.174
Total	23	

(C)

$A\beta_{1-40}$ Aggregate	Significant Appearances	Proportions
State 1	10	0.303
State 2	11	0.333
State 3	6	0.182
State 4	6	0.182
Total	33	

(D)

$A\beta_{1-42}$ Aggregate	Significant Appearances	Proportions
State 1	10	0.250
State 2	12	0.300
State 3	9	0.225
State 4	9	0.225
Total	40	

(E)

$A\beta_{1-42}$ Protofibril	Significant Appearances	Proportions
State 1	16	0.176
State 2	16	0.176
State 3	27	0.297
State 4	25	0.275
State 5	4	0.044
State 6	3	0.033
Total	91	

Table 14 - Population of Rotamer states in various types of simulations. (A) and (B) are the rotamer states shown most prominently by Tyr side-chains in monomers in $A\beta_{1-40}$ and $A\beta_{1-42}$ respectively. (C) and (D) are the rotamer states shown most prominently by Tyr side-chains in amorphous aggregates in $A\beta_{1-40}$ and $A\beta_{1-42}$ respectively. (E) contains the rotamer states shown most prominently by Tyr side-chains in proteins that are part of a beta-sheet $A\beta_{1-40}$ and $A\beta_{1-42}$ respectively.

There are significant changes to the lifetimes during the first 10 hours of experiments, both in the work presented here and in other work [44] [77], but significant aggregation occurs from around 5 hours and continues throughout the experiment (which can be as long as 3 or 4 days). Assuming these rotamer states are connected to the lifetimes, it implies that the early changes to the lifetime environments are related to changes in conformation of the Tyr side-chains seen here. It is clear that monomers prefer states 1 and 2 but can reach states 3 and 4. One of these states could be quenched, explaining why it does not have an associated lifetime. As the amorphous aggregates form, all four states appear to be

more favourable and once the beta-sheets form the fifth and sixth states begin to appear. This could give rise to the fourth lifetime seen in the experiments (assuming both states 5 and 6 have similar lifetimes, or one of the new rotamer states is quenched). These results suggest that the environmental changes seen in the experiments could be due to the misfolding and beta-sheet formation [49] [63] [172]. The true mechanisms are still hidden and require accurate size distributions over time for a more accurate depiction of what is causing the environmental changes, although MD does give us some idea of what could be happening.

7.11. $A\beta_{1-42}$ Protofibrils and Aggregation Conclusions

In conclusion, the trajectories studied in chapter 7 demonstrate the general shape and configuration of a small protofibril use as the building block for fibril formation [63]. The results suggest that there is beta-sheet sections within these protofibrils which are used to maintain its shape and to keep the proteins aggregated closely [49] [63] [171]. These sections are in the vicinity of Glu_3-Arg_5, Gln_{15}-Phe_{20}, Ile_{31}-Gly_{33} and Gly_{38}-Ile_{41}, with some variation seen due to the random nature of the simulations. The intermediate forms are not as stable making many of the candidates unlikely to be part of the aggregation pathway. The most stable of these was the stacking process (stacked dimer and trimer), this has been seen in other work with Aβ fragments giving credibility to the findings [48]. They are the most stable as they do not readily lose their beta-sheet structuring.

The most common rotamer states (3 and 4) are found to be stabilised during aggregation, making them favourable when the Tyr residue has minor external influences. This includes interactions with neighbouring residues on the same backbone as the Tyr, explaining why it is also seen in amorphous aggregates. The two new rotamer states for the Tyr residues found in this chapter only appear in tightly aggregated situations where there are significant external influences from other protein backbones, which can possibly explain the different lifetime responses found in the fluorescence experiments shown between non-aggregating and aggregated systems. This is due to the lifetimes representing different local environments, and the rotamer states found using MD also could be considered to be representing different lifetimes. The differences in the number of rotamers compared to the life times can be explained as some of these rotamer states may

be quenched due to the close proximity of the Tyr residues (causing photons repeatedly excite Tyr residues rather than being detected) [112].

The results for the simulated anisotropy are also consistent with what has been seen in the previous two chapters. As the aggregate gets bigger the graphs of anisotropy suggest a much slower rotation as the decay to 0 takes longer [112] [163]. In some cases the graph cannot decay to 0 within the timeframe of the analysis and in others it will not decay to 0 at all. The initial decay can be directly linked to the Tyr residue as it is clear from the results that a free moving Tyr residue will have a sharp initial decay and a slow moving Tyr residue that is perhaps stuck in one rotamer state for long periods will have a slow initial decay [112] [163]. This was seen most clearly with the protofibril structures. Furthermore, the fitting parameters and equations used for the simulated anisotropy graphs show promising results based of statistical correlations [168] that could be the ground work of making fully simulated anisotropy studies that could eventually account for the excitation and emission of the photons. The results in this section give novel insight into the Tyr residue and its surrounding environment as well as a detailed outlook of the conformational changes within these protofibril structures.

8. Conclusion

In conclusion, fluorescence spectroscopy has been used in order to probe potential environments that $A\beta_{1-40}$ can aggregate in [112]. The results showed no aggregation in deionized water or dilute HCl at pH 7 and 5.5 respectively. Despite this, $A\beta_{1-40}$ MD simulations in water (with and without ions) revealed the potential for some amorphous aggregation. This is likely due to the supersaturated concentrations of the simulation as the waterbox is small relative to an experimental sample [44]. Nonetheless, the MD aggregation was minimal and there was not enough time for fibrils to form. Longer simulations are required, though are not currently reasonable due to the present limitations of processing power within super computers such as ARCHIE-WeSt.

Fluorescence spectroscopy also revealed lifetime contributions and potential aggregation changes for $A\beta_{1-40}$ samples containing NaOH [112] [163]. These changes indicate a lifetime that was not present before and has an initial value of 20ns which drops to 10ns within 10 hours of the experiment starting as seen in this work and others [44]. However it is difficult to determine if one of the shorter lifetimes found in the aggregating samples is scattered light, or a lifetime from the Tyr residues themselves, as it is a similar size to the channel width (lifetime is around 30ps, channel width is 13.5ps/channel) [163]. The aggregation has been confirmed both by fluorescence anisotropy and DLS measurements taken over the course of 3-4 days. The changing lifetime contributions are caused by the changes to the environment of the Tyr residues [112]. A clearer picture of the movements is revealed in the MD simulations. The aggregates become more tightly packed, and the Tyr residues are more likely to be protected from the surrounding water, preventing some quenching from occurring, which in turn can change the lifetime contributions associated with the systems [112].

It was also revealed that after the first 10 hours or so that the lifetime contributions became constant, implying that the environments are no longer changing [112] [163]. However, as was shown with the anisotropy and DLS measurements, aggregate sizes continued to increase after these initial 10 hours. This implies that the Tyr residues find their stable environment's before the aggregation is complete, suggesting the oligomers are protofibrils. MD simulations reveal characteristics of beta-sheet oligomers, which are a likely shape for these early stage aggregates [63].

These oligomers can theoretically form and stack endlessly until no monomers are left [50] [63]. These MD beta-sheet structures appear to have six rotamer states available for the Tyr residues to occupy, which are not seen in amorphous aggregates or monomers. This has been revealed to be due to their local environments pressuring them into these orientations and can only occur in the beta-sheet model due to the close proximity of neighbouring protein backbones.

The monomers and amorphous aggregates consistently show between 1 and 4 rotamer states, depending on the local Tyr environments and length of trajectory. Regardless of unique local environments, statistically all four rotamer states are present when enough proteins are in the system (such as in an experimental sample though previous results suggested only 3 [44]). This is potentially comparable to the results seen for the fluorescence spectroscopy, as the lifetimes revealed here are different local environments associated with the Tyr residues [112]. It was revealed that there are three lifetimes associated with the experiments containing non-aggregating $A\beta_{1-40}$ and potentially four for the experiments which aggregated. These lifetimes and rotamer states are potentially closely linked and the reason that only three lifetimes are present in the experiments (as opposed to the four environments seen in the simulations) could be due to the quenching of the fourth lifetime. This could potentially be another measure of when aggregation occurs; a fourth lifetime begins to contribute. The appearance of this new lifetime could be due to presence of the fifth or sixth rotamer state appearing once beta-sheets form which do not get quenched. Further research into this area could reveal more about the stages of $A\beta$ aggregation, and could lead to a clearer understanding of the aggregation pathway.

The DLS measurements reveal photon count / intensity increases overtime, suggestive of an increasing aggregate size. Apart from this, DLS measurements for both samples in NaOH and HCl reveal very little, due to high polydispersity, which is likely caused by multiple species being present in both systems. This suggests that aggregates begin forming for the NaOH samples even before the first measurement has been taken as the initial stages of $A\beta$ aggregation are incredibly rapid. This also implies that the HCl samples have multiple species within them. However, as the spectroscopy results revealed no changes to the lifetimes and therefor no changes to the Tyr environments, it suggests that the $A\beta$ samples cause too much noise to

obtain quantifiable results, even in the early stages, when at most monomers and oligomers / small amorphous aggregates are likely to be present. An alternative buffer to HEPES that causes less noise in DLS measurements is PBS buffer, however this was not deemed necessary within the work presented here as the Aβ proteins themselves are clearly showing signs of causing too much scatter as is seen with the water, HCL and NaOH measurements. Further work with other buffers and using DLS equipment more suited to Aβ aggregation must be attempted to gain a better understanding of the size distributions over time associated with Aβ aggregation.

This is also true for fluorescence experiments, specifically anisotropy. The low photon count detected creates issues constructing the necessary histograms for $I_{\parallel}$ and $2I_{\perp}$ used to form the anisotropy curve [112]. The time taken to complete each measurement is too long and creates substantial noise within the results, due to the formation of aggregates occurring during the analysis window. This makes analysis of the results difficult and very little can be revealed about the systems. Regardless, the anisotropy reveals the presence of multiple aggregate sizes, which could be partially due to the long measurement time, although this was also apparent in DLS results. Though very little can be revealed about the sizes due to the noise, it has successfully been compared to simulated MD anisotropy results and simulated MC anisotropy, both of which reveal that the sharp initial decay is caused by the Tyr residue moving very quickly and the slower decay is caused by the aggregate rotation itself. The Tyr movements have been studied in depth and compared to the resulting anisotropy graphs and the variation in initial decay was always due to differences in the Tyr environment. This can be compared to the experimental results as there were changes to the initial decay as the aggregation progressed, though there was a lot of noise in these initial values. The longer decay time associated with the bulk rotation was also studied by comparing the larger MD aggregates to the smaller ones, and saw that this created slower final decays to 0. These results show how anisotropy probes the early stages of aggregation and we have interpreted this in terms of the diffusion of the Tyr residues.

MD simulations also share similarities with work found in literature. Both $A\beta_{1\text{-}40}$ and $A\beta_{1\text{-}42}$ show conformational changes before fibril aggregation can occur, which may

be indicative of the misfolding processor the aggregate. The shape is similar to the horseshoe or hairpin motif's discussed in literature.

In future, lower concentrations of Aβ samples would allow for a slower aggregation which could be more readily studied, as some initial stages have potentially been missed in these experiments. We believe that a suitable experimental setup for both DLS and fluorescence anisotropy will allow for the accurate depiction of the size distribution in the Aβ samples, which can then be compared to MC simulations that probe the potential aggregate pathways associated with them. If a MC model can be made that fits the experimental results, it could potentially reveal the true aggregation pathway for Aβ and further work could focus on the various stages seen in these MC simulations.

Longer MD simulations or larger initial simulations that start from pre-aggregated amorphous aggregates could reveal more about these stages too. For example, how the amorphous aggregates form the beta-sheet oligomers could also be revealed with large enough systems, longer trajectories or advanced simulation techniques. As many of these methods are limited by the current available processing power, the simulation of smaller Tyr containing peptides would allow for larger aggregates to be probed on a computationally accessible level and could reveal more about both the rotamer states and what effects the local Tyr environments have on them, as well as give more insight into how aggregation affects anisotropy.

9. Appendices

Works Cited

[1] M. A. Brodney and L.-F. Lau, Alzheimer's Disease (Topics in Medicinal Chemistry), Springer, 2010.

[2] M. Guerchet, M. Prina and M. Prince, “World Alzheimer Report 2013: Journey of Caring: An analysis of long-term care for dementia,” King's College London, London, 2013.

[3] B. O, W. Stenzel, D. Hilton-Jones, M. Sandri, O. Boyer and B. Engelen, “Amyloid deposits and inflammatory infiltrates in sporadic inclusion body myositis: the inflammatory egg comes before the degenerative chicken,” Acta Neuropathol, vol. 129, no. 5, pp. 611-624, 2015.

[4] S. Bedrood, Y. Li, J. M. Isas, B. G. Hegde, U. Baxa, I. Haworth and R. Langen, “Fibril Structure of Human Islet Amyloid Polypeptide,” The Journal of Biological Chemistry, vol. 297, pp. 5235-41, 2012.

[5] W. R. Markesbery, “Oxidative stress hypothesis in Alzheimer's disease,” Free Radical Biology and Medicine, vol. 23, no. 1, pp. 134-147, 1997.

[6] J. C. Stroud, C. Liu, P. K. Teng and D. Eisenberg, “Toxic fibrillar oligomers of amyloid-β have cross-β structure,” Proceedings of the National Academy of Sciences of the United States of America, vol. 109, no. 20, pp. 7717-7722, 2012.

[7] S. Jannis, “Alzheimer's Assocation,” Jannis Productions, [Online]. Available: http://www.alz.org/braintour/healthy_vs_alzheimers.asp. [Accessed 13 08 2017].

[8] V. A. Wagoner, M. Cheon, I. Chang and C. K. Hall, “Impact of sequence on the molecular assembly of short amyloid peptides,” Proteins: Structure, Function, and Bioinformatics, vol. 82, no. 7, p. 1469–1483, 2014.

[9] K. Kirshenbaum and V. Daggett, “pH-Dependent Conformations of the Amyloid β-(1 – 28) Peptide Fragment Explored using Molecular Dynamics,” Biochemistry, vol. 34, p. 7629–7639, 1995.

[10] A. Zykwinska, M. Pihet, S. Radji, J. Bouchara and S. Cuenot, “Self-assembly of proteins into a three-dimensional multilayer system,” Biochimica et Biophysica Acta, vol. 1844, no. 6, pp. 1137-44, 2014.

[11] H. Li, F. Rahimi, S. Sinha, P. Maiti, G. Bitan and K. Murakami, “Amyloids and Protein Aggregation – Analytical Methods,” in Encyclopedia of Analytical Chemistry, Chichester, John Wiley & Sons Ltd, 2009.

[12] M. Gralle and S. T. Ferreira, “Structure and functions of the human,” Progress in neurobiology, vol. 82, pp. 11-32, 2007.

[13] J. L. Holtzman, “Cellular and animal models for high-throughput screening of therapeutic agents for the treatment of the diseases of the elderly in general and Alzheimer’s disease in particular,” Frontiers in Pharmacology, vol. 4, no. 59, pp. 1663-9812, 2013.

[14] M. P. Marzolo and G. Bu, Seminars in cell & developmental biology, vol. 20, pp. 191-200, 2009.

[15] D. J. Selkoe, “Translating cell biology into therapeutic advances in Alzheimer's Disease,” Nature, vol. 299, pp. 23-31, 1999.

[16] H. Zheng and E. H. Koo, “The amyloid precursor protein: beyond amyloid,” Molecular neurodegeneration, vol. 1, p. 5, 2006.

[17] M. Amaro, in Photophysical Studies of Amyloid Aggregation, 2011, p. 12.

[18] J. W. &. S. Ltd, “Nomenclature and Symbolism for Amino Acids and Peptides.,” Eur. J. Biochem, vol. 138, no. 1, pp. 9-37, 1984.

[19] I. T. Marsden, L. S. Minamide and J. R. Bamburg, “Amyloid-β-Induced Amyloid-β Secretion: A Possible Feed-Forward Mechanism in Alzheimer's Disease,” Journal of Alzheimer's Disease, vol. 24, no. 4, pp. 681-691, 2011.

[20] C.-C. Lee, A. Nayak, A. Sethuraman, G. Belfort and G. J. McRae, “A three-stage kinetic model of amyloid,” Biophysical journal, vol. 92, pp. 3448-3458, 2007.

[21] N. Carulla, M. Zhou, M. Arimon, M. Gairi, E. Giralt, C. V. Robinson and C. M. Dobson, “Experimental characterization of disordered and ordered aggregates populated during the process of amyloid fibril formation,” Proceedings of the National Academy of Sciences of the United, vol. 106, pp. 7828-7833, 2009.

[22] S. e. a. Bernstein, “Amyloid-b protein oligomerization and the importance of tetramers and dodecamers in the aetiology of Alzheimer’s disease,” Nature Chemistry, vol. 1, no. 4, pp. 326-331, 2009.

[23] M. Hiltunen, T. v. Groen and J. Jolkkonen, “Functional roles of amyloid-beta protein precursor and amyloid-beta peptides: evidence from experimental studies,” Journal of Alzheimers Disease, vol. 18, no. 2, pp. 401-412, 2009.

[24] S. Sadigh-Eteghad, M. Talebi, M. Farhoudi, S. E. Golzari, B. Sabermarouf and J. Mahmoudi, “Beta-amyloid exhibits antagonistic effects on alpha 7 nicotinic acetylcholine receptors in orchestrated manner,” Journal of Medical Hypotheses and Ideas, vol. 8, no. 2, pp. 49-52, 2014.

[25] Y. Luo, B. Bolon, M. A. Damore, D. Fitzpatrick, H. Liu, J. Zhang, Q. Yan, R. Vassar and M. Citron, “BACE1 (β-secretase) knockout mice do not acquire

compensatory gene expression changes or develop neural lesions over time," Neurobiology of Disease, vol. 14, no. 1, pp. 81-88, 2003.

[26] M. A. Bogoyevitch, I. Boehm, A. Oakley, A. J. Ketterman and R. K. Barr, "Targeting the JNK MAPK cascade for inhibition: basic science and therapeutic potential," Biochimica et Biophysica Acta (BBA) - Proteins and Proteomics, vol. 1697, no. 1-2, pp. 89-101, 2004.

[27] M. Tabaton, X. Zhu, G. Perry, M. A. Smith and L. Giliberto, "Signaling effect of amyloid-β42 on the processing of AβPP," Experimental Neurology, vol. 221, no. 1, pp. 18-25, 2010.

[28] K. Zuo, J.-S. Gong, K. Yanagisawa and M. Michikawa, "A novel function of monomeric amyloid beta-protein serving as an antioxidant molecule against metal-induced oxidative damage," The Journal of Neuroscience, vol. 22, no. 12, pp. 4833-4841, 2002.

[29] R. Baruch-Suchodolsky and B. Fischer, "Aβ40, either Soluble or Aggregated, Is a Remarkably Potent Antioxidant in Cell-Free Oxidative Systems," Biochemistry, vol. 48, no. 20, pp. 4354-4370, 2009.

[30] Z.-X. Yao and V. Papadopoulos, "Function of beta-amyloid in cholesterol transport: a lead to neurotoxicity," The FASEB Journal, vol. 16, no. 12, pp. 1677-1679, 2002.

[31] U. Igbavboa, G. Sun, G. Weisman and W. Wood, "Amyloid β-protein stimulates trafficking of cholesterol and caveolin-1 from the plasma membrane to the Golgi complex in mouse primary astrocytes," Neuroscience, vol. 162, no. 2, pp. 328-338, 2009.

[32] B. Maloney and D. K. Lahiri, "The Alzheimer's amyloid β-peptide (Aβ) binds a specific DNA Aβ-interacting domain (AβID) in the APP, BACE1, and APOE promoters in a sequence-specific manner: Characterizing a new regulatory motif," Gene, vol. 488, no. 1-2, pp. 1-12, 2011.

[33] J. A. Bailey, B. Maloney, Y.-W. Ge and D. K. Lahiri, "Functional activity of the novel Alzheimer's amyloid β-peptide interacting domain (AβID) in the APP and BACE1 promoter sequences and implications in activating apoptotic genes and in amyloidogenesis," Gene, vol. 488, no. 1-2, pp. 13-22, 2011.

[34] S. Soscia, J. Kirby, K. Washicosky, S. Tucker, M. Ingelsson, B. Hyman, M. Burton, L. Goldstein, S. Duong, R. Tanzi and R. Moir, "Functional activity of the novel Alzheimer's amyloid β-peptide interacting domain (AβID) in the APP and BACE1 promoter sequences and implications in activating apoptotic genes and in amyloidogenesis," PlOS One, vol. 5, no. 3, 2010.

[35] M. R. Palmert, M. B. Podlisny, D. S. Witker, T. Oltersdorf, L. H. Younkin, D. J. Selkoe and S. G. Younkin, "The beta-amyloid protein precursor of Alzheimer

disease has soluble derivatives found in human brain and cerebrospinal fluid," Proceedings of the National Academy of Sciences of the United States of America, vol. 86, no. 16, p. 6338–6342, 1989.

[36] G. Irvine, O. El-Agnaf, G. Shankar and D. Walsh, "Protein Aggregation in the Brain: The Molecular Basis for Alzheimer's and Parkinson's Diseases," Mol Med, vol. 14, no. 7-8, pp. 451-464, 2008.

[37] D. L. Nelson and M. M. Cox, Lehninger principles of biochemistry, New York: W.H. Freeman and Company, 2008.

[38] K. McGraph and D. Kaplan, "Protein-Based Materials," Boston, Birkhauser, 1996, p. 269.

[39] P. Hortschansky, V. Schroeckh, T. Christopeit, G. Zandomeneghi and F. M, "The aggregation kinetics of Alzheimer's β-amyloid peptide is controlled by stochastic nucleation," Protein Science, vol. 14, no. 7, pp. 1753-1759, 2005.

[40] R. A. Harvey and D. R. Ferrier, Lippincott's Illustrated Reviews: Biochemstry, Wolters Kluwer, 2004.

[41] A. Masab et al, "Copper-mediated formation of hydrogen peroxide from the amylin peptide: A novel mechanism for degeneration of islet cells in type-2 diabetes mellitus?," FEBS Letters, vol. 581, no. 18, pp. 3489-3493, 2007.

[42] B.J. Tabner et al, "Hydrogen peroxide is generated during the very early stages of aggregation of the amyloid peptides implicated in Alzheimer disease and familial British dementia.," The Journal of Biological Chemistry, vol. 280, no. 42, pp. 35789-92, 2005.

[43] M. Amaro, T. Wellbrock, D. Birch and O. Rolinski, "Inhibition of beta-amyloid aggregation by fluorescent dye labels," Applied Physics Letters, vol. 104, no. 6, 2014.

[44] M. Amaro, K. Kubiak-Ossowska, D. J. S. Birch and O. J. Rolinski, "Initial stages of beta-amyloid Ab1-40 and Ab1-42 oligomerization observed using fluorescence decay and molecular dynamics analyses of tyrosine," Methods and Applications in Fluorescence, vol. 1, p. 13 pages, 2013.

[45] "RCSB Protein Data Bank," [Online]. Available: https://www.rcsb.org/pdb/explore/jmol.do?structureId=1IYT&view=symmetry. [Accessed 2017 07 02].

[46] O. Crescenzi and e. al, "Solution structure of the Alzheimer amyloid beta-peptide (1-42) in an apolar microenvironment. Similarity with a virus fusion domain.," Eur J Biochem, vol. 269, no. 22, pp. 5642-5648, 2002.

[47] L. Serpell, “Alzheimer’s amyloid fibrils: structure and assembly,” Biochimica et Biophysica Acta (BBA) - Molecular Basis of Disease, vol. 1502, no. 1, pp. 16-30, 2000.

[48] L. Larini and J. Shea, “Role of β-Hairpin Formation in Aggregation: The Self-Assembly of the Amyloid-β(25–35) Peptide,” Biophys J., vol. 103, no. 3, p. 576–586, 2012.

[49] G. Petskio and D. Ringe, “Protein Structure and Function,” New Science Press, 2004, p. 16.

[50] P. Herzig et al, “Bloch meets Alzheimer,” SPG Mitteilungen (Progress in Physics), vol. 39, pp. 11-14, 2014.

[51] G. S. Rule and T. K. Hitchens, Fundamentals of Proetien NMR Spectroscopy, Springer Science & Business Media, 2006.

[52] T. M. Shin, J. M. Isas, C.-L. Hsieh, R. Kayed, C. G. Glabe, R. Langen and J. Chen, “Formation of soluble amyloid oligomers and amyloid fibrils by the multifunctional protein vitronectin,” Molecular Neurodegeneration, vol. 3, no. 16, 2008.

[53] M. Zeeb and J. Balbach, “‘Protein Folding Studied by Real-Time NMR Spectroscopy,” Methods, vol. 34, pp. 65-74, 2004.

[54] H. Dyson and P. Wright, “Unfolded Proteins and Protein Folding Studied by NMR,” Chemical Reviews, vol. 104, p. 3607–3622, 2004.

[55] R. Riek, P. Güntert, H. Döbeli, B. Wipf and K. Wüthrich, “NMR Studies in Aqueous Solution Fail to Identify Significant Conformational Differences between the Monomeric Forms of two Alzheimer Peptides with Widely Different Plaque-Competence, Aβ(1 – 40)ox and Aβ(1 – 42)ox,” European Journal of Biochemistry, vol. 268, pp. 5930-5936, 2001.

[56] L. Hou, H. Shao, Y. Zhang, H. Li, N. Menon, E. Neuhaus, J. Brewer, I. Byeon, D. Ray, M. Vitek, T. Iwashita, R. Makula, A. PRzybyla and M. Zagorski, “Solution NMR Studies of the Aβ(1 – 40) and Aβ(1 – 42) Peptides Establish that the Met35 Oxidation State Affects the Mechanism of Amyloid Formation,” Journal of the American Chemical Society, vol. 126, p. 1992–2005, 2004.

[57] G. Esposito, A. Corazza, P. Viglino, G. Verdone, F. Pettirossi, F. Fogolari, A. Makek, S. Giorgetti, P. Mangione, M. Stoppini and V. Bellotti, “Solution Structure of β2-Microglobulin and Insight s into Fibrillogenesis,” Biochimica et Biophysica Acta, vol. 1753, p. 76 – 84, 2005.

[58] J. Talafous, K. Marcinowski, G. Klopman and M. Zagorski, “Solution Structure of Residues 1 – 28 of the Amyloid β-Peptide,” Biochemistry, vol. 33, p. 7788–7796, 1994.

[59] K. Kirshenbaum and V. Daggett, “Sequence Effects on the Conformational Properties of the Amyloid β-(1 – 28) Peptide: Testing a Proposed Mechanism for the α–β Transition,” Biochemistry, vol. 34, p. 7640–7647, 1995.

[60] A. Petkova, R. Leapman, G. Z, W. Yau, M. Mattson and R. Tycko, “Self-propagating, molecular-level polymorphism in Alzheimer's beta-amyloid fibrils,” Science, vol. 14, no. 307, pp. 252-265, 2005.

[61] A. Paravastu, R. Leapman, W. Yau and R. Tycko, “Molecular structural basis for polymorphism in Alzheimer's beta-amyloid fibrils,” Proceedings of the National Academy of Sciences of the USA, vol. 25, no. 105, pp. 18349-18354, 2008.

[62] B. Sarkar, V. Mithu, B. Chandra, A. Mandal, M. Chandrakesan, D. Bhowmik, P. Madhu and S. Maiti, “Significant Structural Differences between Transient Amyloid-beta Oligomers and Less-Toxic Fibrils in Regions Known To Harbor Familial Alzheimer's Mutations,” ANGEWANDTE CHEMIE-INTERNATIONAL EDITION, vol. 53, no. 27, pp. 6888-6892, 2014.

[63] M. A. Wälti and e. al, “Atomic-resolution structure of a disease-relevant Aβ(1–42) amyloid fibril,” Proceedings of the National Academy of Sciences of the United States of America, vol. 113, no. 34, 2016.

[64] G. Holzwarth and P. Doty, “The Ultraviolet Circular Dichroism of Polypeptides,” J. Am. Chem. Soc., vol. 87, no. 2, p. 218–228, 1965.

[65] N. Greenfield and G. Fasman, “Computed circular dichroism spectra for the evaluation of protein conformation.,” Biochemistry, vol. 8, no. 10, p. 4108=4116, 1969.

[66] N. Greenfield, “Using Circular Dichroism Spectra to Estimate Protein Secondary Structure,” Nature Protocols, vol. 1, p. 2876–2890, 2006.

[67] F. Attanasio, S. Cataldo, P. De Bona, M. F. Sciacca, D. Milardi, B. Pignataro and G. Pappalardo, “Copper(II) and zinc(II) dependent effects on Ab42 aggregation: a CD, Th-T and SFM study,” New Journal of Chemistry, vol. 37, no. 1206, 2013.

[68] J. Stohr, N. Weinmann, H. Wille, T. Kaimann, L. Nagel-Steger, E. Birkmann, G. Panza, S. Prusiner, M. Eigen and D. Riesner, “Mechanisms of Prion Protein Assembly into Amyloid,” Proceedings of the National Academy of Sciences of the USA, vol. 105, pp. 2409-2414, 2008.

[69] S. Kumar, S. Mohanty and J. Udgaonkar, “Mechanismof Formation of Amyloid Protofibrils of Barstar from Soluble Oligomers: Evidence for Multiple Steps and Lateral Association Coupled to Conformational Conversion,” Journal of Molecular Biology, vol. 367, pp. 1186-1204, 2007.

[70] P. Picotti, G. D. Franceschi, E. Frare, B. Spolaore, M. Zambonin, F. Chiti, P. D. Laureto and A. Fontana, “Amyloid Fibril Formation and Disaggregation of

Fragment 1 – 29 of Apomyoglobin: Insights into the Effect of pH on Protein Fibrillogenesis," Journal of Molecular Biology, vol. 367, p. 1237–1245, 2007.

[71] M. Sunde, L. Serpell, M. Bartlam, P. Fraser, M. Pepys and C. Blake, "Common Core Structure of Amyloid Fibrils by Synchrotron X-Ray Diffraction," Journal of Molecular Biology, vol. 273, p. 729–739, 1997.

[72] W. Yong, A. Lomakin, M. Kirkitadze, D. Teplow, S. Chen and G. Benedek, "Structure Determination of Micelle-Like Intermediates in Amyloid β-Protein Fibril Assembly by using Small Angle Neutron Scattering," Proceedings of the National Academy of Sciences of the USA, vol. 99, p. 150–154, 2002.

[73] L. Morozova-Roche, J. Zurdo, A. Spencer, W. Noppe, V. Receveur, D. Archer, M. Joniau and C. Dobson, "Amyloid fibril formation and seeding by wild-type human lysozyme and its disease-related mutational variants," Journal of Structural Biology, vol. 130, no. 2-3, pp. 229-251, 2000.

[74] W. Wan and G. Stubbs, "Fiber diffraction of the prion-forming domain HET-s(218-289) shows dehydration-induced deformation of a complex amyloid structure," Biochemistry, vol. 53, no. 14, pp. 2366-2370, 2014.

[75] M. Elghetany and A. Saleem, "Methods for Staining Amyloid in Tissues: A Review," Stain Technology, vol. 63, pp. 201-212, 1988.

[76] M. Elghetany, A. Saleem and K. Barr, "The Congo Red Stain Revisited," Annals of Clinical & Laboratory Science, vol. 19, pp. 190-195, 1989.

[77] R. Khurana, C. Coleman, C. Ionescu-Zanetti, S. Carter, V. Krishna, R. Grover, R. Roy and S. Singh, "Mechanism of Thioflavin T Binding to Amyloid Fibrils," Journal of Structural Biology, vol. 151, p. 229–238, 2005.

[78] A. Ahmad, V. Uversky, D. Hong and A. Fink, "Early Events in the Fibrillation of Monomeric Insulin," The Journal of Biological Chemistry, vol. 280, p. 42669–42675, 2005.

[79] N. Kad, N. Thomson, D. Smith, D. Smith and S. Radford, "β 2-Microglobulin and its Deamidated Variant, N17D form Amyloid Fibrils with a Range of Morphologies In Vitro," Journal of Molecular Biology, vol. 313, p. 559–571, 2001.

[80] H. Yagi, E. Kusaka, K. Hongo, T. Mizobata and Y. Kawata, "Amyloid Fibril Formation of β-Synuclein is Accelerated by Preformed Amyloid Seeds of other Proteins: Implications for the Mechanism of Transmissible Conformational Diseases," Journal of Molecular Biology, vol. 280, p. 38609–38616, 2005.

[81] M. Malisauskas, V. Zamotin, J. Jass, W. Noppe, C. Dobson and L. Morozova-Roche, "Amyloid Protofilaments from the Calcium-Binding Protein Equine Lysozyme: Formation of Ring and Linear Structures Depends on pH and Metal Ion Concentration," Journal of Molecular Biology, vol. 330, p. 879–890, 2003.

[82] H. LeVine III, “Thioflavine T Interaction with Synthetic Alzheimer’s Disease β-Amyloid Peptides: Detection of Amyloid Aggregation in Solution,” Protein Science, vol. 2, pp. 404-410, 1993.

[83] S. Pollack, I. Sadler, S. Hawtin, V. Tailor and M. Shearman, “Sulfonated dyes attenuate the toxic effects of beta-amyloid in a structure-specific fashion,” Neuroscience Letter, vol. 197, no. 3, pp. 211-214, 1995.

[84] G. Bitan, M. Kirkitadze, A. Lomakin, S. Vollers, G. Benedek and D. Teplow, “Amyloid β-protein (Aβ) assembly: Aβ40 and Aβ42 oligomerize through distinct pathways,” Proceedings of the National Academy of Sciences of the USA, vol. 100, no. 1, p. 330–335. , 2002.

[85] A. Roher, M. Chaney, Y. Kuo, S. Webster, W. Stine, L. Haverkamp, A. Woods, R. Cotter, J. Tuohy, G. Krafft, B. Bonnell and M. Emmerling, “Morphology and toxicity of Abeta-(1-42) dimer derived from neuritic and vascular amyloid deposits of Alzheimer's disease.,” The Journal of Biological Chemistry, vol. 271, no. 34, pp. 20631-20635, 1996.

[86] A. Filiano, S. Gadani and J. Kipnis, “Interactions of innate and adaptive immunity in brain development and function,” Brain Research, vol. 1617, pp. 18-27, 2014.

[87] J. Gehrmann, Y. Matsumoto and G. Kreutzberg, “Microglia: intrinsic immuneffector cell of the brain,” Brain Research Reviews, vol. 20, no. 3, pp. 269-287, 1995.

[88] A. Modler, K. Gast, G. Lutsch and G. Damaschun, “Assembly of Amyloid Protofibrils via Critical Oligomers—A Novel Pathway of Amyloid Formation,” Journal of Molecular Biology, vol. 325, no. 1, p. 135–148, 2003.

[89] R. Ward, K. Jennings, R. Jepras, W. Neville, D. Owen, J. Hawkins, G. Christie, J. Davis, A. George, E. Karran and D. Howlett, “Fractionation and characterization of oligomeric, protofibrillar and fibrillar forms of beta-amyloid peptide.,” Biochemical Journal, vol. 384, no. 1, p. 137–144, 2000.

[90] A. Assarsson, E. Hellstrand, C. Cabaleiro-Lago and S. Linse, “Charge dependent retardation of amyloid β aggregation by hydrophilic proteins.,” ACS Chemical Neuroscience, vol. 16, no. 5, pp. 266-274, 2014.

[91] M. H. Cardew and D. D. Eley, “The semiconductivity of organic substances. III. Hemoglobin and some amino acids,” Discussions of the Faraday Society, vol. 27, pp. 115-128, 1959.

[92] A. Shivji, F. Brown, M. Davies, K. Jennings, C. Roberts, S. Tendler, M. Wilkinson and P. Williams, “Scanning tunnelling microscopy studies of beta-amyloid fibril structure and assembly,” FEBS Letters, vol. 371, no. 1, pp. 25-28, 1995.

[93] Z. Wang, C. Zhou, C. Wang, L. Wan, X. Fang and C. Bai, “AFM and STM study of beta-amyloid aggregation on graphite,” Ultramicroscopy, vol. 97, no. 1-4, pp. 73-79, 2003.

[94] D. Losic, L. Martin, A. Mechler, M. Aguilar and D. Small, “High resolution scanning tunnelling microscopy of the β-amyloid protein (Aβ1–40) of Alzheimer’s disease suggests a novel mechanism of oligomer assembly,” Journal of Structural Biology, vol. 155, no. 1, p. 104–110, 2006.

[95] M. T. Colvin, R. Silvers, Q. Z. Ni, T. V. Can, I. Sergeyev‖, M. Rosay‖, K. J. Donovan, B. Michael, J. Wall, S. Linse and R. G. Griffin, ″Atomic Resolution Structure of Monomorphic Aβ42 Amyloid Fibrils,″ Journal of American Chemical Society, vol. 138, no. 30, p. 9663–9674, 2016.

[96] C. Goldsbury and J. Green, “Time-lapse atomic force microscopy in the characterization of amyloid-like fibril assembly and oligomeric intermediates,” Methods in Molecular Biology, vol. 299, pp. 103-128, 2005.

[97] I. Mastrangelo, M. Ahmed, T. Sato, W. Liu, C. Wang, P. Hough and S. Smith, “High-resolution Atomic Force Microscopy of Soluble Aβ42 Oligomers,” Journal of Molecular Biology, vol. 358, no. 1, p. 106–119, 2006.

[98] J. Berg et al, “Section 3.5 Quaternary Structure: Polypeptide Chains Can Assemble Into Multisubunit Structures,” in Biochemistry. 5th edition., New York, W H Freeman, 2002.

[99] C. Brändén and J. Tooze, “Chapter 1 The building blocks,” in Introduction to Protein Structure, New York, Garland Publishing, 1990.

[100] C. Glabe, “Amyloid Oligomer Structures and Toxicity,” The Open Biology Journal, vol. 2, pp. 222-227, 2009.

[101] B. J. Tabner , O. M. El-Agnaf , M. J. German, N. J. Fullwood and D. Allsop, “Protein aggregation, metals and oxidative stress in neurodegenerative diseases.,” Biochem Soc Trans, vol. 33, no. 5, pp. 1082-1086, 2005.

[102] B.J. Tabner et al, “A spectroscopic study of some of the peptidyl radicals formed following hydroxyl radical attack on beta-amyloid and alpha-synuclein.,” Free Radic Research, pp. 731-739, 2006.

[103] V. Minicozzi, F. Stellato, M. Comai, M. Dalla Serra, C. Potrich, W. Meyer-Klaucke and S. Morante, “Identifying the minimal copper- and zinc-binding site sequence in amyloid-beta peptides,” J Biol Chem, vol. 283, no. 16, pp. 10784-10792, 2008.

[104] J. Shearer, P. Callan, T. Tran and V. Szalai, “Cu K-edge X-ray absorption spectroscopy reveals differential copper coordination within amyloid-β oligomers

compared to amyloid-β monomers," Chemical Communications, vol. 46, no. 48, pp. 9137-9139, 2010.

[105] P. Giannozzi, K. Jansen, G. La Penna, V. Minicozzi, S. Morante, G. Rossi and F. Stellato, "Zn induced structural aggregation patterns of β-amyloid peptides by first-principle simulations and XAS measurements," Metallomics, vol. 4, pp. 156-165, 2012.

[106] J. Gallagher, M. Finnegan, B. Grehan, J. Dobson, J. Collingwood and M. Lynch, "Modest Amyloid Deposition is Associated with Iron Dysregulation, Microglial Activation, and Oxidative Stress," JOURNAL OF ALZHEIMERS DISEASE, vol. 28, no. 1, pp. 147-161, 2012.

[107] T. Wales and J. Engen, "Hydrogen exchange mass spectrometry for the analysis of protein dynamics," Mass Spectrometry Reviews, vol. 25, no. 1, pp. 158-170, 2006.

[108] E. Zavoisky, "Spin-magnetic resonance in paramagnetics," Journal of Physics, vol. 9, no. 245, 1945.

[109] N. Whittemore, R. Mishra, I. Kheterpal, A. Williams, R. Wetzel and E. Serpersu, "Hydrogen−Deuterium (H/D) Exchange Mapping of Aβ1-40 Amyloid Fibril Secondary Structure Using Nuclear Magnetic Resonance Spectroscopy," Biochemistry, vol. 44, no. 11, p. 4434–4441, 2005.

[110] T. Lührs, C. Ritter, M. Adrian, D. Riek-Loher, B. Bohrmann, H. Döbeli, D. Schubert and R. Riek, "3D structure of Alzheimer's amyloid-beta(1-42) fibrils," Proceedings of the National Academy of Sciences of USA, vol. 102, no. 48, pp. 17342-17347, 2005.

[111] I. Kheterpal, M. Chen, K. D. Cook and R. Wetzel, "Structural Differences in Aβ Amyloid Protofibrils and Fibrils Mapped by Hydrogen Exchange – Mass Spectrometry with On-line Proteolytic Fragmentation," Journal of Molecular Biology, vol. 361, no. 4, p. 785–795, 2006.

[112] J. Lakowicz, "Principles of Fluorescence Spectroscopy," in Principles of Fluorescence Spectroscopy, Baltimore, Maryland, Springer, 2013.

[113] S. K. Maji, J. J. Amsden, K. J. Rothschild, M. M. Condron and D. B. Teplow, "Conformational Dynamics of Amyloid β-Protein Assembly Probed Using Intrinsic Fluorescence," Biochemistry, vol. 44, no. 40, p. 13365–13376, 2005.

[114] M. Amaro, D. Birch and O. Rolinski, "Beta-amyloid oligomerisation monitored by intrinsic tyrosine fluorescence," Physical Chemistry Chemical Physics, vol. 13, no. 14, pp. 6434-6441, 2011.

[115] L. Stryer, "Fluorescence energy transfer as a spectroscopic ruler," Annual Review of Biochemistry, vol. 47, pp. 819-646, 1978.

[116] H. Scientific, “Horiba Scientific,” [Online]. Available: http://www.horiba.com/fileadmin/uploads/Scientific/Documents/Fluorescence/TechNote-3b-Foerster_resonce_energy_transfer__FRET_.pdf. [Accessed 2017 08 03].

[117] W. Garzon-Rodriguez, M. Sepulveda-Becerra, S. Milton and C. G. Glabe, “Soluble Amyloid Aβ-(1–40) Exists as a Stable Dimer at Low Concentrations,” The Journal of Biological Chemistry, vol. 272, pp. 21037-21044, 1997.

[118] K. Woojin and H. Michael H, “Generic hydrophobic residues are sufficient to promote aggregation of the Alzheimer's Abeta42 peptide.,” Proceedings of the National Academy of Sciences of USA, vol. 103, no. 43, pp. 15824-15829, 2006.

[119] A. Lomakin, G. Benedek and D. Teplow, “Monitoring protein assembly using quasielastic light scattering spectroscopy,” Methods in Enzymology, vol. 309, pp. 429-459, 199.

[120] Malvern Instruments Ltd, “Dynamic light scattering: An introduction in 30 minutes,” in DLS technical note MRK656-01, Worcestershire, Malvern Instruments Ltd, 2010, pp. 1-8.

[121] A. Oliva, M. Llabrés and J. Fariña, “Applications of multi-angle laser light-scattering detection in the analysis of peptides and proteins,” Current Drug Discovery Technologies, vol. 3, pp. 229-242, 2004.

[122] S.-H. Chong and S. Ham, “Site-directed analysis on protein hydrophobicity,” Journal of Computational Chemistry, Vols. 35,, no. 18, p. 1364–1370, 2014.

[123] R. Best and HummerG, “Optimized Molecular Dynamics Force Fields Applied to the Helix−Coil Transition of Polypeptides,” The Journal of Physical Chemistry B, vol. 113, no. 26, p. 9004–9015, 2009.

[124] R. Best, X. Zhu, J. Shim, P. Lopes, J. Mittal, M. Feig and A. MacKerell Jr., “Optimization of the Additive CHARMM All-Atom Protein Force Field Targeting Improved Sampling of the Backbone ϕ, ψ and Side-Chain χ1 and χ2 Dihedral Angles,” J. Chem. Theory Comput., vol. 8, no. 9, p. 3257–3273, 2012.

[125] C. Siwy, C. Lockhard and D. Klimov, “Is the Conformational Ensemble of Alzheimer’s Aβ10-40 Peptide Force Field Dependent?,” Computational Biology, vol. 13, no. 1, 2017.

[126] K. Ball, A. Phillips, D. Wemmer and T. Head-Gordon, “Differences in beta-strand Populations of Monomeric A beta 40 and A beta 42,” BIOPHYSICAL JOURNAL, vol. 104, no. 12, pp. 2714-2724, 2013.

[127] D. Thirumalai, G. Reddy and J. Straub, “Role of Water in Protein Aggregation and Amyloid Polymorphism,” ACCOUNTS OF CHEMICAL RESEARCH, vol. 45, no. 1, pp. 83-92, 2012.

[128] Y. Chebaro, N. Mousseau and P. Derreumaux, “Structures and Thermodynamics of Alzheimer’s Amyloid-β Aβ(16−35) Monomer and Dimer by Replica Exchange Molecular Dynamics Simulations: Implication for Full-Length Aβ Fibrillation,” The Journal of Physical Chemistry B, vol. 113, p. 7668–7675, 2009.

[129] N.G. Sgourakis et al, “Atomic-level characterization of the ensemble of the Aβ(1-42) monomer in water using unbiased molecular dynamics simulations and spectral algorithms.,” Journal of Molecular Biology, vol. 405, no. 2, pp. 570-583, 2011.

[130] S. Kim, T. Takeda, D.K. Klimo,, “Mapping conformational ensembles of aβ oligomers in molecular dynamics simulations.,” Biophysical Journal, vol. 99, no. 6, pp. 1949-1958, 2010.

[131] A. R. Lam, D. B. Teplow, S. E. and U. B, “Effects of the Arctic (E22→G) Mutation on Amyloid β-Protein Folding: Discrete Molecular Dynamics Study,” Journal of the Ameircan Chemical Society, vol. 130, no. 51, p. 17413–17422, 2008.

[132] D. Meral, B. Urbanc, “Discrete molecular dynamics study of oligomer formation by N-terminally truncated amyloid β-protein.,” Journal of Molecular Biology, vol. 425, no. 12, pp. 2260-2275, 2013.

[133] J. Nasica-Labouze et al, “Amyloid β Protein and Alzheimer’s Disease: When Computer Simulations Complement Experimental Studies,” Chemical Reviews, vol. 115, no. 9, pp. 3518-3563 , 2015.

[134] B. Linsea and S. Linse, “Monte Carlo simulations of protein amyloid formation reveal origin of sigmoidal aggregation kinetics,” Molecular BioSystems, no. 7, pp. 2296-2303, 2011.

[135] P. Derreumaux, “From polypeptide sequences to structures using Monte Carlo simulations and an optimized potential,” The Journal of Chemical Physics, vol. 1111, p. 2301, 1999.

[136] S. Mitternacht, I. Staneva and I. A, “Monte Carlo Study of the Formation and Conformational Properties of Dimers of Aβ42 Variants,” Journal of Molecular Biology, vol. 410, no. 2, pp. 357-367, 2011.

[137] M. Li, D. Klimov, J. Straub and D. Thirumalai, “Probing the mechanisms of fibril formation using lattice models,” JOURNAL OF CHEMICAL PHYSICS, vol. 129, no. 17, 2008.

[138] O. Wise-Scira, L. Xu, G. Perry and O. Coskuner, “Structures and free energy landscapes of aqueous zinc(II)-bound amyloid-beta(1-40) and zinc(II)-bound amyloid-beta(1-42) with dynamics,” JOURNAL OF BIOLOGICAL INORGANIC CHEMISTRY, vol. 17, no. 6, pp. 927-938, 2012.

[139] B. Valeu and M. Berberan-Santos, “Molecular Fluorescence: Principles and Applications,” in Molecular Fluorescence: Principles and Applications, Weinheim, Germany, Wiley-VCH, 2013.

[140] W. Becker, “Advanced Time-Correlated Single Photon Counting Techniques,” in Advanced Time-Correlated Single Photon Counting Techniques, Berlin Germany, Springer, 2005.

[141] D. O'Connor and D. Philips, “Time-correlated Single Photon Counting,” London, Academic Press, 1984.

[142] J. R. Lakowicz, “Principles of Fluorescence Spectroscopy,” in Principles of Fluorescence Spectroscopy, 1999, Springer Science & Business Media, p. 41.

[143] W. J. Stine, K. Dahlgren, G. Krafft and M.J. LaDu, “In vitro characterization of conditions for amyloid-beta peptide oligomerization and fibrillogenesis.,” J Biol Chem., vol. 278, no. 13, pp. 11612-11622, 2003.

[144] H. Scientific, “Horiba Scientific: Operation Manual,” [Online]. Available: http://www.horiba.com/fileadmin/uploads/Scientific/Downloads/UserArea/Fluorescence/Manuals/DAS67_Manual.pdf. [Accessed 16 07 17].

[145] H. Li, F. Rahimi, S. Sinha, P. Maiti, G. Bitan and K. Murakami, “Amyloids and Protein Aggregation - Analytical Methods,” in Encyclopedia of Analytical Chemistry, Chichester, John Wiley & Sons, Ltd., 2009.

[146] W. Humphrey, A. Dalke and K. Schulten, “VMD: visual molecular dynamics,” Journal of Molecular Graphics, vol. 14, no. 1, pp. 33-38, 1996.

[147] L. Fornander, B. Feng, T. Beke-Somfai and N. B., “UV Transition Moments of Tyrosine,” The journal of Physical Chemistry, vol. 118, pp. 9247 - 9257, 2014.

[148] G. Meurant, Introduction to Dynamic Light Scattering by Macromolecules, New York City: Elsevier, 1990.

[149] R. Finsy, “Advances in colloid and Interface Science,” Science, vol. 52, p. 79, 1994.

[150] B. Berne and R. Pecora, Dynamic Light Scattering: With Applications to Chemistry, Biology, and Physics, Mineola: Dover Publications Inc, 2000.

[151] C. Johson and D. Gabreil, Laser Light Scattering, Dover Publications Inc., 1994.

[152] B. Saha, J. Mukhopadhyay and R. Johnson, “The Comparative Nano Particle Size Characterization of EEW Alumina Using Various Measurement Techniques,” Particulate Science and Technology, vol. 30, no. 6, 2012.

[153] LS instruments, “Modulated 3D Cross-Correlation Light Scattering,” Ls instruments, [Online]. Available: http://www.lsinstruments.ch/technology/dynamic_light_scattering_dls/modulated_3d_cross-correlation_technology/. [Accessed 22 08 2017].

[154] M. Allen and T. D.J., “Monte Carlo Methods,” in Computer Simulation of Liquids, New York City, Oxford Univeristy Press, 1989, pp. 111-139.

[155] S. Sugio, A. Kashima, S. Mochizuki, M. Noda and K. Kobayashi, “Crystal structure of human serum albumin at 2.5 A resolution.,” Protein Eng., vol. 12, pp. 439-446, 1999.

[156] M. Allen and D. Tildesley, “Molecular Dynamics,” in Computer Simulation of Liquids, New York City, Oxford University Press, 1989, pp. 71-109.

[157] J. Ryckaert and e. al, “Numerical Integration of the cartesian equations of motion of a system with constraints: molecular dynamics of n-alkanes,” J. Comput. Phys., vol. 23, no. 327, 1977.

[158] R. J. Sadus, “The SHAKE Algorithm,” in Molecular Simulation of Fluids: Theory, Algorithms, and Object-orientation, Elsevier, 2002, pp. 239-257.

[159] M. S. Al-Barwani, “Computer Modeling of Liquid Crystals,” PhD Thesis, vol. University of Bristol, 1999.

[160] T. Andruniów, “Molecular Dynamics Part 2: MD Algorimths,” Wroclaw University of Technology.

[161] J.C. Philpis et al, “Scalable molecular dynamics with NAMD.,” Journal of Computational Chemistry, vol. 26, no. 16, pp. 1781-1802, 2005.

[162] H. Butt, K. Graf and M. Kappl, “4.2 Poison Boltzman theory of the diffuse double layer,” in Physics and Chemistry of Interfaces, Berlin, Wiley-VCH, 2003, p. 45.

[163] H. “Fluorescence Anisotropy Studies,” in Fluorescence Technical Note FL-3, HORIBA Jobin Yvon, 2007, pp. 1-4.

[164] A. Rauk, “The Chemistry of Alzheimer's Disease,” Chemical Society Reviews, vol. 38, no. 9, pp. 2698-2715 , 2009.

[165] O. Rolinski, W. T, D. Birch and V. Vyshemirsky, “Tyrosine Photophysics During the Early Stages of B-Amyloid Aggregation Leading to Alzheimer's,” The Journal of Physical Chemistry, vol. 6, pp. 3116-3120, 2015.

[166] F. Teale, “The ultraviolet fluorescence of proteins in neutral solution,” Biochem J., vol. 76, no. 2, pp. 381-388, 1960.

[167] D. P. Millar, “Application of Time-Resolved Fluorescence Spectroscopy to Studies of DNA-Protein Interaction and RNA Folding,” in New Trends in Fluorescence Spectroscopy: Applications to Chemical and Life Sciences, Berlin, Springer-Verlag, 1944, p. 427.

[168] R. Barlow, “2.6.2 Correlation,” in Statistics: A Guide to the Use of Statistical Methods in the Physical Sciences, Chicester, John Wiley & Sons, 1989.

[169] O. J. Rolinski, T. Wellbrock, D. J. S. Birch and V. Vyshemirsky, “Tyrosine photophysics during the early stages of β-amyloid aggregation leading to Alzheimer's.,” Journal of Physical Chemistry Letters, vol. 6, no. 15, pp. 3116-3120, 2015.

[170] I. Kuznetsova, A. Sulatskaya, A. Maskevich, V. Uversky and K. Turoverov, “High Fluorescence Anisotropy of Thioflavin T in Aqueous Solution Resulting from Its Molecular Rotor Nature,” ANALYTICAL CHEMISTRY, vol. 88, no. 1, pp. 718-724, 2016.

[171] A. Chauhan and A. Varma, A Textbook of Molecular Biotechnology, New Delhi: I.K. International Publishing House Pvt Ltd., 2009.

[172] S. Vivekanandan, J. Brender and e. al, “A partially folded structure of amyloid-beta(1–40) in an aqueous environment,” Biochemical and Biophysical Research Communications, vol. 411, no. 2, pp. 312-316, 2011.

[173] P. J.C. and e. al, “Scalable molecular dynamics with NAMD,” Jounral of Computational Chemistry, vol. 26, no. 16, p. 1781–1802 , 2005.

[174] A. Crevenna, H. Naredi-Rainer, D. Lamb, R. Wedlich-Soldner and J. Dzubiella, “Effects of Hofmeister Ions on the α-Helical Structure of Proteins,” biophysical journal, vol. 102, no. 4, pp. 907-915, 2012.

[175] M. Gebbie, H. Dobbs and J. Israelachvili, “Long-range electrostatic screening in ionic liquids.,” Proc Natl Acad Sci U S A. , vol. 112, no. 24, pp. 7432-7437, 2015.

[176] B. Barz, O. Olubiyia and B. Strodel, “Early amyloid β-protein aggregation precedes conformational change,” Chemical Cummunications, vol. 40, 2014.

[177] P. J. Wyatt, “Light scattering and the absolute characterization of macromolecules,” Analytica Chimica Acta, vol. 272, no. 1, pp. 1-40, 1993.

[178] S. Wood, B. Maleeff and R. Watzel, “Physical, morphological and functional differences between ph 5.8 and 7.4 aggregates of the Alzheimer's amyloid peptide Abeta.,” Journal of Molecular Biology, vol. 256, no. 5, pp. 870-877, 1996.

[179] Y. Wong, K. Binger, G. Howlett and M. Griffin, “Methionine oxidation induces amyloid fibril formation by full-length apolipoprotein A-I,” Proceedings of the National

Academy of Sciences of the United States of America, vol. 107, no. 5, pp. 1977-1982, 2010.

[180] N. Whittemore, R. Mishra, I. Kheterpal, A. Williams, R. Wetzel and E. Serpersu, “(Hydrogen-deuterium (H/D) exchange mapping of A ss(1-40) amyloid fibril secondary structure using nuclear magnetic resonance spectroscopy),” Biochemistry. , vol. 44, no. 11, pp. 4434-4441, 2005 .

[181] L. Whitmore and B. Wallace, “Protein Secondary Structure Analyses from Circular Dichroism Spectroscopy: Methods and Reference Databases,” Biopolymers, vol. 89, pp. 392-400, 2008.

[182] C. Wasmer, A. Lange, H. V. Melckebeke, A. Siemer, R. Riek and B. Meier, “Amyloid fibrils of the HET-s(218-289) prion form a beta solenoid with a triangular hydrophobic core.,” Science, vol. 319, no. 5869, pp. 1523-1536, 2008.

[183] D. Walsh, D. Hartley, Y. Kusumoto, Y. Fezoui, M. Condron, A. Lomakin, G. Benedek, D. Selkoe and D. Teplow, “Amyloid beta-protein fibrillogenesis. Structure and biological activity of protofibrillar intermediates.,” The Journal of Biological Chemistry, vol. 274, no. 36, pp. 25945-25952, 1999.

[184] D. Walsh, A. Lomakin, G. Benedek, M. Condron and T. DB, “Amyloid beta-protein fibrillogenesis. Detection of a protofibrillar intermediate,” The Journal of Biological Chemistry, vol. 272, no. 35, pp. 22364-22372, 1997.

[185] H. Ushikubo, Y. Tanimoto, K. Abe, T. Asakawa, T. Kan and T. Akaishi, “3,3',4',5'-tetrahydroxyflavone induces formation of large aggregates of amyloid β protein,” Biological & Pharmaceutical Bulletin, vol. 37, no. 5, pp. 748-754, 2014.

[186] V. Tõugu, A. Karafin and P. P, “Binding of zinc(II) and copper(II) to the full-length Alzheimer's amyloid-beta peptide.,” Journal of Neurochemistry, vol. 104, no. 5, pp. 1249-1259, 2008.

[187] M. Török, S. Milton, R. Kayed, P. Wu, T. McIntire, C. Glabe and R. Langen, “Structural and Dynamic Features of Alzheimer's Aβ Peptide in Amyloid Fibrils Studied by Site-directed Spin Labeling,” The Journal of Biological Chemistry, vol. 277, no. 43, pp. 40810-40815, 2002.

[188] B. Smith, L. Oswald and S. Franzen, “Single-Pass Attenuated Total Reflection Fourier Transform Infrared Spectroscopy for the Prediction of Protein Secondary Structure,” Analytical Chemistry, vol. 74, p. 3386–3391, 2002.

[189] A. Sen, U. Baxa, M. Simon, J. Wall, R. Sabate, S. Saupe and A. Steven, “Mass analysis by scanning transmission electron microscopy and electron diffraction validate predictions of stacked beta-solenoid model of HET-s prion fibrils.,” The Journal of Biological Chemistry, vol. 282, no. 8, pp. 5545-5550, 2006.

[190] M. Selenica, X. Wang, L. Ostergaard-Pedersen and A. Westlind-Danielsson, “Cystatin C reduces the in vitro formation of soluble Aβ1-42 oligomers and protofibrils,” Scandinavian Journal of Clinical & Laboratory Investigation, vol. 67, no. 2, pp. 179-190, 2007.

[191] R. Y. Rubinstein and D. P. Kroese, Simulation and the Monte Carlo Method, John Wiley & Sons, 2011, 2011.

[192] D. Ridgley, E. Claunch and J. Barone, “Characterization of large amyloid fibers and tapes with Fourier transform infrared (FT-IR) and Raman spectroscopy,” Applied Spectroscopy, vol. 67, no. 12, pp. 1417-1426, 2013.

[193] A. Reymera, K. Frykholma, K. Morimatsua, M. Takahashic and B. Nordéna, “Structure of human Rad51 protein filament from molecular modeling and site-specific linear dichroism spectroscopy,” Proceedings of the National Academy of Sciences of the USA, vol. 106, no. 32, p. 13248–13253, 2009.

[194] D. Rapaport, The Art of Molecular Dynamics Simulation, Cambridge: Cambridge University Press, 2004, 2004.

[195] A. Paravastu, I. Qahwash, R. Leapman, S. Meredith and R. Tycko, “Seeded growth of beta-amyloid fibrils from Alzheimer's brain-derived fibrils produces a distinct fibril structure,” Proceedings of the National Academy of Sciences, vol. 106, no. 18, pp. 7443-7448, 2009.

[196] A. Paravastu, R. Leapman, W. Yau and R. Tycko, “Molecular structural basis for polymorphism in Alzheimer's beta-amyloid fibrils,” National Academy of Sciences of the USA, vol. 105, no. 47, pp. 18349-18354, 2008.

[197] M. Nybo, S. Svehag and E. H. Nielsen, “An Ultrastructural Study of Amyloid Intermediates in Aβ1–42 Fibrillogenesis,” Scandinavian Journal of Immunology, vol. 49, no. 3, pp. 1365-3083, 2002.

[198] M. Nichols, M. Moss, D. Reed, W. Lin, R. Mukhopadhyay, J. Hoh and T. Rosenberry, “Growth of beta-amyloid(1-40) protofibrils by monomer elongation and lateral association. Characterization of distinct products by light scattering and atomic force microscopy.,” Biochemistry, vol. 41, no. 19, pp. 6115-6127, 2002.

[199] R. Nabuurs, R. Natté, F. de Ronde, I. Hegeman-Kleinn, J. Dijkstra, S. van Duinen, A. Webb, A. Rozemuller, M. van Buchem and L. van der Weerd, “MR Microscopy of Human Amyloid-beta Deposits: Characterization of Parenchymal Amyloid, Diffuse Plaques, and Vascular Amyloid,” JOURNAL OF ALZHEIMERS DISEASE, vol. 34, no. 4, pp. 1037-1049, 2013.

[200] K. Murakami, H. Hara, Y. Masuda, H. Ohigashi and K. Irie, “Distance measurement between Tyr10 and Met35 in amyloid beta by site-directed spin-labeling ESR spectroscopy: implications for the stronger neurotoxicity of Abeta42 than Abeta40.,” ChemBioChem, vol. 8, no. 18, pp. 2308-2314., 2007.

[201] L. Miles, K. Wun, G. Crespi, M. Fodero-Tavoletti, D. Galatis, C. Bagley, K. Beyreuther, C. Masters, R. Cappai, W. McKinstry, K. Barnham and M. Parker, “Amyloid-β-Anti-Amyloid-β Complex Structure Reveals an Extended Conformation in the Immunodominant B-cell Epitope,” Journal of Molecular Biology, vol. 377, pp. 181-192, 2008.

[202] R. Michaela, J. Rosandića, G. Montenegroa, E. Lobatoa, F. Tresserrac, R. Barraquera and G. Vrensend, “Absence of beta-amyloid in cortical cataracts of donors with and without Alzheimer's disease,” Experimental Eye Research, vol. 106, pp. 5-13, 2013.

[203] K. E. Marshall and L. C. Serpell, “Insights into the Structure of Amyloid Fibrils,” he Open Biology Journa, vol. 2, pp. 185-192, 2009.

[204] J. R. Lakowicz, Principles of Fluorescence Spectroscopy, Springer, 2007.

[205] W. Kim, Y. Kim, J. Min, D. Kim, Y. Chang and M. Hecht, “A High-Throughput Screen for Compounds That Inhibit Aggregation of the Alzheimer’s Peptide,” ACS Chemical Biology, vol. 1, no. 7, pp. 461-469, 2006.

[206] J. Kim and M. Lee, “Observation of multi-step conformation switching in β-amyloid peptide aggregation by fluorescence resonance energy transfer,” Biochemical and Biophysical Research Communications, vol. 316, no. 2, p. 393–397, 2004.

[207] I. Kheterpal, H. Lashuel, D. Hartley, T. Walz, P. L. Jr. and R. Wetzel, “Aβ Protofibrils Possess a Stable Core Structure Resistant to Hydrogen Exchange,” Biochemistry, vol. 42, no. 48, p. 14092–14098, 2003.

[208] I. Kheterpal, A. Williams, C. Murphy, B. Bledsoe and W. R, “Structural features of the Abeta amyloid fibril elucidated by limited proteolysis,” Biochemistry, vol. 40, no. 39, pp. 11757-11767, 2001.

[209] S. Jiang and J. H. t. Horst, “Crystal Nucleation Rates from Probability Distributions of Induction Times,” Crystal Growth & Design, vol. 11, no. 1, p. 256–261, 2011.

[210] A. Irbäck and S. Mitternacht, “Spontaneous beta-barrel formation: an all-atom Monte Carlo study of Abeta16-22 oligomerization.,” Proteins, vol. 1, pp. 207-214, 2008.

[211] K. R. G. J. Ionescu-Zanetti C1, J. Petrick, L. Trabachino, L. Minert, S. Carter and A. Fink, “Monitoring the assembly of Ig light-chain amyloid fibrils by atomic force microscopy,” Proceedings of the National Academy of Sciences of USA, vol. 96, no. 23, pp. 13175-13179, 1999.

[212] H. Inouye and D. Kirschner, “Alzheimer's beta-amyloid: insights into fibril formation and structure from Congo red binding,” Subcellular Biochemistry, vol. 38, pp. 203-224, 2005.

[213] C. He, Y. Han, Y. Fan, M. Deng and W. Y, “Self-assembly of Aβ-based peptide amphiphiles with double hydrophobic chains.,” Langmuir, vol. 28, no. 7, pp. 3391-3396, 2012.

[214] J. Haile, Molecular Dynamics Simulation, Wiley, 1997, 1997.

[215] C. Goldsbury, U. Baxa, M. Simon, A. Steven, A. Engel, J. Wall, U. Aebi and S. Müller, “Amyloid structure and assembly: insights from scanning transmission electron microscopy,” Journal of Structural Biology, vol. 173, no. 1, pp. 1-13, 2011.

[216] M. Goldberg and A. Chaffotte, “Undistorted Structural Analysis of Soluble Proteins by Attenuated Total Reflectance Infrared Spectroscopy,” Protein Science, vol. 14, p. 2781–2792, 2005.

[217] Y. Fezoui, D. Hartley, J. Harper, R. Khurana, D. Walsh, M. Condron, D. Selkoe, P. J. Lansbury, A. Fink and D. Teplow, “An improved method of preparing the amyloid beta-protein for fibrillogenesis and neurotoxicity experiments,” Amyloid, vol. 7, no. 3, pp. 166-178, 2000.

[218] P. Faller and C. Hureau, “Impact of metallic ions in Alzheimer's disease: insights from XAS spectroscopy,” L'ACTUALITE CHIMIQUE, vol. 356, no. 57, pp. 88-90, 2011.

[219] J. Durand, G. Meloni, C. Talmard, M. Vašákc and P. Faller, “Zinc release of Zn7-metallothionein-3 induces fibrillar type amyloid-β aggregates,” Metallomics, vol. 2, pp. 741-744, 2010.

[220] P. Divry, “Etude Histochimique des Plaques Seniles,” J. Belge. Neurol. Psychiatr, vol. 27, pp. 643-657, 1927.

[221] M. Coles, W. Bicknell, A. Watson, D. Fairlie and D. Craik, “Solution Structure of Amyloid β-Peptide(1 – 40) in a Water-Micelle Environment. Is the Membrane-Spanning Domain where we think it is?,” Biochemistry, vol. 37, pp. 11064-11077, 1998.

[222] D. A. Butterfield, “Amyloid β-Peptide [1 – 42] Associated Free Radical-Induced Oxidative Stress and Neurodegeneration in Alzheimer’s Disease Brain: Mechanisms and Consequences,” Current Medicinal Chemistry, vol. 10, pp. 2651-2659, 2003.

[223] Z. Budrikis, G. Costantini, C. A. La Porta and S. Zapperi, “Protein accumulation in the endoplasmic reticulum as a non-equilibrium phase transition,” Nature Communications, vol. 5, no. 3620, 2014.

[224] G. Bitan, B. Tarus, S. Vollers, H. Lashuel, M. Condron, J. Straub and D. Teplow, “A molecular switch in amyloid assembly: Met35 and amyloid beta-protein oligomerization,” Journal of the American Chemical Society, vol. 125, no. 50, pp. 15359-15365, 2003.

[225] B. Alder and T. Wainwright, “Phase Transition for a Hard Sphere System,” Journal of Chemical Physics, vol. 27, pp. 1208-1209, 1957.

[226] A. Yang, C. Wang, B. Song, W. Zhang, Y. Guo, R. Yang, G. Nie, Y. Yang and C. Wang, “Attenuation of beta-Amyloid Toxicity In Vitro and In Vivo by Accelerated Aggregation,” NEUROSCIENCE BULLETIN, vol. 33, no. 4, pp. 405-412, 2017.

[227] M. Staderini, M. Martin, M. Bolognesi and J. Menendez, “Imaging of beta-amyloid plaques by near infrared fluorescent tracers: a new frontier for chemical neuroscience,” CHEMICAL SOCIETY REVIEWS, vol. 44, no. 7, pp. 1807-1819, 2015.

[228] F. W. J. Teale, G. Weber, “Ultraviolet fluorescence of the aromatic amino acids,” Biochmedical Journal, vol. 65, no. 3, p. 476–482, 1957.

[229] W. A. Gunderson, J. Hernandez-Guzman, J. W. Karr, L. Sun, V. A. Szalai and K. Warncke, “Local structure and global patterning of Cu2+ binding in fibrillar amyloid-β [Aβ(1-40)] protein,” American Chemical Society, vol. 134, no. 44, pp. 18330-18337, 2012.

[230] H. Eury, C. Bijani, P. Faller and C. Hureau, “Copper(II) Coordination to Amyloid β: Murine versus Human Peptide,” Angewandte Chemie, International Edition, vol. 50, no. 4, pp. 901-905, 2011.

[231] A. D. Simone and P. Derreumaux, “Low molecular weight oligomers of amyloid peptides display β,” The Journal of Chemical Physics, vol. 132, 2010.

[232] K. Lindorff-Larsen, N. Trbovic, P. Maragakis, S. Piana and D. E. Shaw, “Structure and Dynamics of an Unfolded Protein Examined by Molecular Dynamics Simulation,” Journal of the Amiercan Chemical Society, vol. 134, no. 8, p. 3787–3791, 2012.

[233] P. Derreumaux, “Generating Ensemble Averages for Small Proteins from Extended Conformations by Monte Carlo Simulations,” Physical Review Letters, vol. 85, no. 1-3, p. 206, 2000.

[234] J. Zierenberg and W. Janke, “From amorphous aggregates to polymer bundles: The role of stiffness on structural phases in polymer aggregation,” Europhyiscs Letters, vol. 109, no. 2, 2015.

[235] A. Irback, S. Jonsson, N. Linnemann, B. Linse and S. Wallin, “Aggregate Geometry in Amyloid Fibril Nucleation,” PHYSICAL REVIEW LETTERS, vol. 110, no. 5, 2013.

[236] O. Coskuner, “Divalent copper ion bound amyloid-beta(40) and amyloid-beta(42) alloforms are less preferred than divalent zinc ion bound amyloid-beta(40) and amyloid-beta(42) alloforms,” JOURNAL OF BIOLOGICAL INORGANIC CHEMISTRY, vol. 21, no. 8, pp. 957-973, 2016.

[237] R. Sabaté and S. Saupe, “Thioflavin T fluorescence anisotropy: An alternative technique for the study of amyloid aggregation,” Biochemical and Biophysical Research Communications, vol. 360, no. 1, pp. 135-138, 2007.

[238] M. Mycek and B. Pogue, “Time Resolved Fluorescence Spectroscopy of Tissue,” in Handbook of Biomedical Fluorescence, New York, CRC Press, 2003, pp. 403-408.

[239] M. Amaro, K. Kubiak-Ossowska, D. Birch and O. Rolinski, “Initial stages of beta-amyloid Aβ1−40 and Aβ1−42 oligomerization observed using fluorescence decay and molecular dynamics analyses of tyrosine,” IOP Publishing Ltd , vol. 1, no. 1, 2013.

[240] C. Ianuzzi, R. Maritato, G. Irace and S. I, “Misfolding and Amyloid Aggregation of Apomyoglobin,” Int J Mol Sci. , vol. 14, no. 7, p. 14287–14300, 2013.

[241] W.-F. Xue, A. L. Hellewell, E. W. Hewitt and S. E. Radford, “Fibril fragmentation in amyloid assembly and cytotoxicity,” Prion, vol. 4, no. 1, p. 20–25, 2010.

[242] K. Wun et al “Crystallization and Preliminary X-Ray Diffraction Analysis of the Fab Fragment of WO2, an Antibody Specific for the Aβ Peptides Associated with Alzheimer’s Disease,” Acta Crystallographica Section F Structural biology and crystallization communications, vol. 64, pp. 438-441, 2008.

[243] A. Buell, C. Dobson, T. Knowles and M. Welland, “Interactions between Amyloidophilic Dyes and Their Relevance to Studies of Amyloid Inhibitors,” Biophys H, vol. 99, no. 10, pp. 3492-3497, 2010.

[244] N.V Buchete, R. Tycko and G. Hummer, “Molecular Dynamics Simulations of Alzheimer's β-Amyloid Protofilaments,” J Mol Bio, vol353, no. 4, pp. 804-821

Appendix 1 (Chapter 2.3): MC simulated anisotropy code:

These are important notes about the MC program. Please note the “line x:” are not part of the code and are just used to highlight lines:

- **Line 4:** Integer steps must be kept in degrees
- **Line 15:** Example naming convention is “SmallRangestepstep=1 => S1, LargeRangestep=10 => Lt, lConstraint=30 => c30
- **Line 19:** Initial loop is used for defining all starting points and Tyr is constrained somewhere between the backbone angle and the backbone angle+180
- **Line 33:** The second loop-set records a small step size change “dphi” and “dtheta” which are the angles in 3 dimensions. Which are linked to the proteins backbone movement and are applied to both backbone and Tyr angles. Then a large step size is applied only to the Tyrosine faster (but more constrained) movement in 2 dimensions. Simulating the slow bulk rotation and fast Tyr movements between rotamer states. The steps are changed to radians for all angles.
- **Line 46:** A step to ensure Tyr step does not “pass through” the backbone will cause a new angle to be selected.
- **Line 72:** Once the vectors for these points have been calculated, the anisotropy can be calculated by tracking the movements of the Tyr
- **Line 79:** If multiple monomers / oligomers are being used average anisotropy and must be created
- **Line 95:** Current MC timestep and anisotropy for that movement is recorded to text file to be graphed.

```
        PROGRAM angles
        IMPLICIT NONE
         INTEGER, PARAMETER  :: monTot = 1, timeTot=200000, acRang=10000, tRang=timeTot
Line 4:  INTEGER, PARAMETER  :: smallStep=0.0, smallRangeStep=smallStep/2, largeStep=16, largeRangeStep=largestep/2
         INTEGER, PARAMETER  :: lConstraint= 65, hConstraint=180-lConstraint
         REAL, PARAMETER     :: pi=3.14159265359

         REAL, DIMENSION(1:monTot,0:timeTot)    :: thetaB,thetaT,rTA,phiB,phiT,x,y,z
         REAL                                   :: ANG,rt
         INTEGER                                :: i,t,u,time
         REAL                                   :: r,r2,rTTA(0:timeTot)

        CALL RANDOM_SEED(put=(/54,5,23,12,23,653,75,975,213,34,35,46/))

LINE 15:OPEN(7,file='__S0_00L08C65.dat')
        write(*,*)"Start"
        time = 0

Line 19:                DO i = 1,monTot
                                CALL RANDOM_NUMBER(r)
                                phiB(i,0)=(r*360)

                                CALL RANDOM_NUMBER(r)
                                thetaB(i,0)=(r*360)

                                CALL RANDOM_NUMBER(r)
                                phiT(i,0) = phiB(i,0) + lConstraint + r*(hConstraint - lConstraint)
                                thetaT(i,0) = thetaB(i,0)

                END DO
        write(*,*)"Done start"

line 33:    DO i = 1,monTot
               DO t = 1,timeTot
                  CALL RANDOM_NUMBER(r)
                  phiB(i,t)=phiB(i,t-1)+(r*smallStep)-smallRangeStep
                  phiT(i,t)=phiT(i,t-1)+(r*smallStep)-smallRangeStep

                  CALL RANDOM_NUMBER(r2)
                  thetaB(i,t)=thetaB(i,t-1)+( (r2*smallStep)-smallRangeStep )/sin(pi*phiB(i,t)/180.0)

                  CALL RANDOM_NUMBER(r)
                  phiT(i,t)=phiT(i,t)+(r*largeStep)-largeRangeStep
                  thetaT(i,t) = thetaB(i,t)

Line 46:          DO WHILE ((phiT(i,t).LT.(phiB(i,t)+lConstraint)) .or. (phiT(i,t).GT.(phiB(i,t)+hConstraint)))
                         phiT(i,t)=phiT(i,t) - ((r*largeStep)-(largeRangeStep))
                         CALL RANDOM_NUMBER(r)
                         phiT(i,t)=phiT(i,t-1)+((r*largeStep)-(largeRangeStep))
                  END DO

              END DO
           END DO
        write(*,*)"Movement Complete"

                rTA=0.0

                        phiT = pi*phiT/180.0
                        thetaT = pi*thetaT/180.0
                        DO i = 1,monTot
                                DO t=0,timeTot
                                        x(i,t)=sin(phiT(i,t))*cos(thetaT(i,t))
                                        y(i,t)=sin(phiT(i,t))*sin(thetaT(i,t))
                                        z(i,t)=cos(phiT(i,t))
                                END DO
                        END DO
        write(*,*) "Getting V-coors"

                DO i = 1,monTot
                        DO t=0,(tRang-acRang)
                                DO u=0,acRang-1
line 72:                        ANG=(x(i,t)*x(i,t+u))+(y(i,t)*y(i,t+u))+(z(i,t)*z(i,t+u))
                                rt=0.4*( ( ( 3.0*(ANG*ANG) ) -1.0 )/ 2.0 )
                                rtA(i,u)=rtA(i,u)+rt
                                END DO
                        END DO
                END DO
```

```
Line 79:DO i = 1,monTot
                DO t=0,acRang-1
                rtA(i,t)=rTA(i,t)/(tRang - acRang +1)
                END DO
        END DO

        rTTA=0.0
        DO t=0,acRang-1
                DO i = 1,monTot
                rTTA(t)=(rTTA(t)+rtA(i,t))
                END DO
                rTTA(t)=rTTA(t)/monTot
        END DO

        DO t=0,acRang-1,10

Line 95:        WRITE(7,'(i6,A1,f10.5)')t,'     ',rTTA(t)

        END DO

        END PROGRAM
```

Appendix 2 (Chapter 2.4): MD Programs

Appendix 2.1 – Rotamer Tracking

A simple program to track what rotamer state the Tyr residues is currently positioned in.

Lines 13 -47: Determine which rotamer the current value will fall into

```
Line 1: Sub Button29_Click()
Line 2: Dim x(5003), y(5003) As Double
Line 3: Dim l, m, result(5003) As Integer
Line 4:
Line 5:   m = InputBox("Which protein do you want? A=1, B=2...")
Line 6:   ran = InputBox("Number of frames?")
Line 7:
Line 8:   For l = 0 To ran
Line 9:   x(l) = Cells(1 + l, 31 + ((m - 1) * 5)).Value
Line 10:
Line 11:  y(l) = Cells(1 + l, 32 + ((m - 1) * 5)).Value
Line 12:
Line 13:  If x(l) <= 180 Then
Line 14:      If y(l) >= 0 And y(l) <= 120 Then
Line 15:          result(l) = 2
Line 16:      Else
Line 17:
Line 18:          If y(l) > 120 And y(l) <= 240 Then
Line 19:              result(l) = 3
Line 10:          Else
Line 21:
Line 22:              If y(l) > 240 And y(l) <= 360 Then
Line 23:                  result(l) = 5
Line 24:              End If
Line 25:          End If
Line 26:      End If
Line 27:      Else
```

```
Line 28:  If x(l) > 180 Then
Line 29:      If y(l) >= 0 And y(l) <= 120 Then
Line 31:          result(l) = 1
Line 32:      Else
Line 33:
Line 34:          If y(l) > 120 And y(l) <= 240 Then
Line 35:              result(l) = 4
Line 36:          Else
Line 37:
Line 38:              If y(l) > 240 And y(l) <= 360 Then
Line 39:                  result(l) = 6
Line 41:              End If
Line 42:          End If
Line 43:      End If
Line 44:
Line 45:  End If
Line 46:  End If
Line 47:  Next
Line 48:
Line 49:  For l = 0 To ran

Line 52:  Cells(1 + l, 58 + m).Value = result(l)
Line 53:  Next
Line 54:
Line 55:  End Sub
```

Appendix 2.2 – Anisotropy Calculations

VMD tcl script for tracking Cz and Cg:

```
line 1: proc coor_xyz {{mol top}} {
line 2:
Line 3:   set sel [atomselect $mol "index 764" ]
line 4:   set num_steps [molinfo $mol get numframes]
line 5:
Line 6: set fp [ open "./SB_DoubAgg_CG_xyz_coor.dat" w+ ]
line 7:
Line 8:   for {set frame 0} {$frame < $num_steps} {incr frame} {
line 9:     $sel frame $frame
Line 10:    set coord [$sel get {x y z}]
line 11:    puts $fp "$frame $coord"
line 12:
line 13:  }
line 14:close $fp
line 15:}
```

Line 1: Name of the TCL script

Line 3: Selects the atom (by its index number, must be done separately for C_γ and C_Z)

Line 4: Number of repetitions is set by number of frames in the trajectory

Line 6: Name of file to save the coordinates too

Line 8: Starts the loop

Lines 9-11: The frame and coordinates are selected and saved to the file set in line 6

Vector and Anisotropy program:

Line 8: AC range is the number of frames used in the final and anisotropy plot; it varies for each simulation depending on amount of frames available

Line 10: T range is the total number of frames in the dataset and truncation is possible

Line 26-43: this loop is used to turn the coordinates for the two C_γ and C_Z atoms of the Tyr into vectors (xv,xy,xz), which is then normalised (nx, ny, nz) usign the vector length (vlen). in order to get an angle with respect to the Z axis

Line 48-54: create the anisotropy data by taking the dot product of the current normalized vector coordinates and normalized vector coordinates from another time. which are then put into line 64 which is the FORTRAN equivalent of Eqn. 2.4.12.

Line 57-67: are used to create the average anisotropy and converts the MCS into nanoseconds and is then output to a text file to be graphed.

```
                PROGRAM anisotropy
                 IMPLICIT NONE
                 INTEGER                 ::  n,i,frame,counter,acRang,tRang,frames,start,ncounter,startframe,extra,sP
                 REAL, PARAMETER         :: PI1=3.14159265359
                 REAL, DIMENSION(0:10000) :: x1,y1,z1,x2,y2,z2,xv,yv,zv,vLen,vLen2,xn,yn,zn,theta,P,rtA,anglez,anglex,angley
                 REAL                    :: DOT(0:5000,0:5000),rt(0:5000,0:5000),iC

line 8:         acRang=400

line 10:        tRang=1000
                start=0

                  rt = 0.0
                  DOT = 0.0

                  OPEN(7,file='BetaSheet_B.dat')
                  OPEN(8,file='BSheet_B_Rt.dat')
                  OPEN(9,file='Bsheet_B_Angles.dat')

                  DO n = 0,start-1
                     READ(7,*) frame,x1(n),y1(n),z1(n),x2(n),y2(n),z2(n)
                  END DO

                startframe= frame+1

line 26:          DO n = 0,(tRang-start)
                     READ(7,*) frame,x1(n),y1(n),z1(n),x2(n),y2(n),z2(n)

                     xv(n)=x1(n)-x2(n)
                     yv(n)=y1(n)-y2(n)
                     zv(n)=z1(n)-z2(n)

                     vLen(n)=((xv(n)**2)+(yv(n)**2)+(zv(n)**2))**0.5

                     xn(n)=xv(n)/vLen(n)
                     yn(n)=yv(n)/vLen(n)
                     zn(n)=zv(n)/vLen(n)

                    anglez(n)=acos(zn(n))/PI1*180
                    angley(n)=acos(yn(n))/PI1*180
                    anglex(n)=acos(xn(n))/PI1*180
                   WRITE(9,*)anglex(n),angley(n),anglez(n)
line 43:           END DO

                       WRITE(*,*)'Start Frame = ',startframe
                       WRITE(*,*)'Final Frame = ',frame
```

```
line 48:            DO n=0,(tRang - start - acRang)
                       DO i=n,n+(acRang-1)
                          DOT(n,i)=(xn(n)*xn(i))+(yn(n)*yn(i))+(zn(n)*zn(i))
                          rt(n,i)=0.4*( ( (3.0*(DOT(n,i)*DOT(n,i)))-1.0)/ 2.0 )
                          IF((i-n).EQ.400) WRITE(*,*)'n = ',n,' dot(n,n+450) = ',DOT(n,i)
                       END DO
line: 54:           END DO

                  rtA=0
line 57:          DO n= 0,(tRang-start-acRang)
                     DO i=0,acRang-1
                          rtA(i)=rtA(i)+rt(n,n+i)
                       END DO
                     END DO

                  DO i=0,acRang-1
                    rtA(i)=rTA(i)/(tRang - start - acRang +1)
                    iC= i * 100.0/ 2500.0
                    WRITE(8,'(i6,A1,f10.5,A1,f10.5)')i,'  ',iC ,' ',rtA(i)
line 67:          END DO


                  END PROGRAM
```

Appendix 3: Experimental Extras

Appendix 3.1: All χ^2 values for Fluorescence Spectroscopy/ Anisotropy results

Though some values have poor fits, the majority are adequately fit with appropriate χ^2 values. It can be assumed that these χ^2 values are outliers.

3.1a: Experimental Spectroscopy χ^2 Values

Aβ in water:

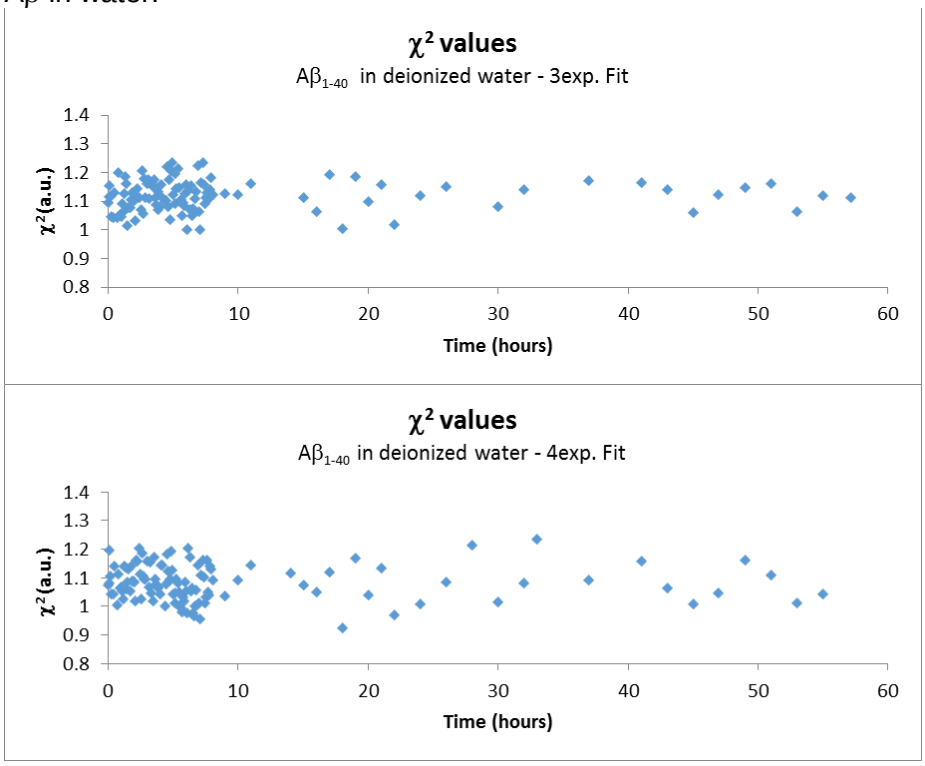

Aβ in Hydrochloric Acid:

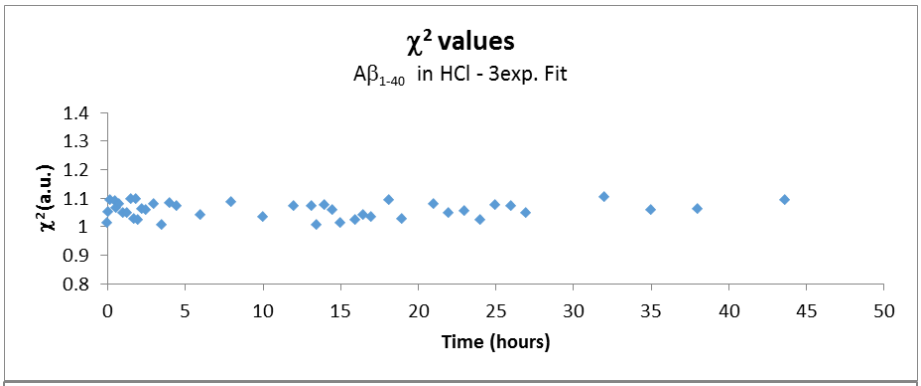

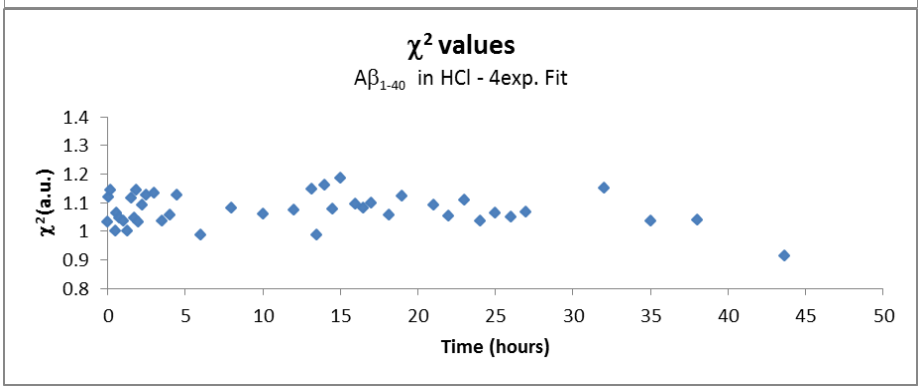

Aβ in NaOH:

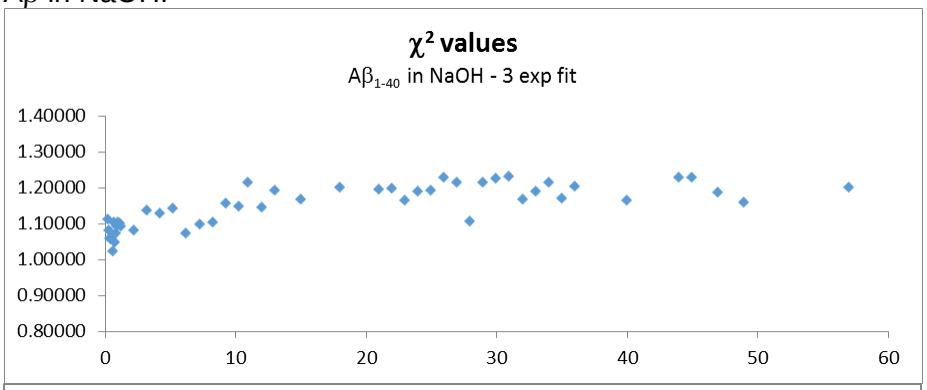

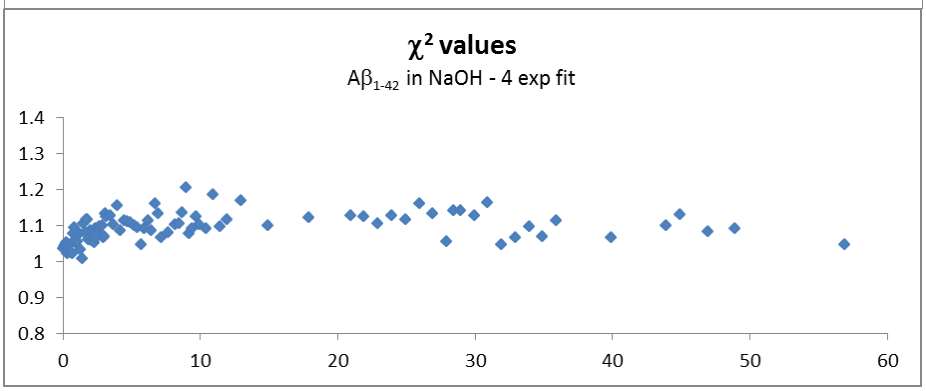

The difference here is a general trend of increase c2 values starting to generally be above 1.2 which could be indicative of the requirement of a 4exp fit.

Appendix 3.2: Spectroscopy Fits

4exp. graph for Aβ in HCl

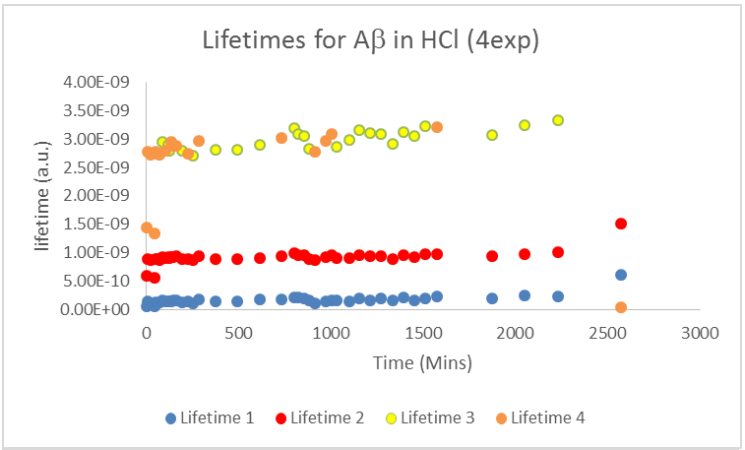

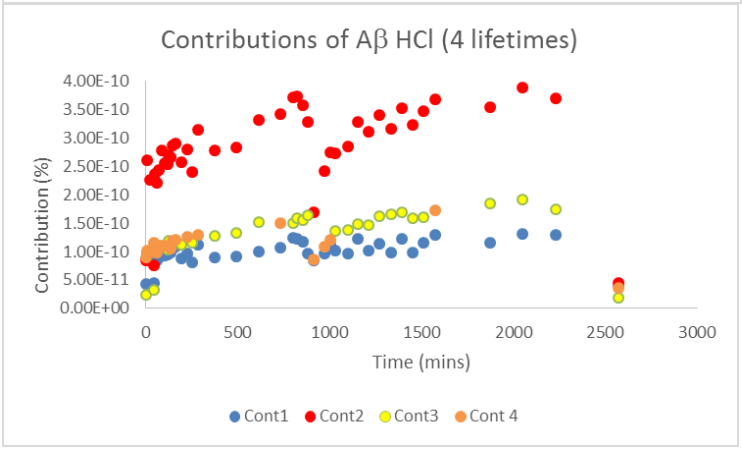

Note the axis for these contributions are almost 0, with the four lifetime being generally at almost 1. This implies the results are not sufficient and three exponential fit is more appropriate.

4exp. Full Graph for Aβ in NaOH

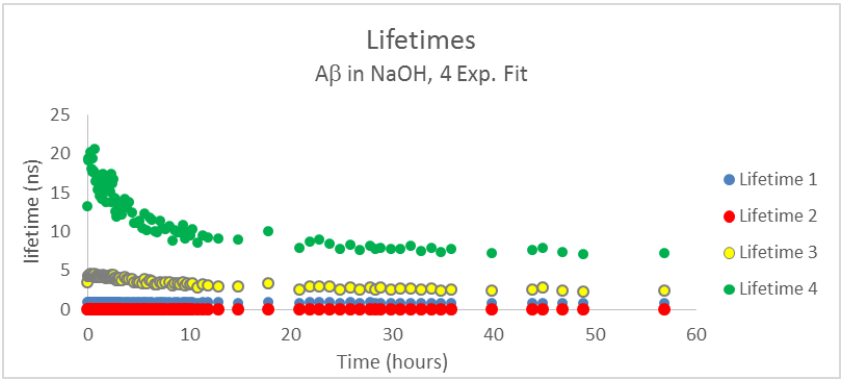

Appendix 3.3: All DLS correlations

3.3a: Acceptable DLS Correlations Associated With BSA Results inHEPES and PBS

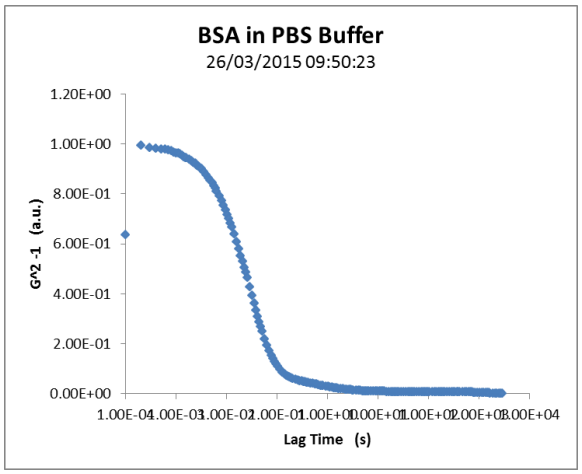

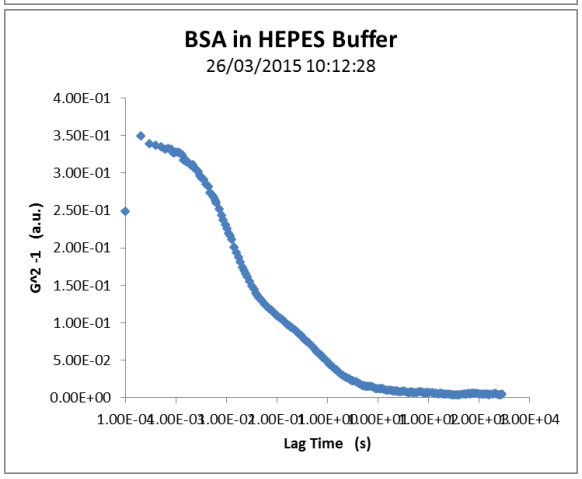

The resulting correlations are similar, which suggests that there should be no issue using HEPES in Ab experiments. Despite this, it seems that the use of PBS buffer is better, as it scatters less.

3.3b: DLS results for all samples in Zetasizer "Nano"

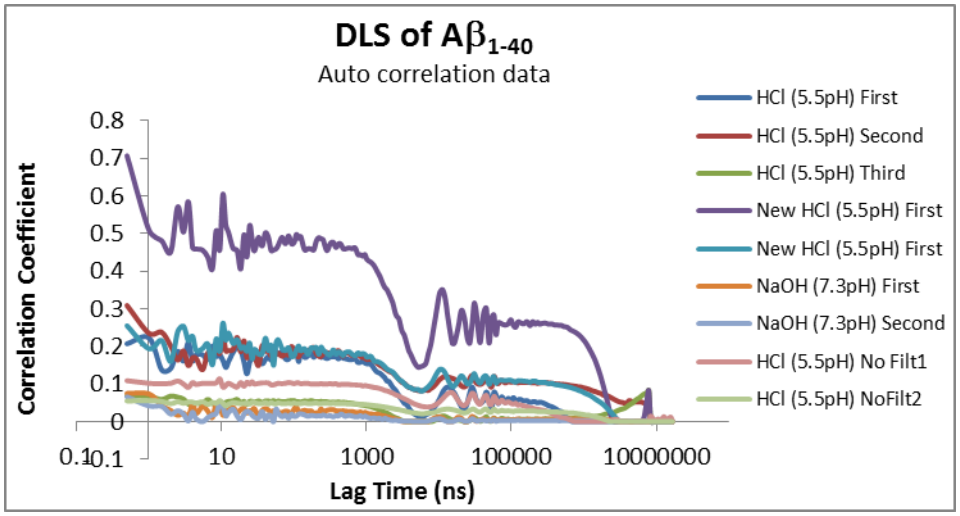

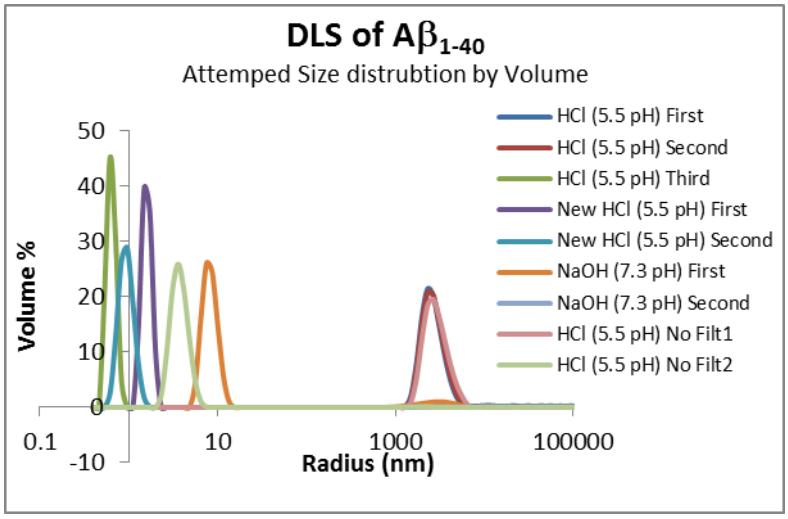

The first three results are three attempted studies of Aβ in dilute HCl from the same sample, which initially show very large aggregates then showed a small aggregate. The next two are from a different sample with similar properties, showing a small particle and an apparent negative sized species which should not be possible. The next two results are two attempts of Aβ in NaOH again showing a slightly different size from the others, which could be related to the aggregation. The final two are results for Aβ in an unfiltered dilute HCl solution.

Despite the large particle being similar for all there are no patters to the size distributions they appear random and size does not increase with time (sometimes large, sometimes small with no distributions in between). There are also negative size distributions. These results do not give any valuable information and cannot be

trusted, as expected based on these correlations; there are no useable measurements available here. The only notable information here is that the NaOH sample shows a larger particle around 10ns which could be related to the aggregation, though as the results cannot be trusted this could be coincidence.

Appendix 3.4: Stochastic Optimiser for Anisotropy Best Fits

```
Line 1:   Sub thirddiStochast()
Line 2:   Dim y, x(8), xlo(8), xhi(8), xnew(8), dx(8), safe(8), ynew, random, beta As Double
Line 3:   Dim i, j, k, l As Integer
Line 4:
Line 5:   Application.ScreenUpdating = False
Line 6:   beta = 0.01
Line 7:   If Cells(4, 4).Value > 9 Or Cells(4, 4).Value < 2 Then
Line 8:       MsgBox ("Please choose a number of variables between 2 and 9")
Line 9:   Else
Line 10:      y = Cells(5, 4).Value
Line 11:
Line 12:  For k = 0 To (Cells(4, 4).Value - 1)
Line 13:      x(k) = Cells(8, 4 + k).Value
Line 14:      xlo(k) = Cells(9, 4 + k).Value
Line 15:      xhi(k) = Cells(10, 4 + k).Value
Line 16:      dx(k) = (xhi(k) - xlo(k))
Line 17:  Next
Line 18:
Line 19:  For k = 0 To (Cells(4, 4).Value - 1)
Line 20:      x(k) = xlo(k) + (xhi(k) - xlo(k)) / 3
Line 21:      Cells(8, 4 + k).Value = x(k)
Line 22:      Cells(4, 7 + k).Value = x(k)
Line 23:  Next
Line 24:
Line 25:      y = Cells(5, 4).Value
Line 26:      Cells(2, 7).Value = y
Line 27:
Line 28:  For j = 0 To 5 Step 1
Line 29:  For i = 1 To 200
Line 30:
Line 31:      For k = 0 To (Cells(4, 4).Value - 1)
Line 32:          Do
Line 33:            random = (2 * Rnd() - 1)
Line 34:            xnew(k) = x(k) + (dx(k)) * random
Line 35:          Loop Until (xnew(k) >= xlo(k)) And (xnew(k) <= xhi(k))
Line 36:
Line 37:          Cells(8, 4 + k).Value = xnew(k)
Line 38:      Next
Line 39:      ynew = Cells(5, 4).Value
Line 40:
Line 41:       If Rnd() < Exp(beta * (y - ynew)) Then
Line 42:              y = ynew
Line 43:              Cells(2, 7).Value = y
Line 44:              For k = 0 To (Cells(4, 4).Value - 1)
Line 45:              x(k) = xnew(k)
Line 46:              Cells(4, 7 + k).Value = x(k)
Line 47:              Cells(4, 7 + k).Interior.ColorIndex = 50
Line 48:              Next '
Line 49:          End If
Line 50:
Line 51:  Next
Line 52:  beta = beta * 2
Line 53:  Cells(3, 4).Value = beta
Line 54:  Next
Line 55:
Line 56:  For j = 0 To 5 Step 0.2
Line 57:  For i = 1 To 200
Line 58:
Line 59:      For k = 0 To (Cells(4, 4).Value - 1)
Line 60:          Do
Line 61:            random = (2 * Rnd() - 1)
Line 62:            xnew(k) = x(k) + (dx(k) * 10 ^ -j) * random
Line 63:          Loop Until (xnew(k) >= xlo(k)) And (xnew(k) <= xhi(k))
Line 64:
Line 65:          Cells(8, 4 + k).Value = xnew(k)
Line 66:      Next
Line 67:      ynew = Cells(5, 4).Value
Line 68:
Line 69:          If ynew < y Then
Line 70:              y = ynew
Line 71:              Cells(2, 7).Value = y
Line 72:              For k = 0 To (Cells(4, 4).Value - 1)
Line 73:              x(k) = xnew(k)
Line 74:              Cells(4, 7 + k).Value = x(k)
Line 75:              Cells(4, 7 + k).Interior.ColorIndex = 50
Line 76:              Next
Line 77:          End If
Line 78:
Line 79:  Next
Line 80:  Next
Line 81:      End If
Line 82:  Application.ScreenUpdating = True
Line 83:
Line 84:  End Sub
```

Line 2: Array of 0-8 used i.e. 9 variables used which would create a three exp. Fit.

Line 5: Screen updating off to increase efficiency.

Line 6: Beta value starting value selected and is used in the annealing portion of the program.

Lines 7-26: Assigns the initial values of the fitted parameters into the system with y being the total error of the fit.

Lines 33-39: Selects a random number (between -1 and 1) to be the step change to the variables (loops until a valid input is found). New value of y (totally error) is recorded.

Lines 41-54: This is the annealing section of the code. A random number (between 0 and 1) is selected and compared the resulting value of exp(beta*(ΔY), the change in error (and the variables) is only accepted when this result is less than the random number. This is then repeated with a larger Beta value. At first the program will allow for changes both positive and negative (increases and decreases in error), and will slowly become less inclined to take results that lead to an increase in error. The J loops dictate the accuracy by fine tuning how big of a change to the variables are before the beta value is increased with each cycle of I. This means that at first, there will be large changes in error and it will slowly pin point the best fit for the system. The beta variable is used to ensure that the resulting fit does not accidently become stuck incorrectly at point that appears to be the best fit. This can happen as a change to one variable, could result in a better fit being found, but in reality, is a poor change for the overall fit of all variables.

Lines 56-77: This is the stochastic optimisation portion of the code. Works in a similar way to the anneal but only accepts decreases in error as by this point we assume that it has most likely found the correct region of variables and this area is used to do a fine tune of the resulting fit. The screen is then updated and the resulting graph can be extracted for the best fit.

Appendix 3.5: Sample Anisotropy Correlation Calculation

$$cov(x,y) = \frac{1}{N}\sum_i (x_i - \bar{x})(y_i - \bar{y}))$$

(A3.5.1)

Where, x is the recorded value of anisotropy (r_a), and y is the fitted value of anisotropy (r_f) $\bar{x}$ and $\bar{y}$ are the mean values of all r_a values and the mean values of all r_f values respectively [1].

$$\rho = \frac{cov(x,y)}{\sigma_x \sigma_y}$$

(A3.5.2)

Where σ_x and σ_y are the standard deviations of all r_a values and the standard deviations all r_f values, respectively [1].

For experimental anisotropy data at 0 hours and 0 minutes (Time=0), correlated over 50ns of the analysis window.

$\bar{x}$=0.104321784, $\bar{y}$ =0.098034522, and so $cov(x,y)$ over the 50ns window = 0.000887897

σ_x=0.084845717, σ_y=0.029023181$\rho = \frac{0.000887897}{0.084845717 * 0.029023181}$

$$\rho = 0.360363452$$

$$\rho = 0.3604$$

Microsoft Excel has an in built function for this that produces the same results.

Appendix 3.6: Rotational Times from Anisotropy Data

3.6a Parameters for HEPES experiment and χ^2 for graphs

Day	Clock	Time	Slow T_1 (ns)	Fast T_2 (ns)	B_1	B_2	A	χ^2
1	1600	15m	16.76	0.69	-0.06	0.38	0.11	1.09
1	1700	1h15m	12.22	0.71	-0.05	0.38	0.10	1.03
1	1800	2h15m	5.21	0.90	-0.12	0.63	0.11	1.24
1	2000	4h15m	120.61	0.69	-0.29	0.34	0.35	1.00
1	2200	6h15m	13.55	0.84	-0.11	0.51	0.15	1.16

Day	Clock	Time	Slow T_1 (ns)	Fast T_2 (ns)	B_1	B_2	A	χ^2
2	0900	17h15m	9.76	1.16	-0.17	0.66	0.16	1.72
2	1200	20h15m	11.44	1.02	-0.12	0.59	0.14	1.43
2	1700	25h15m	9.74	1.00	-0.11	0.52	0.14	1.18
2	2200	30h00m	10.58	1.60	-0.24	0.73	0.17	3.59
3	0534	37h34m	414.12	1.12	-3.19	0.31	3.21	1.20
3	1135	43h35m	2589.37	1.06	-20.75	0.23	20.76	1.17
3	1508	47h08m	47.80	1.30	-0.58	0.33	0.56	1.22
4	1508	71h08m	1176.12	2.69	-72.92	0.88	72.64	0.99
4	2223	78h23m	1191.21	2.88	-124.58	1.07	124.10	1.00

Here we see increase pre-exponentials, with random changes in time scale that are outside the scope of the window of analysis and so do not make sense, despite the good errors. These fits are not acceptable.

3.6b Manipulated fits for HEPES experiment to get increasing rotational times

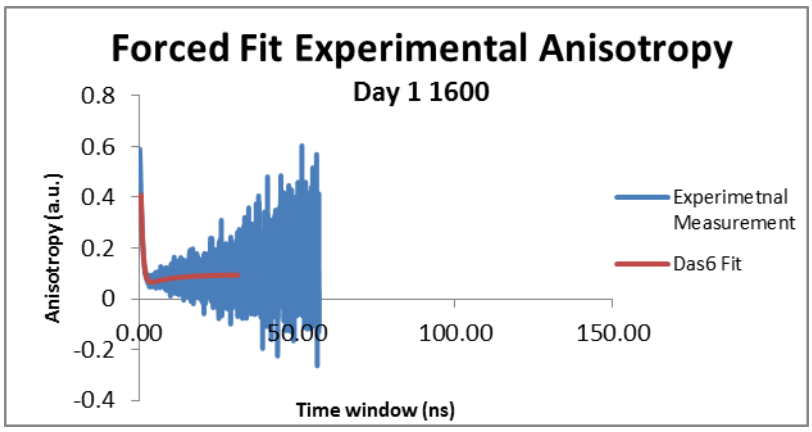

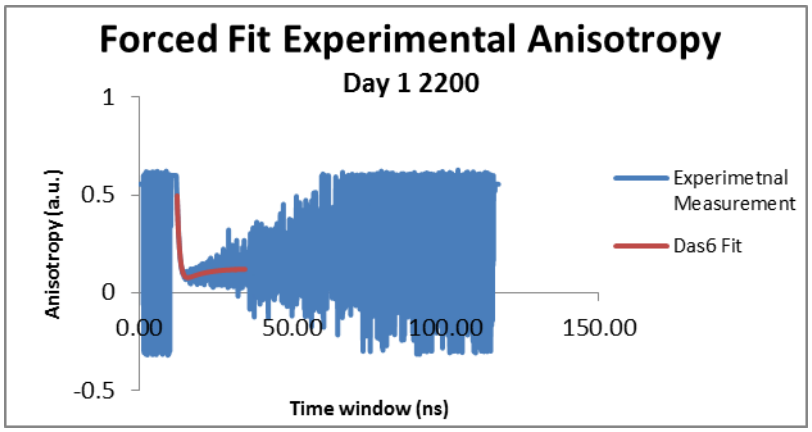

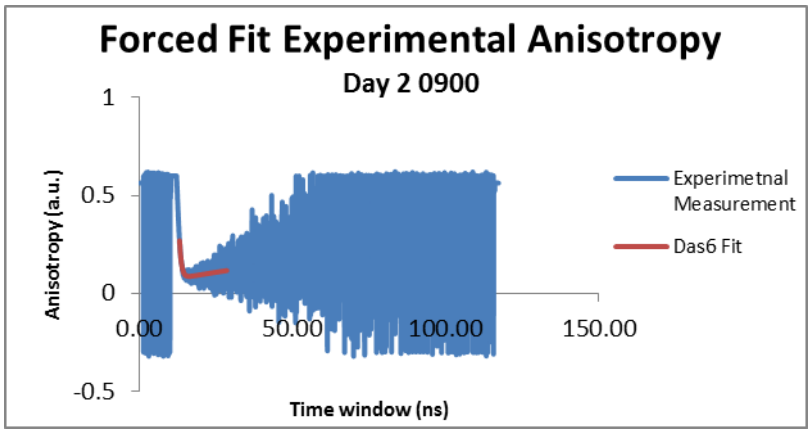
Forced Fit Experimental Anisotropy
Day 2 0900
Anisotropy (a.u.)
1
0.5
0
-0.5
0.00
50.00
100.00
150.00
Time window (ns)
Experimetnal Measurement
Das6 Fit

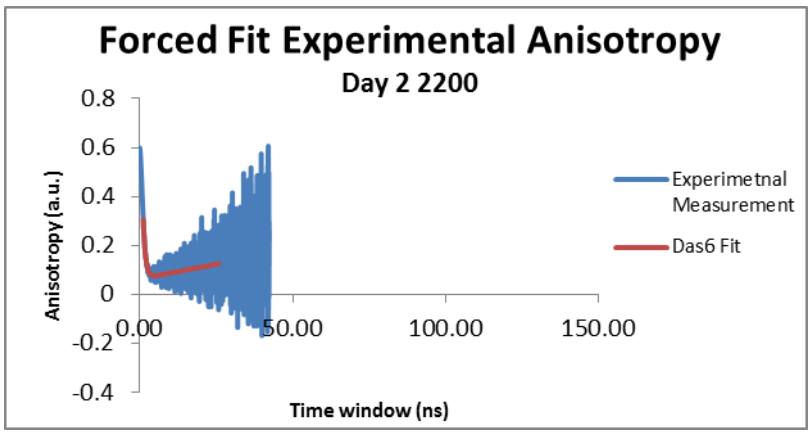
Forced Fit Experimental Anisotropy
Day 2 2200
Anisotropy (a.u.)
0.8
0.6
0.4
0.2
0
-0.2
-0.4
0.00
50.00
100.00
150.00
Time window (ns)
Experimetnal Measurement
Das6 Fit

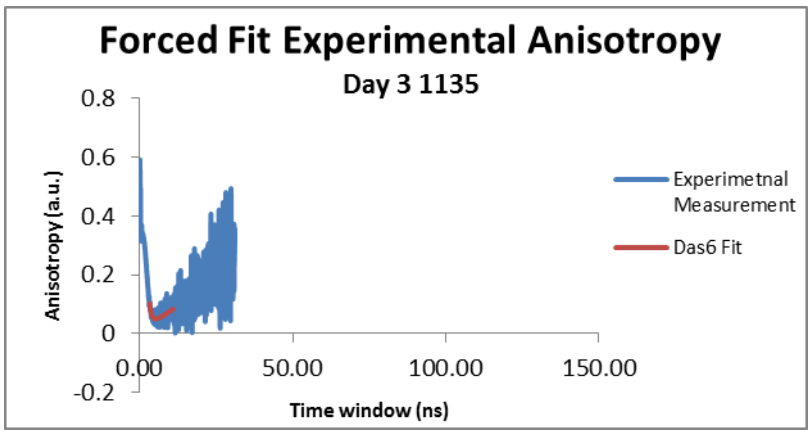
Forced Fit Experimental Anisotropy
Day 3 1135
Anisotropy (a.u.)
0.8
0.6
0.4
0.2
0
-0.2
0.00
50.00
100.00
150.00
Time window (ns)
Experimetnal Measurement
Das6 Fit

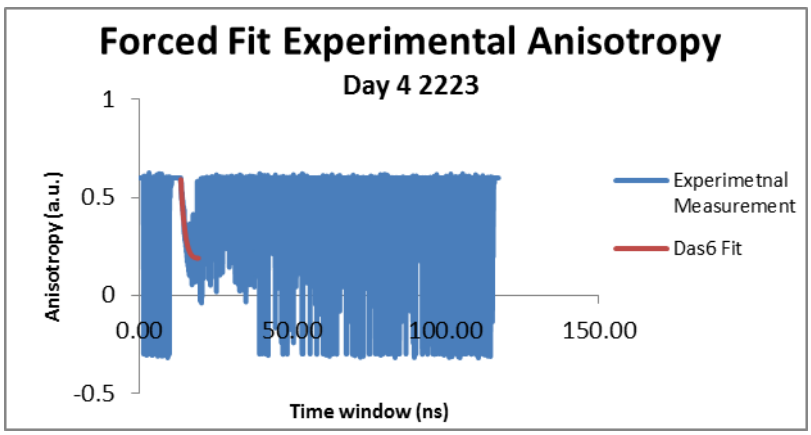
Forced Fit Experimental Anisotropy
Day 4 2223
Anisotropy (a.u.)
1
0.5
0
-0.5
0.00
50.00
100.00
150.00
Time window (ns)
Experimetnal Measurement
Das6 Fit

Day	Clock	Time	Slow T_i (ns)	Fast T_i (ns)	χ^2
1	1600	15mins	7.76	0.69	1.09
1	2200	6h15m	13.55	0.84	1.16
2	0900	17h15m	110.85	0.67	1.03
2	2200	30h15m	309.58	0.77	1.07
3	1135	43h50m	655.63	0.77	1.14
4	2223	78h38m	1191.21	2.88	1.00

As can be seen above, almost all results have so much scatter that almost no data can be recovered from them. Unlike the fits attempted in Appendix 3.6a the time window for these fits is small portions, resulting in good c2 values and increasing rotational time. However, the values seen here are far too large, as they are times that would occur out with the analysis window

Appendix 3.7: Rotational Times and χ^2 for 3exp NaOH Fits

Day	Clock	Time	T_1 (ns)	T_2 (ns)	T_3 (ns)	χ^2
1	1202	5m	16.70	2632.39	0.60	1.129619
1	1417	2h20m	11.95	1326.39	0.57	1.086469
1	1622	4h25m	10.69	1413.18	0.57	1.044086
1	2027	8h30m	11.19	1447.81	0.58	1.094932
1	2234	10h37m	9.62	1232.90	0.54	1.051851
2	0053	12h56m	8.63	1324.31	0.54	1.074314
2	0325	15h28m	9.66	2723.52	0.61	1.143533
2	0542	17h45m	6.05	2597.75	0.53	1.081241
2	0757	19h00m	5.21	2532.80	0.53	1.020308
2	0958	21h01m	4.38	2501.11	0.53	1.086757
2	1157	23h00m	3.54	2468.65	0.53	1.063187
2	1352	24h55m	2.69	1910.32	0.56	1.118648
2	1541	26h44m	3.66	43.38	0.61	1.048921
2	1722	28h25m	8.19	14.34	0.68	1.117438
2	1904	30h07m	1.77	73.45	0.62	1.040459
2	2051	31h54m	16.85	17.04	1.26	1.063225
3	1152	46h55m	2.61	11.88	2.51	0.973257
3	1432	48h35m	3.56	6.62	8.51	1.020241
3	1824	51h27m	1.93	1.89	1.97	0.631293
3	2023	53h26m	0.54	2.74	2.83	0.969869

Except the initial result the first 1- hours show very similar results, after this there is a significant (and fairly sustained) increase in one of the timescales, possibly associated with the aggregation or the environmental changes that occur around this time. All results after the first 24 hours stop following any sort of pattern. They do have the most scatter and graphically they appear to have extremely long times associated with them as they have an r_∞ value of around 0.3 though it is impossible to tell due to the scatter and cannot be fit to past a certain point (around 11667ns of a total 29167ns). Regardless, no useful information can be extracted from these results. This is also true of the pre exponential functions seen below.

Day	Clock	Time	B_1 (ns)	B_2 (ns)	B_3 (ns)	A
1	1202	5m	0.137	-9.679	0.279	9.61
1	1417	2h20m	0.102	-3.811	0.226	3.78
1	1622	4h25m	0.093	-3.638	0.230	3.61
1	2027	8h30m	0.094	-3.783	0.226	3.76
1	2234	10h37m	0.095	-4.149	0.160	4.13
2	0053	12h56m	0.088	-4.611	0.165	4.59
2	0325	15h28m	0.084	-9.084	0.229	9.07
2	0542	17h45m	0.072	-7.338	0.160	7.34
2	0757	19h00m	0.067	-6.582	0.147	6.59
2	0958	21h01m	0.066	-6.360	0.161	6.37
2	1157	23h00m	0.068	-6.649	0.164	6.65
2	1352	24h55m	0.067	-5.211	0.177	5.22
2	1541	26h44m	0.083	-0.219	0.171	0.20
2	1722	28h25m	0.280	-0.358	0.186	0.12
2	1904	30h07m	0.096	-0.254	0.131	0.25
2	2051	31h54m	5.978	-6.106	0.212	0.12
3	1152	46h55m	-10.892	-0.324	11.234	0.41
3	1432	48h35m	3.503	-11.227	8.078	0.16
3	1824.00	51h27m	-1467.87	1591.46	-123.64	51.27
3	2023.00	53h26m	0.04	15.43	-15.37	0.32

Appendix 4 (Chapter 5): MD Simulations for Aβ1-40

Appendix 4.1 – One Protein System (No Ions) Rotamer movements

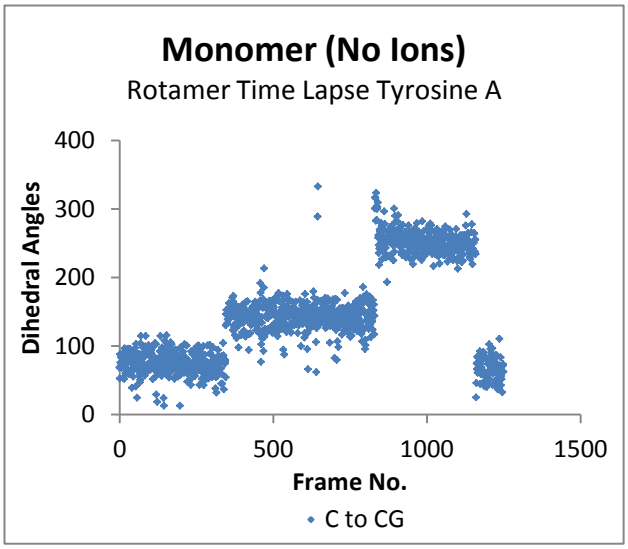

Appendix 4.2 – One Protein System (Ions) Rotamer movements

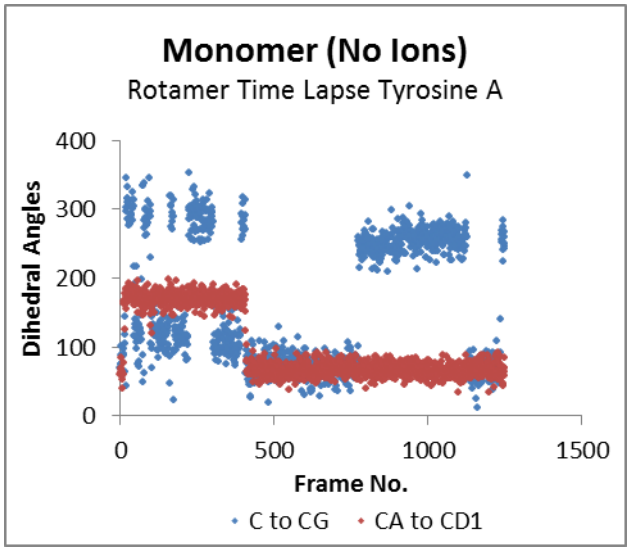

Appendix 4.3a – Two Protein System (Monomers) Rotamer movements

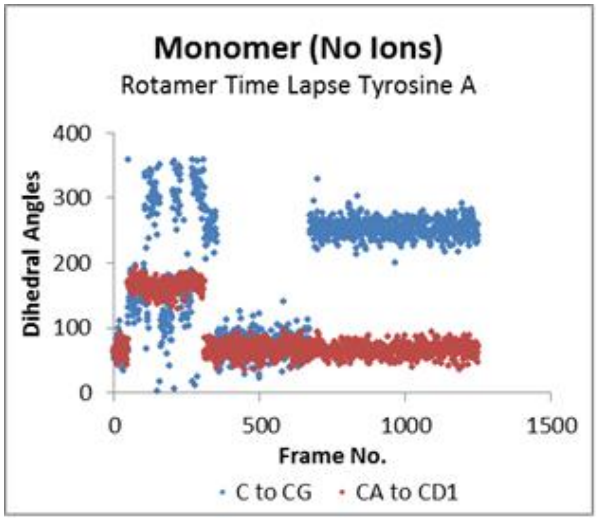

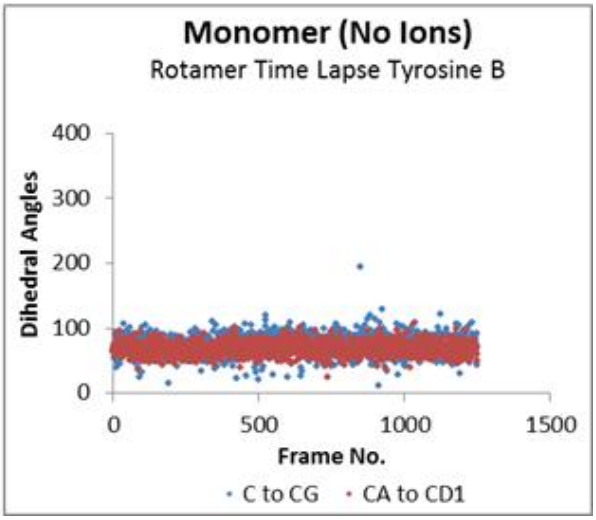

Appendix 4.4a – Two Protein System (Dimer with Big Waterbox) Rotamer movements

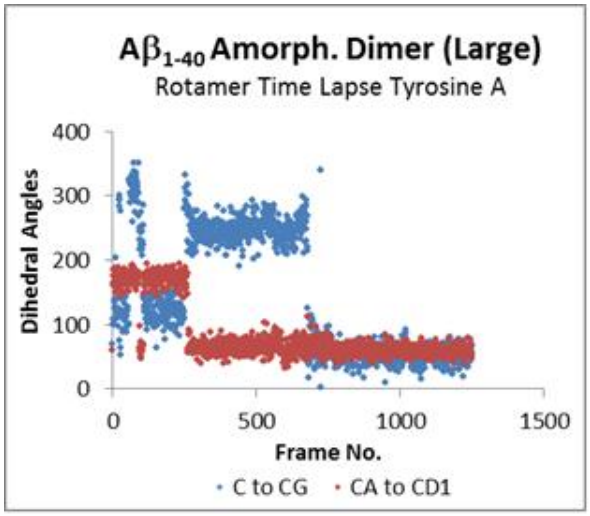

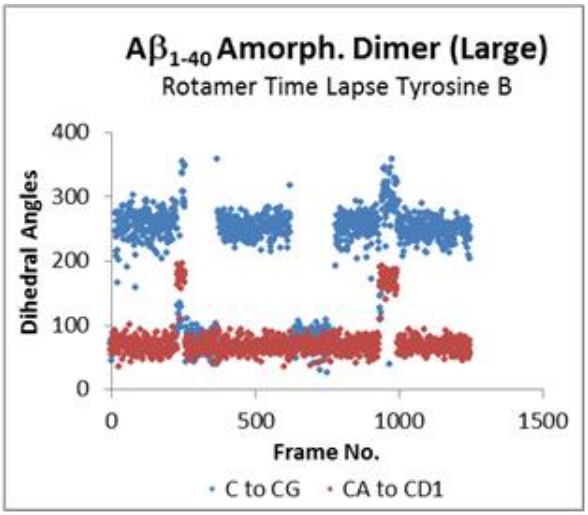

Appendix 4.4b – Two Protein System (Dimer with Big Waterbox) Fitting parameters

Simulation	riT+riB	roT-riT	TT	roB-riB	TB	Correl.
Dimer (Big)	-0.05	0.072426	31.74529	0.377574	1.74806	0.952699
Sng exp.	-0.04	-	-	0.439978	2.681594	0.966012

When fitted to the initial decay and the rise is ignored it gives a contribution for a one exponential fit. Despite this the resulting fit for the single exponential is identical to that of the two exponential seen initially.

Appendix 4.5a – Two Protein System (Dimer with Small Waterbox) Hydrophobic sections

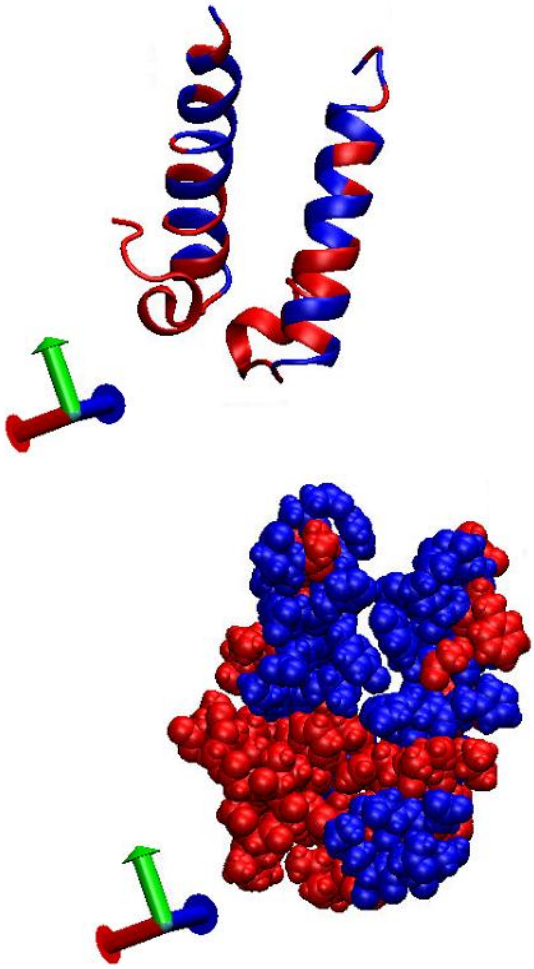

As expected the tails have buried themselves into each other allowing the aggregation to occur.

Appendix 4.5b – Two Protein System (Dimer with Small Waterbox) Rotamer movements

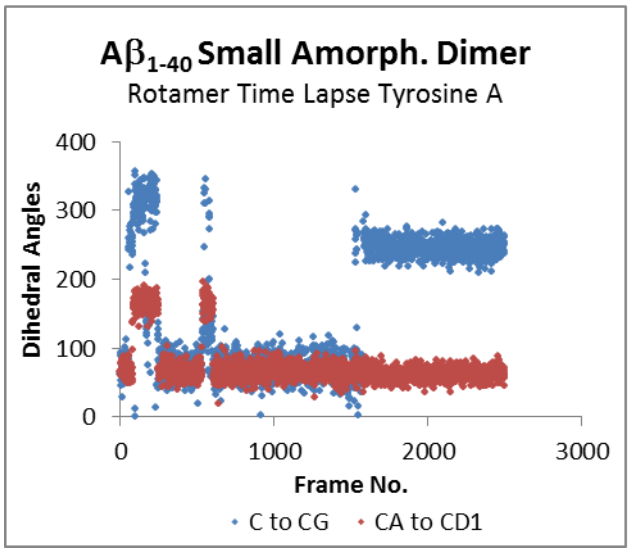

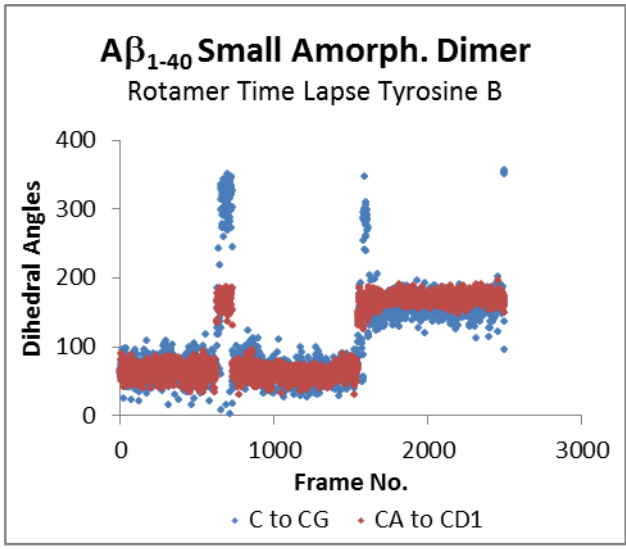

Appendix 4.6 – Three Protein System (Dimer and Monomer) Rotamer movements

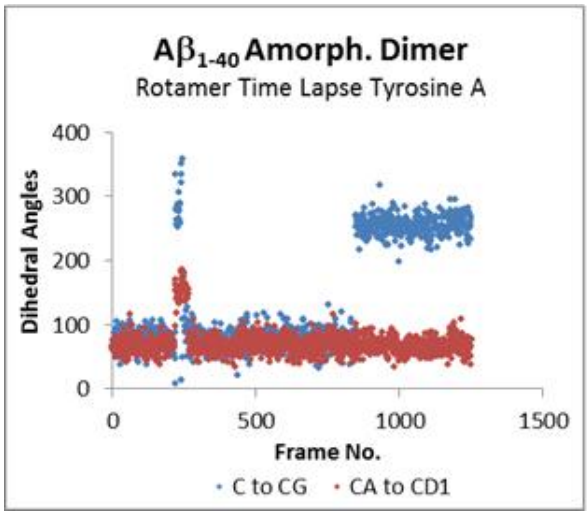

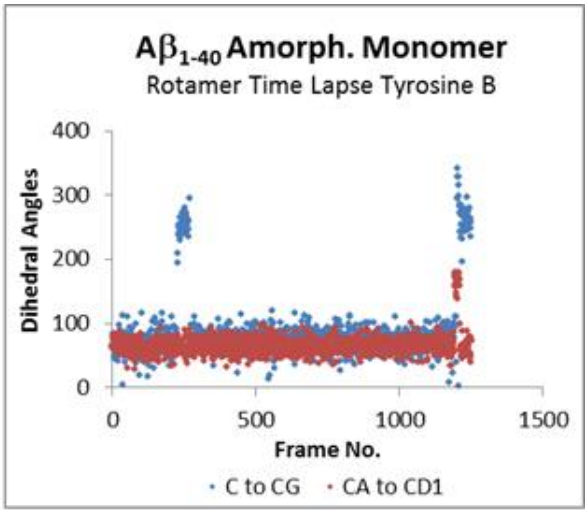

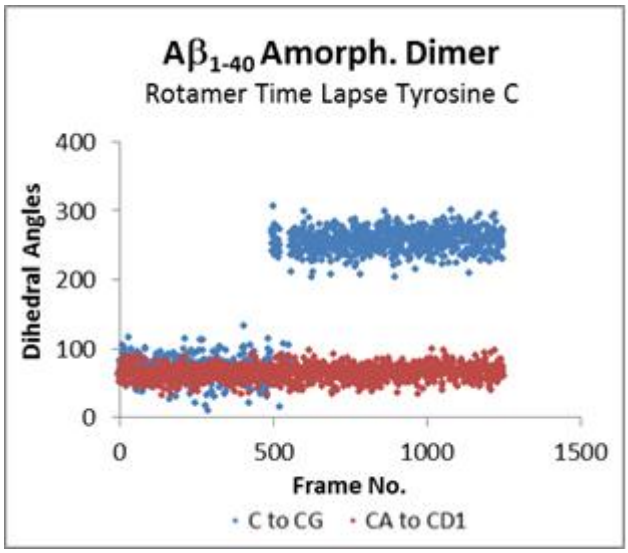

Appendix 4.7 - Three Protein System (Trimer with ions) Rotamer movements

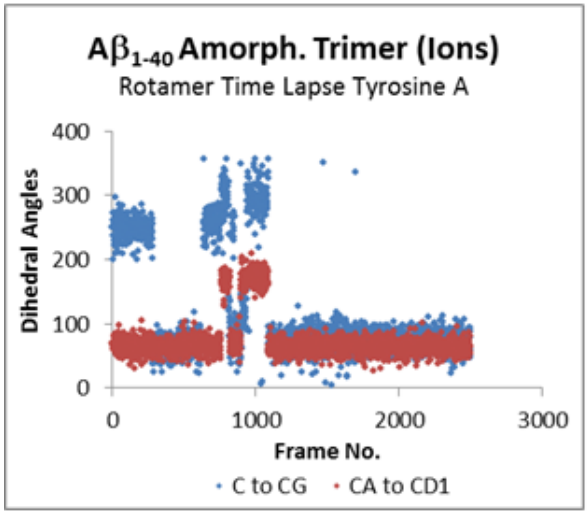

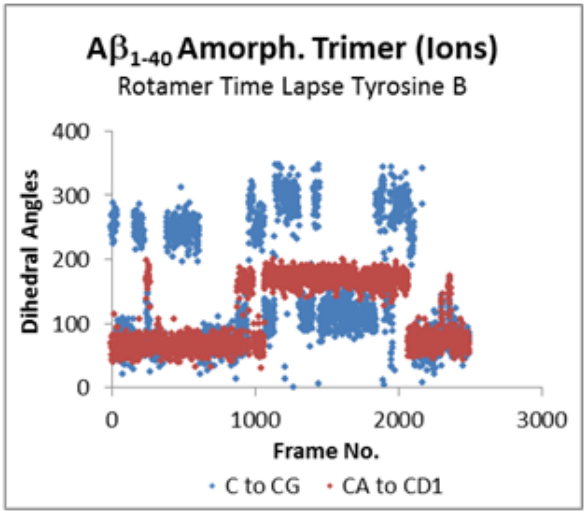

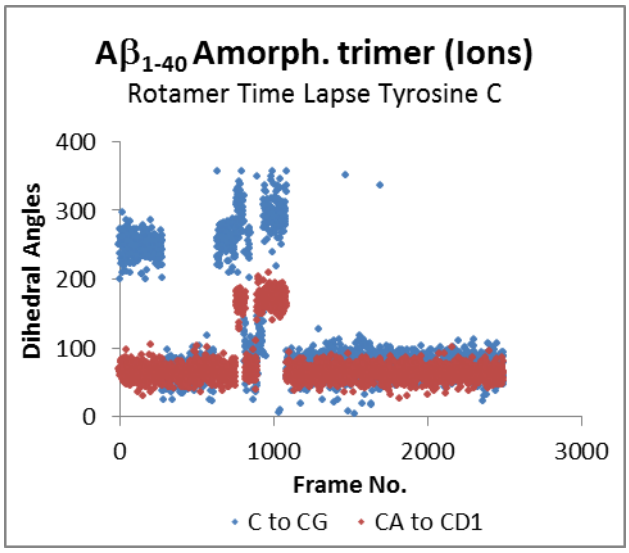

Appendix 4.8 - Four Protein System (Tetramer) Rotamer movements

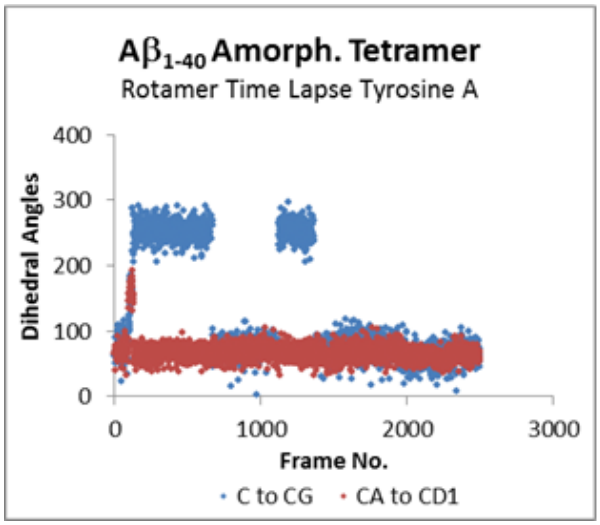

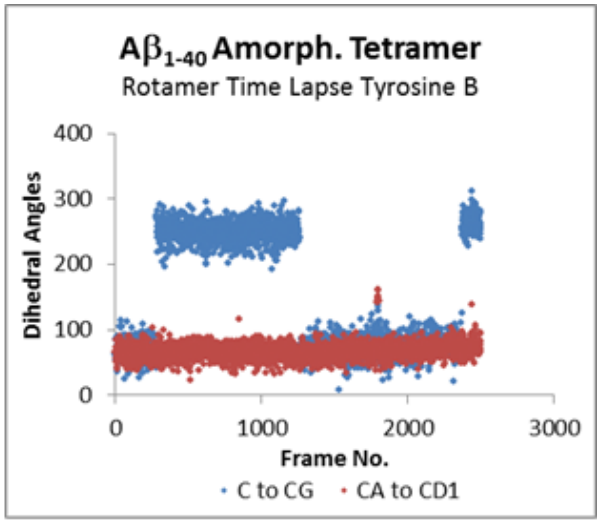

Appendix 5 (Chapter 6) MD Simulations for amorphous Aβ1-42

*Appendix 5.1 - **Three Protein System (No Aggregation, no ions)** Rotamer movements*

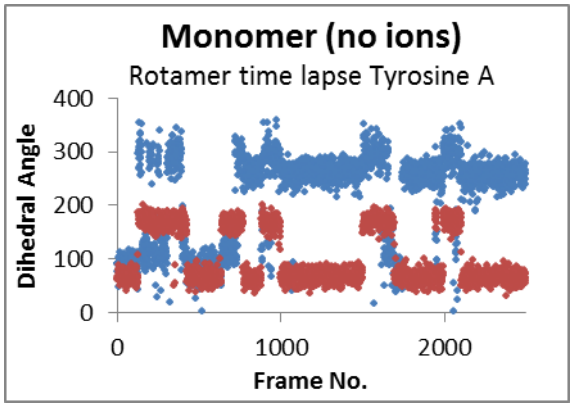

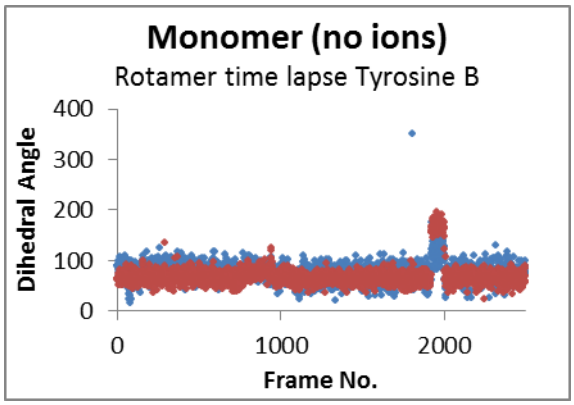

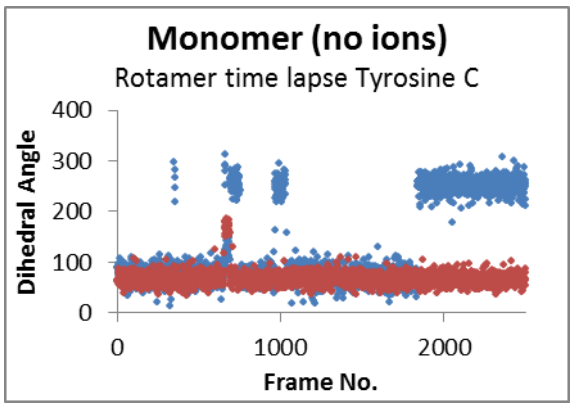

*Appendix 5.2 - **Three Protein System (Amorphous Dimer + Monomer)** Rotamer movements*

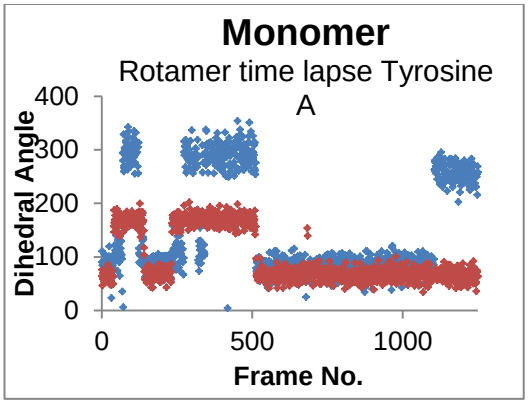

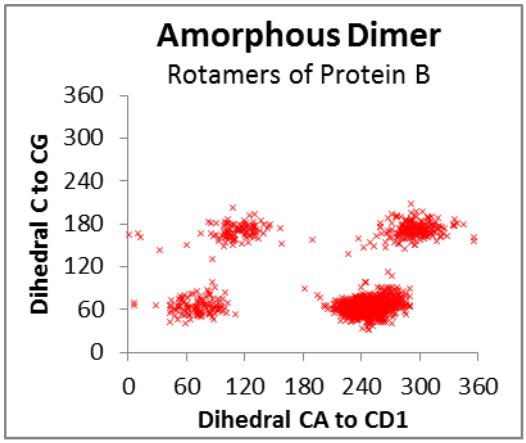

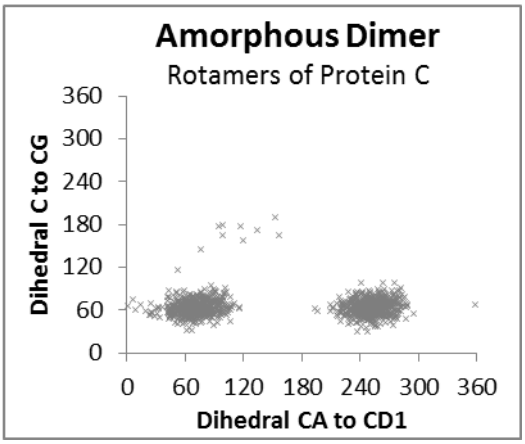

*Appendix 5.3 - **Three Protein System with Ions (No aggregation)** Rotamer movements*

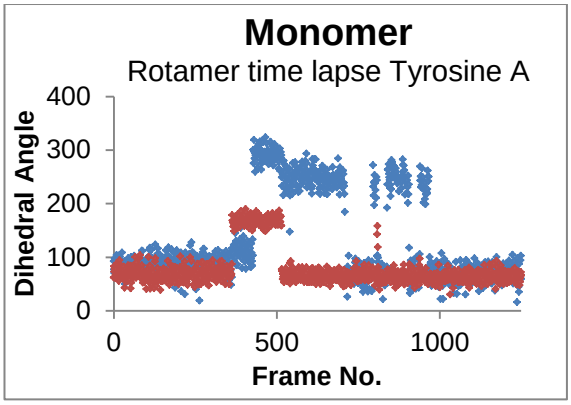

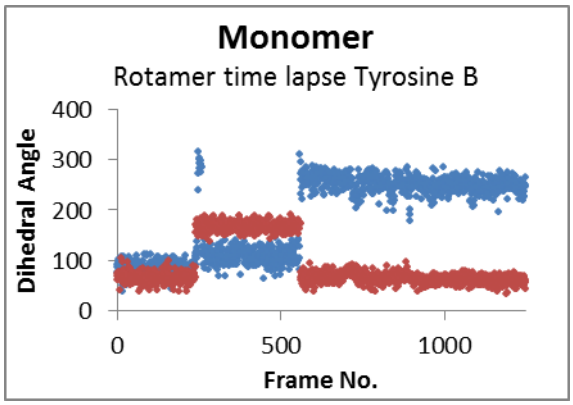

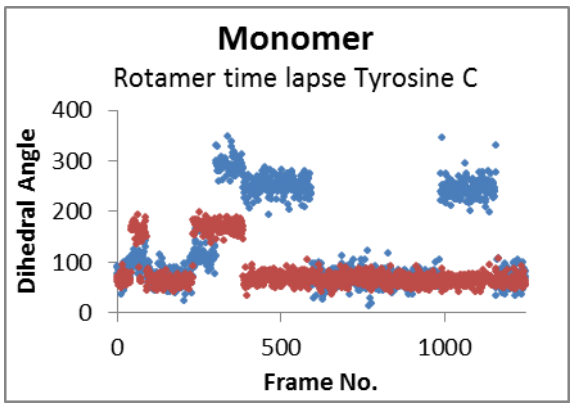

*Appendix 5.4 - **Four Protein System (with Aggregation)** Rotamer movements*

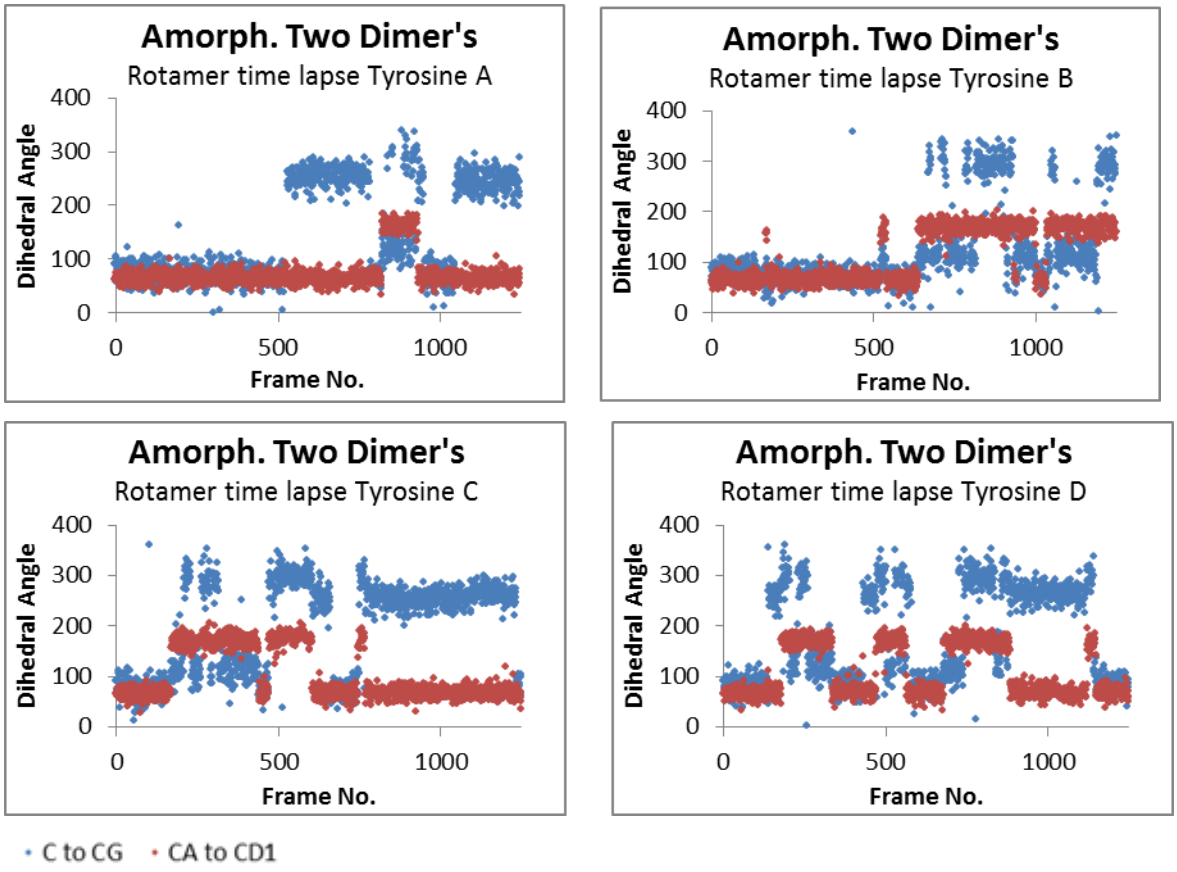

*Appendix 5.4 - **Six Protein System (Tetramer/dimer chain breaking)** Rotamer movements*

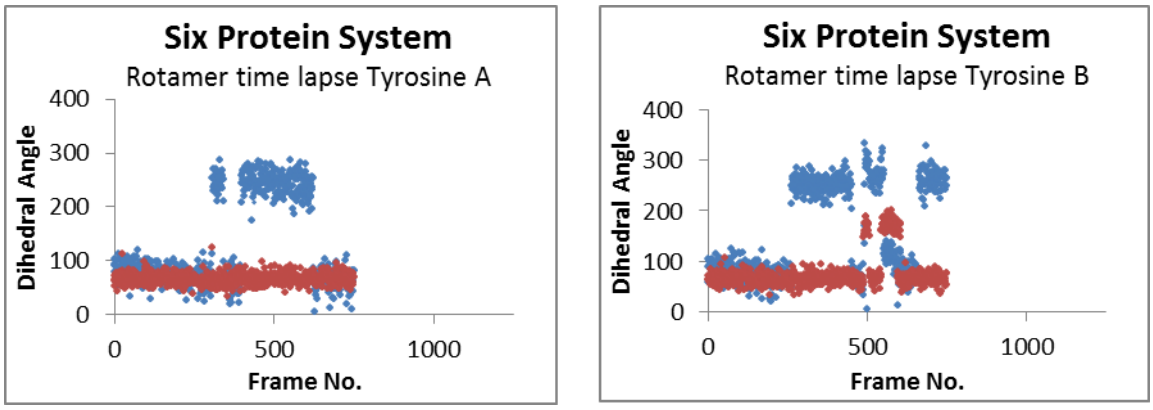

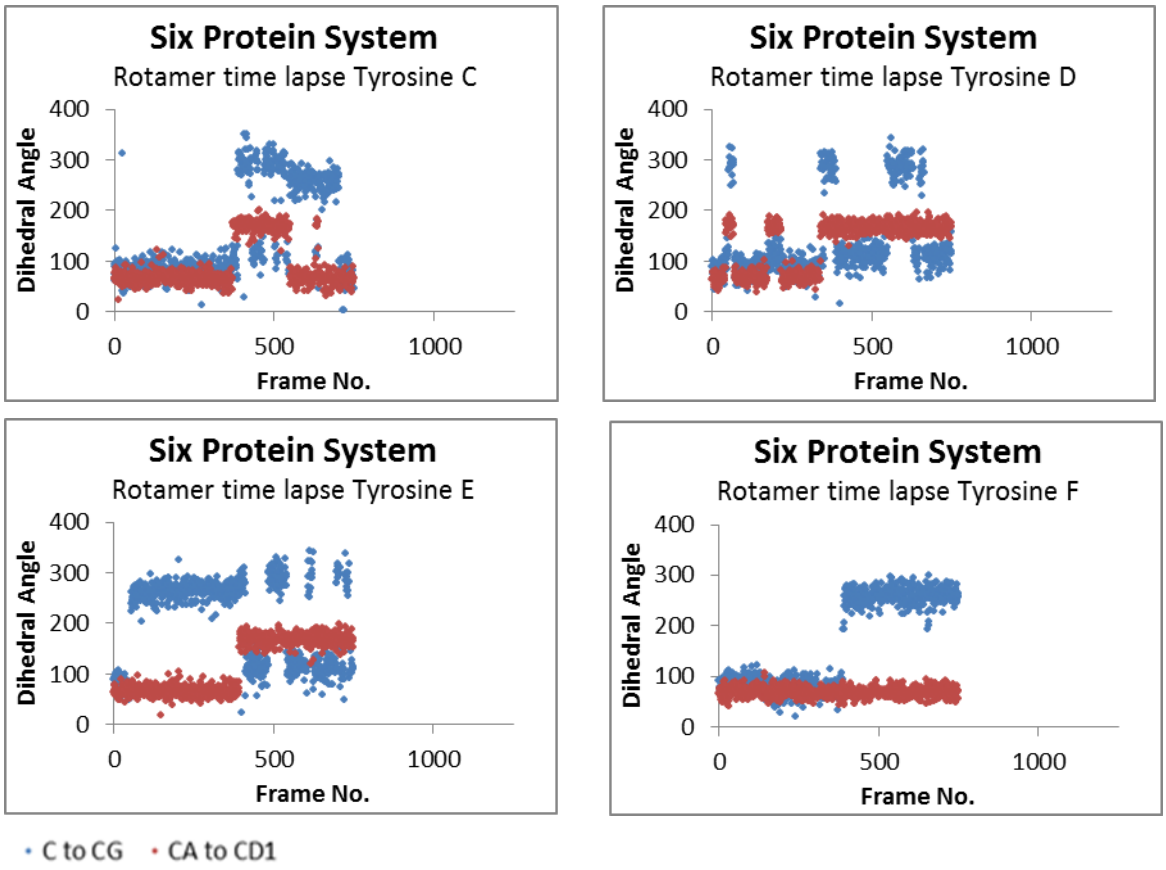

Appendix 5.6 - Four Protein System (with Aggregation) with crash.

The following amorphous system did not complete its full 1250 frame (50ns) trajectory as the waterbox was too small (as shown by the repeating blue protein seen in Figure 152 below), in an attempt to save processing power. Nevertheless, information can be extracted from the results up to 40ns (1000 frames) (see Figure 152). At approximately frame 1050, monomer A begins interacting with monomer B, which then interacts with monomer C. Monomer C passes through the periodic boundary, aggregating with monomer A. This creates a percolating aggregate that nominally has an infinite size; the simulation crashed after this point.

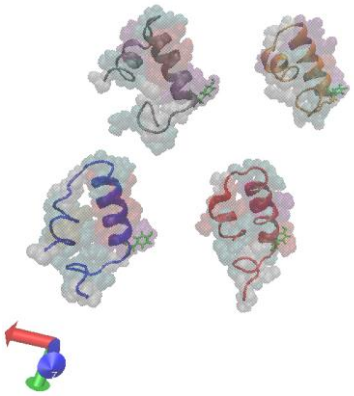	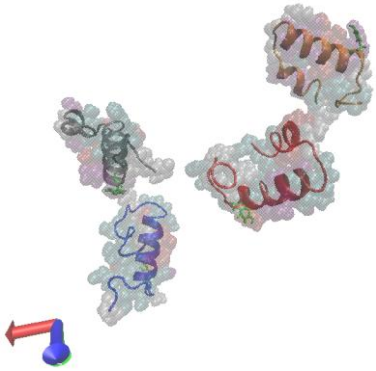	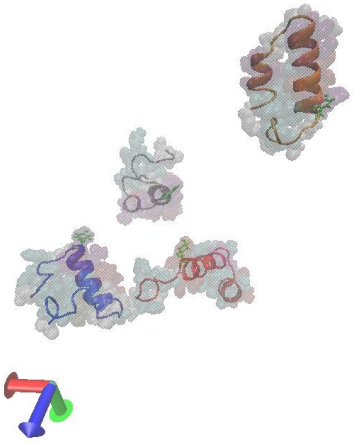
T=0ns	T=20ns	T=40ns
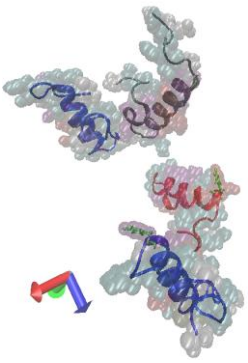		
43ns (Crash)		

Figure 152 – Failed Four Monomer System at time = 0ns, 20ns, 40ns, with crash at 43ns after infinite aggregate formed as apparent from the blue protein appearing twice. With protein A shown in blue, protein B shown in red, protein C shown in grey and protein D shown in orange. The VDW spheres are shown in grey.

As the trajectory begins monomer A and C move away from any neighbouring proteins and monomers B and D initially move closer together. As the trajectory progresses monomer B moves away from D, and begins to move closer to A and C. At this point monomer A is already interacting with monomer C through the periodic boundary. Monomer B starts interacting with monomer A and C simultaneously. This creates an interaction between A and B, B and C, and (through the boundary) C and A, which in turn creates the infinite loop of interactions.

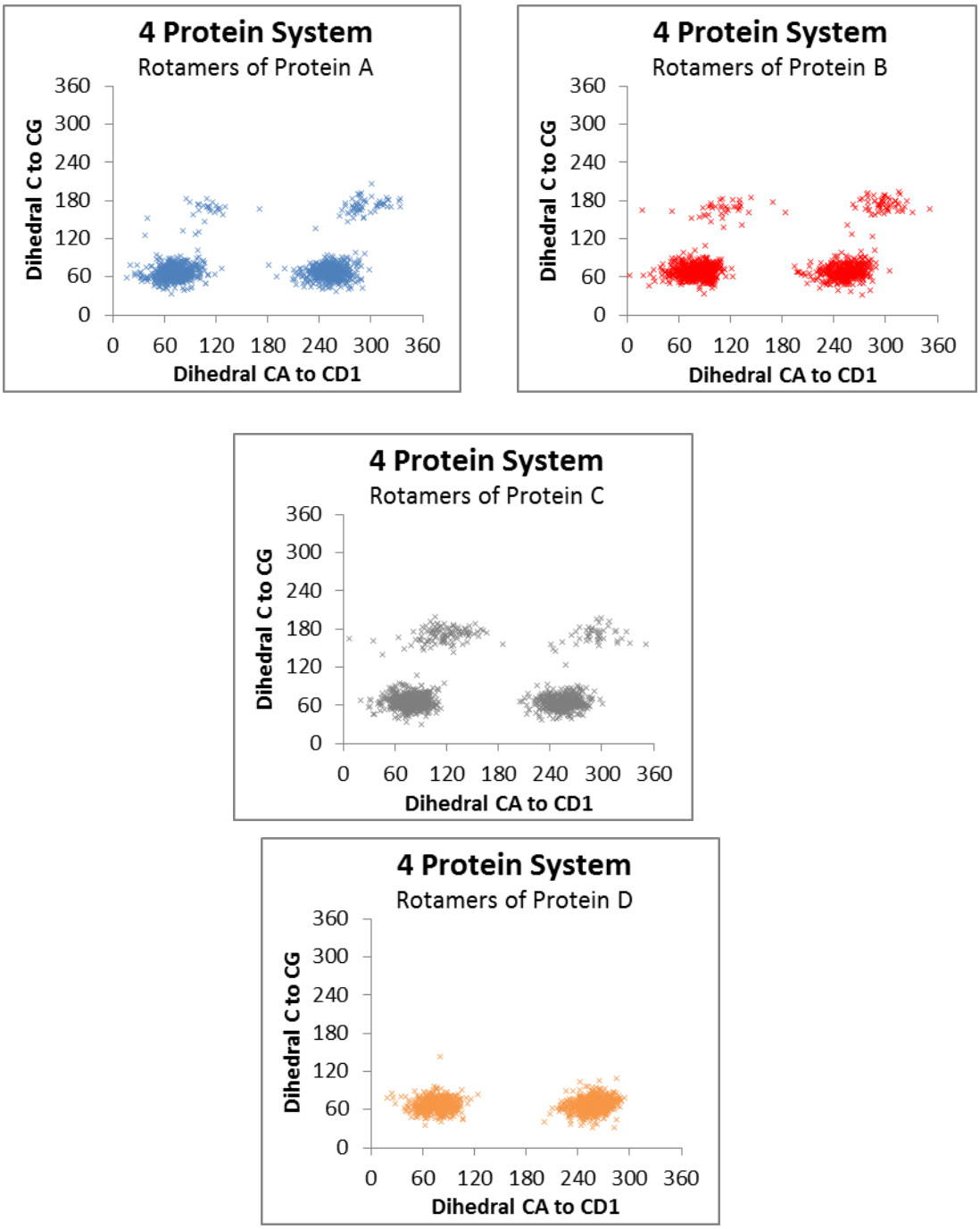

Figure 153 – Failed Four Monomer System Rotamer Response. The centre for each is approximately (65,60), (250,60),(100,170) and (290,175) for Tyr A. Tyr B has approximately (70,65), (250,65),(100,170) and (300,175). Tyr C has (70,65), (65, 250) (110,170) and (170,290). Tyr D has (70,65), (65, 260)

Tyr A B and C all have traditional rotamer angle distributions with some slight variation consistent with other monomers / amorphous aggregates (see Figure 153). In contrast, Tyr D remains a monomer throughout the simulation and has minimal

interactions with other proteins. It only occupies states 1 and 2, which suggests the interactions are influencing its movements.

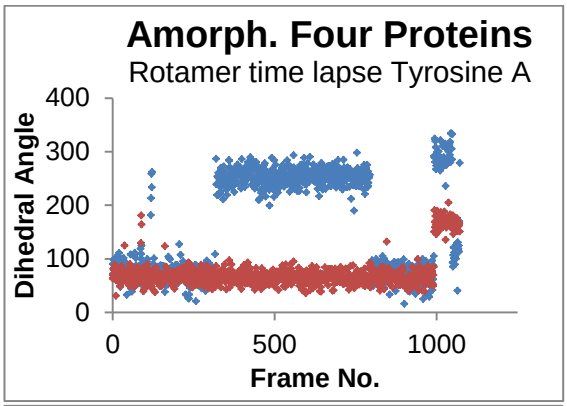

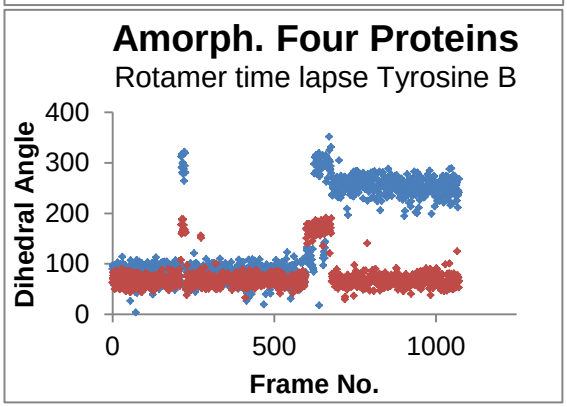

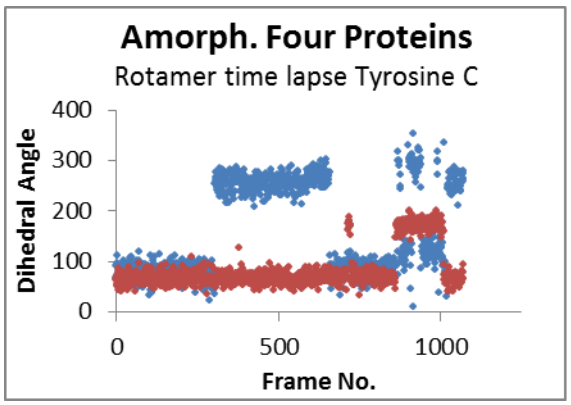

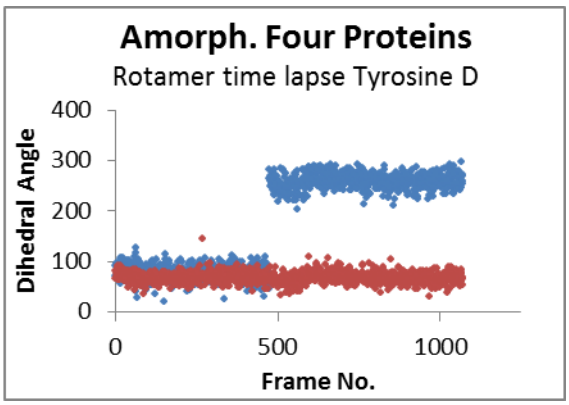

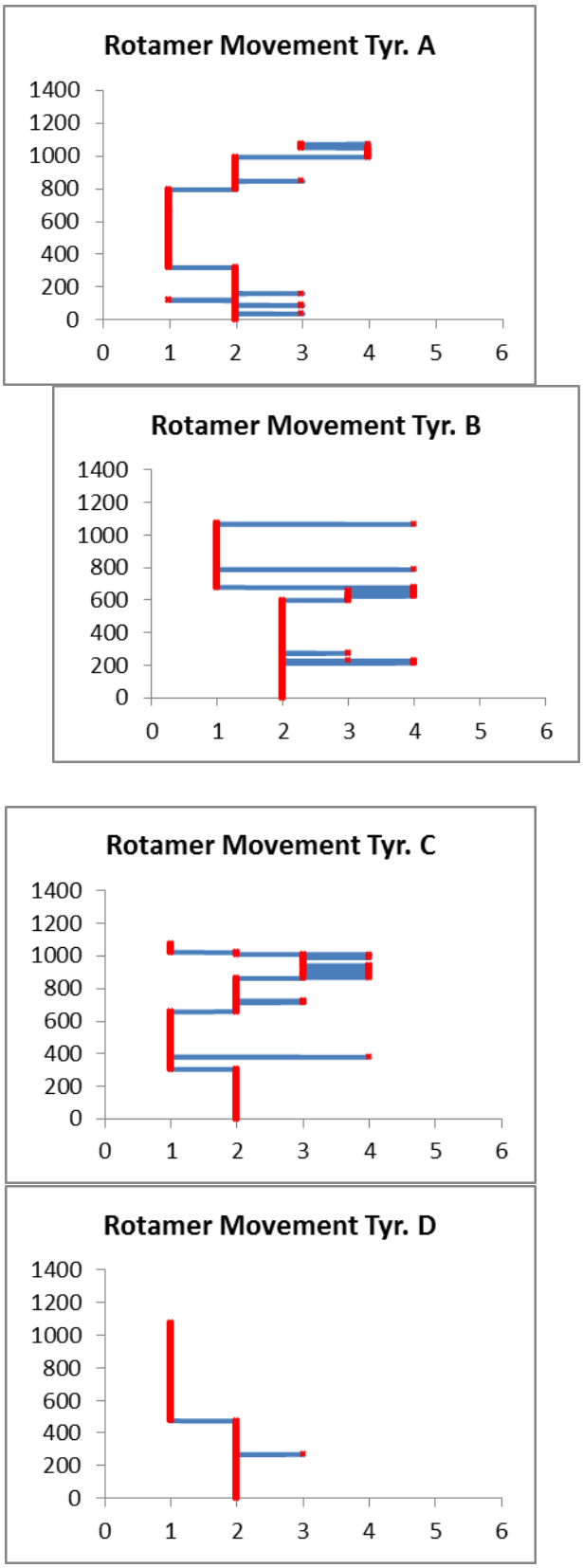

Figure 154 - Time Lapse Rotamer Response of Failed Four Monomer System

Figure 154 shows that the three interacting proteins (A,B and C), which begin to form an aggregate, have Tyr side-chains that move between the four rotamer states relatively regularly. These show a fair degree of influence from their surroundings, causing the Tyr to twist into states 3 and 4. Despite the aggregate forming as this trajectory begins, it is reasonable that these Tyr side-chains will show a preference to states 1 and 2. This is because it is in the process of aggregating and therefore the Tyr side-chains are not necessarily always being influenced by their surroundings, creating the necessary twist in the C to C_G dihedral angle. This is reflected in the graphs as they start to show more of preference to states 3 and 4 near the middle and end of the trajectories, as the proteins start to interact more prominently.

Tyr D as a monomer shows the expected preference to states 1 and 2 but has little movement, possibly due to interactions being caused across the periodic boundary due to small waterbox used, influencing the movement of the Tyr side-chain.

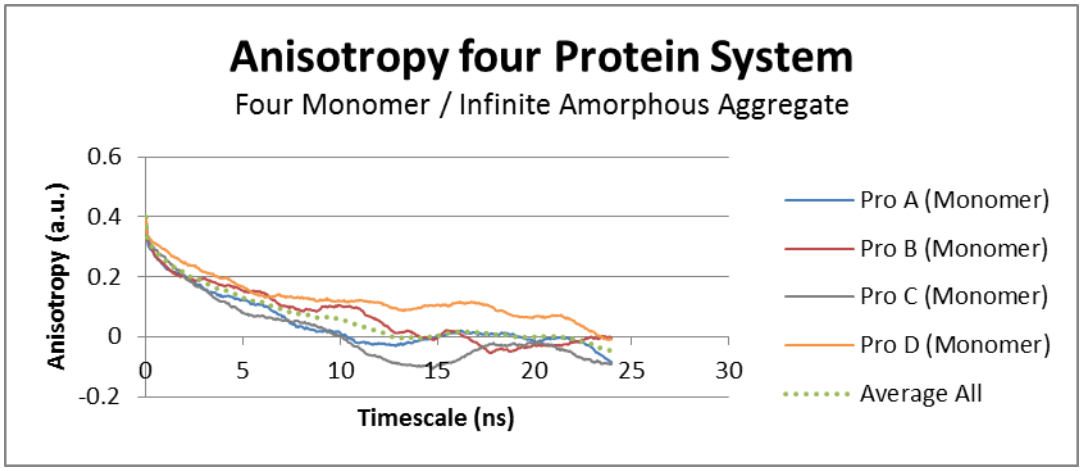

Figure 155 - Simulated Anisotropy of Failed Four Protein System. This graph shows the simulated anisotropy of both Proteins A (blue), B (red) C (grey) and D (orange) as well as the average (dotted green).

Proteins A and C have similar initial decays followed by a rapid relaxation to 0 at a correlation time of 10ns. Proteins B has a shorter lived initial decay and a second sharp decay at around a correlation time of 10ns and decays to 0 at about 13ns. The slower decay for Protein B is likely due to spending more time in states 1 and 2 without moving between the states as often as Proteins A and C (Figure 155).

These responses are similar to that seen for monomers due to the fast movements of the Tyr side-chains, although they take significantly longer to reach 0 than a monomer suggesting some aggregation is beginning to take place. The reason it does not have a higher plateau value is because the trajectory is too short (due to the crash) and as such the pre- and post-aggregation movements of the proteins will be included. This creates significantly more movement in the proteins as they move closer together and also try to become stable in the aggregate. It is likely that if the trajectory could have continued, and an analysis of the end section of simulation was undertaken, a more defined aggregate decay curve would have been found.

Protein D has an aggregate-like response, as it has a slower initial decay and a relaxation period that does not reach 0 until the end of the decay at a correlation time of 23ns. This is due to the lack of movement for the Tyr side-chain and also the lack of movement for the protein. This is because it will have limited space to move around due to the small waterbox.

The average decay for this system has a short lived initial decay and a long relaxation period that reaches 0 at a correlation time of approximately 14ns. This result suggests aggregation is, at the very least, beginning to occur.

Best fits

The monomer's best fit graph (Figure 110 and Table 11) shows that the fast Tyr movements have a significantly higher contribution than the bulk aggregate rotation. This is reasonable as there is limited ability for the proteins to move due to the small waterbox (as seen clearly with monomer D.) The other proteins do have more room to move as they begin to aggregate, creating more space to move temporarily until they aggregate, which will slow down their rotation when they are part of the bulk aggregate.

The system has an r_∞ value of 0 due to the movements as expected, a fast 0.04ns τ_r value for the Tyr movements and a 5.209ns τ_r value for the bulk rotation, which is reasonably slower than a monomer as this is a monomer system that is slowly aggregating.

Appendix 6 (Chapter 7) MD Simulations for Beta-sheet Aβ1-42

Appendix 6.1 - Flat-sheet Dimer Rotamer movements

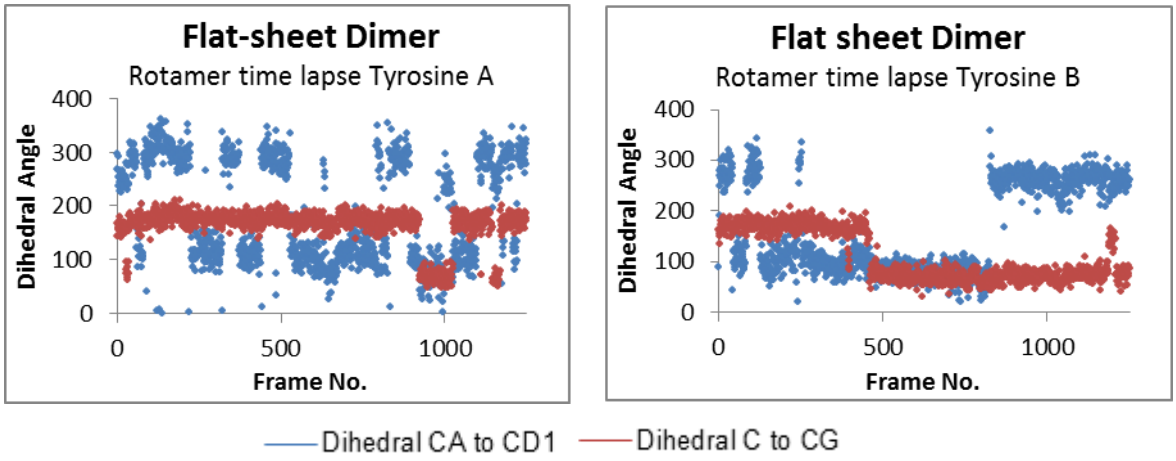

Appendix 6.2 - Stacked Dimer Rotamer movements

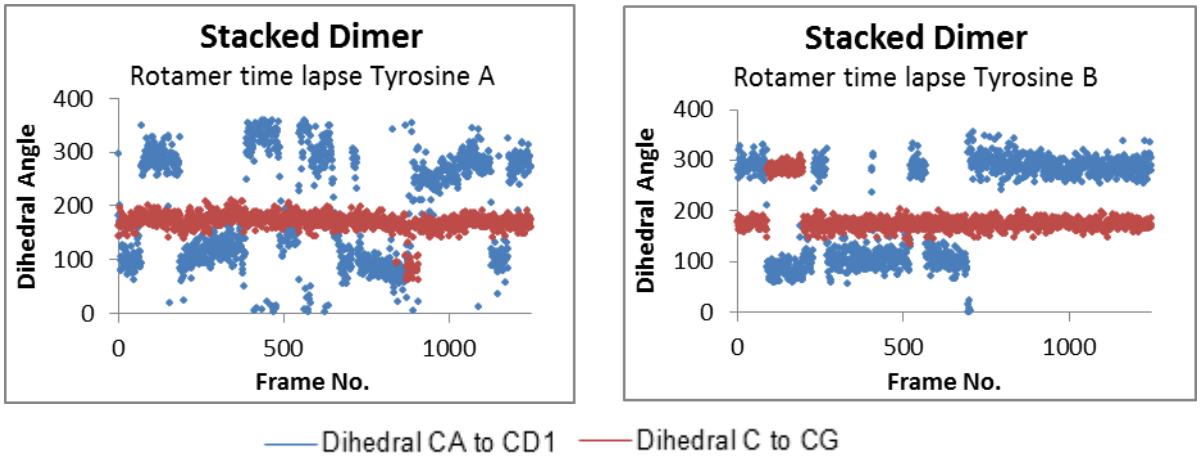

Appendix 6.2 - L-Shaped Trimer Rotamer movements

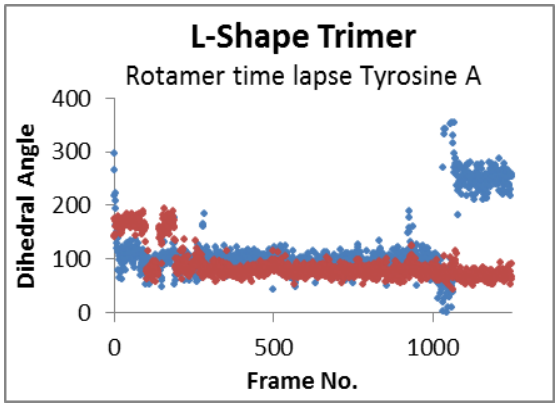

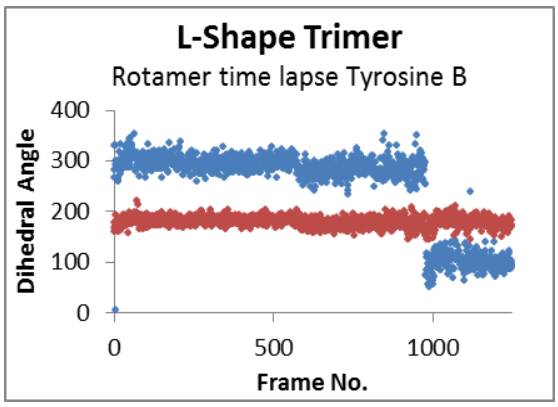

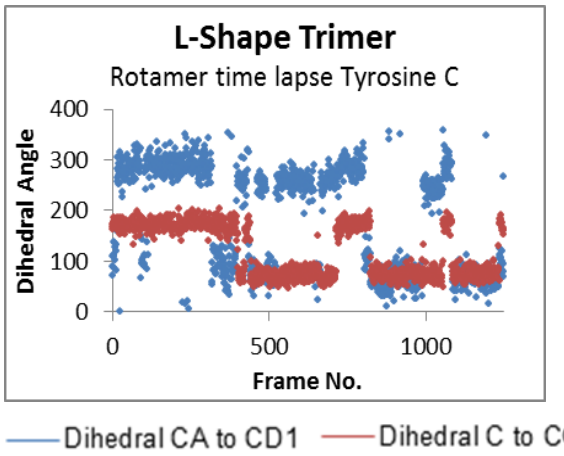

Appendix 6.3 - Stacked Trimer Rotamer movements

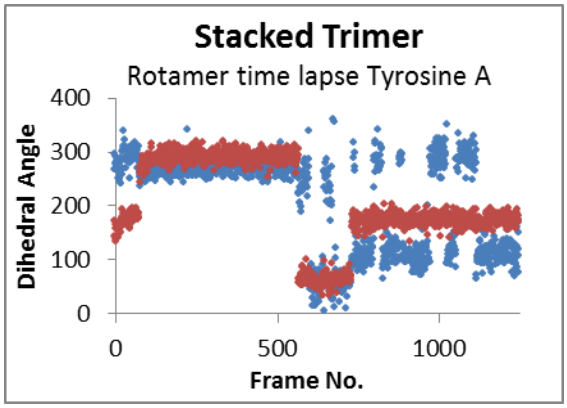

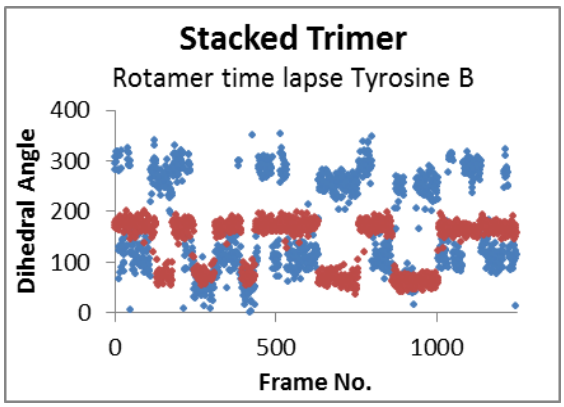

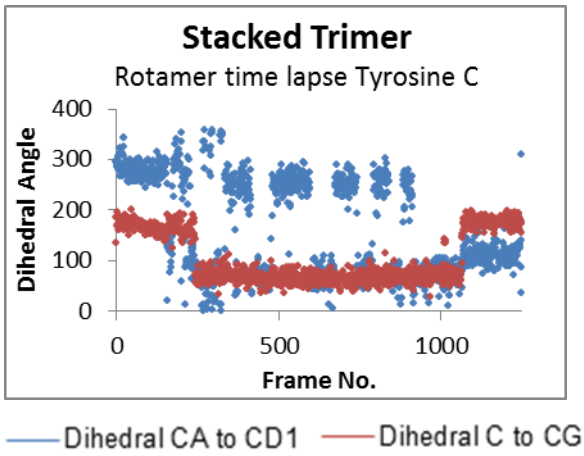

Appendix 6.4 - Flat-sheet Tetramer Rotamer movements

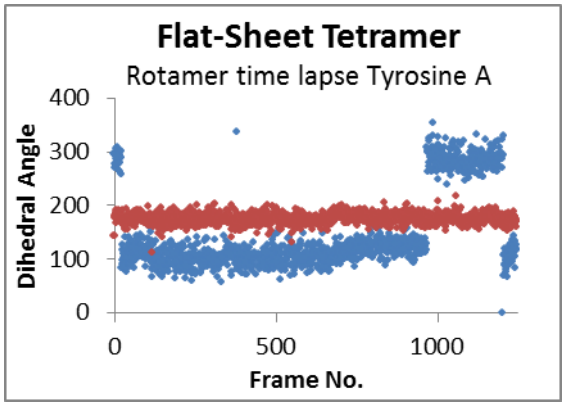

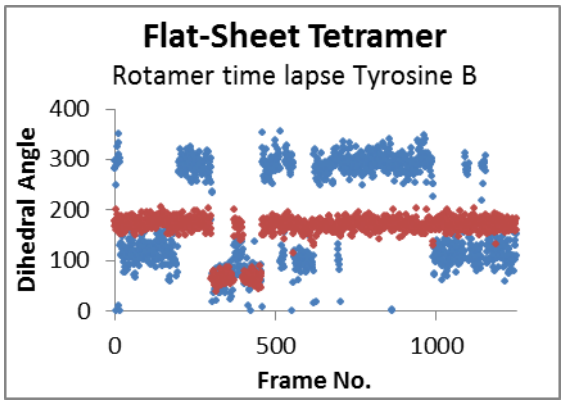

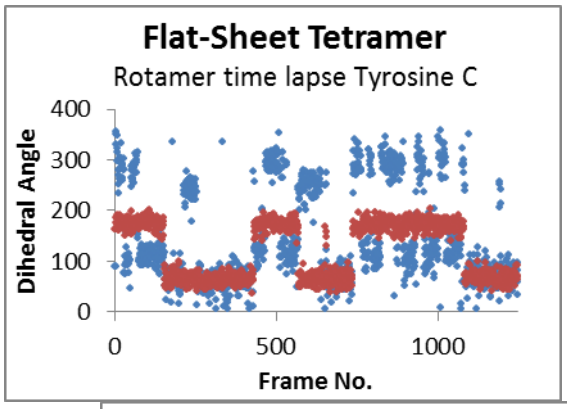

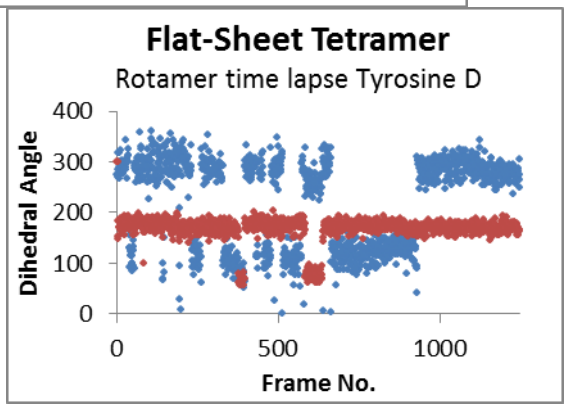

Dihedral CA to CD1 Dihedral C to CG

Appendix 6.5 - L-Shaped Tetramer Rotamer movements

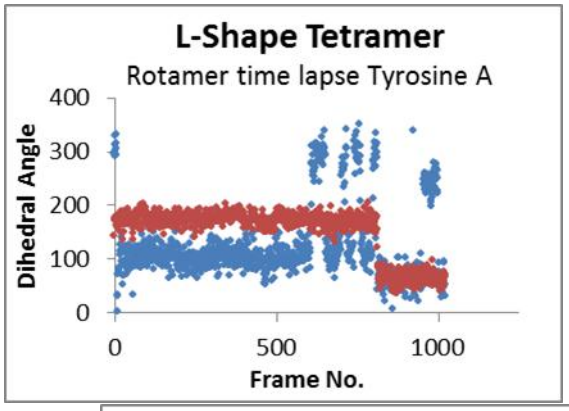

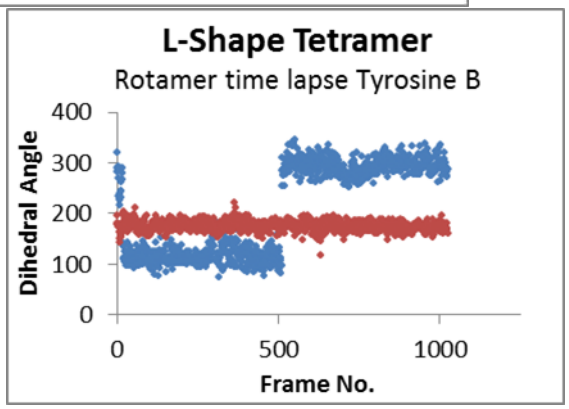

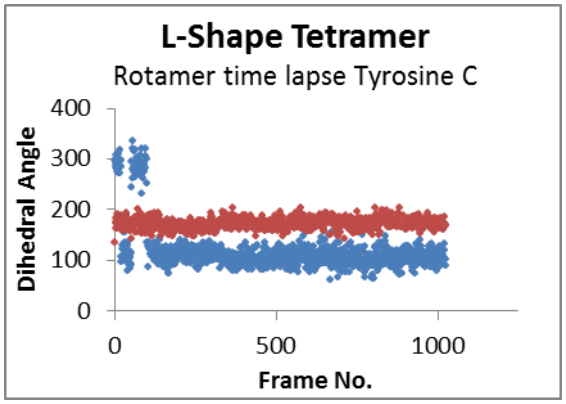

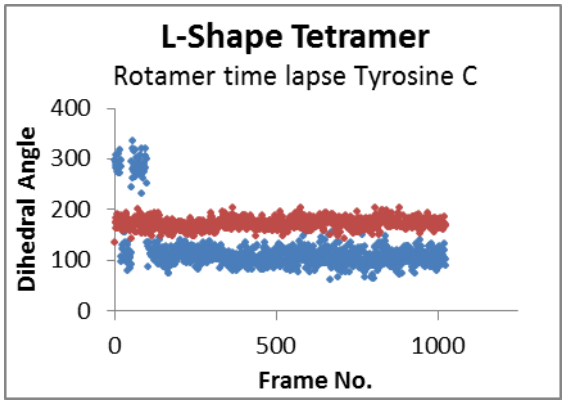

Dihedral CA to CD1 Dihedral C to CG

Appendix 6.6 - Beta-sheet Hexamer without Ions Rotamer movements

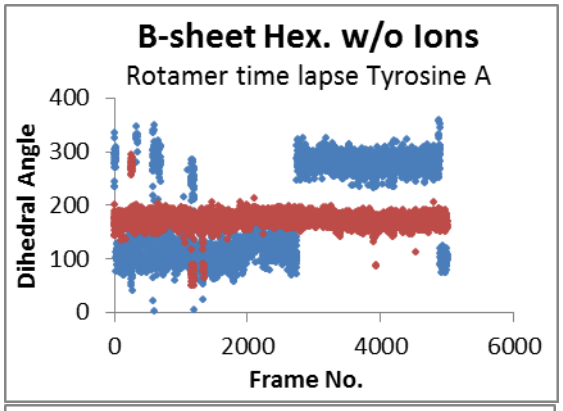

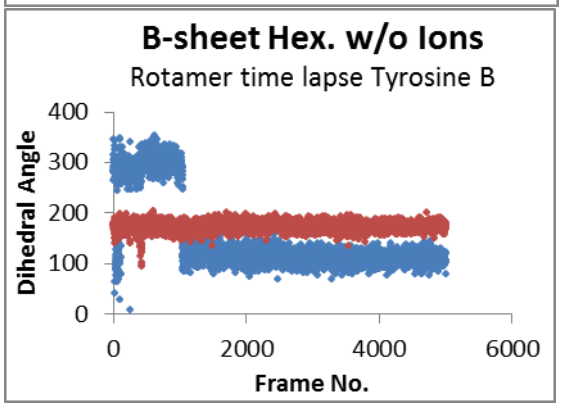

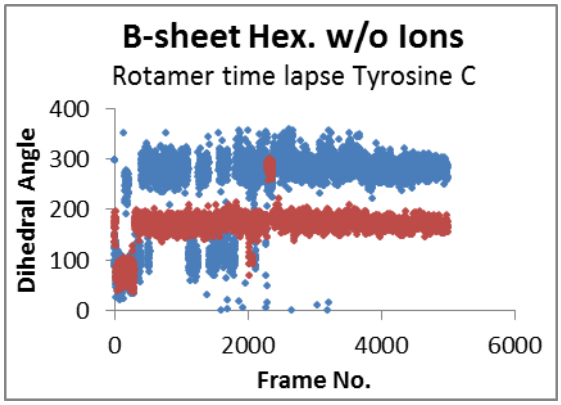

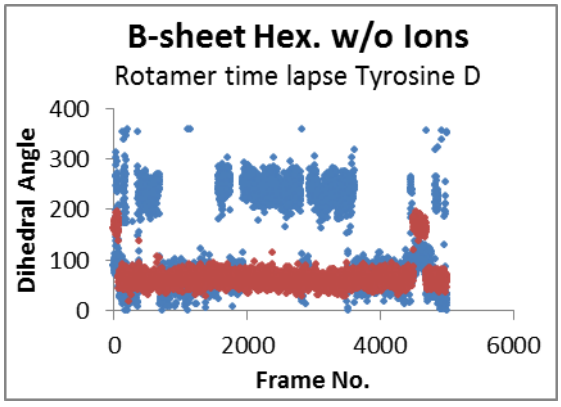

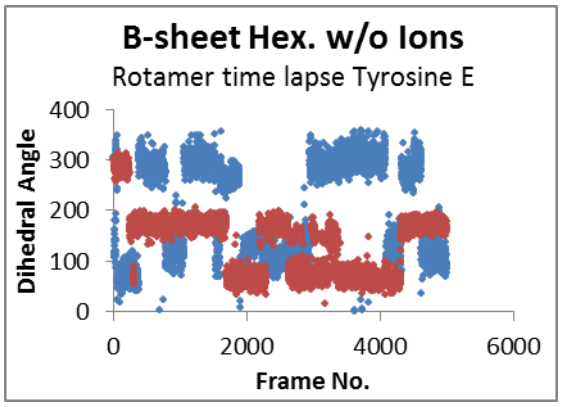

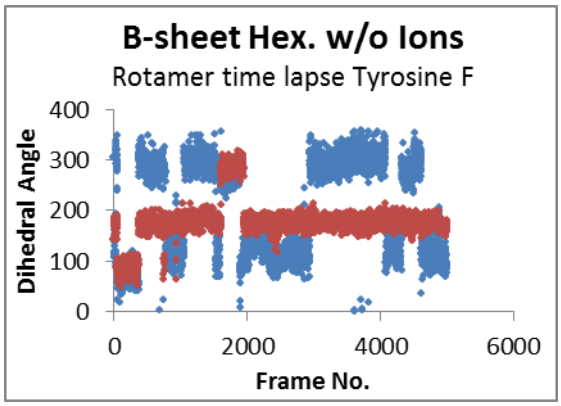

Dihedral CA to CD1 Dihedral C to CG

Appendix 6.7 - Beta-sheet Hexamer with Ions Rotamer movements

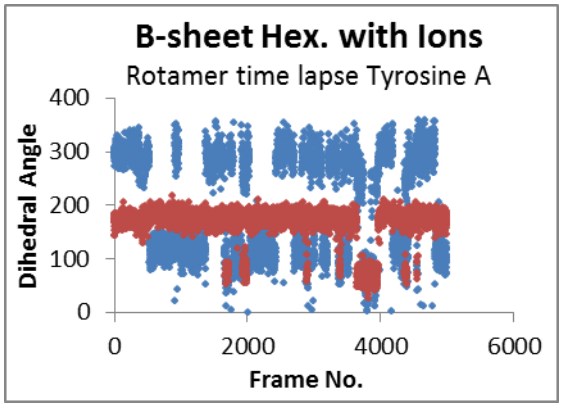

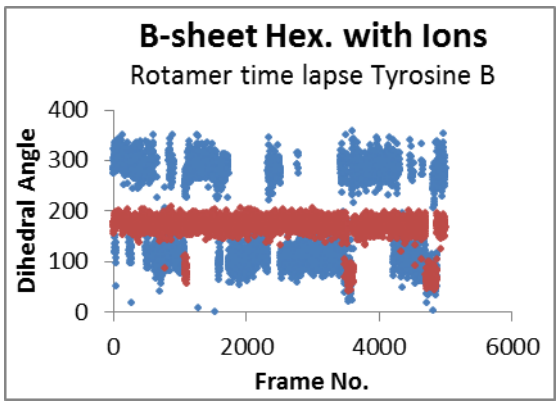

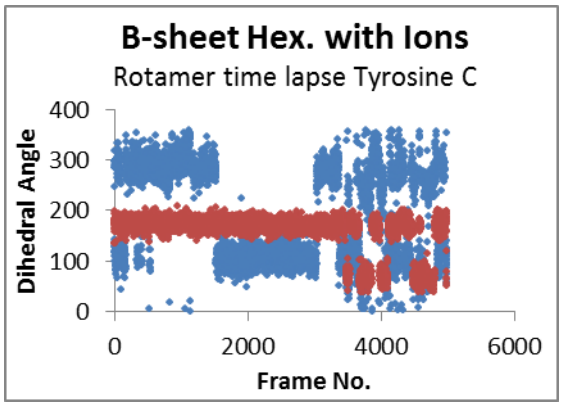

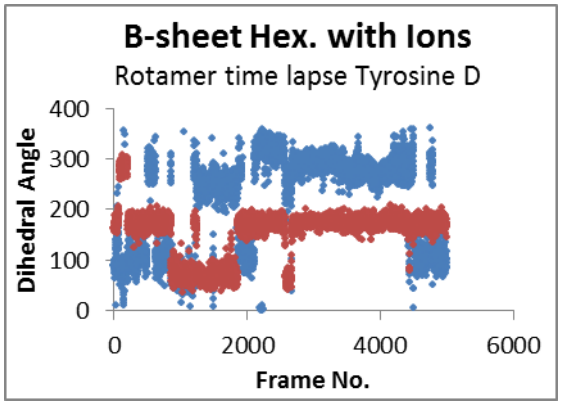

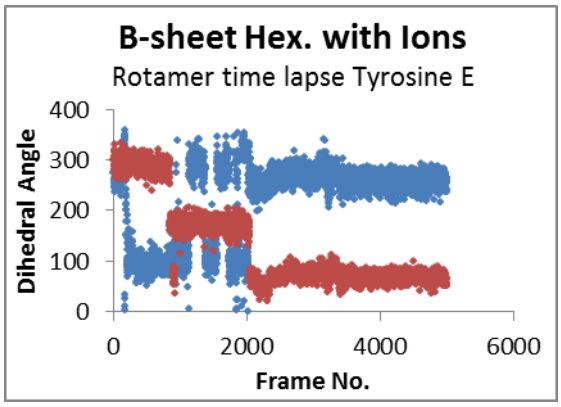
B-sheet Hex. with Ions
Rotamer time lapse Tyrosine E
Dihedral Angle
400
300
200
100
0
0
2000
4000
6000
Frame No.

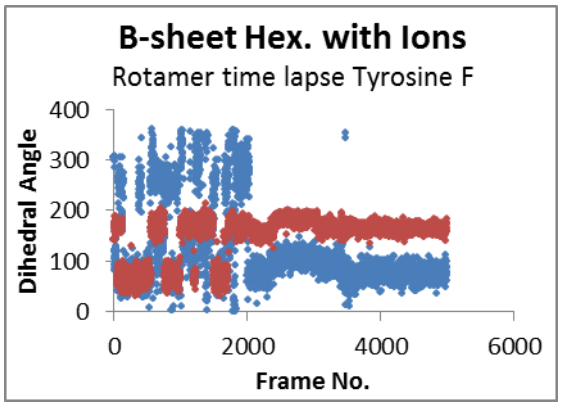
B-sheet Hex. with Ions
Rotamer time lapse Tyrosine F
Dihedral Angle
400
300
200
100
0
0
2000
4000
6000
Frame No.


Dihedral CA to CD1
Dihedral C to CG